
Theses and Dissertations

Spring 2012

Exploring the benefits of satellite remote sensing for flood prediction across scales

Luciana Kindl da Cunha
University of Iowa

Copyright 2012 Luciana Kindl da Cunha

This dissertation is available at Iowa Research Online: <https://ir.uiowa.edu/etd/2848>

Recommended Citation

Cunha, Luciana Kindl da. "Exploring the benefits of satellite remote sensing for flood prediction across scales." PhD (Doctor of Philosophy) thesis, University of Iowa, 2012.
<https://doi.org/10.17077/etd.es9ooi4m>.

Follow this and additional works at: <https://ir.uiowa.edu/etd>



Part of the [Civil and Environmental Engineering Commons](#)

EXPLORING THE BENEFITS OF SATELLITE REMOTE SENSING
FOR FLOOD PREDICTION ACROSS SCALES

by

Luciana Kindl da Cunha

An Abstract

Of a thesis submitted in partial fulfillment
of the requirements for the Doctor of Philosophy degree
in Civil and Environmental Engineering in
the Graduate College of
The University of Iowa

May 2012

Thesis Supervisor: Professor Witold F Krajewski

ABSTRACT

Space-borne remote sensing datasets have the potential to allow us to progress towards global scale flood prediction systems. However, these datasets are limited in terms of space-time resolution and accuracy, and the best use of such data requires understanding how uncertainties propagate through hydrological models. An unbiased investigation of different datasets for hydrological modeling requires a parsimonious calibration-free model, since calibration masks uncertainties in the data and model structure. This study, which addresses these issues, consists of two parts: 1) the development and validation of a multi-scale distributed hydrological model whose parameters can be directly linked to physical properties of the watershed, thereby avoiding the need of calibration, and 2) application of the model to demonstrate how data uncertainties propagate through the model and affect flood simulation across scales.

I based the model development on an interactive approach for model building. I systematically added processes and evaluated their effects on flood prediction across multiple scales. To avoid the need for parameter calibration, the level of complexity in representing physical processes was limited by data availability. I applied the model to simulate flows for the Cedar River, Iowa River and Turkey River basins, located in Iowa. I chose this region because it is rich in high quality hydrological information that can be used to validate the model. Moreover, the area is frequently flooded and was the center of an extreme flood event during the summer of 2008. I demonstrated the model's skills by simulating medium to high-flow conditions; however the model's performance is relatively poor for dry (low flow) conditions. Poor model performance during low flows

is attributed to highly nonlinear dynamics of soil and evapotranspiration not incorporated in the model.

I applied the hydrological model to investigate the predictability skills of satellite-based datasets and to investigate the model's sensibility to certain hydro-meteorological variables such as initial soil moisture and bias in evapotranspiration. River network structure and rainfall are the main components shaping floods, and both variables are monitored from space. I evaluated different DEM sources and resolution DEMs as well as the effect of pruning small order channels to systematically decreasing drainage density. Results showed that pruning the network has a greater effect on simulated peak flow than the DEM resolution or source, which reveals the importance of correctly representing the river network. Errors on flood prediction depend on basin scale and rainfall intensity and decrease as the basin scale and rainfall intensity increases. In the case of precipitation, I showed that simulated peak flow uncertainties caused by random errors, correlated or not in space, and by coarse space-time data resolution are scale-dependent and that errors in hydrographs decrease as basin scale increases. This feature is significant because it reveals that there is a scale for which less accurate information can still be used to predict floods. However, the analyses of the real datasets reveal the existence of other types of error, such as major overall bias in total volumes and the failure to detect significant rainfall events that are critical for flood prediction.

Abstract Approved: _____

Thesis Supervisor

Title and Department

Date

EXPLORING THE BENEFITS OF SATELLITE REMOTE SENSING
FOR FLOOD PREDICTION ACROSS SCALES

by

Luciana Kindl da Cunha

A thesis submitted in partial fulfillment
of the requirements for the Doctor of Philosophy degree
in Civil and Environmental Engineering in
the Graduate College of
The University of Iowa

May 2012

Thesis Supervisor: Professor Witold F Krajewski

Graduate College
The University of Iowa
Iowa City, Iowa

CERTIFICATE OF APPROVAL

PH.D THESIS

This is to certify that the Ph.D. thesis of

Luciana Kindl da Cunha

has been approved by the Examining Committee
for the thesis requirement for the Doctor of Philosophy
degree in Civil and Environmental Engineering at the May 2012 graduation.

Thesis Committee:

Witold F. Krajewski, Thesis Supervisor

Allen Bradley

James Smith

Larry Weber

Nandita Basu

Ricardo Mantilla

To my sweet parents and siblings,

Joao Carlos da Cunha and Sieglinde Kindl da Cunha
Carolina Kindl da Cunha and Luiz Frederico Kindl da Cunha

ACKNOWLEDGEMENTS

This thesis would not have been possible without the help of great many individuals. First and foremost I offer my sincerest gratitude to my supervisor, Prof. Witold Krajewski. I thank him for continuous support and encouragement throughout the course of this thesis. He provided the best guidance, steered me in the right direction, while always allowing me the room to work in my own way. What I have learned from him is not limited to science, but it is a whole life style. I would like to extend my gratitude to Dr. Ricardo Mantilla, Allen Bradley, James Smith, Larry Weber, and Nandita Basu for serving on my thesis committee, and for their useful suggestions. I also would like to thank my master adviser, Alexandre Guetter, for believing in me since the beginning of my carrier.

I would like to thank my lab mates Renato Frasson, Piotr Lewandowski, Pradeep Mandapaka, Gabriele Villarini, Achilleas Tsakiris, Filippo Bressan, and others, for their friendship, and for their help during various phases of the thesis,. Special thanks to Renato, for helping me with literally everything since I have moved to USA. According to my mom I find angels that help me wherever I go; Renato is one of them. Thanks to Radoslaw Goska for his help with the graphics often on a very short notice. I would also like to thank the administrative and computer staff of IIHR-Hydroscience and Engineering and from the Department of Civil and Environmental Engineer for their efficient handling of all non-research matters.

I take this opportunity to thank all the good friends I have made in Iowa for all the good times, and for the incredible support provided during good and bad moments. Special thanks to Milena, my best friend and twin soul! Also thanks to all my Brazilian friends, Bruno Uzeda, Bruno Paula, Vica, and many others, for bringing a little bit of my country to USA, Nikhil for adding a lot of adrenaline to my life, the UN group for all the

fun. I also would like to thanks all my friends in Brazil, specially Cris Staub, Cris Burmester, and Deborah Carvalho, for the long distance support.

It is impossible to put in words, the role of my Mom and Dad in shaping my career. I am grateful to them for their unconditional love and support and for instilling in me the value for education. I would like to thank my loving brother and sister for their constant encouragement. Last but not the least, my lovely family for all the love.

ABSTRACT

Space-borne remote sensing datasets have the potential to allow us to progress towards global scale flood prediction systems. However, these datasets are limited in terms of space-time resolution and accuracy, and the best use of such data requires understanding how uncertainties propagate through hydrological models. An unbiased investigation of different datasets for hydrological modeling requires a parsimonious calibration-free model, since calibration masks uncertainties in the data and model structure. This study, which addresses these issues, consists of two parts: 1) the development and validation of a multi-scale distributed hydrological model whose parameters can be directly linked to physical properties of the watershed, thereby avoiding the need of calibration, and 2) application of the model to demonstrate how data uncertainties propagate through the model and affect flood simulation across scales.

I based the model development on an interactive approach for model building. I systematically added processes and evaluated their effects on flood prediction across multiple scales. To avoid the need for parameter calibration, the level of complexity in representing physical processes was limited by data availability. I applied the model to simulate flows for the Cedar River, Iowa River and Turkey River basins, located in Iowa. I chose this region because it is rich in high quality hydrological information that can be used to validate the model. Moreover, the area is frequently flooded and was the center of an extreme flood event during the summer of 2008. I demonstrated the model's skills by simulating medium to high-flow conditions; however the model's performance is relatively poor for dry (low flow) conditions. Poor model performance during low flows

is attributed to highly nonlinear dynamics of soil and evapotranspiration not incorporated in the model.

I applied the hydrological model to investigate the predictability skills of satellite-based datasets and to investigate the model's sensibility to certain hydro-meteorological variables such as initial soil moisture and bias in evapotranspiration. River network structure and rainfall are the main components shaping floods, and both variables are monitored from space. I evaluated different DEM sources and resolution DEMs as well as the effect of pruning small order channels to systematically decreasing drainage density. Results showed that pruning the network has a greater effect on simulated peak flow than the DEM resolution or source, which reveals the importance of correctly representing the river network. Errors on flood prediction depend on basin scale and rainfall intensity and decrease as the basin scale and rainfall intensity increases. In the case of precipitation, I showed that simulated peak flow uncertainties caused by random errors, correlated or not in space, and by coarse space-time data resolution are scale-dependent and that errors in hydrographs decrease as basin scale increases. This feature is significant because it reveals that there is a scale for which less accurate information can still be used to predict floods. However, the analyses of the real datasets reveal the existence of other types of error, such as major overall bias in total volumes and the failure to detect significant rainfall events that are critical for flood prediction.

TABLE OF CONTENTS

LIST OF TABLES	x
LIST OF FIGURES	xi
CHAPTER I INTRODUCTION.....	1
Motivation.....	1
Objectives and research questions	3
Literature Review: Progress towards a global scale flood prediction system	4
State-of-the-art hydrological modeling	4
Direct and indirect application of remotely sensed data for flood prediction.....	9
Study Area	11
Methodology.....	14
Overview of thesis chapters.....	18
CHAPTER II TOWARDS A CALIBRATION-FREE HYDROLOGICAL MODEL.....	28
Criteria for model design.....	28
Model development: general model components and complexity level	30
Landscape decomposition and control volumes	33
General model description.....	35
Model input: Hydrometeorological variables.....	37
Model parameters	38
Balance equations and fluxes.....	49
Conclusions.....	56
CHAPTER III MODEL APPLICATION.....	66
Introduction.....	66
Model results	67
Why should we avoid calibration?	72
Synthetic rainfall simulations	72
Simulation using real rainfall event.....	74
Major model limitations	76
Conclusions.....	79
CHAPTER IV IMPACT OF DEM SOURCE, RESOLUTION, AND NETWORK PRUNING ON THE CHARACTERIZATION OF THE RIVER NETWORK AND ON ESTIMATION OF PEAK FLOW MAGNITUDE AND TIMING ACROSS SCALES.....	95
Introduction.....	95
Rainfall	99
Digital elevation models.....	99
Methodology.....	100
Landscape decomposition method	101
Criteria for DEM evaluation: geomorphological properties and hydrological simulation	102
Results.....	104

River network extraction	104
River network properties: width function and maximum of the width function.....	106
Effects on hydrological simulation: 2008 Iowa flood event	107
Effects on hydrological simulation: synthetic rainfall.....	110
Conclusions.....	111
 CHAPTER V IMPACT OF RADAR-RAINFALL ERROR STRUCTURE ON ESTIMATED FLOOD MAGNITUDE ACROSS SCALES.....	125
Introduction.....	125
Study area and model version.....	129
Methodology.....	131
Radar rainfall error model and ensemble generator	133
Results and Discussion	136
Radar error structure scenarios.....	136
Validation of hydrological simulations	138
Analysis of error propagation.....	142
Conclusions.....	146
 CHAPTER VI IMPLICATIONS OF PRECIPITATION RESOLUTION AND SAMPLING INTERVAL FOR PEAK FLOW SIMULATION	160
Introduction.....	160
Dataset - rainfall	163
Methodology.....	164
Results and Analysis.....	165
Impact of coarse spatial and temporal resolution.....	165
Impact of low temporal sampling.....	167
Conclusions.....	168
 CHAPTER VII EVALUATION OF DIFFERENT PRECIPITATION DATASETS AND THEIR IMPACT ON FLOOD PREDICTION	173
Introduction.....	173
Datasets.....	174
Weather radar datasets.....	174
Satellite-based datasets.....	179
Other datasets	180
Comparison of rainfall totals for different products	182
For the 2008 flood event.....	182
For years 2002, 2003, and 2004	183
Comparison of simulated peak flow based on different products	183
For the 2008 flood event.....	183
Peak flow simulation for years 2002, 2003, and 2004	186
Conclusions.....	187
 CHAPTER VIII THE IMPACT OF EVAPOTRANSPIRATION AND SOIL MOISTURE INITIAL CONDITION ON FLOOD PEAK SCALING	199
Introduction.....	199
Datasets.....	200
Potential evapotranspiration	200
Soil moisture initial conditions.....	201

Methodology.....	201
Results and Analysis.....	202
Conclusions.....	203
CHAPTER IX CONCLUSIONS AND RECOMMENDATIONS FOR FURTHER STUDIES.....	207
APPENDIX NETWORK HYDRAULIC GEOMETRY.....	211
Introduction.....	211
Data.....	214
At-a-station HG and scaling dependence	215
Network hydraulic geometry (N-HG)	217
Application for flood simulation	218
Flood wave velocity versus water velocity	218
Parameter estimation for real events simulation	220
Effects of N-HG on the scaling properties of flood.....	221
Conclusions.....	223
REFERENCES	231

LIST OF TABLES

Table I-1. Space-based remote sensing and global datasets, and high resolution datasets used to represent physical processes and properties responsible for flood generation	22
Table I-2. USGS sites in the Cedar River (CR), Iowa River (IR), and Turkey River (TR) basin.....	24
Table II-1. Processes representation and data requirements for different models version with multiple complexity levels.....	58
Table II-2. List of model’s parameters, forcing, fluxes, and state variables.....	60
Table III-1. Dataset used in the simulations	81
Table IV-1. Different sources of DEM data with main characteristics and links for data repository	114
Table IV-2. List of DEM used to extract the river network of Clear Creek and Cedar River basin and main properties of the extracted network	115
Table V-1. Rainfall error scenarios considered in this study.....	148
Table V-2. Statistics for CUENCAS and the Sacramento model.....	149
Table VII-1. Precipitation satellite products.....	189

LIST OF FIGURES

Figure I-1. Study area with USGS sites for which streamflow data is available.....	26
Figure I-2. Water balance for the Cedar River and Iowa River sites, from 2002 to 2009. All units are in mm/year: (a) annual rainfall; (b) annual evapotranspiration; (c) annual runoff; (d) annual water balance (difference between rainfall and sum of evapotranspiration and runoff).....	27
Figure II-1. Hydrological processes simulated by CUENCAS. Green box indicated the processes that were developed in this thesis.....	63
Figure II-2. Schematic representation of the scales simulated by the hydrological model: from local (hillslope) to Watershed scale (Cedar River basin)	63
Figure II-3. Schematic representation of the hillslope and channel physical properties and fluxes. The figure on the top (a) presents the fluxes between the hillslope surface and soil and the channel. The figures in the bottom presents a convex (b.1) and a concave (b.2) and their main physical properties.	64
Figure II-4. Soil properties for the study area. The maps in the top present SSURGO data that were used for the simulations presented in Chapter III. On the left I present saturated hydraulic conductivity (m/s) and on right available water capacity of soil (cm/150 cm of soil). On the bottom I present data provided by the Iowa Geological Survey, DNR. Bedrock surface elevation (ft) is presented on the left, and soils requiring tile drainage for full productivity on the right.	65
Figure III-1. Model results for 2008, Cedar River sites. Discharge is normalized by the mean annual flood. Dark blue lines are observed; gray lines are simulated by CUENCAS; and light blue lines are simulated by SAC-SMS. The numbers on the left indicate the site number (refer to Figure 1-1) and the basin drainage area. The numbers on the right are the statistics for CUENCAS and SAC-SMS (Nash coefficient, correlation coefficient). The last plot presents simulated (gray lines) and observed (blue line, based on MODIS 16) evapotranspiration results for the year 2008.	82
Figure III-2. Simulation of 2008 flood event for Iowa River sites. Gray line is simulated by CUENCAS, light blue is simulated by SAC-SMS, and dark blue line is observed.	83
Figure III-3. Simulation of 2008 flood event for Turkey River sites. Gray line is simulated by CUENCAS, light blue is simulated by SAC-SMS, and dark blue line is observed.	84
Figure III-4. Simulation of 2004 flood event for Cedar River sites. Gray line is simulated by CUENCAS, light blue is simulated by SAC-SMS, and dark blue line is observed.	85
Figure III-5. Simulation of 2004 flood event for Iowa River sites. Gray line is simulated by CUENCAS, light blue is simulated by SAC-SMS, and dark blue line is observed.	86

Figure III-6. Simulation of 2004 flood event for Turkey River sites. Gray line is simulated by CUENCAS, light blue is simulated by SAC-SMS, and dark blue line is observed.	87
Figure III-7. Simulation of 2002 streamflow for Cedar River sites. Gray line is simulated by CUENCAS, light blue is simulated by SAC-SMS, and dark blue line is observed.	88
Figure III-8. Simulation of 2003 streamflow for Cedar River sites. Gray line is simulated by CUENCAS, light blue is simulated by SAC-SMS, and dark blue line is observed.	89
Figure III-9. Observed (dark blue dots) peak flow and peak flow predicted by CUENCAS (gray) and SAC-SMS (light blue, when available) for the Cedar River basin for 2002 to 2009. The red line is a non-parametric regression line that estimates the expected value of peak flow as a function of area. The orange line is the mean annual flow.	90
Figure III-10. Same as Figure 1-12, but for years 2004 and 2008 for the Iowa and Turkey Rivers.	91
Figure III-11. Simulation results based on different rainfall total accumulations (60 and 120mm) with fixed duration (60 minutes). The different lines represent simulations with different channel velocities. The black line represents the most complete version of the hydrological model that was demonstrated to capture peak flow scaling for real events. Model specifications are specified in the top of each plot. Model complexity increases from the top to bottom.	92
Figure III-12. Simulated streamflow (dark blue) based on the following parameters: 0.8 runoff coefficient, 1.0 m/s channel velocity, and 0.01 m/s hillslope velocity. Observed values are presented in gray, and simulated values based on SAC-SMS, used as a reference, are presented in light blue. I present results for 3 sites (Wolf Creek, Beaver Creek, and Cedar River) for 2008, 1 site (Wolf Creek) for 2002, 1 site (Wolf Creek) for 2003, and 2 sites (Wolf Creek and Cedar River) for 2004.	93
Figure III-13. Simulated streamflow (dark blue) based on the following parameters: 0.2 runoff coefficient, 1.0 m/s channel velocity, and 0.01 m/s hillslope velocity. Observed values are presented in gray, and simulated values based on SAC-SMS, used as a reference, are presented in light blue. I present results for 3 sites (Little Cedar River, Wolf Creek, and Cedar River) for 2003, 2 sites (Little Cedar River and Cedar Rapids) for 2002, one site (Little Cedar River) for 2004, and 3 sites (Little Cedar River, Winnebago River, and Cedar River) for 2008.	94
Figure IV-1. Study area. The background shows the 90 meters NED DEM. Blue (selected sites which hydrographs are shown in Figure 6) and red dots represented streamflow sites. In the state wide map I also present the location of the 4 weather radar that cover the area.	117
Figure IV-2. Cedar River basin boundaries delineated based on (a) NED 30 meters DEM and (b) ASTER 30 meters DEM. In Figure (b) I also include the NED 30 meters DEM delineation in white for a reference.	118

Figure IV-3. Width function for Clear Creek at Coralville extracted from different DEMs. The red line indicates the position of the maximum of the width function. The number in square brackets indicate the number of pixels in the DEM contained in the basin	119
Figure IV-4. Width function for Cedar River basin at Cedar Rapids extracted from different DEMs. The red line indicates the position of the maximum of the width function. The number in square brackets indicate the number of pixels in the DEM contained in the basin.....	120
Figure IV-5. Width function maxima for Cedar River extracted from different DEMs Statistical self-similarity of width function maxima in terms of drainage area obtain based on different DEMs for Cedar River basin. The ordinary least square regression is used to obtain the relationship between drainage area and width function maxima. The parameters of the scaling relationship are presented in the square brackets: [coefficient, exponent, correlation.....	121
Figure IV-6. Normalized simulated and observed streamflow for sites located in the Clear Creek and Cedar River basin. Discharge was normalized by the mean annual flood. Observed values are plotted in gray, simulated using NED 90 m DEM in green, simulated with NED 180 m in magenta, and simulated with NED HO6 in cyan. Values in the left corner indicate the site number (figure 1) and drainage area, and the values in the right indicate goodness-of-fit statistics [correlation, Nash] for the simulation with 90m NED.....	122
Figure IV-7. Scaling of peak flow for the 2008 Iowa flood event. Dark gray values are observed, dark blue are predicted with NED 90 m DEM. The lines were estimated based on non-parametric regression between basin drainage area and peak flows for all the links in the river network. Light gray dots represent the simulated peak flow obtained with the NED 90 m DEM. The red line correspond to the mean annual flood.	123
Figure IV-8. Results from the simulation based on synthetic rainfall. First and second lines present results based on accumulated rainfall equal to 30 and 120 mm, respectively. Simulation with the reference network (90 meters) is plotted in dark blue, and for this simulation the peak flow values for each link are represented by gray dots. Peak flow scaling obtained based on datasets with different source (column 1), resolution (column 2) and pruning (column 3) are presented in red, green and magenta.	124
Figure V-1. Accumulated mean areal precipitation for the 7 rainfall error scenarios for the Cedar and Iowa Rivers.....	151
Figure V-2. (a) Schematic representation of the deterministic and random transformations; (b) Deterministic scenarios; (c) random scenarios; (d) spatial correlation scenarios	152
Figure V-3. Observed (dark blue line) and simulated hydrographs produced by CUENCAS (gray line) and SAC-SMA (light blue line) models for the Iowa River basin. The basin drainage area is presented on the left side, and the site number (refer to Figure 1) and Nash coefficients are presented on the right side (CUENCAS, SAC-SMA).....	153

Figure V-4. Same as Figure 3 for the Cedar River basin.....	154
Figure V-5. Peak flow scaling for the Cedar and Iowa Rivers. Gray dots are simulated by CUENCAS, dark blue observed, and light blue simulated by SAC-SMS. The red line was obtained by non-parametric regression between drainage area and peak flow simulated by CUENCAS. The orange line represent mean annual flood.....	155
Figure V-6. Hydrographs for 4 sites on the Iowa River showing results of the simulation for rainfall error scenarios 2 (a) and 5 (b). The discharge is normalized by mean annual flood. The dark blue line represents observed hydrographs; the black line is simulated by CUENCAS using the reference rainfall; the gray shadow represents the lowest and highest values for the ensemble hydrographs simulated by CUENCAS using the 50 ensembles of rainfall; the dash gray line is the median of the ensemble; the light blue line represents the hydrographs simulated by SAC; and the red line reflects mean annual flood.....	156
Figure V-7. Same as Figure 6 for 6 sites in the Cedar River basin.....	157
Figure V-8. Relative differences between the ensemble and the reference areal mean accumulated rainfall (a and b) and maximum rainfall intensity (c and d). Plots e and f presents the relative difference between simulated peak flow using the reference rainfall as input (black dots) and the ensemble rainfall (gray dots) and observed peak flow. Plots a, c, and e are for scenario 2, while plots b, d, and f are for scenario 5, Cedar River basin.	158
Figure V-9. Gray dots: difference between the 95th ($Qp95$) and 5th ($Qp5$) percentile ensemble flow values normalized by the median ($Qp50$) ensemble flow value; Green dots: normalized difference between the median ensemble value and the reference peak discharge ($Qpref$).....	159
Figure VI-1. The relative difference in simulated peak flow due to spatial and temporal precipitation resolution.....	171
Figure VI-2. The effect of sampling frequency on flood prediction uncertainty (a) and error band of 50 samples generated based on the simulation of temporal sampling (b). Blue dots: the difference between the 95 th ($Qp95$) and 5 th ($Qp5$) percentile ensemble flow values normalized by the median ($Qp50$) ensemble flow value; Green dots: the normalized difference between the median ensemble value and the reference peak discharge (Qp^*).	171
Figure VI-3. Hydrographs with error bands for Cedar Rapids sites using 50 different ensembles that mimic uncertainty due to sampling frequency. These results simulate the case for which one sample is obtained each three hours. Observed values are presented in dark blue and simulated based on SAC-SMS in light blue.....	172
Figure VII-1. Rain total map of the Stage IV for May 30 to June 15 in 2008 over the Iowa River and Cedar River Basins.	190
Figure VII-2. Rain total maps for different products (indicated in the figure) for the period of May 28 th to July 1 st 2008.....	191

Figure VII-3. Rain total maps for different products (indicated in the figure) for the period of March 1 st to October 1 st for years 2002, 2003, and 2004.....	192
Figure VII-4. Selected hydrographs showing observed and simulated hydrographs: gray lines represent observed, light blue light simulated using SAC, dark blue continuous line simulated by CUENCAS forced by Stage IV, and dark blue dashed line simulated by CUENCAS forced by HN-3 – 60 min.	193
Figure VII-5. Relative difference in simulated peak flow based on Stage IV (reference) and other rainfall datasets for the 2008 events. The rainfall dataset is indicated in each plot.....	194
Figure VII-6. 2008 hydrographs simulated based on (1) NLDAS-2, (2) NWS-MAP, (3) CMORPH, and (4) PERSIANN.....	195
Figure VII-7. Relative difference in simulated peak flow based on Stage IV (reference) rainfall and other rainfall datasets for 2002 (column 1), 2003 (column 2), and 2004 (column 3). The rainfall dataset is indicated in each plot.....	196
Figure VII-8. 2003 hydrographs simulated based on (1) NLDAS-2, (2) NWS-MAP, (3) CMORPH, and (4) PERSIANN.....	197
Figure VII-9. 2004 hydrographs predicted based on (1) NWS-MAP and (2) PERSIANN.....	198
Figure VIII-1. Relative difference between peak flow simulated based on NLDAS and MODIS potential evapotranspiration (line 1) and for the modified NLDAS potential evapotranspiration datasets by a constant rate of 0.8 (line 2), 1.2 (line 3), 1.4 (line 4), and 1.7 (line 5) for the years 2002 (column 1), 2003 (column 2), 2004 (column 3), and 2008 (column 4), respectively.....	205
Figure VIII-2. Relative difference between peak flow simulated based on spatially variable soil volumetric moisture; initial condition provided by NLDAS output and constant soil volumetric moisture initial condition equal to 0.3 (line 1), 0.5 (line 2), and 0.7 (line 3).	206
Figure A.1. Relationship between at-a-station HG parameters (coefficient and exponent) and basin area for the four hydraulic variables considered in this work.....	225
Figure A.2. N-HG parameters estimated for the US. The top plots are reference maps that provide insight into the dominant processes that control parameter variability. The second, third, and fourth lines present the parameters for velocity, water surface width, and water depth, respectively. The coefficient, discharge exponent, and area exponent of the N-HG relationships are presented in the first, second, and third columns, respectively.	226
Figure A.3. Scaling of peak flow for different sets of N-HG parameters and rainfall events' intensity and duration (rainfall volume=60mm): variability was added to the velocity coefficient through the definition of an average value (equal to 0.9) and a standard deviation.....	227

Figure A.4. Scaling of peak flow for different sets of N-HG parameters and rainfall events' intensity and duration (rainfall volume=60mm): results for different values of the discharge exponent.....	228
Figure A.5. Scaling of peak flow for different sets of N-HG parameters and rainfall events' intensity and duration (rainfall volume=60mm): results for different values of the area exponent.....	229
Figure A.6. N-HG velocity parameters for the Iowa River, Cedar River, and Turkey River basins.	230

CHAPTER I

INTRODUCTION

Motivation

For centuries, floods have been one of the most destructive global natural disasters. The impacts of floods are expected to increase in the coming years due to population growth, population migration to coastal areas, and climate change (Feyen *et al.*, 2006). Complete protection is both unfeasible and unsustainable because of high costs and intrinsic uncertainty (Schanze, 2006). In this context, more accurate flood prediction would greatly enhance the effectiveness of flood mitigation measures. The development of near-global flood forecasting systems has been cited as one of the major challenges the hydrological community faces (Lettenmaier and De Roo, 2006; Wood *et al.*, 2011). Reliable flood prediction is a difficult scientific challenge, especially for ungauged or poorly gauged basins and scenarios involving rapid land cover and climate change.

Floods are controlled by storm properties, soil and surface physical properties, and initial wetness conditions, all of which are to some degree monitored by remote sensing. Remote sensing provides key information for simulating floods due to its low cost, near global coverage, robustness during extreme events, and continuous spatial and temporal sampling. These features make it possible to predict floods globally, including in data-sparse regions. However, the best use of such data requires the development of appropriate modeling techniques that are specially designed to use available information most effectively. This process considers the limitations imposed by the inherent features of these products, such as retrieval error, infrequent sampling, and low spatial resolution. The use of remote sensing information for hydrological prediction requires a better understanding of how these uncertainties propagate through hydrological models.

One of the major barriers to the implementation of global flood prediction systems is the reliance of traditional hydrological methods on calibration. Calibration is usually performed based on the optimal match between observed and simulated stream flow at a specific spatial scale. However, historical datasets are lacking in many parts of the world. Moreover, since calibration camouflages problems related to the model's structure and/or data uncertainty, it eliminates the opportunity to learn from incorrect predictions (Sivapalan et al., 2003; Kavetski and Fenicia, 2011). As argued by Kirchner (2006), scientific knowledge should be achieved by the "collision of theory and data, rather than through increasingly elaborate and parameter-rich models that may succeed as mathematical marionettes, dancing to match the calibration data."

A third limitation of calibration is the focus on the few points in the basin for which data is available, normally in the basin outlet. This procedure guarantees a good match between observed and simulated data, but it does not assure that model performs equally well for other sites or other scales. Even when good agreement is achieved, calibrated models do not provide an unbiased framework from which to evaluate different datasets and understand the effects of data errors on flood prediction.

To avoid the aforementioned issues related to calibration, I first developed a fully distributed, physically-based, and calibration-free hydrological model. Instead of calibrating parameters, I adopted a systematic and interactive approach to model building. I systematically added processes to the model and evaluated their effects on flood prediction across multiple scales. The level of complexity adopted to represent physical processes was limited by data availability since I attempted to avoid parameters that require calibration. I demonstrate the model's capability to correctly represent the hydrologic response to heavy rainfall using high resolution and accuracy datasets, e.g. rainfall and digital elevation models. Since estimated parameters were not adjusted based on the high resolution datasets, the model provides an unbiased tool to evaluate lower resolution and less accurate datasets (especially ones that are remotely sensed) and

investigates how data uncertainty affects floods. It is important to point out that since model parameters were not best-fit to a particular scale or location, the model is equally able to *predict floods everywhere*, in the spirit of the PUB initiative (Sivapalan *et al.*, 2003).

In the next section, I present the main objectives and research questions that guided this work. Next I present a brief review of the literature including two main topics: (1) state-of-the-art hydrological modeling and (2) applications of remote sensing for flood prediction. Section 1.4 describes the study area chosen to test our modeling framework. Section 1.5 outlines the general methodology followed in this thesis. The last section presents a brief overview of the thesis chapters.

Objectives and research questions

The broad motives of this study are to contribute to the evaluation of the value of remote sensing data for flood prediction across multiple scales and to provide a rational basis for future data requirements. Floods are the result of the complex interaction of meteorological processes, land surface and soil properties, and antecedent moisture conditions. On one side, remote sensing information provides insights about all of the variables that should be accounted for in a flood prediction system, with near global coverage and relatively low costs. On the other, coarse spatial and temporal resolution, sampling frequency, and retrieval errors limit its applicability for flood prediction at small scales. Our main hypothesis is that uncertainties in flood simulation due to data limitations (accuracy or resolution) decrease as basin scale increases. Therefore, there is a scale for which remote sensing information can be used to predict floods with an acceptable level of accuracy. The specific goal of this work is to estimate this scale as closely as possible.

In order to achieve this goal, I need to assess the usefulness of different remotely sensed datasets for flood prediction. The unbiased evaluation of different datasets

requires a calibration-free, multi-scale framework. Therefore, in this work, I first develop such a framework, taking into consideration currently available remote sensing data relevant to flood prediction. Once I demonstrate the flood prediction skills of the developed framework, I apply it to the following research questions:

1. How do uncertainties in the input data or in the data used to estimate model parameters (digital elevation model, land cover) affect flood prediction?
2. How do errors change with basin scale?
3. What are the errors and limitations involved in using satellite remote-sensed data for flood prediction?
4. What are the main features of remote sensing information that should be improved or modified in order to yield accurate global flood prediction systems?

Literature Review:

Progress towards a global scale flood prediction system

In this section, I present a brief literature review of the subjects that motivated the development of this thesis. I start with a brief discussion about the current state of hydrological modeling, focusing on the main challenge of *predicting floods everywhere*. In the subsequent section, I list the main datasets available to predict floods. I also include a list of current and future satellite remote sensing missions that measure relevant variables for monitoring and predicting floods.

State-of-the-art hydrological modeling

The development of hydrological models started in the 60s and was enhanced by the advance of high-speed computers and by the demand imposed by advanced water management engineering projects. Due to computer limitations and lack of spatial information, lumped models were initially applied. Spatial variability of the characterization of the landscape, hydro-meteorological forcings, or initial conditions were not explicitly accounted for in this type of formulation. To overcome these

weaknesses, effective parameters were calibrated based on the hydrograph at the outlet of the basin. Parameter calibration guaranteed good fit and a correct overall mass balance but did not guarantee the correct representation of physical processes, especially across scales. A well-known example of a lumped model is The Sacramento Soil Moisture Accounting Model (Burnash et al, 1973), which is the main model used for river forecasting by the National Weather Service River Forecast Centers across the United States.

During this first phase of the hydrological model development, calibration was justified by the lack of spatial/temporal information describing catchments' physical properties (e.g. land cover, soils types, landscape) and hydro-meteorological (e.g. precipitation, evapotranspiration) and state (e.g. soil moisture) variables. At that point, appropriate data were not available to test the basic hypothesis adopted to build the models. Calibration was used to fit estimated to observed data under the assumption that the model structure and data uncertainty were much smaller problems than the scarcity of data. When data is sparse, calibration is an acceptable procedure, especially when the model is used for operational predictions rather than being used in a scientific context.

With the advances in Geographical Information System (GIS), increasing computer resources and availability of spatially distributed data through remote sensing technologies, models that explicitly account for spatial heterogeneities began to be conceptualized. With hydrological distributed models, a new challenge emerged, "dynamic parametric complexity" (Gupta, 2004). With explicit consideration of spatial variability, the number of parameters increased exponentially since one set of parameters has to be specified for each model control volume. A large number of observations that covers all spectrums of hydrological functions and spatio-temporal scales would be required to correctly estimate these parameters through calibration (Sawicz et al., 2011). Even in that case, we would have to guarantee that the data are error free. When streamflow at the outlet of the basin is the only information used to calibrate these

models, the large number of degrees of freedom results in equifinality, i.e. a limited ability to uniquely identify parameters (Ebel and Loague, 2006). If parameter calibration is based on a dataset with a limited number of observations (hydrographs at the outlet of the basin), then we can never be sure if the model is “right for the right reasons” or if errors in the data and model structure are being compensated for by errors in parameter values (Refsgaard, 2004; Ajami et al., 2007).

Lack of scaling consideration is another common issue in traditional hydrological models. Hydrological processes are highly nonlinear, heterogeneous in space and time, and cannot be extrapolated across scales (Wood et al., 1988; Sivapalan and Kalma, 1995; Blöschl, 2001; Sivapalan et al., 2004). However, due to the lack of understanding of the scaling properties of hydrological processes, they are commonly assumed to be scale invariant, and the same equations are applied to represent physical processes at a large range of scales (Beven, 1995). In this case, “effective” parameters have to be calibrated to represent the processes at scales different from the ones for which they were initially conceptualized. To avoid this issue, the scales’ physical processes that are conceptualized in the model should be defined a priori and should not change from one application to the other since governing equations are sensitive to scale. When possible, governing equations that represent the punctual description of physical phenomena should be avoided. Attention should be focused on representing properties and processes that emerge with increasing scales. This approach would allow the construction of minimally parameterized models that attempt to represent the macro-scale properties of the physical system (McDonnell et al., 2007).

Besides the known mathematical difficulties involved in parameter calibration, this procedure is still widely used and somehow accepted as a standard procedure in hydrology. Many current studies attempt to establish criteria and develop better methods for parameter calibration (Wang et al., 2010; Lombardi et al., 2011; Luo et al., 2011) (Refsgaard, 2001). However, even if calibration methods could be improved to the extent

that a unique optimal solution could be found, parameter calibration is only justifiable under the assumption that the model's structure is perfect and all data used in the calibration procedure, including input, output, and datasets used to estimate measurable parameters of the watershed (DEM), are error free. This *faultless* situation is unlikely, due to the large complexity and variability of natural systems that complicate their accurate quantification in space and time. Moreover, parameter calibration based on historical series is not applicable under non-stationary conditions caused by land cover or climate change.

Recent publications reveal that the hydrological community now recognizes that the calibration procedure imposes barriers to knowledge development, and members of the community have been searching for approaches that promote systematic learning (Buttle, 2006; Kirchner, 2006; Sidle, 2006; Soulsby et al., 2006; Tetzlaff et al., 2008; Sivapalan, 2009; Loague et al., 2010; Kavetski, 2011). Calls have been made for more unified and holistic theories based on natural laws and on the concept of catchments as self-organizing systems (Beven, 2007; Sivapalan, 2009; Gupta et al., 2010). One example is the work presented by Gupta (2004), who introduced the idea that hydrologic systems should be treated as statistical–mechanical systems. In this case, hydrological systems can be compared to thermodynamic systems, for which macroscopic parameters emerge from microscopic statistical dynamical equations governing molecular motions. Thermodynamic equilibrium, for example, is described only by macroscopic variables, even though microscopic statistical fluctuations are still present. According to the author, flood properties observed at larger scales (e.g. peak flow scaling) can be related to statistical physical properties observed at small scales (hillslopes). This approach would eliminate the need for calibration since parameters would be related to measurable physical variables, like rainfall, or basin properties.

According to Gupta et al (2010), peak flow macro behavior arises from the aggregative effect of the river network that works as a filter for small-scale variability.

This dynamic is reflected in peak flow scaling power law relationships, which parameters are related to river network properties and hillslope scale processes space–time variability. This hypothesis is the basis for the geophysical flood theory (Gupta, 2004). This framework provides the advantage of requiring statistical distributions of certain properties (precipitation, runoff generation) at the hillslope scale in addition to their exact values everywhere. In a recent publication, the same authors (Gupta et al., 2010) reinforce the concepts behind this theory using the extreme flood event that occurred in Iowa in the summer of 2008. The authors also propose methods and procedures that should be adopted to test different theories related to the links between macro and micro properties.

To better understand the links between macro and micro properties, Gupta et al. (2010) propose a framework that allows testing different hypotheses related to the dynamics of the hydrological systems and how they change across scales. I follow their recommendations to conceptualize the model developed in this work. Hydrological processes are described at the hillslope scale, and space-time variability is introduced when the basin area consists of a large number of hillslopes. The river network provides the link across different scales. I avoid calibration by estimating parameters that describe physical processes at the hillslope scale and that are based on measurable physical properties (Barnes, 1995). This is now possible due to recent advances in the indirect measurement of land surface properties (Wolfe et al., 2009), water storage (Zaitchik et al., 2008), and hydro-meteorological variables (Huffman et al., 2007) on a global scale. The potential use of these databases for hydrological modeling and flood prediction is yet to be explored and constitutes one of the goals of this work.

Direct and indirect application of remotely sensed data for flood prediction

Remote sensing technology provides key information for evaluating the local, regional, and global water balance (Schultz, 1996; Bindlish et al., 2009; Conesa-Garcia et al., 2010). These datasets can potentially be used to predict floods, but some limitations are imposed by the coarse resolution of the information in space and time, the sampling interval, and retrieval uncertainties (Lakshmi, 2004). To optimally apply these data, we need to understand the information content of each dataset and determine the best way to apply them specifically to flood prediction. In some cases, the monitored information (e.g. digital elevation model and precipitation) is directly used in the flood prediction model. In other cases, the remote sensing information is used as forcing for continental scale land surface models that perform water and energy flux analysis (Lohmann et al., 2004). The outputs of these models are potentially useful for flood prediction (e.g. soil and surface moisture states, vegetation interception, actual evaporation). Even when uncertainties are involved, these models are able to capture anomalies in terms of soil moisture and runoff conditions, as demonstrated by Xia et al. (2012).

The value of remote sensing data for flood prediction will also depend on the area of application. These datasets will present higher values for data scarce regions. For example, in the US, the National Weather Service operates a network of 159 high-resolution Doppler weather radars that provides high temporal and spatial resolution rainfall maps that nearly cover the entire country. In this case, satellite rainfall data will be used as a supplementary source of information, to fill up gaps in the operation, or to provide information for regions that are not covered by radars. However, for many developing countries, satellite-based precipitation is the only dataset that provides space-time rainfall information covering a large area. Due to the economic situation, these regions are also extremely vulnerable to natural disasters such as floods. Even though the value of remote sensing data is higher for regions where data is scarce, evaluation of

these datasets should be performed in data rich regions. This way it is possible to isolate uncertainties due to data and model structure.

In this section, I will present a summary of the information with potential value for peak flow simulation. Available remote sensing information can be classified as “Static” or “Dynamic.” “Static” variables (e.g. topography) usually present better accuracy and resolution than “dynamic” variables (e.g. precipitation, soil moisture, snow melt, and land cover dynamics). Table I-1 presents a list of physical processes and variables that should be accounted for in flood prediction. In this table, I include different datasets that are classified according to the source of information: satellite remote sensing or other. This list is not exhaustive, but the intent is to demonstrate what type of information is available to represent different physical variables and processes.

Throughout this document, I will discuss the main features and limitations of some of these datasets. I use the same event to investigate the relative contributions of different datasets to uncertainties in predicting floods. I first perform simulations using high resolution and accuracy datasets, when available. When these datasets are not available, remote sensing datasets or continental land surface model inputs and outputs are used. Since I do not use streamflow and precipitation to calibrate parameters, the differences between observed and predicted streamflow reflect uncertainties in the datasets and/or model structure. I then perform simulations using the degraded datasets to investigate the effect of the error on flood prediction. I focus on identifying the main data error features that cause major errors in flood prediction. This allows us to formulate guidelines for flood prediction using currently available information and to define what should be the major data requirements of future missions.

I do not focus on evaluating existing satellite-based products, since the capability to monitor hydro-meteorological variables from space will improve considerably in the near future with the launch of new missions that focus on monitoring the environment. The most relevant ones for flood prediction are the Global Precipitation Mission

(GPM)(Smith et al., 2007), the Soil Moisture Active Passive (SMAP) mission (Entekhabi et al., 2010), the Surface Water and Ocean Topography mission (SWOT) (Durand et al., 2010), the Cold region hydrology high-resolution observatory (CoReH2O) (Rott et al., 2010), and the GRACE II mission (Zaitchik et al., 2008). GPM will be launched in 2014 and promises to achieve temporal sampling equal to 3 hours 90% of the time. It also includes dual-wavelength precipitation radar at 13.6 and 35.5 GHz, which presents the high sensitivity necessary to detect light rain and snow as low as 0.3 mm h⁻¹. SMAP is also set to be launched in 2014 and will provide global measurements of the land surface soil moisture and distinguish frozen from thawed land surfaces. CoReH2O will provide the extent and water equivalent of the snow cover with resolutions ranging from 100 to 500 m. SWOT will provide water elevations along rivers, lakes, streams, and wetlands and over the ocean's surface using swath altimetry. GRACE II will provide high-temporal-resolution gravity fields for tracking large-scale water movement.

Study Area

In our work, I analyze the Iowa, Cedar, and Turkey River Basins that are located almost entirely in the state of Iowa. The total drainage area of the Iowa River is 7,234 km² (at Marengo), 16,853 km² for the Cedar River (at Cedar Rapids), and 4,000 km² for the Turkey River (at Garber). Some analyses with high resolution data (DEM) will be performed for a tributary of the Iowa River, Clear Creek, that presents a drainage area around 254 km² (at Coralville). Clear Creek makes part of the CUAHSI WATERS Test Bed catchment. The locations of these catchments are presented in Table I-1.

I chose this study area for two main reasons. First, the region is rich in hydrologic information. Four NEXRAD weather radars (in Des Moines and Davenport in Iowa, La Cross, Wisconsin, and Minneapolis, Minnesota) cover the two basins; also 24 USGS streamflow gauges collect data at the outlet of drainage areas ranging from approximately 22 to 16,853 km². Figure I-1 presents a map of the study area with the location of the

weather radars and the USGS streamflow sites. The second reason for selecting the area is its frequent flooding. The region was the center of an extreme flood event in 2008 that affected approximately 1.2 million acres of Iowa's agricultural land and many communities throughout the state. About 1,300 blocks in the city of Cedar Rapids were flooded, which affected more than 5,000 homes and 900 businesses. In Iowa City, sixteen buildings on The University of Iowa campus were reported flooded, and the total cost of recovery from the flood reached \$750M. I will use the 2008 flood event to demonstrate the hydrological model's ability to predict floods across scales and to investigate the effect of rainfall uncertainty on the prediction of floods. The climate in this region is characterized by cold winters, hot summers, and wet springs, with mean annual precipitation of 864 mm (source: Oregon Climate Service), potential evaporation of 1060 mm, and actual evaporation of 580 mm (based on MOD16). The dominant land cover is used for agriculture, consisting mainly of a corn-soybean rotation. The agricultural practice imposes a strong seasonality on land cover dynamics. The planting season usually starts in May and concludes in November.

In this study, I simulate streamflow for the period of 2002 to 2009. I performed an annual water balance with the goal of better understanding the climatology and intra-annual variability of the components of the hydrological cycle. Areal rainfall, evapotranspiration, potential evapotranspiration, and runoff were calculated for all of the basins for which streamflow data is available for the period of 2002 to 2009. To estimate areal average precipitation, I used Stage IV precipitation products with 1-hour temporal and 4 km spatial resolution obtained on the NCEP website. Evapotranspiration and potential evapotranspiration were estimated using 8 days of temporal and 1 km spatial resolution MODIS products (see Mu et al., 2011 for details on MODIS 16 product), obtained on the website maintained by the Numerical Terradynamic Simulation Group, the University of Montana (www.ngts.umt.edu/modis/). DEM data with 90 m resolution was obtained from the USGS National Elevation Dataset (NED) project and was used in

the delineation of each sub-catchment with observed streamflow. The time series of precipitation, evapotranspiration, and streamflow were aggregated to the annual scales for all sub-watersheds. In Figure I-2, I present the results for all years (2002-2009) and sites (blue dots represent different sites and red dots the average for all sites). Figure I-2 (a) presents annual precipitation, Figure I-2 (b) annual evapotranspiration, Figure I-2 (c) annual runoff, and Figure I-2 (d) the difference between total annual inflow (precipitation) and outflow (evaporation and runoff). All quantities are in mm.

Assuming that ground-water flow is negligible, differences between watershed inflow (precipitation) and outflow (evapotranspiration and runoff) are equal to changes in soil storage. When inflow is larger than outflow, recharge occurs, whereas the soil is depleted in the opposite case. Figure I-2 demonstrates different hydrological and climatological conditions observed during the period of 2002 to 2009. For the years 2002 and 2003, total inflow (precipitation) and outflow (evaporation and runoff) were very similar, so no large differences in soil storage occurred. From 2004 to 2007, inflow was much larger than outflow. The difference was probably retained in the soil storages. The situation changed during 2008, when an extreme flood occurred in the region. Even though accumulated precipitation was very similar to that observed in the previous year (around 1000 mm), runoff for 2008 was on average 30% larger than in 2007.

A possible explanation for the extremely high runoff ratio observed in 2008 was given by Krajewski et al. (2010). According to the author, aside from the large volume of precipitation, the occurrence of a perfect storm was noted as a determining factor that led to an event of such extreme magnitude. A perfect storm might not be extremely large in terms of total accumulations, but it occurs at the perfect time and location to cause a coordinated rise of the river levels. This feature highlights the importance of representing space-time rainfall variability to correctly simulate floods. As indicated by the author, the main storm that occurred in 2008 followed the river network path (from northwest to southeast). In this way, the flood waves and storm clusters travelled in the same

direction, intensifying the situation in already critically flooded areas. Another assumption is that old water, i.e. the water that was accumulated in the soil during previous years, contributed significantly to runoff generation.

An overall look at the spatial (for different sites in the same year) and annual (across years) variability of the diverse components of the water balance provides clues about the temporal and spatial variability of the different components of the water balance. Evapotranspiration remains almost constant throughout the years (around 580 mm), and a variation of less than 5% is observed from site to site. Precipitation varies from 560 mm (minimum in 2003) to 1150 mm (maximum in 2008). Spatial variation is also significant: for 2003, precipitation values varied from 560 mm to 790mm, a difference of more than 200mm. Total annual runoff presents the highest variability in space and time among the water balance variables. This is expected since runoff generation depends on a large number of factors including space-time variability of rainfall, soil moisture conditions, and land surface and soil properties.

The large variability in runoff generation and soil storage summarized in this picture demonstrates the complexity of runoff generation processes. It is clear that a simple translation from rainfall into runoff is not possible, so in order to accurately predict floods there is a need to represent all relevant hydrological processes, including precipitation, infiltration, overland flow, evapotranspiration, soil dynamics, baseflow, and transport through the river network. In this thesis, I attempt to design a coupled hydrological model that is able to represent all the complexities and feedback involved in flood generation.

Methodology

Predictability skill is defined as the accuracy and the degree of precision to which a system's state can be predicted using a specific model and dataset. Perfect predictability can only be achieved for strict deterministic processes, i.e. if all

complexities are known and included in the model and if all the essential data to describe these processes and how they change in time and space are available with the required accuracy and resolution. In the case of a natural system, this situation is unfeasible considering all of the existing non-linearities and heterogeneities. Therefore, it is essential to investigate how data predictability skill is affected by different datasets and model structures and to determine what are the dominant processes that must be included in the model.

As stated in the introduction of this thesis, the fair evaluation of different datasets for flood prediction requires a multi-scale calibration-free simulation framework that isolates uncertainties due to model structure, parameter estimation, and data. The first component of this study constitutes the development of a fully distributed, physically-based, and calibration-free hydrological model. Calibration is avoided with the use of parameters that are directly linked to the physical properties of the watershed (e.g. soil water storage, hillslope shape, and channel flow velocity). The fact that the model parameters are not calibrated to fit the discharge data implies that the uncertainties in the input are independent of the errors in the simulated discharge. This also means that I have avoided favoring the scales at which I have available discharge observations. So, theoretically, the model is equally able to *predict floods everywhere, without the need of calibration*, in the spirit of the PUB initiative (Sivapalan et al., 2003). Chapter 2 presents a description of the models.

I adopt the downward approach to model building (Sivapalan et al., 2003). I start with a simple model that accounts for first-order controls in flood generation, and I systematically add different processes to the model formulation in response to deficiencies in reproducing observations. In the process, I question whether the discrepancy between the model's simulated and observed responses could be due to the uncertainty in the input or to a neglected process. This technique allows the identification of the dominant processes that have to be included in the model's

formulation in order to capture the necessary dynamics of flood generation across scales. I also identify the level of complexity needed to correctly represent the processes. I opt for simple conceptualizations that capture the overall behavior of the system, without over-parameterizing the model. I do not include physical processes for which no data is available to support parameterization.

Prior to using the model as a tool to evaluate different datasets, I evaluate the model's performance in accurately representing the hydrologic response to heavy rainfall. First, the model is implemented using the datasets with the highest available resolution and accuracy. This way I minimize errors due to input and parameterization and are able to identify the model's structural insufficiencies. Once I am confident that all required components (dominant processes and level of complexity) are identified and adequately represented in the model, I can use it to investigate the predictability skills of satellite-based datasets that are less accurate and have lower resolution.

I use two criteria to evaluate predictability skills of different datasets. The first is based on the nonlinear geophysical theory of floods (Gupta et al., 2010). Rainfall intensity, duration, and variability, the river network topology and flow dynamics, and rainfall-runoff mechanisms shape the relationship between peak flow and drainage area. In a diagnostic framework, I explore how peak flow scaling changes as I degrade data accuracy or resolution. Normally, a power law relationship is used to describe peak flow scaling. The parameters of the power law relationship (coefficient and exponent) are estimated based on least-square regression. However, during the development of this work I concluded that as coefficients and exponents are correlated, the least square method is not robust. Therefore, when necessary, I opt to use a non-parametric kernel regression to estimate peak flow scaling relationships. The advantage of nonparametric regression is to directly estimate the regression function between the independent variable (in this case drainage area) and the dependent variable (peak flow) rather than to estimate parameters. This type of regression relaxes the linearity assumption required for

parametric methods (Black and Smith, 2004). In the majority of the cases, I compared various datasets by analyzing the relative difference between peak flows simulated based on the reference dataset (e.g Stage IV for rainfall) and the degraded ones (satellite-based rainfall) across scales. Other important features of the area versus peak flow power laws are the scatter around the fitted line and the presence or absence of a change in the slope of the line, indicating a scale break.

The second criterion evaluates the performance of the model in simulating observed hydrographs across scales. Two standard indices, the correlation coefficient (CC) and the Nash-Sutcliffe efficiency coefficient (Krause et al., 2005), were used to evaluate the model's performance. The CC is a measure of how much of the observed dispersion is explained by the prediction and indicates how well the model captures the timing of the hydrographs (rising and falling). However, since only the dispersion is quantified, models that systematically over- or under-predict still present high correlation. The NSC index takes values over the range of $[-\infty, 1]$. Values equal to zero indicate that the model's predictions are as accurate as the mean of the observed data, whereas efficiency less than zero occurs when the observed mean is a better predictor than the model. I compare observed and simulated hydrographs for sites ranging in area from 22 to approximately 17,000 km².

Our goal is to evaluate flood prediction sensibility to data accuracy and resolution and to identify the scales for which remotely sensed data is beneficial for flood prediction. Two types of simulation studies are performed. Synthetic simulations follow the methodology adopted by Mandapaka (2009). The author used synthetic events to investigate the effects of rainfall duration, intensity, and intermittence on flood scaling parameters. In this case, I force the model with synthetic data and adopt a systematic diagnostic framework to further understand the role of different inputs, variables, and processes in the scaling structure of peak flows. This methodology allows complete freedom to explore a large number of model and data scenarios and to determine their

effects on the scaling properties of floods. I also perform real event simulations using the extreme flood event that occurred during the summer of 2008 in Iowa.

Overview of thesis chapters

In Chapter 2, I describe the hydrological model developed in this work. In Chapter 3, I present model results. I apply the most complete version of the model to simulate streamflow for the period of 2002 to 2009 for the Iowa River, Cedar River and Turkey River basin. I then illustrate the importance of a multi-scale evaluation of model results and why calibrated models can yield misleading interpretations of model capabilities, especially if the model is calibrated for specific events or climatological conditions at one specific location. For this analysis, I use very simple models with a limited number of parameters (2 or 3).

Once I demonstrate the skills of the model on simulating flood events, I apply it as a tool to investigate how data uncertainty propagates through the model and to ascertain what the potential requirements and limitations of using remote sensing data to predict floods are. I focus on the two main variables that shape floods: river network structure and rainfall intensity and space-time variability. DEMs are used to extract the river network, outline model control volumes (e.g grid, sub-watersheds, hillslopes), and calculate land surface slopes, which controls runoff transport. In Chapter 4, I investigate the impact of the DEM source, resolution, and network pruning on the characterization of the river network and on estimation of peak flow magnitude and timing across scales. Results presented in this chapter reveal the importance of correctly representing the river network and its property in hydrological models that focus on peak flow forecasting.

Rainfall is the main input to hydrological models, and its uncertainties may strongly affect streamflow simulation (e.g. Arnaud et al. 2011). In Chapters 5, 6 and 7, I investigate the effects of rainfall uncertainty on flood prediction across scales. Weather radars are the only operational instruments capable of providing rainfall estimates over

large domains with high space-time resolution. Radar-rainfall estimates are subject to significant uncertainty (see Villarini and Krajewski (2010) for a review), and their use for flood prediction requires a better understanding of how the estimation errors propagate through hydrological models and affect streamflow prediction across scales. In Chapter 5, I explore the effects of uncertainties in radar-estimated rainfall on streamflow prediction at a range of spatial scales. I applied a recently proposed statistical model of radar-rainfall error structure to produce input ensembles of different expected radar-rainfall error scenarios, used the generated ensembles as input for the hydrological model, and summarized the effects on flow sensitivities using a relative measure of the ensemble peak flow dispersion for every link in the river network.

In Chapter 6, I perform simulation studies to investigate the potential of using satellite-based rainfall maps for flood prediction. I first use high-resolution radar rainfall maps to reproduce data with the same characteristics of the product obtained by satellites, including coarser resolution and lower temporal sampling. I use the manipulated datasets as input to the model to evaluate the possible effects of these data properties on flood simulation. I independently investigate the effect of coarse spatial and temporal resolution as well as sampling frequency on peak flow estimation across multiple spatial scales.

In Chapter 7 I perform simulations using various available rainfall products to evaluate how different they are from each other, and to assess how these differences propagate through the hydrological model. The main goal of this chapter is to understand what the current limitations of satellite rainfall data for flood prediction are and to provide a rational basis for future data requirements and improvements. I included in the analyses four radar-based products (Stage IV and higher resolution products produced by the Hydro-NEXRAD system), two gauged based products (NLDAS-2 and MAP-NWS), and two satellite products (PERSIANN AND CMORPH). The description of each one of these datasets is provided in the Chapter. The results presented in this chapter

demonstrate the difficulties on correctly estimating rainfall space-time variability and intensity even when weather radars and rain gauge data are available.

In Chapter 8 I present preliminary results of a sensitive analysis to assess the impacts that bias on the estimation of PE or soil moisture initial conditions have on simulated peak flow across scales. I investigate the impact of these variables on simulated peak flow for the following years: 2002 (dry condition), 2003 (medium condition), 2004 (intense flood), and 2008 (extreme flood). Even though I have used very simple methods to simulate evapotranspiration and to estimate soil moisture initial conditions, I demonstrate that these processes have a less significant effect on peak flow simulation as compare to the effects of rainfall uncertainties.

Chapter 9 presents the thesis summary, concluding remarks, and recommendations for future studies. I also include a discussion in terms of the main limitations of the model developed in this work and recommendations for further improvements.

I included an appendix that describes the methodology used to propagate the flow through the river network. I adopt the Network Hydraulic Geometry concept proposed by Mantilla (2007). In Mantilla's formulation, velocity is a non-linear function of discharge in each link and the corresponding upstream area. The parameters of this equation can be estimated using hydraulic measurements provided by the USGS. I first perform a data analysis to investigate how these parameters change across the US. I then use the measurements available for the Cedar River, the Iowa River, and the Turkey River, IA, to estimate the parameters for the study area. I subsequently perform a simulation study to investigate the effects of river flow dynamics on the statistical structure of peak flow and demonstrate that flow dynamics affect peak flow scaling of large basins, while hillslope processes mainly control the response of small-scale basins.

In the second part of the study, I use the estimated parameters to simulate real events. The direct use of these parameters results in overestimation of flows since water

seems to flow faster than expected. A constant advection correction factor can be used to correct the parameters that are estimated using real data, which slows down the flow across scales. A discussion of the assumptions that result in a faster movement of the water across the network will be presented in the final version of the thesis.

Table I-1. Space-based remote sensing and global datasets, and high resolution datasets used to represent physical processes and properties responsible for flood generation

PHYSICAL PROCESSES	Space-based remote sensing and global datasets	High resolution
STATIC VARIABLES		
Landscape representation (river network and hillslope shape)	ASTER GDEM (* $\Delta S=30$ meters-1'', updated 2009) SRTM (* $\Delta S=30$ meters-1'' for US and $\Delta S=90$ meters =3'' globally, updated 2005)	LIDAR ($\Delta S=1$ meter) NED (* $\Delta S=10$ -1/3'' or 30 -1'' meters for US and $\Delta S=90$ meters -3'' globally, updated each two months)
Hydraulic Measurements	MODIS Band 2 data (near infrared, 0.841–0.876 m) for estimating width (* $\Delta S=250$ meters globally, updated 2005)	USGS hydraulic measurements
Soil properties	Harmonized World Soil Database ($\Delta S=0.5'$) SRIC-WISE derived soil properties ($\Delta S=5'$) FAO Digital map of the world	SURGO and STATSCO $\Delta S=$ polygons with 1 to 10 acres (~0.05km ²)
DYNAMIC VARIABLES		
Rainfall	TRMM-V6 (** $\Delta T=3$ hours and $\Delta S=0.25^\circ$) (Available from 1997 – include different product versions, almost real-time) CMORPH-2 ($\Delta T=3$ hours and $\Delta S=0.25^\circ$) (Available from December 2002, almost real-time) PERSIANN ($\Delta T=3$ hours and $\Delta S=0.25^\circ$) (Available from March 2000, almost real-time) Precipitation – North American Regional Reanalysis (NARR) (originally with 3 hours, 32 km resolution) - disaggregated and interpolated to produce NLDAS-2 Model Input ($\Delta T=1$ hour; $\Delta S=0.125^\circ\sim 13$ km, available from 1979, available with 1 week delay)	Radar Stage IV - NWS ($\Delta T=1$ hour and $\Delta S=0.05^\circ$, almost real-time) Hydro-NEXRAD – super resolution ($\Delta T=15$ min and $\Delta S=0.016^\circ$)

Table I-1 Continued

Land cover type and vegetation dynamics (rainfall-runoff transformation and evapotranspiration)	MODIS Land Cover Type ($\Delta T=1$ year and $\Delta S=0.5\text{km} \sim 0.008^\circ$) MODIS Land Cover Dynamics ($\Delta T=1$ year and $\Delta S=1\text{km} \sim 0.016^\circ$) MODIS Vegetation Indices ($\Delta T=16$ days and $\Delta S=0.25\text{km} \sim 0.004^\circ$) (all MODIS products are available from 2000)	National Land Cover Database (NLCD) 1992, 2001, 2006 ($\Delta S=30$ meters $\sim 1''$)
Soil moisture (initial condition)	AMSR-E monthly averaged soil moisture ($\Delta T=1$ day; $\Delta S=25$ km $\sim 0.25^\circ$) (available from June 2002, available in real time) Total soil column wetness (0-200 cm) - NLDAS-2 Model Output ($\Delta T=1$ hour; $\Delta S=0.125^\circ \sim 13\text{km}$) (available from 1979, available with 1 week delay)	
Snow melt and snow cover	AMSR-E daily global snow water equivalent ($\Delta T=1$ day; $\Delta S=0.25^\circ \sim 25\text{km}$) (available from 1 June 2002, available in real time) Snow melt - NLDAS-2 Model Output ($\Delta T=1$ hour; $\Delta S=0.125^\circ \sim 13\text{km}$) (available from 1979, available with 1 week delay)	
Potential Evapotranspiration	MODIS Potential Evapotranspiration Dataset (MOD 16) ($\Delta T=8$ days; $\Delta S=0.016^\circ \sim 1\text{km}$) (available from 2001 – not available in real time) Potential evaporation from North American Regional Reanalysis - NLDAS-2 Model Input ($\Delta T=1$ hour; $\Delta S=0.125^\circ \sim 13\text{km}$) (available from 1979, available with 1 week delay)	
VARIABLES FOR MODEL VALIDATION		
Evapotranspiration	MODIS Evapotranspiration Dataset (MOD 16) ($\Delta T=8$ days; $\Delta S=0.016^\circ \sim 1\text{km}$) (available from 2001 – not available in real time)	
Streamflow		USGS streamflow measurements ($\Delta T=1/4$ or 1 hour) (availability depends on the site, real time)

* ΔS – spatial resolution in minutes ($'$), Arc-seconds ($''$), degrees ($^\circ$) or km

** ΔT – temporal resolution in minutes, hours, days or years

Table I-2. USGS sites in the Cedar River (CR), Iowa River (IR), and Turkey River (TR) basin

Basin	ID Map	ID USGS	Site Name	HU	Area (km ²)
CR	1	5457000	Cedar River Near Austin, MN	7080201	1033
CR	2	5457700	Cedar River at Charles City, IA	7080201	2729
CR	3	5458000	Little Cedar River near Ionia, IA	7080201	792
CR	4	5458300	Cedar River at Waverly, IA	7080201	4005
CR	5	5458500	Cedar River at Janesville, IA	7080201	4300
CR	6	5459500	Winnebago River at Mason City, IA	7080203	1362
CR	7	5462000	Shell Rock River at Shell Rock, IA	7080202	4520
CR	8	5458900	West Fork Cedar River at Finchford,	7080204	2190
CR	9	5463000	Beaver Creek at New Hartford, IA	7080205	898
CR	10	5464220	Wolf Creek near Dysart, IA	7080205	774
CR	11	5463500	Black Hawk Creek at Hudson, IA	7080205	784
CR	12	5464000	Cedar River at Waterloo, IA	7080205	13322
CR	13	5464500	Cedar River at Cedar Rapids, IA	7080205	16854
IR	14	5464942	Hoover Cr at Hoover, W Branch, IA	7080206	7
IR	1	5451210	S Fork Iowa R NE New Providence,	7080207	580
IR	2	5451500	Iowa River at Marshalltown, IA	7080208	3966
IR	3	5451700	Timber Creek near Marshalltown, IA	7080208	306
IR	4	5451900	Richland Creek near Haven, IA	7080208	145
IR	5	5452200	Walnut Creek near Hartwick, IA	7080208	184
IR	6	5453000	Big Bear Creek at Ladora, IA	7080208	489
IR	7	5453100	Iowa River at Marengo, IA	7080208	7233
IR	8	5454090	Muddy Creek at Coralville, IA	7080209	23
IR	9	5454000	Rapid Creek near Iowa City, IA	7080209	66
IR	10	5454220	Clear Creek near Oxford, IA	7080209	151
IR	11	5454300	Clear Creek near Coralville, IA	7080209	254
IR	12	5452000	Salt Creek near Elberon, IA	7080208	520
IR	13	5455500	English River at Kalona, IA	7080209	1486
TR	1	5411850	Turkey River near Eldorado, IA	7060004	1660

Table I-2 Continued

TR	2	5412020	Turkey River at Elkader, IA	7060004	2338
TR	3	5412400	Volga River at Littleport, IA	7060004	901
TR	4	5412500	Turkey River at Garber, IA	7060004	4000

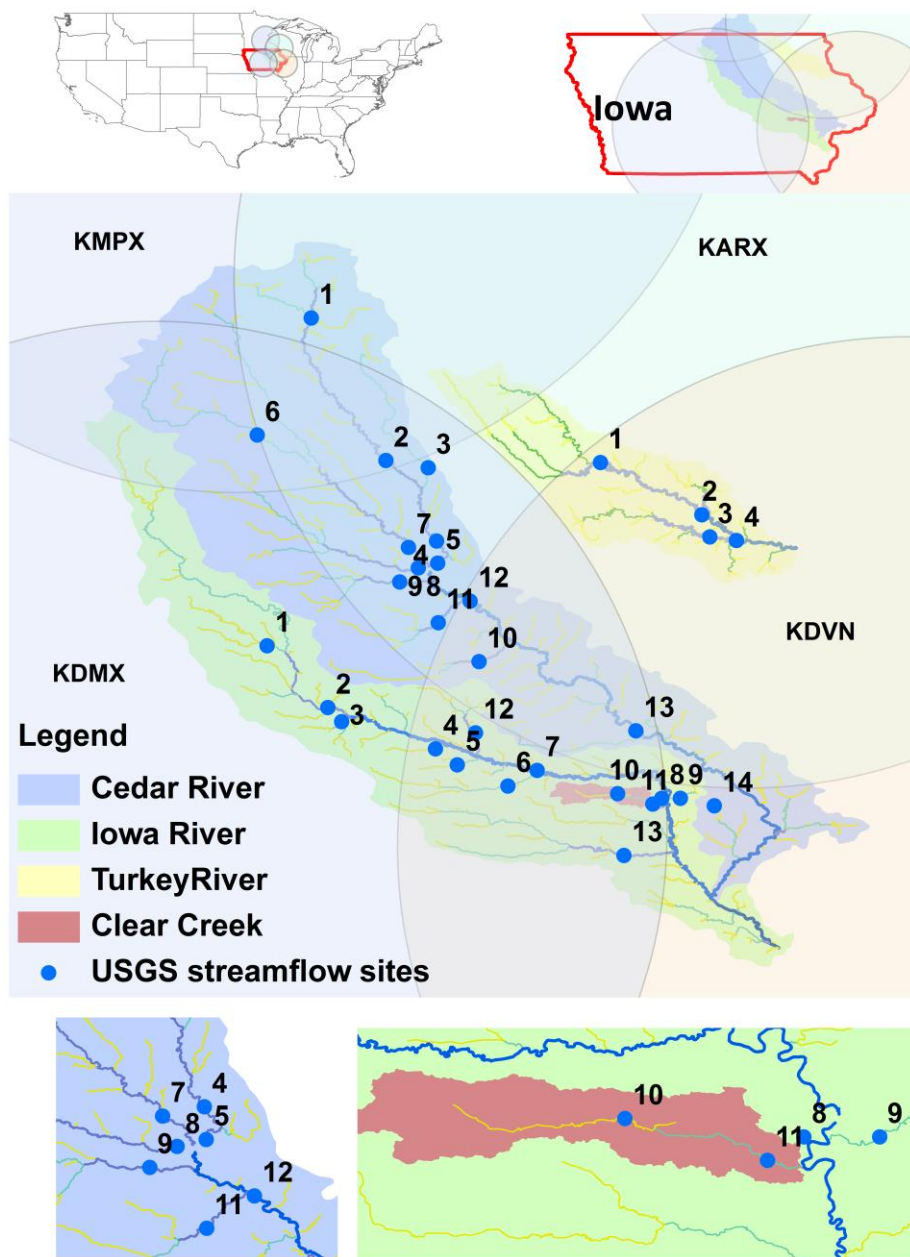


Figure I-1. Study area with USGS sites for which streamflow data is available

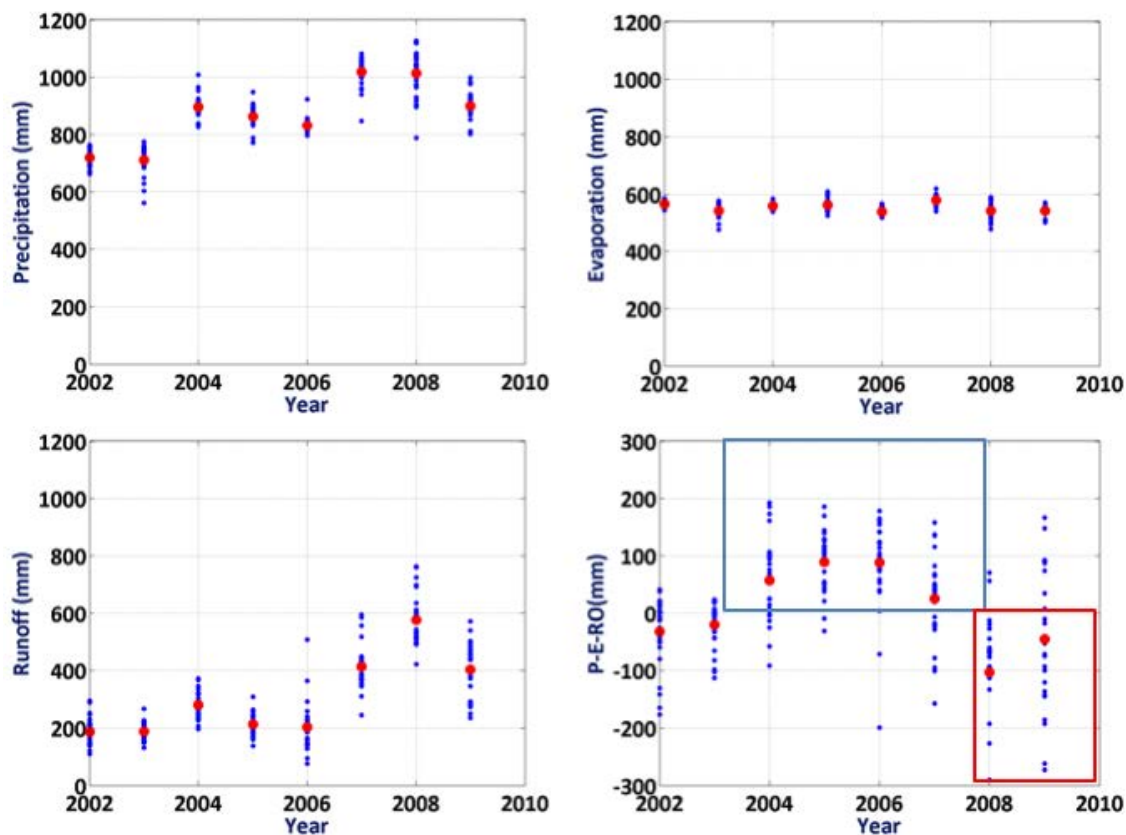


Figure I-2. Water balance for the Cedar River and Iowa River sites, from 2002 to 2009. All units are in mm/year: (a) annual rainfall; (b) annual evapotranspiration; (c) annual runoff; (d) annual water balance (difference between rainfall and sum of evapotranspiration and runoff)

CHAPTER II

TOWARDS A CALIBRATION-FREE HYDROLOGICAL MODEL

Criteria for model design

I adopt the downward approach for model building (Sivapalan, 2003), for which complexity is systematically added to the model until all the main features responsible for flood generation are well represented in the model. The development began with a simple conceptualization of the hydrological model that just included first order controls in flood generation. The process that should be added to or improved upon was chosen based on the data signature patterns that were not being well reproduced by the model. Some authors have discussed and/or applied this approach (Klemes, 1983; Yilmaz and Gupta, 2008; Sivapalan, 2009). However, these studies are still based on hydrological models that rely on calibration. As discussed before, once you calibrate the model you cannot guarantee that good results are being achieved for the right reasons. In this work, I avoid calibration by using parameters that can be prescribed *a priori* using physical properties of the watershed.

I conceptualize our model by focusing on the elimination of some of the inconsistencies commonly encountered in hydrological models:

Landscape decomposition and scale considerations: many models currently in use adopt a square-grid decomposition of the landscape. Another widely-used technique involves decomposition of the study area in sub-watersheds using an ad-hoc and subjective criterion. Examples of this type of decomposition are found, for example, in models that adopt control volumes that change depending on the physical characteristics of the study area, data availability, and study goal. For example, Reggiani and Sivapalan (1998) stated that a representative elementary watershed (REW) can encompass the entire watershed or any smaller sub-watershed. They stated that the size of the REW depends

on the spatial and temporal resolution for which the model is applied and on the spatial and temporal level of details of the available data sets.

The fundamental problem with this approach is that governing equations used to describe the physical processes in hydrologic models are sensitive to the scale (Klemes, 1983; Kirchner, 2006). However, these models use the same governing equations even when very different scales are adopted. In this work, I assume the existence of a fundamental hillslope (Montgomery and Dietrich, 1994) and decompose the landscape based on standard methodologies that attempt to identify the extent of the channel and the size of the hillslopes from Digital Elevation Models (DEM). Model governing equations were specified to represent physical processes at these specific scales.

Multi-scale evaluation of model results: In general, hydrological models are calibrated and validated using the observed responses at the basin outlet. Good agreement between observed and predicted streamflow for this site, assured by parameter calibration, does not guarantee that internal processes are being correctly represented. Therefore, investigating the capability of the distributed hydrological model for making reasonable predictions across scales is vital (Smith et al., 2004; Hunukumbura et al., 2011). To certify that processes are being correctly represented across scales, I validate the model using observed streamflow at the outlet of nested basins ranging in scale from about 20 to 16,000 km².

Numerical methods: Clark and Kavetski (2010) recently demonstrated the unreliability of numerical techniques usually adopted in hydrological modeling. They showed that numerical errors caused by fixed step explicit schemes overcome errors due to the model's structure and further encumber the calibration procedure. The authors recommend the use of the adaptive substepping method that is controlled by error tolerance. To avoid numerical errors and to guarantee the numerical stability of the model, I adopted the Runge-Kutta-Felberg adaptive algorithm bounded to user specified maximum errors.

Direct or indirect measurable parameters: I avoid calibration through the adoption of parameters that represent average properties of our control volumes and that can be estimated based on available data. This approach is in accordance with the ideas presented by Dooge (1986) that recommended micro-scale processes parameterization in order to achieve an understanding of hydrological laws at the catchment scale. Beven (2012) recommended the use of appropriate scale-dependent sub-grid parameterization that accounts for epistemic uncertainties as a way to avoid the need for “*hyper-resolution*” datasets for the implementation of global land surface modeling (Wood et al., 2011). Similar methods have been successfully applied in other fields of natural science. For example, in weather prediction, model parameterization is used to represent sub-grid processes for which observations are not available or are difficult to obtain.

While parameterizations are simplified and idealized representations of complex physical processes, they retain the essential behavior of the processes they represent (Stensrud, 2007). I parameterize all the processes that occur for scales smaller than the fundamental hillslope. In the development of our process conceptualization, I took advantage of available distributed datasets. Digital elevation models, land use, evapotranspiration potential, and soil properties are some of the observed data used for the model. While not free from uncertainties, these datasets provide important information about average hillslope physical properties.

Model development:

general model components and complexity level

For the reasons formerly mentioned, instead of using complex conceptualizations that suffer from equifinality, I opted for a simplified model formulation that does not require calibration and that does not provide an impartial tool to understand how errors propagate through the model. Since I estimate parameters based on data, complexities in the model formulation are limited by data availability. As noted by Blöschl (2001), for a

certain availability of data there is an optimum model complexity. If more complex models are developed based on the same datasets, problems of parameter identification and model structure non-uniqueness become significant and reduce predictive performance. I acknowledge that some important processes are not being represented in the model (e.g. soil macropores), but I believe that model complexity should follow the steps of data availability. Therefore, the structure of the model should be improved as more data become available. I focus on developing models that are just complex enough to represent the features that are relevant for flood prediction.

Our specific goal for the model is that it should simulate basin response to rainfall forcing at a wide range of scales, with the smallest being a hillslope scale. I reduce complexities in the hillslope dynamics by parameterizing known macro-scale hydrological behavior (McGlynn et al., 2002; Graham and McDonnell, 2010). The function of the hillslopes is to partition the rainfall input into surface runoff, infiltration, and evapotranspiration. This is accomplished by using empirically based parameterizations of the relevant processes documented in the literature. Runoff generated at the hillslopes is transported via the drainage network of connected links. Model equations at the hillslope and the link scale are based on mass and momentum conservation principles.

Table II-1 presents a list of models with different levels of complexity and data requirements. All of the models account for a realistic representation of the landscape (hillslope-link) and space-time rainfall variability. I remap the radar rainfall squared grid units to the hillslope-link structure adopted in the model. For model 1, I use a constant runoff coefficient in space and time and an average river channel velocity. This model only requires the digital elevation model (DEM) for its river network delineation and rainfall information as its main input. These two datasets are provided by satellite-based techniques on a near-global base: 30 (ASTER) and 90 (SRTM) meters DEM and rainfall maps with 3-hour temporal and $0.25^{\circ} \times 0.25^{\circ}$ spatial resolution (3B42, CMORPH,

PERSIANN, and others). However, the runoff coefficient and average channel velocity have to be estimated somehow. I demonstrate in Chapter 3 that if I “calibrate” these parameters based on observed streamflow, I obtain a reasonable match between observed and simulated discharge for a single event (or year), but these parameters cannot be extrapolated for other sites or different climatological conditions.

Complexity is added to the other models in terms of flow propagation through the hillslope and channel, rainfall-runoff generation, and the dynamics of water transport and storage in the soil. This is accomplished by using empirically based parameterizations of the relevant processes documented in the literature. For model 2, I add hillslope delay and define a constant velocity for the transport in the hillslope. Model 3 accounts for non-linear hillslope and channel routing mechanisms. For the hillslope, I use the Manning equation in which velocity is a function of the land cover type and the depth of water in the surface. For the channel, I employ a recent formulation of flow velocity for a network of channels in which velocity is a function of basin scale and discharge. I avoid using Manning equations to simulate transport through the channel since average channel slopes cannot be precisely estimated from DEMs. Models 4 and 5 account for space-time variability in runoff generation. Model 5 is the most complex version of the model and accounts for space-time variability in rainfall and rainfall-runoff generation, non-linear transport in the hillslope and channel, and baseflow. For model 4, I increase complexity in terms of rainfall-runoff dynamics but decrease the complexity in terms of routing by using a constant channel and hillslope velocity. Model 5 is the most complex model and includes complexity in runoff generation and routing. I describe this model version in the following sections. Examples of applications of the other models will be presented in Chapter 3.

All the parameters of model 5 are estimated based on data. The model uses the information on land cover and land use, soil types, and topography based on readily available data that are mapped to the scale of the hillslopes. The function of the

hillslopes is to partition the rainfall input into surface runoff, infiltration, and evapotranspiration. The selected water velocity model attenuates the aggregated discharge. The model has a power law functional form, with the velocity dependent on the magnitude of the discharge and the upstream drainage area. The coefficients of the velocity model are calibrated by using the USGS collected and published discharge and water velocity data. The fact that the model's parameters are not calibrated to fit observed discharge implies that the uncertainties in the input are independent of the errors in the simulated discharge. Differences between observed and simulated values are due to data uncertainty or model structure. Data uncertainty includes uncertainty in the observed input (precipitation and potential evapotranspiration) and output (streamflow) variables or in the datasets used to represent the physical properties of the basin (e.g. DEM, land cover, soil properties). Model uncertainty can be due to processes that are not accounted for or not correctly represented in the model. This approach allows us to recognize missing or incorrect processes as well as problems with observations.

Landscape decomposition and control volumes

Grid-based hydrological models have become popular (see a list of models in Kampf, 2007) since the raster format is largely adopted for land surface properties (land cover, DEM) and input data (precipitation). However, in nature, a watershed is made up of hillslopes, where rainfall-runoff transformation occurs, and these areas are connected by the river network (links) that transports to higher order streams. Grids are not natural control volumes and cannot accurately reproduce the paths of the water in a watershed (Dehotin and Braud, 2008). Another strategy for landscape decomposition accounts for the generation of an unstructured grid that is based on Delaunay triangulation and uses the river network, watershed boundary, elevation contours, vegetation, and geology as constraints (Duffy, 2007). In this case, delineated control volumes can have any size

since they depend on user specification or internal variability of physical properties. When the sizes of the control volumes are considerably different, scaling problems arise from the fact that the governing equations are not scale independent.

In this work, I adopted a hillslope-linked based model. This type of landscape compartmentalization provides a more accurate representation of the river network, with lower computational requirements. The river network plays an important role in the scaling parameters of the peak flow power laws (Gupta et al., 1996; Menabde et al., 2001; Gupta, 2004), and its correct representation is essential for simulating floods across multiple scales. This method is also computationally more efficient when compared to grid cell models since it operates directly at the hydrological scale of interest (i.e. the hillslope). To achieve the same level of accuracy in representing the river network using grid decomposition, a very fine mesh would have to be defined. In this case, the large computational cost of the calculations performed by grid cells would constrain the applications to small areas (Yang et al., 2002). Moreover, using hillslopes as the main control volumes allows the direct application of methods and theory developed in the field of hillslope hydrology. Advances in this area have been made through field and numerical experiments (Jones and Swanson, 2001). Hillslope-linked models provide a framework to extrapolate these findings to larger areas.

The river network structure is extracted from DEMs using algorithms based on the maximum gradient method and pruning algorithms to determine the initial location of the river network (Mantilla, 2005). In this procedure, all DEM pixels are classified either as hillslope or river network. Figure II-2 presents the hillslope-link discretization for the Cedar River basin. In this example, an area equal to approximately 17,000 km² was divided into more than 60,000 hillslopes and links with an average hillslope area equal to 0.2 km². Sub-watershed models (e.g. HBV, Kineros, SWAT) also use the discretization of the watershed in sub-areas where runoff is generated. However, these models usually do not specify a clear criterion for the partition of the watershed, and the decision about

how to proceed is transferred to the user. In the literature, we can find applications of these models for areas that vary in scale from hillslopes ($\sim 1 \text{ km}^2$) to large watersheds (Gu et al., 2010). However, in all of these applications, the model equations are kept the same.

General model description

I use a set of four coupled non-linear ordinary differential equations that describe changes in mass balance in each control volume to represent hydrological and hydraulic processes at hillslopes and links. The four equations account for water balance in the (1) link; (2) surface hillslope storage; (3) saturated soil zone; and (4) unsaturated soil layers. All state variables are solved simultaneously using a time-adaptive numerical method to avoid numerical inconsistencies (Kavetski, 2011). The solutions to these equations provide hydrographs at each channel junction in the network and continuously account for moisture states in the surface, saturated and unsaturated soil layers, and channels over the entire basin domain.

Hillslope physical properties are averaged over its elementary area to provide information about average fluxes and travel time for different hydrological components that contribute to runoff generation. As in nature, small scale heterogeneities in runoff generation are averaged out by the effect of the river network that links different areas in the basin and organizes flow transport. Figure II-3 presents a schematic representation of the model's main control volumes and fluxes. The definition of the balance equations, fluxes, and parameters will be presented throughout this chapter. I use upper case letters for static variables (e.g. total hillslope area) and lower case for dynamic variables (e.g. time series of precipitation, soil volumetric moisture).

I implemented the model equations as part of the code built into CUENCAS, initially introduced by Mantilla and Gupta (2005) as a research tool to investigate morphological characteristics of the river network and its role in flow scaling.

Mandapaka et al. (2009) applied a simplified version of the model to investigate the effect of rainfall variability on the statistical structure of peak flow. To investigate land cover changes' effects on flood risk, Cunha et al., (2011) applied a more complete version of the model that includes surface and subsurface processes. Gupta et al. (2010) referred to CUENCAS as an important tool to perform theoretical investigations that would explain the link between peak flow versus area scaling parameters and physical properties of the inputs and watershed. Figure II-1 presents a flowchart with the main processes simulated by the model. We indicate in the figure the processes that were introduced in the model during the development of this thesis and the processes that were previously implemented by Mantilla (2007).

A semi-parallel version of the code was developed based on the compartmentalization of the basin into sub-basins according to a specific Horton order specified by the user. The sub-basins are solved in parallel using as many processors as available or needed. Initially, just external sub-basins that do not have a link contributing to it can be solved. Once external links are solved, the internal sub-basins are solved. This process is followed systematically until all of the sub-basins are covered.

In the next section, I present the description of model 5 listed in Table II-1. I start with a brief description of the main model's hydro-meteorological inputs. Following this section, I summarize all the parameters used to characterize hillslope and channels. Once all forcing and parameters are characterized, I introduce the balance equations for each control volume with correspondent fluxes.

An Appendix will be included in the final version of the thesis with the equations in the version prepared by Dr. Rodica Curtu. Dr. Curtu, from The University of Iowa's Department of Mathematics, is exploring the role of non-linear hillslope and channel dynamics on flood generation. The equations were worked out to a version more suitable for the study of the dynamical systems. All variables were normalized and are dimensionless. Dr. Scott Small is implementing this version of the equations in a more

efficient solver written in C language that takes advantage of parallel computing and will be the basis for a flood forecast system for Iowa, supported by the Iowa Flood Center (IFC) (Small et al., submitted).

Model input: Hydrometeorological variables

The model is forced by three main hydro-meteorological processes: precipitation ($p(i, t)$), snow melt ($s_m(i, t)$), and potential evapotranspiration ($e_{pot}(i, t)$).

Precipitation (rainfall and snow) and evaporation are first-order controls in flood generation. Rainfall and snow melt intensity, duration, and spatio-temporal distribution, combined with the river network structure, drive the way in which water is distributed in the landscape. The focus of this study is on flood events caused by heavy rainfall.

However, it is important to account for evaporation and snowmelt, since these processes define the basin moisture conditions that precede rainfall events.

Precipitation is the main driver of floods; therefore three chapters of this thesis will be dedicated to investigate the effect of rainfall uncertainties on flood prediction across scales. In Chapter 5, bias corrected radar rainfall is used as a reference in order to understand the impact of different types of rainfall error structures on peak flow prediction. For long-term simulations, I will use Stage IV - NWS products (2002 to 2009) with approximately 4 km spatial resolution and 1 hour temporal resolution. In Chapter 6, I focus on errors introduced by rainfall space-time resolution or sampling interval. In Chapter 7 I compare different rainfall datasets.

Quantification of snow contribution is important because it sets soil and channel states for the beginning of the wet season. Remote sensing is the only source of snow information that covers large areas and is continuous in space and time. However, the coarse resolution of remote sensing datasets may not be appropriate for snow mapping and flow simulation in small basins. In this work, I evaluate two different sources of snow information: (1) Snow melt products derived by the North American Land Data

Assimilation System (NLDAS) with hourly resolution in time and 1/8 degree resolution in space (Pan et al., 2003) and (2) snow water equivalent retrieval from AMSR-E L3 data (Tedesco and Narvekar, 2010). In the second case, I neglect sublimation and snowmelt is calculated by the difference in the values of the snow water equivalents between two days.

Dingman (2002) defines potential evapotranspiration (PE) as "the rate at which evapotranspiration would occur from a large area completely and uniformly covered with growing vegetation which has access to an unlimited supply of soil water and without advection or heat-storage effect." PE strongly affects soil moisture content, especially between rainfall events in the summer and spring seasons, and consequently plays an important role in runoff generation. In this version of the model, I use potential PE to estimate the actual evaporation from the surface and from the unsaturated and saturated layers of the soil. Using PE to calculate actual evaporation assumes that the only limitation for evaporation is water availability. No limitations are imposed on the evaporation of water from the surface storage.

The soil evaporation from unsaturated layers are limited by the soil volumetric moisture and relative depth of water compared to the total depth of soil. When a large amount of water is available, PE limits maximum evaporation. I adopted two different data sources: (1) PE estimated based on remote sensing (MODIS 16) and (2) PE used as forcing by NLDAS-2 that was computed in NCEP North American Regional Reanalysis using the modified Penman scheme of Mahrt and Ek (1984). MODIS products are provided with 1 km in space and 8 days resolution in time, while the NLDAS-2 products are provided with hour resolution in time and 1/8° (~13km) resolution in space.

Model parameters

In this study, I obtain all model parameters directly or indirectly from data and do not use calibration. A summary of all parameters used in the model 5 (Table II-1)

version of the model is presented in Table II-2. Some of the parameters are directly measured (e.g. slope, hillslope area), while others are linked to physical properties of the watershed using empirical methods, data analysis, or hydraulic theories (e.g. infiltration parameters, velocity of runoff transport in the hillslope). In this section, I will describe all of the parameters used in the model and discuss how they are obtained. Some of the parameters are schematically represented in Figure II-3.

Measurable hillslope and link parameters are obtained from the digital elevation model: hillslope relief $H_H(i)$, measured in meters, hillslope drainage area $A_H(i)$, measured in km^2 , hillslope length $L_H(i)$ that is equal to the link length, also measured in meters, and average surface slope $S_H(i)$, measured in m/m. DEM also provides the relationship between hillslope relief and area (see Figure II-3). This function describes the curvature of the hillslope, which has a strong effect on saturated storage and, consequently, on the generation of overland flow (Talebi et al., 2008).

I adopt a simplified conceptualization of the hillslope subsurface geometry to estimate impermeable area as a function of hillslope shape and water volume in the saturated soil layer. In Figure II-3, I present a schematic representation of this geometry for convex (b-1) and concave (b-2) hillslopes. Hillslope shape is an important factor affecting rainfall-runoff partitioning. Convex hillslopes exhibit higher transport power (due to higher slope) and lower saturation capacity than concave hillslopes (Sabzevari et al., 2010) (see Figure II-3 b-1 and b-2). O'Loughlin (1981) demonstrated the relationship between impermeable area and topographic parameters using idealized hillslopes.

I assume that the bedrock surface is parallel to the hillslope surface, so the water table is calculated as a function of water volume in the saturated soil layer. I use the topography data (DEM) to estimate a relationship between the water table and the percentage of impermeable area (for an example, see plots in Figure II-3 b-1 and b-2).

To represent this relationship, I fit a third order polynomial function to the topographic data extracted from the DEM:

$$\frac{a_I(i,t)}{A_H} \left(\frac{h_{rel}(i,t)}{H_{relmax}} \right) = b(i) \left(\frac{h_{rel}(i,t)}{H_{relmax}} \right) + c(i) \left(\frac{h_{rel}(i,t)}{H_{relmax}} \right)^2 + d(i) \left(\frac{h_{rel}(i,t)}{H_{relmax}} \right)^3 \quad \text{Equation II-1}$$

In this equation, a_I is impermeable (saturated) area, a_I/A_H (%) is the fraction of the total hillslope area that is impermeable when the water table is equal to h_{rel} , and h_{rel}/H_{relmax} (%) is the water table normalized by total hillslope relief. The parameters a, b, c, and d are subject to the following constraints:

- (1) $a(i) = 0$ – Impermeable area is equal to zero if water table is equal to zero;
- (2) $b(i) + c(i) + d(i) = 1$ –impermeable area is equal to hillslope area when water table is equal to hillslope relief ($h_{rel}/H_{relmax} = 1 \rightarrow a_I/A_H = 1$);

The derivative of this equation with respect to the water table describes how the impermeable area changes when the water table level changes:

$$\frac{da_I(i,t)}{dh} (h_{rel}(i,t)) = \frac{A_H}{H_{relmax}} \left[b(i) + 2c(i) \left(\frac{h_{rel}(i,t)}{H_{relmax}} \right) + 3d(i) \left(\frac{h_{rel}(i,t)}{H_{relmax}} \right)^2 \right] \quad \text{Equation II-2}$$

In the literature, many theoretical and conceptual models are used to simulate soil dynamics and to predict subsurface flow. The solution of high-dimensional physical models (Richards' equations for subsurface flow) are not computationally efficient, especially if applied to a large number of hillslopes in a catchment scale model. Conceptual models are computationally efficient but usually present parameters that are not physically well-defined. Basha and Maalouf (2005) derived models that simulated soil saturated flow in the hillslope, which combine a sound theoretical basis with the simplicity of conceptual models. The authors demonstrated that simple models based on physical assumptions perform well in simulating soil drainage, while they also have the potential to be easily incorporated into large scale models.

The model applied in this study was developed to simulate floods in a large range of basin scales. Therefore, adopting a very complex physical model to simulate the soil

dynamics would be computationally unfeasible. Also, I attempt to estimate the model's parameters by using information that is available on a nearly global basis. Models with a high level of complexity present a large number of parameters and, consequently, have large data requirements. For flood prediction, it is important to correctly estimate the soil water balance and residence time to continuously estimate soil water content. Another option is to assimilate remote sensing or the land surface model information of soil moisture to initialize flood simulations.

I opted to implement a simplified model of soil dynamics that is computationally efficient but still preserves the link with physical parameters that can be estimated or measured. I will demonstrate that despite the simple soil conceptualization, the model is able to capture the main hydrological processes that occur across scales. Some assumptions have been made in the current version of the model in order to obtain this simplified representation of soil dynamics:

1. The bedrock surface is presumed to be parallel to the hillslope surface, with $H_b(i)$ representing the *effective* distance between these two layers. The *geometric* distance between the two layers is equal to $H_b(i)$ divided by the soil porosity. This parameter characterizes the soil's potential to store water.
2. Hillslope relief is much larger than the effective depth of the impermeable layer, so the volume of water can be stored in the soil can be estimated by $V_T(i) = H_b(i) \times A_H(i)$.
3. The soil is divided into two layers: above (unsaturated zone) and below (saturated zone) the water table level. The average soil hydraulic properties are defined for each layer.
4. The contributions from the confined aquifer located below the impermeable layer of rock are neglected.
5. The hydraulic conductivity $K_{SAT}(i)$ of the soil layer is considered to be constant with depth, and unsaturated hydraulic conductivity $K_{UNSAT}(i)$ is calculated as a

function of the soil volumetric moisture. Soil hydraulic conductivity usually decreases with depth, while in the unsaturated layer, unsaturated hydraulic conductivity can increase or decrease depending on soil conditions (Davidson et al., 1969). The implementation of more complex soil models would require detailed information about the spatial distribution of soil hydraulic properties, which is currently not available.

6. For each hillslope, the water table is parallel to the reference level ($dh_{rel}/dx = 0$), as indicated in Figure II-3. Based on this assumption and assumptions (1) and (2), the volume of water in the saturated zone is $v_{sat}(i, t) = H_b(i) \times a_l(i, t)$ and the volume available in the unsaturated zone is $v_{unsat}(i, t) = V_T(i) - v_{sat}(i, t)$. Soil volumetric moisture is defined as the difference between the volume of water in the unsaturated zone and the volume available in the unsaturated zone:

$$\theta(i, t) = \frac{v_{w_unsat}(i, t)}{v_{s_unsat}(i, t)} \quad \text{Equation II-3}$$

The effective depth of the impermeable layer $H_b(i)$ [L] is one of the most sensitive model parameters. For some regions of the world, very detailed soil databases are available and can provide accurate values of $H_b(i)$. For other regions, not a lot of soil information is available, and global datasets or a methodology based on the Soil Conservation Service – Curve Number (SCS-CN) method is proposed. Therefore, based on the definition of $H_b(i)$ and data availability, I define three different methods to estimate the effective depth of the impermeable layer:

1. Using SURGO or STATSCO datasets: H_b is equal to the Available Water Storage (AWS) at 150 cm, defined as “the volume of water that the soil, to a depth of 150 centimeters, can store that is available to plants.” I recognize that this value will be inaccurate for regions where the bedrock depth is much greater than 150

meters. However, due to the high quality of the SURGO, I opted to use this dataset in this study.

2. The harmonized gridded global data set of soil parameters derived from the ISRIC-WISE soil database (Batjes, 2005) also provides available water storage with the same definition presented by SURGO.
3. The Soil Conservation Service – Curve Number (SCS-CN) method estimates the potential maximum retention of the soil as a function of land cover and soil type. In the traditional way of applying the SCS-CN method, the potential maximum retention S_{cn} of the soil is specified as a function of three classes of previous moisture conditions.

In this work, I apply the SCS method in a continuous way and fix the potential maximum retention based on soil properties provided by the SSURGO dataset. Soil's water available storage changes dynamically according to soil fluxes (infiltration, percolation, base flow). The original SCS-CN limitations have already been discussed in the literature (Michel, 2005; Durbude et al., 2011), and some solutions have been proposed. In this work, I take advantage of the method's definition and the large amount of data used to empirically estimate the method's parameters as a function of available information (Land cover, soil hydrologic group), and I address inconsistencies in the original method through the use of a dynamic soil model.

In Figure II-4 we present some soil properties for the study area. The two maps in the top are based on SSURGO dataset and were used to estimate model parameters for the for the simulations presented in Chapter III. On the left I present saturated hydraulic conductivity (m/s) and on right available water capacity of soil (cm/150 cm of soil). On the bottom I present data provided by the Iowa Geological Survey, DNR. Bedrock surface elevation (ft) is presented on the left, and soils requiring tile drainage for full productivity on the right. These two datasets could be used in the model if information

was available for the part of the basin located in the Minnesota State. These dataset was just available for Iowa State

Hydraulic conductivity is another soil property that shapes hydrological dynamics in the soil layer. This variable is also provided in the datasets described in items (1) and (2). For the Soil Conservation Service method, a relationship between the soil hydrological group and soil hydraulic conductivity is used. As discussed before, due to the lack of detailed information on the vertical distribution of soil properties, average soil hydraulic properties are defined for each layer. Hydraulic conductivity is estimated based on the datasets described before, and the unsaturated hydraulic conductivity is estimated using the empirical formula proposed by Davidson et al. (1969):

$$K_{UNSAT}(i, t) = K_{SAT}(i) \times e^{(bs(i) \times (\theta(i,t) - 1))} \quad \text{Equation II-4}$$

Where K_{SAT} is the saturated hydraulic conductivity, $K_{UNSAT}(i, t)$ is the unsaturated hydraulic conductivity, $\theta(i, t)$ is the volumetric soil moisture, and b is a constant. Using this equation, the author demonstrates that water draining from a soil profile is usually well represented using an average of hydraulic conductivity versus soil water content. In the same paper, the author estimated the parameters b for three different types of soil: Yolo loam (48.2), Miller silty clay (196.5), and Cobb loamy sand (82.7).

Hillslope is the fundamental model element where the partition of rainfall into interception, infiltration, evaporation, and runoff occurs. Figure II-3 (a) presents a schematic representation of all the fluxes in the model, and weather radar rainfall is the main input. I remap the radar rainfall squared grid units to the hillslope-link structure adopted in the model. Once rainfall reaches the surface, it is transformed into surface ponding, and the ponding water infiltrates, evaporates, or runs to the channel. The model accounts for the Hortonian overland flow (HOF) and saturation excess overland flow (SEOF). HOF occurs when ponding water exceeds the infiltration capacity at the areas of

the basin where the soil is not saturated (permeable areas, represented by green in Figure II-3 (a)). In this region, the percentage of surface water that infiltrates depends on the deficit of water in the soil (soil volumetric moisture) as well as on the soil infiltration capacity. Soil properties are provided by SSURGO. SEOF occurs in the areas of the basin where soil is saturated (impermeable areas, represented by gray in Figure II-3 (a)) (Freeze, 1980). As in nature, HOF and SEOF might occur simultaneously in the same hillslope. The transport of the ponding water is simulated using Manning equations. Roughness parameters are estimated based on land cover data.

At the hillslope scale, I estimate infiltration based on the Soil Conservation Service Curve Number Method (SCS-CN). SCS-CN is an empirical model that has been studied extensively since 1956 and has been applied by the hydrological community to solve diverse problems (Tsihrintzis, 1997; Mishra and Singh, 1999; 2004; Schneider and McCuen, 2005). The method is based on empirical experiments conducted in watersheds with areas similar in size to the unit area defined by CUENCAS (0.05 km²). This model's main advantage is its reliance on only one parameter, i.e. CN that is directly linked to H_b . The original SCS-CN method was derived to compute surface runoff as a result of an isolated rainfall event. The method is based on the water balance equation and two fundamental hypotheses. The first hypothesis states that the ratio of direct runoff to maximum potential runoff is equal to the ratio of infiltration to maximum potential soil retention (H_b). The second hypothesis is related to the initial abstraction that is estimated as the fraction of the potential maximum retention:

$$P = I_a + F + Q \quad \text{Equation II-5}$$

$$\frac{Q}{P-I_a} = \frac{F}{H_b} \quad \text{Equation II-6}$$

$$I_a = \alpha H_b \quad \text{Equation II-7}$$

By combining the previous equations, accumulated runoff is calculated by:

$$Q = \frac{(P-I_a)^2}{P-I_a+H_b} \quad \text{Equation II-8}$$

In this equation, Q (mm) is the accumulated runoff and P (mm) the accumulated rainfall since the beginning of the event. Taking the derivative of Equation 1-8 with respect to time, we obtain:

$$\frac{dQ}{dt} = q = \frac{dQ}{dP} \times \frac{dP}{dt} = \frac{(P-I_a)(P+2S-I_a)}{(P-I_a+H_b)} \times \frac{dP}{dt} \quad \text{Equation II-9}$$

The left side of Equation 1-9 represents the percentage of rainfall that runs off into the river. Infiltration is represented by $(1-RC)$. I modified the original SCS-CN version to account for soil and surface moisture that are continuously calculated by the model. The first modification is related to the initial abstraction. The initial abstraction accounts for surface storage, interception, and infiltration before runoff begins. I explicitly account for these variables in the continuous version of the model. I also assume that water from precipitation is first stored at the surface. Once on the surface, this water becomes available to infiltrate, evaporate, or run to the river. Infiltration is a function of the surface storage ($S_p(i, t)$) and the deficit of water in the soil $d_{soil}(i, t)$ that is continuously calculated by the model:

$$d_{soil}(i, t) = (1 - \theta(i, t)) \times H_b(i) \quad \text{Equation II-10}$$

This model better represents reality since infiltration happens when there is available ponded water (and not just during rainfall events), and the soil storage potential is not a fixed value but depends on the soil moisture's initial conditions. Infiltration occurs continuously until all the water from precipitation runs to the river, evaporates, or infiltrates. Under the previous assumption, I obtain a time dependent equation to estimate the infiltration and runoff coefficient:

$$RC(i, t) = \left(\frac{s_p(i,t) \times (s_p(i,t) + 2 \times (d_{soil}(i,t)))}{(s_p(i,t) + d_{soil}(i,t))^2} \right) \quad \text{Equation II-11}$$

Soil infiltration is also controlled by the maximum infiltration rate that is equal to $K_{SAT}(i)$:

$$if(s_p(i, t) < K_{SAT}(i) \quad \text{Equation II-12}$$

$$inf(i, t) = K_T \times s_p(i, t) \times (1 - RC(i, t)) \quad \text{Equation II-13}$$

Otherwise:

$$inf(i, t) = K_{SAT}(i) \times (1 - RC(i, t)) \quad \text{Equation II-14}$$

Where K_T is a recession coefficient equal to [1/hour].

At the same time that infiltration occurs, part of the ponded water is also being transported from the hillslope to the river. A non-linear reservoir method is used to propagate the water from the hillslope surface to the channel. The flux from the surface to the link is a function of the amount of water stored in the hillslope ($q = K(s_p) \times s_p(i, t)$). The method is non-linear since $K(s_p)$ is also a function of the storage on the surface. $K(s_p)$ is related to the average time required for water to leave the hillslope and enter the channel, so it is dependent on hillslope size and geometry (larger catchments have larger T), slope, and land use (Dingman, 2002). To estimate an average $K(s_p)$ for each time interval, I estimate an average velocity using Manning's equation divided by the average distance followed by the water, assuming uniform ponding over the hillslope. The average distance is equal to the distance from the hillslope's center of mass to the channel. Considering that the hillslope area is divided in two by the channel, the hillslope width is approximated by $A_H(i)/(2 \times L_H(i))$, and the center of mass is located approximately at 0.6 of this distance (USDA-NRCS):

$$v_H(i, t) = \frac{1}{n(i)} \times S_H(i)^{1/2} \times (s_p(i, t))^{2/3} \quad \text{Equation II-15}$$

$$K(i, t) = \frac{v_H(i, t)}{L_{CM}(i)} = v_H(i, t) \times \frac{1}{0.6} \times \left(\frac{2 \times L_H(i)}{A_H(i)} \right) \quad \text{Equation II-16}$$

The spatial distribution of Manning's roughness coefficient for hillslopes was then determined based on the land use map and the Manning coefficient that are a function of the land cover (Dingman, 2002).

Once the water leaves the hillslope, flow is propagated throughout the river network. In order to solve the mass conservation equation that accounts for storage in each link, a relationship between link storage and link discharge should be established. Assuming that water depth is constant in a link (kinematic assumption), Mantilla (2007) defines channel discharge as a function of channel storage as $q = (v/l) \times S_c$. In order to solve the balance equation for a channel link, I need to estimate flow velocities. One option is to consider flow velocity as constant throughout the network. However, this scenario is unrealistic since flow velocities exhibit great variability in space and time. Another option would be to consider the Manning equations, but in this case I need an estimation of channel slope, which is not accurately provided by DEMs.

To overcome these issues, Mantilla (2007) proposed a non-linear model to describe space-time flow velocities throughout the river network as a function of the instantaneous discharge q and the upstream drainage area $A(i)_{ups}$:

$$v = v_0 \times q^{\lambda_1} \times A(i)_{ups}^{\lambda_2} \quad \text{Equation II-17}$$

Where v_0 , λ_1 , λ_2 are parameters that can be estimated based on hydraulic data collected throughout the river network. Mantilla (2007) derived this equation under the following assumptions:

- The geometry of the link can be represented by an average cross section;
- Flow depth at a given moment in time t is the same along the link (kinematic assumption);
- Flow velocity v in the channel is a function of the hydraulic radius and the channel slope;
- Hydraulic similarity, i.e. different links in the network will share a common rescaled rating curve, holds for all channels in the river network.

Paik (2004) derived the same equation by assuming an empirical relationship between peak flows of different return periods with basin area and a frequency factor

reported by Stall and Fok (1968). The author used this equation to investigate the effect of non-linearity of flow routing on the timing and magnitude of the geomorphic instantaneous unit hydrograph (GIUH) peak flow.

The role of flow velocities on the variability of flood peaks was investigated by Mantilla et al. (2006) and Mandapaka et al. (2009) in simulations of synthetic events with idealized runoff generation conditions for Walnut Gulch and Whitewater basin, respectively. In our work, I extend the studies of these authors for more realistic rainfall-runoff scenarios and investigate how it affects the simulation of real flood events. The estimation of these parameters and the validity of this relationship to real flood events and the effects on peak flow simulation are discussed in Appendix A of this thesis.

Balance equations and fluxes

Our mathematical model comprises four differential equations that represent the dynamics of fluxes at the local control volume i , defined by one hillslope-link pair in the landscape: (1) Runoff transport; (2) Surface hillslope storage; (3) Water table; and (4) Soil volumetric moisture in the unsaturated zone. These equations will be described below. All the fluxes in these equations are in mm/hour. I normalized the flux equations by hillslope area in order to compare fluxes generated in different control volumes. The first equation accounts for runoff transport through the river network. Gupta (1998) proposed this equation based on the mass conservation in a channel link. The link between channel storage and discharge and a space and time formulation for velocity in the river network were introduced by Mantilla (2007), which I briefly described in the previous section. Combining these formulations, I obtain the equation that models runoff transport through the river network:

$$[\tau] \frac{d}{dt} q(i, t) = [q]^{\lambda_1} \left(A_H(i) \left(q_{p,l}(i, t) + q_{s,l}(i, t) + s_m(i, t) \right) + q_{in}(i, t) - q(i, t) \right)$$

Equation II-18

Where $q_{p,l}(i, t)$ is the flux from the ponded area (surface) to the link, $q_{s,l}(i, t)$ is the baseflow (soil saturated layer to link), $s_m(i, t)$ is the snow melt, $q_{in}(i, t)$ is the sum of the discharge from the upstreams links, and $q(i, t)$ is the outflow from the link. τ is a scale-dependent property of the river network based on the velocity equation introduced by Mantilla (2007) and defines the timescale of the process:

$$\tau = \frac{(1-\gamma_1) \times L_H}{60 \times v_o \times A(i)^{\gamma_2}} \quad \text{Equation II-19}$$

The function $q_{in}(i, t)$ represents the sum of fluxes from incoming channel-links, defined by j-th, connected directly to the link i-th:

$$q_{in}(i, t) = \sum_{j \in \text{Link}(i)} q(j, t) \quad \text{Equation II-20}$$

The second equation accounts for the ponded water on the surface of the hillslope:

$$\frac{d}{dt} s_p(i, t) = \left(q_p(i, t) - q_{p,l}(i, t) - q_{p,u}(i, t) - e_s(i, t) \right) \quad \text{Equation II-21}$$

In this equation, $q_p(i, t)$ is the input signal in the form of rainfall, $q_{p,u}(i, t)$ is the infiltration from the surface into the soil matrix, $q_{p,l}(i, t)$ is the flux from the ponded area (surface) to the link, and $e_s(i, t)$ is evaporation from the surface. I will next describe all the fluxes in Equation 2-18 and Equation 2-21.

Once it rains, water is accumulated on the surface and is available for infiltration or runoff. Surface runoff may be dominated by infiltration excess (Horton mechanism), saturation excess (Dunne mechanism), or a combination of both (Loague et al., 2010). Horton overland flow (HOF) occurs when the rainfall rate is higher than the soil surface infiltration capacity, resulting in the ponding of water. The rate of infiltration that occurs in the permeable area is equal to:

$$q_{p,u}(i, t) = \frac{a_p(i, t)}{A_H(i)} * \text{inf}(i, t) \quad \text{Equation II-22}$$

Where $\text{inf}(i, t)$ is the infiltration capacity, which was defined previously as a function of the current soil moisture state, maximum soil infiltration rate, and surface water availability. Saturation excess overland flow (SEOF) occurs when the soil saturated zone reaches the surface, resulting in an impermeable or almost impermeable layer. This mechanism occurs with the portion of the precipitation that falls over impermeable surfaces. The total water that will be accumulated on the surface is equal to the SEOF plus the portion that exceeds infiltration capacities in the permeable surface. This water is available for runoff.

As described before, flux from the hillslope surface to the link channel ($q_{s,l}(i, t)$) is based on a non-linear reservoir method and Manning's equation. An average distance followed by the water in the hillslope is estimated by assuming uniform ponding over the basin and that the hillslope center of mass is at 0.6 of the distance between the center point of a link and the basin divide:

$$q_{p,l}(i, t) = \frac{1}{0.6} * \left(\frac{2 \times L_H(i)}{A_H(i)} \right) \times v_H(i, t) \times s_p(i, t) \quad \text{Equation II-23}$$

The flux $e_s(i, t)$ corresponds to the evaporation from the surface. All evaporation components, including the ones from the saturated and unsaturated layers of the soil, are described at the end of this section. I do not directly account for transpiration from plants. However, the datasets used in this work provide potential evapotranspiration, which is the sum of potential evaporation and transpiration (Mu et al., 2007). Water will also be removed from the soil depending on water availability in the saturated and unsaturated layers.

The flux $q_{s,l}(i, t)$ represents baseflow, i.e. the flux from the saturated layer of the soil to the link. The flow of water in a saturated medium is described by a modified version of Darcy's law: $q = -K_{SAT}(i) \times dh/dx$, h being the hydraulic head. dh/dx is equal to the topographic hillslope slope S_H . This equation would be valid if the soil were totally saturated ($v_{s\text{sat}}(i, t) = V_T(i)$). However, as the soil is not completely saturated,

baseflow is also a function of the ratio between the saturated and the total soil volume.

The final equation for baseflow, normalized by the hillslope drainage area, is:

$$q_{s,l} = K_{SAT}(i) \times S_H(i, t) \times \left(\frac{v_{s,sat}(i,t)}{V_T(i)} \right) \times \left(\frac{a_1(i,t)}{A_H(i)} \right) \quad \text{Equation II-24}$$

It is important to point out that this soil representation was developed considering the available information for parameter estimation. It is possible that other locations would require other conceptualizations, depending on processes that dominate soil dynamics. For example, in this work I did not consider the existence of tiles in agricultural fields. In the next chapter, I will demonstrate that even without the representation of tiling I achieved a reasonable representation of the soil dynamics. It is probable that model results would be better if tiling had been considered. However, at this point I do not have enough information about tiling locations, quantities, or even maintenance states to consider it in watershed scale models, even if I was to adopt very conceptual formulations. This topic should constitute the object of future research.

In this version of the model, I neglected snowmelt infiltration and sublimation and assumed that all snowmelt is directly transformed into runoff. Snow water movement through the frozen soil layer is a complex process and is not the focus of this study. On the one hand, soil ice content affects hydraulic conductivity through pore constriction because ice blockage decreases soil permeability and thereby impedes infiltration (Iwata et al., 2010). On the other hand, due to the low permeability of frozen soils, much of the snow melt flows to depressions and ponds and then infiltrates at a rate comparable to saturated soil hydraulic conductivity (Hayashi et al., 2003). Prediction of snowmelt dynamics would require a large amount of data. As the focus of this work is on extreme flood events, snowmelt is just being considered here due to its importance in the establishment of the initial soil and channel conditions for the beginning of the flood season. Future improvements on the model should include the implementation of a snowmelt infiltration model that accounts for the main controls on snow infiltration.

The next equation accounts for the water table level $h_w(i, t)$. The total soil volume is divided into saturated and unsaturated soil volumes. The volume changes as water is added or removed from the saturated layer and, consequently, the water level changes. Applying the chain rule, the water table variation is calculated by:

$$\frac{dh_{rel}(i,t)}{dt} = \frac{dh_{rel}(i,t)}{dv_{s,sat}(i,t)} \frac{dv_{s,sat}(i,t)}{dt} \quad \text{Equation II-25}$$

The variation in the water table as a result of a change in the volume of the saturated soil layer (first term in Equation 2-26) is given by the hillslope curvature function (Equation 2-1) multiplied by $H_b(i)$. The second term in Equation 1-26 (?) accounts for the fluxes in and out of the saturated soil layer:

$$\frac{dh_{rel}(i,t)}{dt} = \frac{A_H(i)}{H_b(i) \times \frac{da_l}{dh_w}(h_{rel})} \left(q_{u,s}(i, t) - q_{s,l}(i, t) - e_{sat}(i, t) \right) \quad \text{Equation II-26}$$

Where $q_{u,s}(i, t)$ is based on the extension of Darcy's law to partially saturated media proposed by Buckingham (1907). The author postulated that Darcy's law is also valid for soils that are just partly saturated, and in this case (unsaturated) hydraulic conductivity is a function of water content. The flux from the unsaturated to the saturated zone is defined as:

$$q_{u,s}(i, t) = K_{UNSAT}(i) \times \theta(i, t) \times \frac{a_l(i,t)}{A_H(i)} \quad \text{Equation II-27}$$

The rate of change of unsaturated hydraulic conductivity with soil water content is a function of soil properties (Davidson et al., 1969):

$$K_{UNSAT}(i) = K_{SAT}(i) \times e^{bs(\theta-1)} \quad \text{Equation II-28}$$

This model was chosen since it presents just one parameter, bs , whose values are provided by the same author. However, I recognize that the dynamics of flow in the soil are much more complex than it is being conceptualized here. Soil unsaturated hydraulic conductivity depends on soil properties (e.g. texture or porosity, particle size distribution) and on the existence of alternative paths such as macropores. Nevertheless, I opt to

maintain a parsimonious model in which parameters are linked to measureable properties of the watershed.

The fourth differential equation accounts for changes in the unsaturated soil layer. By definition, volumetric soil moisture is the ratio between the volume of the water in the unsaturated layer of the soil and the total volume of this layer:

$$\frac{d\theta(i,t)}{dt} = \frac{d(v_{w_unsat}(i,t)/v_{s_unsat}(i,t))}{dt} \quad \text{Equation II-29}$$

I use the quotient rule to determine this derivative:

$$\frac{d\theta(i,t)}{dt} = \frac{1}{v_{s_unsat}(i,t)^2} \left(\frac{d(v_{w_unsat}(i,t))}{dt} \times v_{s_unsat}(i,t) - \frac{d(v_{s_unsat}(i,t))}{dt} \times v_{w_unsat}(i,t) \right)$$

Changes in the volume of water in the unsaturated layer are caused by fluxes in and out of this control volume, while changes in the total unsaturated volume are equal to the negative of the changes in the volume of the saturated layer:

$$\frac{d\theta(i,t)}{dt} = \frac{1}{v_{s_unsat}(i,t)^2} \left[v_{s_unsat}(i,t) \times (A_H(i) \times q_{p,u}(i,t) - A_H(i) \times q_{u,s}(i,t) - A_H(i) \times e_{unsat}(i,t)) - (\theta(i,t) \times v_{s_unsat}(i,t)) \times \frac{d(v_{st}-v_{s_sat}(i,t))}{dt} \right] \quad \text{Equation II-30}$$

Simplifying this equation, I obtain the equation that models the water table level in the hillslope:

$$\frac{d\theta(i,t)}{dt} = \frac{A_H(i)}{v_{s_unsat}(i,t)} \left[\begin{array}{l} (q_{p,u}(i,t) - q_{u,s}(i,t) - e_{unsat}(i,t)) \\ + \theta(i,t) (q_{u,s}(i,t) - q_{s,l}(i,t) - e_{sat}(i,t)) \end{array} \right] \quad \text{Equation II-31}$$

As previously described, I use potential evapotranspiration ($e_{pot}(i, t)$) to estimate the actual evaporation from the surface ($e_s(i, t)$) and from the saturated ($e_{sat}(i, t)$) and unsaturated layers of the soil ($e_{unsat}(i, t)$). The amount of water that evaporates from each one of these compartments depends on water availability and potential evapotranspiration. No limitation is imposed on evaporation from the surface or saturated layer. Evaporation from the unsaturated layer is a function of the soil's volumetric moisture and the relative depth of water in this layer. I first estimate the amount of water that can be removed from each compartment depending on water availability and potential evaporation:

$$Ce_{surf} = s_p(i, t)/e_{pot}(i, t) \quad \text{Equation II-32}$$

$$Ce_{sat} = \frac{ai}{A_H(i)} \times \frac{H_b(i)}{K_{SAT}(i)} \quad \text{Equation II-33}$$

$$Ce_{unsat} = \phi(i, t) \times \frac{v_{s,unsat}(i,t)}{ap} \times \frac{ap}{A_H(i)} \quad \text{Equation II-34}$$

Water evaporates from all of the compartments at the same time, but the amount of water that evaporates from each compartment depends on potential evaporation and water availability. To guarantee that the maximum evaporation is equal to the potential evaporation, I calculate a correction coefficient in the event that the sum of the coefficients is larger than one:

$$\begin{aligned} \text{if}(Ce_{surf} + Ce_{sat} + Ce_{unsat} > 1) \text{Corr} &= \frac{1}{Ce_{surf} + Ce_{sat} + Ce_{unsat}} \\ \text{else } \text{Corr} &= 1 \end{aligned} \quad \text{Equation II-35}$$

The final evaporation for each layer is given by the following equations:

$$e_s(i, t) = \text{Corr} \times Ce_{surf} \times e_{pot}(i, t) \quad \text{Equation II-36}$$

$$e_{sat}(i, t) = \text{Corr} \times Ce_{sat} \times e_{pot}(i, t) \quad \text{Equation II-37}$$

$$e_{unsat}(i, t) = \text{Corr} \times Ce_{unsat} \times e_{pot}(i, t) \quad \text{Equation II-38}$$

Conclusions

The hydrological community has recognized the need for a paradigm change in hydrology. Traditional hydrological models face a number of intrinsic problems, many of which are covered in this chapter. Recent advances in computer science, together with the capability to monitor hydrological variables from space, provide the opportunity for a change. However, no advance will be achieved if I continue to expend our energy learning how to calibrate models instead of learning what hydrological processes are not well represented in our models.

In this study, I progress toward the development of a calibration-free multi-scale hydrological model. Processes were conceptualized taking into consideration the dominant processes for flood generation, model complexity, and data availability. I attempt to represent all of the hydrological processes that are relevant for flood generation. However, I opted to use simple parsimonious methods that utilize parameters that can be directly linked to physical properties monitored by remote sensing or a low cost field campaign. Consequently, I discard over-parameterized methods that employ parameters that are determined simply through calibration.

One important feature of the proposed model is the truthful decomposition of the landscape in areas where runoff is generated (hillslope) and in the river network. The hillslope-link structure of the model allows a realistic representation of the landscape. The achievement of the same level of detail with a grid-based model is unfeasible since it requires the specification of very small domains (pixels), which dramatically decreases the computational efficiency of such models. The correct representation of the river network structure is essential for multi-scale flood prediction since it has been demonstrated that channel network topology, together with rainfall and runoff generation, plays a key role in determining the peak flow scaling.

In the following chapters of this thesis, I use the proposed hydrological model to simulate real and synthetic flood events. I first demonstrate the model's ability to predict

streamflow and peak flow for different basin scales and under different hydrological conditions. Once I am confident that the model is able to represent hydrological processes without the need for calibration, I will perform simulations studies to better understand the role of data uncertainty or resolution in hydrograph and peak flow scaling prediction.

Table II-1. Processes representation and data requirements for different models version with multiple complexity levels

Processes representation: → increasing complexity → increasing data requirements →					
Model	1	2	3	4	5
Landscape decomposition	Hillslope-link	Hillslope-link	Hillslope-link	Hillslope-link	Hillslope-link
Rainfall	Space-time	Space-time	Space-time	Space-time	Space-time
EVPT				Space-time	Space-time
Infiltration				empirical	empirical
Overland flow	Constant runoff coefficient	Constant runoff coefficient	Constant runoff coefficient	HOF, SEOF	HOF, SEOF
Hillslope transp.		Constant velocity	Non-linear	Constant velocity	Non-linear
Percolation				Darcy-type	Darcy-type
Baseflow				Darcy-type	Darcy-type
Channel flow	Constant velocity	Constant velocity	Non-linear	Constant velocity	Non-linear
Data requirements: → increasing data needs →					
Landscape decomposition	DEM	DEM	DEM	DEM	DEM
Rainfall	Radar data	Radar data	Radar data	Radar data	Radar data
EVPT				MODIS or NLDAS	MODIS or NLDAS
Infiltration				LC, soil prop	LC, soil prop
Overland flow	Average runoff coefficient	Average runoff coefficient	Average runoff coefficient	LC, soil prop	LC, soil prop
Hillslope transport		Average hillslope velocity	LC, Slope	Average hillslope velocity	LC, Slope
Percolation				LC, soil properties & initial con.	LC, soil properties & initial con.

Table II-1 Continued

Baseflow				LC, soil properties & initial con.	LC, soil properties & initial con.
Channel flow	Ave channel velocity	Ave channel velocity	Hydraulic measure.	Ave channel velocity	Hydraulic measure.

EVPT = evapotranspiration, HOF = Hortonian overland flow, SEOF = saturated excess overland flow, LC = land cover, Cte = constant, Ave = average

Table II-2. List of model's parameters, forcing, fluxes, and state variables

Parameter	Symbol	Units	Inference method
Hillslope			
Drainage area	$A_H(i)$	L^2	Based on the DEM
Total relief	$H_T(i)$	L	Based on the DEM
Channel length	$L_H(i)$	L	Based on the DEM
Average Hillslope slope	$S_H(i)$	L/L	Based on the DEM
Curvature	$b(i), c(i), d$		Based on the DEM
Maximum water table	$H_{relmax}(i)$	L	Based on the DEM
Manning's coefficient	$n(i)$		Based on the DEM and land cover
Soil			
Storage water potential (virtual distance to the bedrock)	$H_b(i)$	L	Based on soil datasets or SCS method
Total soil water volume potential	$V_T(i)$	L^3	A function of $H_b(i)$ and $A_H(i)$
Hydraulic conductivity	$K_{SAT}(i)$	L/T	Based on soil datasets or SCS method
Unsaturated hydraulic conductivity	$K_{UNSAT}(i)$	L/T	Based on soil datasets and pedotransfer functions or SCS method
Soil constant	$bs(i)$		Based on soil datasets
Channel			
Velocity equation parameters	$v_0, \lambda_1, \lambda_2$		Based on USGS hydraulic measurements
Channel scale dependent constant	$\tau(i)$		Based on velocity parameters and channel properties
Dynamic variables			
Impermeable area	$a_I(i, t)$	L^2	Based on hillslope curvature and water table
Permeable area	$a_P(i, t)$	L^2	Based on hillslope curvature and water table
Average slope of the impermeable area	$S_{HI}(i, t)$	L/L	Based on water table and hillslope geometry
Volume of the saturated soil	$v_{s_sat}(i, t)$	L^3	Based on impermeable area

Table II-2 Continued

Parameter	Symbol	Units	Inference method
Volume of water in the unsaturated soil layer	$v_{w_unsat}(i, t)$	L ³	A function of permeable area and soil volumetric moisture
Volume of the unsaturated soil layer	$v_{s_unsat}(i, t)$	L ³	A function of permeable area
Deficit of water in the soil	$d_{soil}(i, t)$		A function of soil volumetric moisture
Overland flow velocity	$v_H(i, t)$	L/T	Based on Manning equation and is a function of hillslope slope, Manning coefficient, and surface storage
Forcing	Symbol	Units	Inference method
Precipitation	$q_p(i, t)$	L/T	Radar/satellite rainfall maps
Potential Evaporation	$e_{pot}(i, t)$	L/T	Potential evapotranspiration maps (MOD16, or based on land surface models)
Snow	$s_m(i, t)$	L/T	Snow melt maps based (based on snow water equivalent or land surface models)
Fluxes	Symbol	Units	Inference method
Discharge from upstream	$q_{in}(i, t)$	L/T	Model output
Infiltration	$inf(i, t)$	L/T	Based on soil deficit and surface storage
Overland flow	$q_{p,l}(i, t)$	L/T	A function of surface storage and overland flow velocity
Percolation	$q_{p,u}(i, t)$	L/T	A function of permeable area and infiltration rate
Baseflow	$q_{s,l}$	L/T	A function of soil properties and water table
Evaporation from the surface	$e_s(i, t)$	L/T	A function of potential evapotranspiration and water surface
Evaporation from the unsaturated soil layer	$e_{unsat}(i, t)$	L/T	A function of potential evapotranspiration and soil volumetric moisture
Evaporation from the saturated soil layer	$e_{sat}(i, t)$	L/T	A function of potential evapotranspiration impermeable area
State variables	Symbol	Units	Inference method

Table II-2 Continued

Channel discharge	$q(i, t)$	L3/T	Model output
Surface storage	$S_p(i, t)$	L	Model output
Water table	$h_{rel}(i, t)$	L	Model output
Soil volumetric moisture	$\theta(i, t)$	L3/ L3	Model output

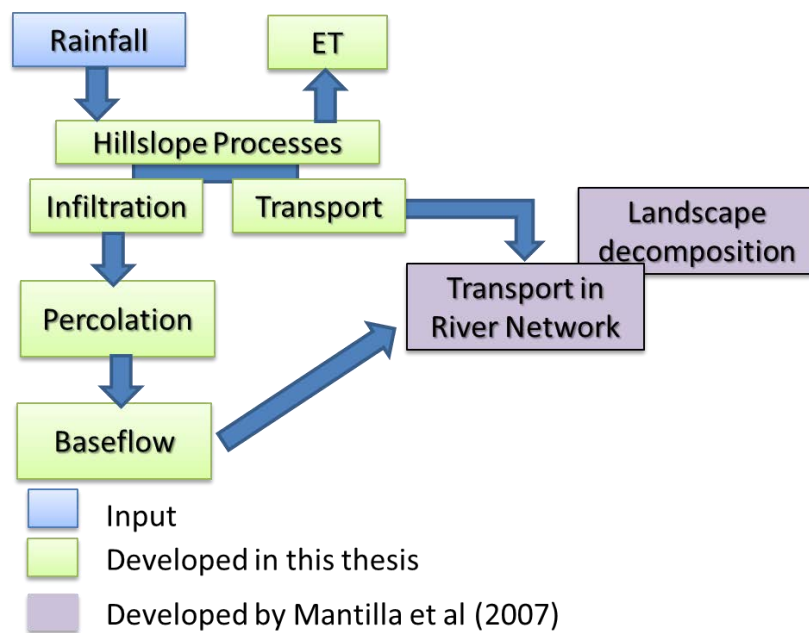


Figure II-1. Hydrological processes simulated by CUENCAS. Green box indicated the processes that were developed in this thesis

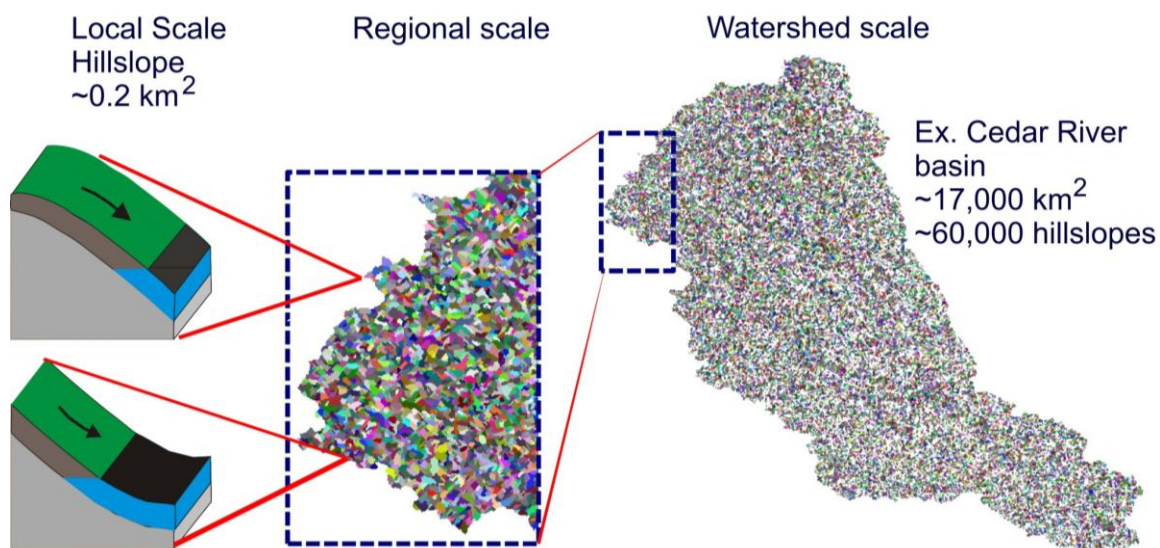


Figure II-2. Schematic representation of the scales simulated by the hydrological model: from local (hillslope) to Watershed scale (Cedar River basin)

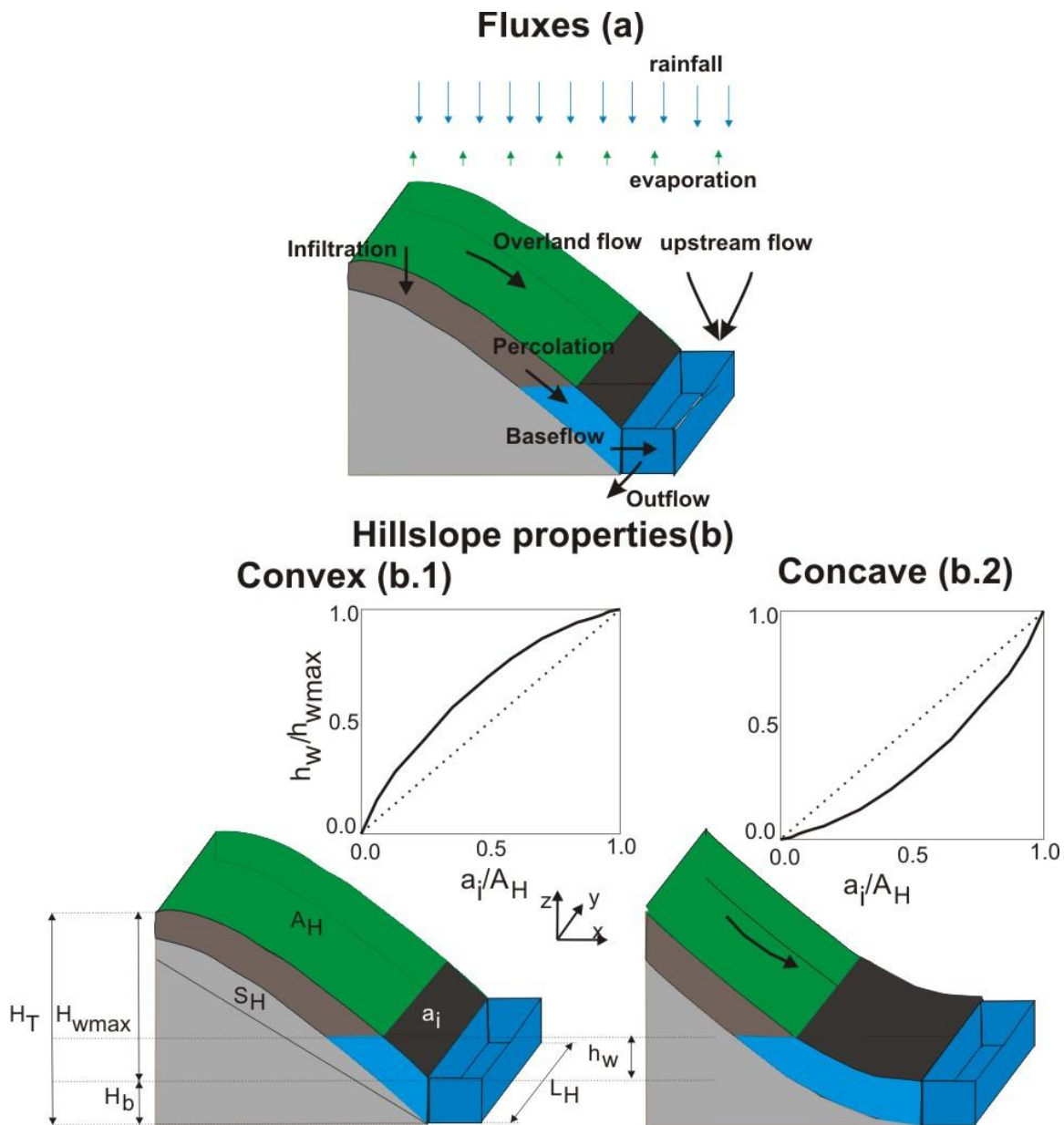


Figure II-3. Schematic representation of the hillslope and channel physical properties and fluxes. The figure on the top (a) presents the fluxes between the hillslope surface and soil and the channel. The figures in the bottom presents a convex (b.1) and a concave (b.2) and their main physical properties.

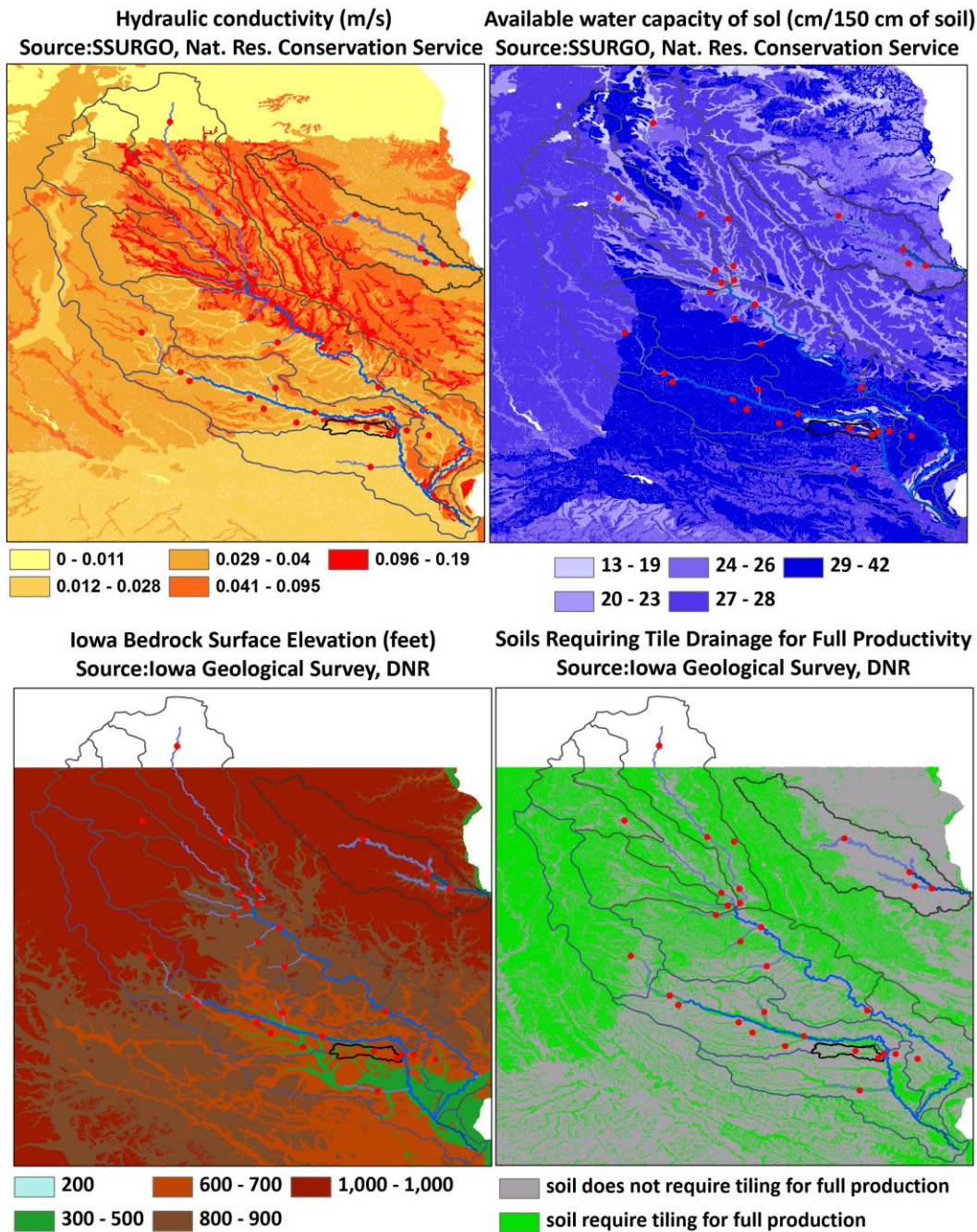


Figure II-4. Soil properties for the study area. The maps in the top present SSURGO data that were used for the simulations presented in Chapter III. On the left I present saturated hydraulic conductivity (m/s) and on right available water capacity of sol (cm/150 cm of soil). On the bottom I present data provided by the Iowa Geological Survey, DNR. Bedrock surface elevation (ft) is presented on the left, and soils requiring tile drainage for full productivity on the right.

CHAPTER III MODEL APPLICATION

Introduction

In this thesis, I developed a calibration-free hydrological model that allows us to isolate uncertainties due to parameter estimation and input. To use this model to compare different datasets, I first needed to demonstrate the model's ability to mimic the dominant processes of hydrologic response to rainfall. In this section, I apply the model to simulate real events for the Cedar River, Iowa River, and Turkey River basins and a large number of streamflow sites covering a large range of drainage areas and different climatological conditions during the period of 2002 to 2009. I demonstrate the model's capability to predict floods across different scales and discuss the model's limitations and components that need improvement.

Once I demonstrate the model's ability to represent flood events, I use the model to simulate synthetic rainfall/flood events. The goal is to demonstrate the value of a multi-scale framework and to show why calibration based on a single streamflow site does not guarantee that physical processes are being correctly represented across scales.

I then repeat this exercise using real events for the Cedar and Iowa Rivers. I adopt very simple model configurations to simulate these events. I manually calibrated a single parameter of the hydrological model to obtain good matching between simulated and observed streamflow for a specific hydrological event and site in the watershed and then extrapolated this parameter to simulate streamflow for the following cases: (1) other sites in the same basin area with different scales, (2) sites with similar hydrological conditions and similar scales, and (3) the same site, but for a different climatological condition. This exercise demonstrates that even if a very simple and unrealistic model is used, I can achieve reasonable results for the simulation of streamflow for a single site and event if parameters are calibrated. However, the calibrated parameters cannot be extrapolated for different events or sites.

Model results

In this section, I present results of the simulations performed with the model described in Chapter 2. These results were obtained with the most complete version of the model (model version 6, Table II-1), and parameters were estimated based on the different datasets listed in Table II-2. The model includes the following processes: space-time rainfall and runoff generation processes, hillslope transport, soil dynamics, channel transport, and evapotranspiration.

I validated the model by comparing model results with observed streamflow data and simulated streamflow generated by a semi-distributed version of the SAC-SMA. Since 1960, the Sacramento soil moisture accounting model (*Burnash, 1995*) has been used by most of the NWS River Forecast Centers as the main flood prediction model (*Welles et al., 2007*). The model is classified as deterministic, continuous, and non-linear. SAC-SMA contains parameters that describe the rainfall-runoff and evaporation dynamics as well as parameters that describe channel flow transport between two sub-basins (*Ajami et al., 2004*). In the semi-distributed version of SAC-SMA, for which results are presented here, one set of parameters is calibrated for each sub-basin using the 6-hour mean areal precipitation (MAP) products produced by the National Weather Service (*Johnson et al., 1999*). If the kinematic wave method is used, the model uses fourteen parameters to describe the rainfall-runoff processes at the watershed scale and two parameters to describe channel routing.

Results for different basins and years are presented in Figure III-1 and Figure III-2. The number of sites analyzed for each year depends on the availability of streamflow data for that year. For 2008, for example, 11 sites were in operation for the Cedar River, 12 for the Iowa River, and 4 for the Turkey River. Therefore, for 2008, results are presented for a total of 27 sites. For each site, I included observed streamflow (dark blue), streamflow simulated by CUENCAS (gray), and streamflow simulated by the Sacramento Soil Moisture Accounting (SAC-SMA) model (light blue). I normalize the

discharge by the mean annual flood that is used as an approximation for the bankfull discharge (red line) (Leopold et al., 1964). I calculate the mean annual flood as a function of drainage area using USGS historical data for the Cedar and Iowa Rivers. Values above this line approximate flow levels above the riverbank, characterizing a flood event. The site number (refer to the map presented in Figure 1-1 for site location) and the area of each site are shown in the left corner, and goodness-of-fit statistics for both models are presented in the right corner. In the last plot of each figure, I include simulated and observed accumulated actual evapotranspiration. Observed evapotranspiration is presented in dark blue and was calculated based on the MODIS-16 evapotranspiration product that was produced entirely from remotely sensed information. The value plotted represents the basin average accumulated actual evapotranspiration in mm. Accumulated values of simulated actual evapotranspiration for different hillslopes are presented in gray.

The comparison of CUENCAS and SAC-SMS model results was introduced in this study since I found it difficult to properly judge the model's results based solely on observed streamflow data. First, the time series of observed streamflow had many missing points, which introduced bias into the estimation of traditional goodness-of-fit statistics. Moreover, streamflow observed time series are subject to large uncertainties due to instrument errors and limitations, rating curve extrapolation, and hysteresis. I chose the SAC-SMS semi-distributed model for the comparison since it has been used for operational forecasts for more than 60 years. Also, results from the SAC-SMS were used as criteria to evaluate the models' performances during the Distributed Model Intercomparison Project - 1 (DMIP-1) (Smith et al., 2004). One of the main conclusions of DMIP-1 was that in most cases, the lumped model outperformed the distributed model. Another relevant conclusion was that, "gains from calibration indicate that determining reasonable a priori parameters directly from physical characteristics of a watershed is generally a more difficult problem than defining reasonable parameters for a conceptual

lumped model through calibration” (Reed et al, 2004). The results from SAC-SMS were provided by Prof Allen Bradley.

I first show results for the year for which values above the mean annual flood were observed for some of the streamflow sites, characterizing a flood event. I start with the extreme flood event that occurred in 2008. Figure III-1, Figure III-2, and **Error! Reference source not found.** present results for the Cedar River, Iowa River and Turkey River sites for 2008. Note that for some sites in the Iowa River and Cedar River basins and all the sites in the Turkey River basin, simulations for the SAC-SMS model were not included since they were not available. In this case, I included a missing value (-9.0) in the statistics for SAC-SMS. For many of the sites, CUENCAS and SAC-SMS models perform in a very similar way. Both models were able to capture peak flow and the time to peak for practically all the sites in the Cedar River and Turkey River basins. For the Iowa River basin, for which streamflow sites with smaller drainage area are available, CUENCAS performed better in many cases. Neither CUENCAS nor SAC-SMS were able to reproduce the hydrograph for the Marengo site that represents the outlet of the simulated part of the Iowa River basin. The difficulty in simulating flow for this site probably arises from flow transport effects that are not accounted for by the kinematic wave approximation used in the model. However, CUENCAS correctly predicted the peak, while SAC-SMS underestimated the peak flow at this site.

Results for 2004 are presented in Figure III-4, Figure III-5, and **Error! Reference source not found.** for sites in the Cedar River, Iowa River and Turkey River basins, respectively. For the Cedar River, results for both models were similar, while for the Iowa River, CUENCAS underestimated the streamflow response for the majority of the sites. A primary cause could be error in the Stage IV data, since streamflow was underestimated across the basin. For the Turkey River basin, CUENCAS reproduced the 2004 hydrographs very well.

Note that I correctly simulated the time to peak across multiple scales and for all the studied watersheds using the river propagation method proposed by Mantilla (2007). However, I had to apply an advection correction factor to the parameters that were estimated based on the USGS hydraulic measurements data. The need for the correction arises from basic assumptions adopted by the author to derive the formulation. A more detailed explanation of this is presented in the Appendix A.

In Figure III-7 and Figure III-8, I present results for a dry year (2002) and for a relatively wet year (2003) in which discharge was close to but did not exceed the mean annual flood. As can be seen for these two cases, the model does not perform as well for dry conditions. Note that for the year 2002, SAC-SMS also did not perform well. For the year 2003, SAC-SMS performed better than CUENCAS. Note that the SAC-SMS model has 16 calibrated parameters to represent rainfall –runoff transformation, so it is probable that it would capture highly non-linear dynamics during dry events better than CUENCAS, which presents a simplified representation of soil dynamics with a very parsimonious formulation (3 parameters). This means that the current version of the model cannot capture highly non-linear processes that occurred during dry conditions. This is probably because of the simplified representations adopted by soil and evapotranspiration processes. For example, for this specific study area, tiling systems might interfere with the accurate representation of soil dynamics. In a long period simulation, as it is the case presented here (7 month simulations instead of event-based simulations), bias in representing these two processes accumulates in time and strongly affects soil moisture conditions and, consequently, streamflow generation.

Difficulties simulating dry periods are very common in hydrological modeling (e.g. Liden and Harlin, 2000 and Hunukumbura et al, 2011). Two main reasons are often mentioned as the causes for poor model performance for dry periods: (1) lack of consideration of surface water–groundwater interactions (Anderson et al., 2004; Hughes, 2004; Fleckenstein et al., 2006; Herron and Croke, 2009) and (2) the existence of

additional water pathways in the soil matrix that are hard to simulate and quantify (Lang et al., 2008; Hunukumbura et al., 2011; Kim et al., 2011; Staudinger et al., 2011). These aspects should constitute the subject of future work.

Figure III-9 presents peak flow scaling for the Cedar River basin for the years 2002 to 2009. In Figure III-10, I included the peak flow scaling for the Iowa River and Turkey River for 2004 and 2008. In this figure, blue dots are observed peak flow and dark gray and light blue dots are simulated peak flow for CUENCAS and SAC-SMA, respectively. In orange I present the mean annual flow values across scales. The red line presents the scaling of peak flow fitting line obtained through non-parametric regression. The light gray dots are peak flow simulated by CUENCAS for all the links in the basin. Even though CUENCAS does not satisfactorily capture hydrographs' shapes for dry climatological conditions, it does capture reasonably well the scaling behavior of peak flow for all of the simulated years. For 2004 and 2008, (flood) peak flow scaling is captured very effectively. It is important to note that the model developed in this work was initially conceptualized to simulate flood events. A model is considered efficient for flood prediction if it does not provide false alarms (predict floods when they have not occurred) or miss forecasts (does not predict floods that occurred) and if it can accurately predict peak flow and time to peak during flood events. I can analyze these criteria by considering the scaling plots. For example, in the case of a flood event, observed (dark blue dots) peak flow values are above the orange line. If, in this case, simulated (light blue or gray) values are below the same line, it characterizes a flood warning that should have been issued but was not during a real flood event. The opposite case would be when observed values are below the orange line, so flow is below bankfull level, but simulated values are above the same line. In this case a warning was issued in the case that a flood event did not really occur. All the criteria mentioned before are reached for almost all sites and years.

Why should we avoid calibration?

Synthetic rainfall simulations

In this section, I present a simulation study to demonstrate the value of evaluating model results at multiple scales rather than calibrating model parameters for a unique site in the watershed. I show that the peak flow observed in a single site can be captured through the calibration of a single parameter. However, this procedure does not guarantee that peak flows are correctly simulated across scales. I use different model configurations to demonstrate the impact that adding different processes (e.g. hillslope delay) has on peak flow scaling.

For this exercise, I adopted synthetic, spatially uniform rainfall of varying total accumulated rainfall (60, and 120 mm) and a fixed duration equal to 60 minutes, resulting in different rainfall intensities (60, and 120mm/h). Simulations are performed using three different models:

- Model 1 (model 1 in **Table II-1**): the model configuration accounts for runoff generation and transport through the river network. A constant runoff coefficient and channel velocity was adopted throughout the study area and for the whole duration of the rainfall event. Runoff coefficient is equal to 1.0 and different lines in the plot represent simulations obtained with different flow velocities (from 0.2, to 1.00 m/s).
- Model 2 (model 2 in **Table II-1**): in this version of the model, I added hillslope-delayed that was simulated by a linear reservoir with constant velocity (0.01m/s) and adopted the same scenarios specified for model 1 in terms of the runoff coefficient and channel velocity.
- Model 3 (model 3 in **Table II-1**): in this version of the model, channel and hillslope velocity are represented by non-linear function. In the case of the channel, velocity depends on the drainage area and on the discharge. In the case

of the hillslope velocity depends on the storage on the surface, the land cover type, and on the hillslope slope. I adopted 4 different velocities for the channel, with v_0 in the non-linear velocity equation varying from 0.4 to 0.8.

- Model 4 (model 6 in **Table II-1**): this version of the model corresponds to the version used to simulate the real events whose results were presented in the beginning of the chapter. This is the most complex version of the models which parameters are estimated based on data. Since I have demonstrated the model's ability to simulate flood events, I assumed that results obtained by this model are close to reality. For this simulation study, I used the parameters estimated for the Cedar River basin and set initial soil condition to 0.5. This scenario is represented in the figure by the black line that was estimated based on the gray dots.

The goal of this experiment is to illustrate the range of simulated values obtained through modifying just one of the model parameters (channel velocity). The simulation results are shown in Figure III-11. I can see that peak flow scaling changes significantly from model to model. Results obtained by model 3 are considered as a reference close to the actual basin response, since I have demonstrated the model's ability to simulate flood events across scales. The lack of hillslope delay in model 1 causes overestimation of peak flow for small basins, and the effects decrease as basin scale increases. For model 2, I adopted a very low constant hillslope velocity what result in underestimation of peak flow for small scales.

Now let us suppose I would like to calibrate model 1 or 2 based solely on the observed discharge for a single streamflow site and, consequently, a single point in the peak flow-scaling plot, I could easily manipulate one parameter (e.g. for the different results in Figure III-11 I manipulated channel velocity) to match the observed peak flow at this specific site. The calibration of a single parameter would allow us to match exactly the peak flow discharge for this specific site; however, the difference in slope among different models demonstrates that this procedure does not guarantee that peak

flow scaling is being correctly simulated across all basin areas. It also does not guarantee that the good match is achieved for the right reasons. For example, if I kept the runoff coefficient equal to one and chose to calibrate channel velocity, I would actually obtain a velocity that is lower than the real one to compensate for the wrong runoff coefficient. In this sense, calibration based on just one streamflow site is a meaningless exercise that does not provide any information about physical processes.

Now, let us consider that I have streamflow observations for two sites in the basin, with drainage areas of around 10 km^2 and 1000 km^2 . In this case, the modification of just one parameter would probably not allow the match observed peak flow for both sites, since in this case I would also have to capture the slope of the peak flow scaling relationship.

It is interesting to notice the effect that rainfall intensity has on the range of possible simulated values. If I compare the less (plot in the left corner) and more (plot in the right corner) intense rainfall scenarios, I conclude that variability among the different models for large basins decreases as the amount of water introduced into the basin increases. The model configuration that best matches the reference result (model 4) also changes across scenarios. This demonstrates the importance of introducing non-linear effects, even though models with constant velocities are sometimes able to reproduce hydrographs at specific locations and for specific events.

This exercise demonstrates the diagnostic framework proposed by the geophysical theory of floods. As indicated by Gupta et al. (2010), the use of highly parameterized models and calibration complicates the adoption of this diagnostic framework since it prevents the identification of model, data, or parameter uncertainty.

Simulation using real rainfall event

In this section, I use real events for the study area to verify the concepts demonstrated in the previous section. In this exercise, I apply model 2 that accounts for

constant runoff coefficient, channel velocity, and hillslope velocity and force the model with Stage IV rainfall data. I fixed channel velocity equal to 1.0 m/s and hillslope velocity equal to 0.01m/s and manually calibrated the runoff coefficient for a specific site and year. I used the same years for which I presented results from model 6 (**Table II-1**) in the first part of this chapter. The goal is to demonstrate the variability of behavior observed during these years. I then extrapolate this parameter for other sites in the same watershed, simulating the parameter regionalization method. Next, I apply the determined parameters to simulate streamflow for the same site, but for different years, in this case simulating the practice of model validation or forecast. The results of this experiment are presented in Figure III-12 and Figure III-13.

Figure III-12 presents the case for which I use a wet year (2008) for calibration. I calibrate model parameters to match streamflow for Wolf Creek, near the Dysart site at the Cedar River, with a drainage area equal to 774 km². In Figure III-13, gray lines represent simulated values and blue lines reflect observed values. I kept the results obtained by SAC-SMS for reference. The calibrated runoff coefficient in this case is equal to 0.8. The model did not perform as well when the same parameter was applied to different sites in the same basin area and period. For a site with a similar basin area (Beaver Creek at New Hartford, 898 km²), peak discharge was underestimated by 50%, and for the Cedar River basin, the first peak was overestimated and I did not capture the timing and shape of the hydrograph. Even worse results were obtained when the same parameter was used to simulate 2002 and 2003, which correspond to very dry and dry years, respectively. In both cases, discharge for the same site was strongly overestimated during the entire period. For 2004, which is also a wet year, I obtained reasonable fit for the same site but strongly overestimated discharge for Cedar Rapids.

Figure III-13 presents the same exercise for a dry year (2003). I calibrated streamflow for the Little Cedar River, near Ionia with a drainage area equal to 792 km², obtaining an optimal runoff coefficient equal to 0.2. Even though the hydrograph timing

for the small-scale sites seems to be reasonably captured by the model, channel velocity seems to be too fast for this event since the simulated peak occurs before the observed one for the large-scale basins. This is due to the use of a constant channel velocity for all flow conditions (low or high) and indicates the need for a non-linear relationship between velocity and channel discharge. I then applied the runoff coefficient equal to 0.2 to simulate discharge for the same site for the year 2002 (dry). Even with a very low runoff coefficient, I overestimated discharge for this year. This is probably due to large velocities of propagation for the amount of water in the hillslope and channels. For 2004 and 2008, I strongly underestimated discharge, with the exception of one site in the Cedar River basin, for which a reasonable match was obtained. This demonstrates the high variability of hydrological response, not just for different climatological conditions (year to year) but also for different regions in the basin during the same year.

Major model limitations

In this work, I focused on hydrological processes that play an important role in flood generation and that can be parameterized using spatially distributed information about the watershed, especially the ones provided by remote sensing. Our goal was to investigate how well floods can be predicted using information from space. There are other hydrological processes that were not included in the presented version of the model that can potentially affect flood generation, and their inclusion could potentially improve model results. Future extensions of this work should consider the inclusion of some of these processes. This section presents a discussion of the main weakness of the current formulation of the model. Future extension of this work should focus on improving the model components discussed here.

The most relevant basin property that was not explicitly included in the model formulation is the type of vegetation and how it affects runoff generation and propagation through the hillslope. The only consideration in the current version of the model is

related to the general land cover class, as proposed by the National Land Cover Database (NLCD). Due to agricultural practices in Iowa, vegetation changes abruptly from May, the beginning of the planting season, to September, when the harvest usually occurs (National Agricultural Statistics Service. 2007). Vegetation indices (e.g. leaf area index, normalized difference vegetation index) are provided by remote sensing and can be used to parameterize these processes.

Vegetation interferes with the balance of water on the surface (interception), the resistance to surface runoff (roughness of the surface), and transpiration patterns. The first two processes have a more direct effect on floods. Breuer et al. (2003) define vegetation interception capacity as the maximum amount of water left on the canopy at the end of a precipitation event under zero evaporation conditions and after dripping has stopped. Therefore, this volume of water does not contribute to runoff or infiltration. The same authors provide a review of studies that attempts to estimate vegetation interception capacity and, based on this review, propose values for different types of plants and vegetation density. Vegetation also affects surface roughness, slowing down and reorganizing overland flow. Jin and Romkens (2000) demonstrate that overland flow in non-submerged vegetative can be described by the Petryk and Bosmajian's modified Manning's formula with a variable roughness coefficient. In this case, resistance due to vegetation is related to vegetation density and flow depth.

During the beginning of model development, I used a simplified representation of the soil dynamics. However, the validation of the model with real data for very dry periods demonstrated that even though the soil model is able to represent soil dynamics during very wet periods, it does not capture the whole complexity of soil dynamics during dry periods. In the current version of the model, I adopt a simplified conceptualization of the soil properties based on the definition of an average hydraulic conductivity and average soil properties for the hillslope. In this case soil properties are considered to be constant for the entire vertical soil profile. I also do not account for

different soil conductivities that arise from the existence of macropores in the soil. For future work, I propose to implement a dual-permeability model that accounts for fast flow, due to macropores and fractures effects, and a slow flow, that happens in the soil matrix. Examples of this type of model were presented by Durner (1994), Mohanty and Bowman (1997), and Mohanty (2007). A review of model applications for structured soils was presented by Kohne et al. (2009). I also recommend considering the inclusion of soil dynamics that result in the installation of tiling systems. The main deterrent to including complexities to the soil dynamics is the lack of information. For the tiling systems, for example, many of them were installed many years ago, and no official register of their installation is available. Even for the places for which a tiling map is available, due to the lack of maintenance, it is hard to determine whether the system is still working properly. Therefore, to test these components, a small scale study that focuses on a hillslope for which information is available would be the ideal setup for testing more complex conceptualization of the soil dynamics

The current version of the model also presents a very simple representation of snow processes. I neglected infiltration, sublimation, and all the snow-melt runoffs to the river. A better representation of how much of the snow-melt infiltrates into the soil would be appropriate, but it requires such information as snow cover and frozen soil properties. The next step would be the inclusion of a simplified model to represent infiltration under limited conditions imposed by frozen soils. Different snow-melt infiltration information is available, and a good start to improving these model components is the implementation of the model proposed by Gray et al. (2001) since it was developed to be applied at the hillslope scale.

The last model component that requires special attention is evapotranspiration. Even though evapotranspiration is not a relevant process for flooding in event-based simulations, it controls soil moisture states for longer period simulations. I opted to use available datasets of potential evapotranspiration instead of developing a component in

the model that would estimate it internally. Once potential evapotranspiration is known, I estimate evaporation based on the available water in the system. In the model version presented in this work, I use conceptual equations to estimate how much water evaporates from the soil. However, water from the soil can be removed by plant transpiration. Estimation of plant transpiration is a complex process that depends on vegetation stomatal conductance, which is sensitive to diurnal changes in absorbed photosynthetically active radiation, vapor pressure deficit, leaf temperature, hydraulic conductance within the plant, and soil moisture near the roots (Mu et al., 2007). Since the contribution of evapotranspiration is only significant for long-term simulations, I recommend data assimilation to correct for errors introduced by the simple model conceptualization. Implementing a complex evapotranspiration model would significantly increase data requirements and model running-time. I will demonstrate models sensitivity to evapotranspiration in Chapter 8.

Conclusions

Before using a model to evaluate the potential of different datasets for flood prediction, the model's ability to simulate real flood events has to be demonstrated. In this chapter, I present results for the Cedar River, Iowa River, and Turkey River basins. I began by presenting results for the 2008 flood event, and I demonstrated that the model performs well when simulating high-flow conditions across scales for all basins adopted in this study. I compared the results obtained by CUENCAS with a well-established hydrological model (SAC-SMS) that has been used for operational flood prediction by the National Weather Service for more than 60 years. I concluded that both models performed similarly for flood events.

I then applied the model to simulate flows for a very dry (2002) and a relatively dry year (2003). In this case, the model did not perform as well due to the high-nonlinearity of soil and evapotranspiration dynamics. The model developed in this work

adopts simplified conceptualization of these processes, since the main goal was to be able to estimate model parameters based on data. Therefore, model complexity is tied to data availability. Future work should focus on how to improve model conceptualization of these processes for dry periods. It is important to point out that degraded model performance during very dry periods is a very common issue in hydrological modeling.

I then presented a study based on synthetic rainfall to illustrate the importance of a multi-scale framework in hydrological modeling. This exercise demonstrated that even simplistic models can be calibrated to simulate peak flow for one streamflow site and under specific hydrological conditions. However, the good match between observed and simulated values does not guarantee that the model correctly represents hydrological processes across scales. I used the same real events that I used to verify the model's skill in the first part of this chapter to demonstrate the large variability of hydrological response across different years and different sites. I confirmed the experiment realized with synthetic rainfall using real events and calibrated the runoff coefficient for a single site. The regionalization or extrapolation of this parameter for different sites and hydrological conditions resulted in poor simulation of hydrological response. This exercise also demonstrates that there is no direct conversion of rainfall into runoff and that other hydrological variables should be included in the model formulations. In the complete version of the model, for example, the response of the basin to a rainfall event will depend on moisture initial condition in the soil and on the surface, soil and land surface properties, and space-time variability of rainfall.

Table III-1. Dataset used in the simulations

Physical processes and properties	Datasets
Input	
Rainfall	Radar Stage IV - NWS ($\Delta T=1$ hour and $\Delta S=0.05^\circ$, almost real-time)
Potential Evapotranspiration	PE from North American Regional Reanalysis - NLDAS-2 Model Input ($\Delta T=1$ hour; $\Delta S=0.125^\circ\sim 13\text{km}$)
Parameterization	
DEM	NED - $\Delta S=90$ meters
Hydraulic Measurements	USGS hydraulic measurements
Soil properties	SURGO - $\Delta S=$ polygons with 1 to ten acres ($\sim 0.05\text{km}^2$) size map delineation
Land cover	National Land Cover Database (NLCD) - $\Delta S=30$ meters -2001
Initial condition	
Soil moisture (initial condition)	Total soil column wetness (0-200 cm) - NLDAS-2 Model Output ($\Delta T=1$ hour; $\Delta S=0.125^\circ\sim 13\text{km}$)
Validation	
Streamflow	USGS streamflow measurements for a total of 25 sites in the study area ($\Delta T=1/4$ or 1 hour)
Streamflow	Simulated streamflow – SAC model
Evapotranspiration	MODIS Evapotranspiration Dataset (MOD 16) ($\Delta T=8$ days; $\Delta S=0.016^\circ\sim 1\text{km}$) (available from 2001 – not available in real time)

* ΔS – spatial resolution in minutes (′), arc-seconds (″), degrees (°), meters (m), or kilometers (km)

** ΔT – temporal resolution in minutes, hours, days, or years

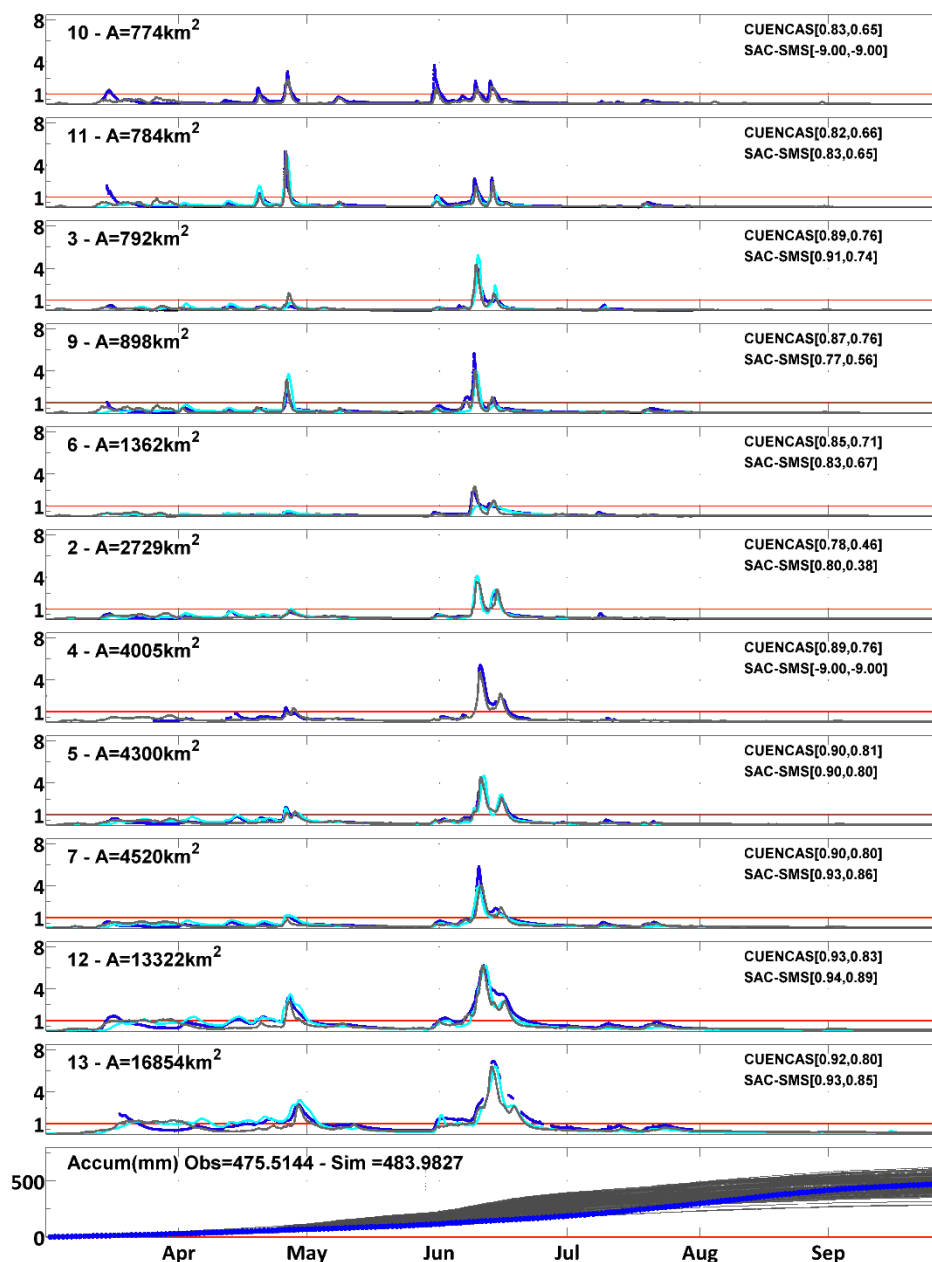


Figure III-1. Model results for 2008, Cedar River sites. Discharge is normalized by the mean annual flood. Dark blue lines are observed; gray lines are simulated by CUENCAS; and light blue lines are simulated by SAC-SMS. The numbers on the left indicate the site number (refer to Figure 1-1) and the basin drainage area. The numbers on the right are the statistics for CUENCAS and SAC-SMS (Nash coefficient, correlation coefficient). The last plot presents simulated (gray lines) and observed (blue line, based on MODIS 16) evapotranspiration results for the year 2008.

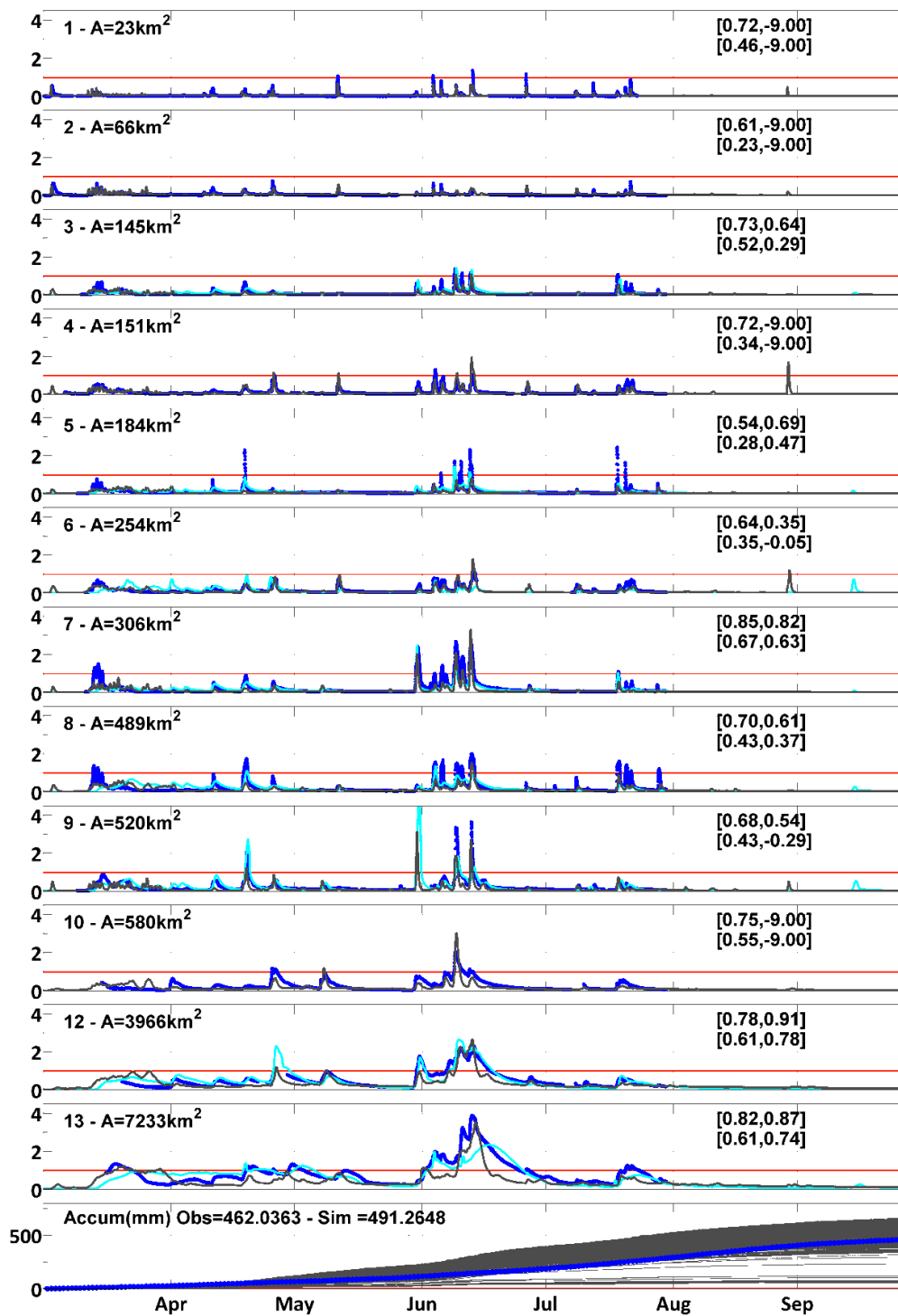


Figure III-2. Simulation of 2008 flood event for Iowa River sites. Gray line is simulated by CUENCAS, light blue is simulated by SAC-SMS, and dark blue line is observed.

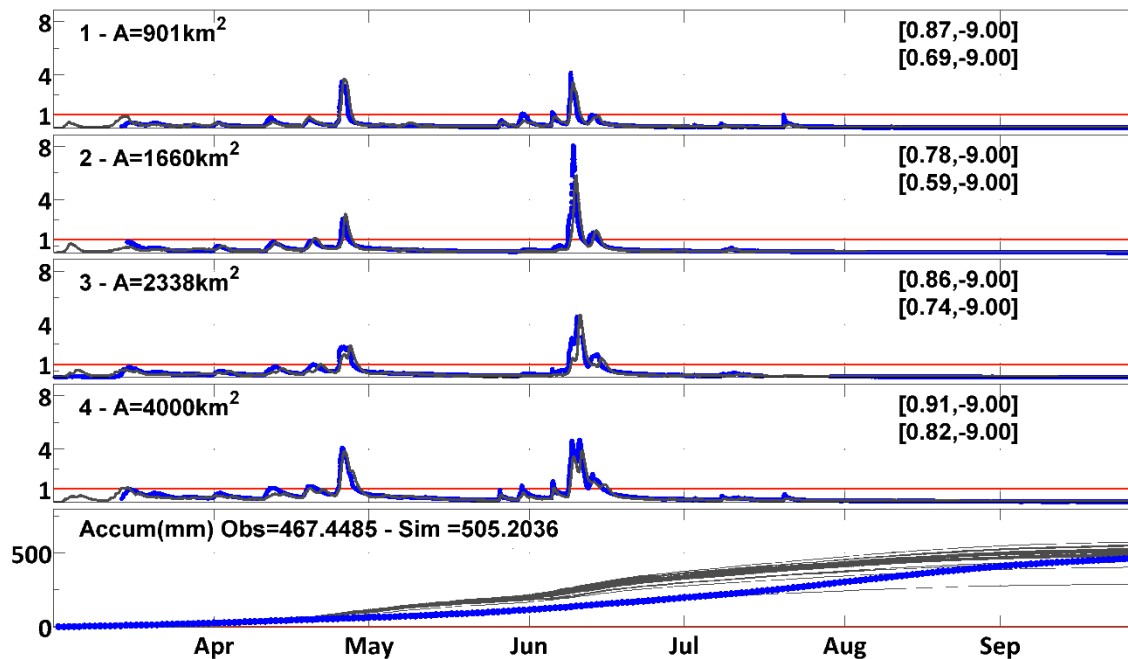


Figure III-3. Simulation of 2008 flood event for Turkey River sites. Gray line is simulated by CUENCAS, light blue is simulated by SAC-SMS, and dark blue line is observed.

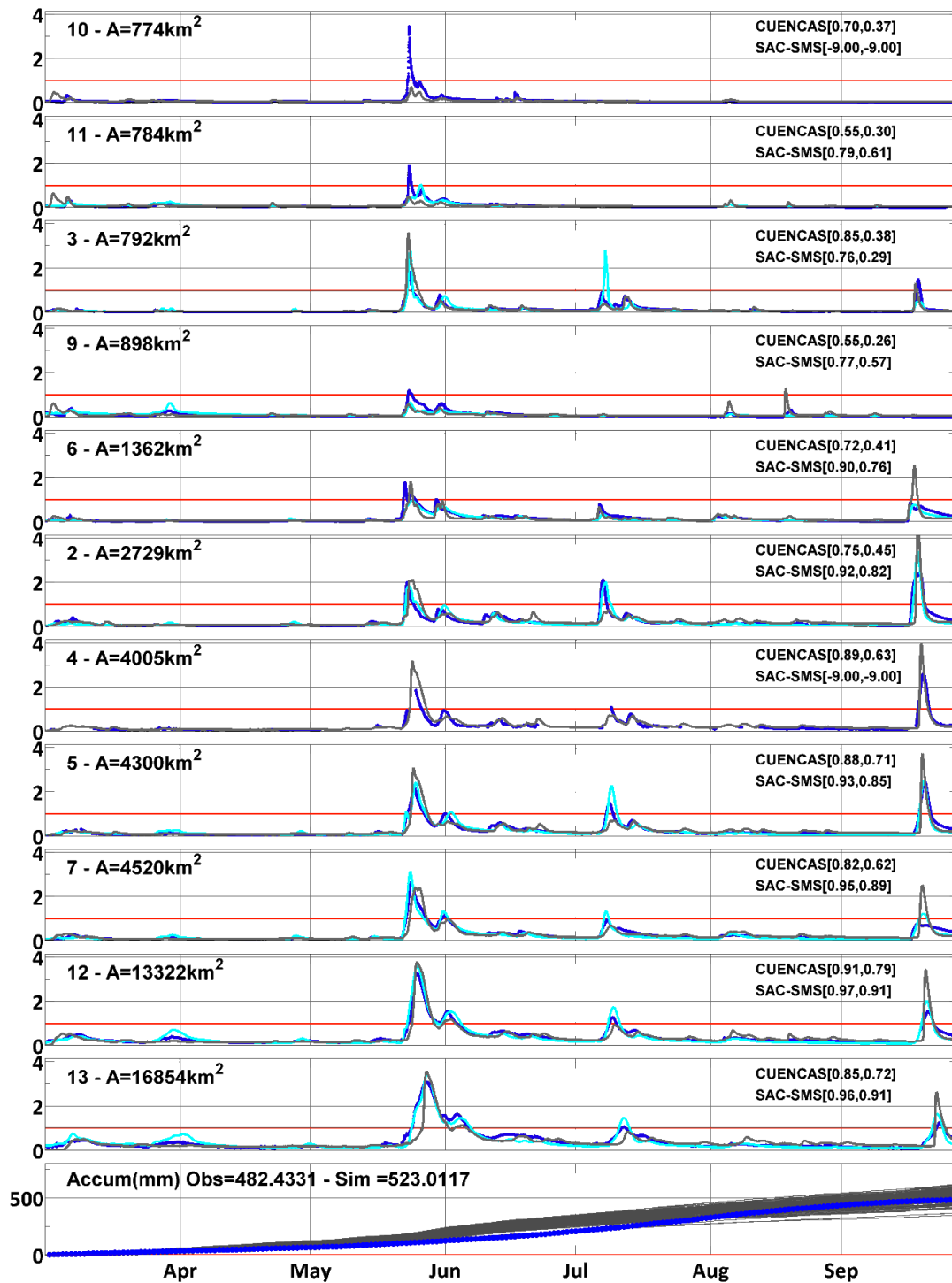


Figure III-4. Simulation of 2004 flood event for Cedar River sites. Gray line is simulated by CUENCAS, light blue is simulated by SAC-SMS, and dark blue line is observed.

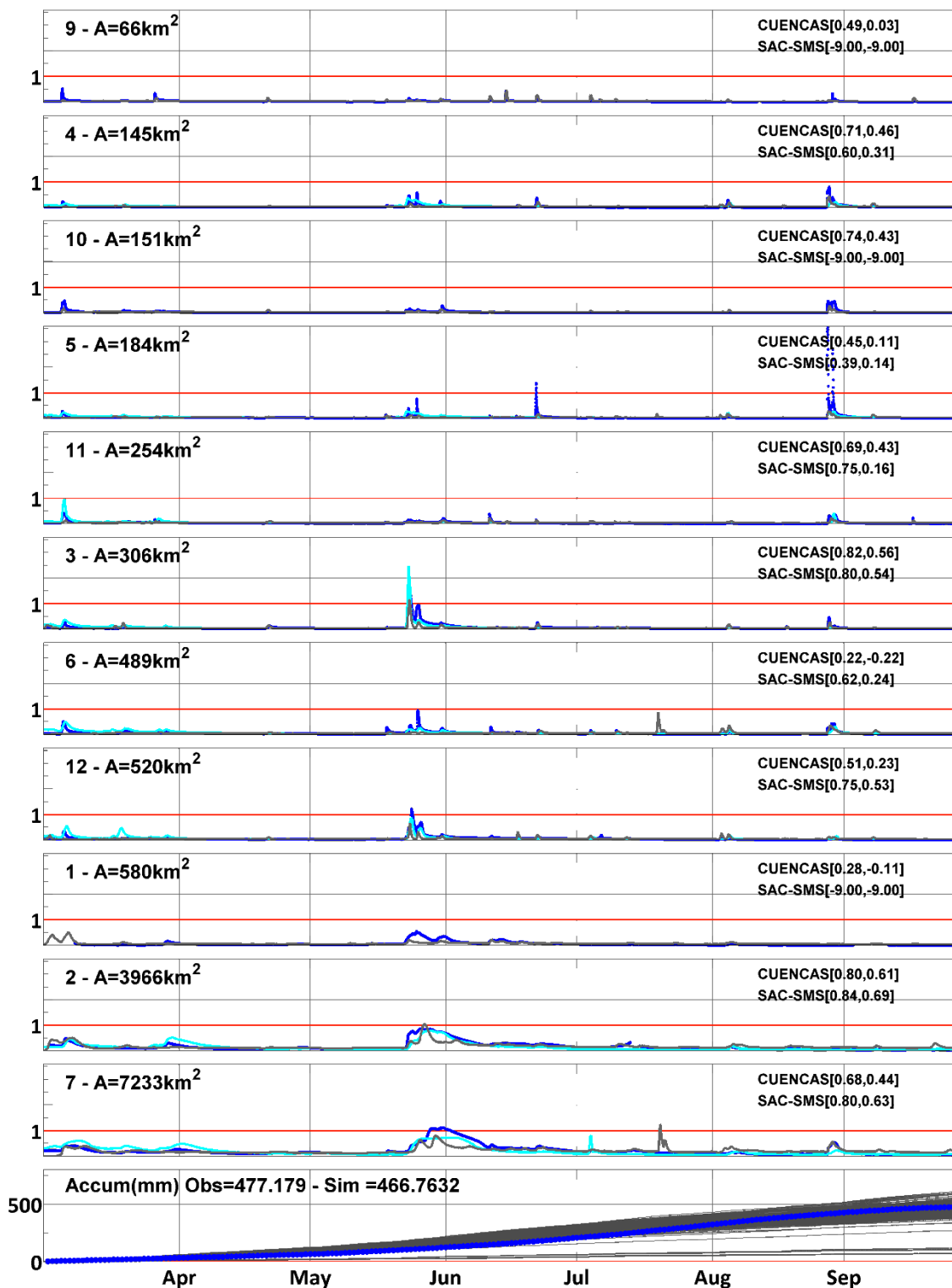


Figure III-5. Simulation of 2004 flood event for Iowa River sites. Gray line is simulated by CUENCAS, light blue is simulated by SAC-SMS, and dark blue line is observed.

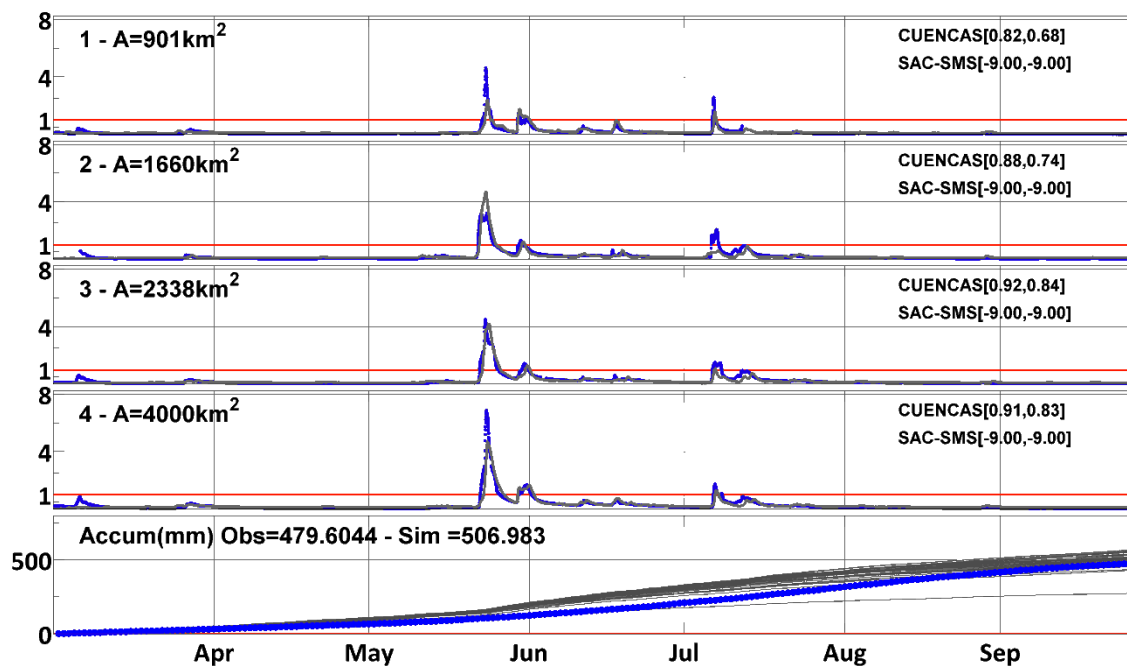


Figure III-6. Simulation of 2004 flood event for Turkey River sites. Gray line is simulated by CUENCAS, light blue is simulated by SAC-SMS, and dark blue line is observed.

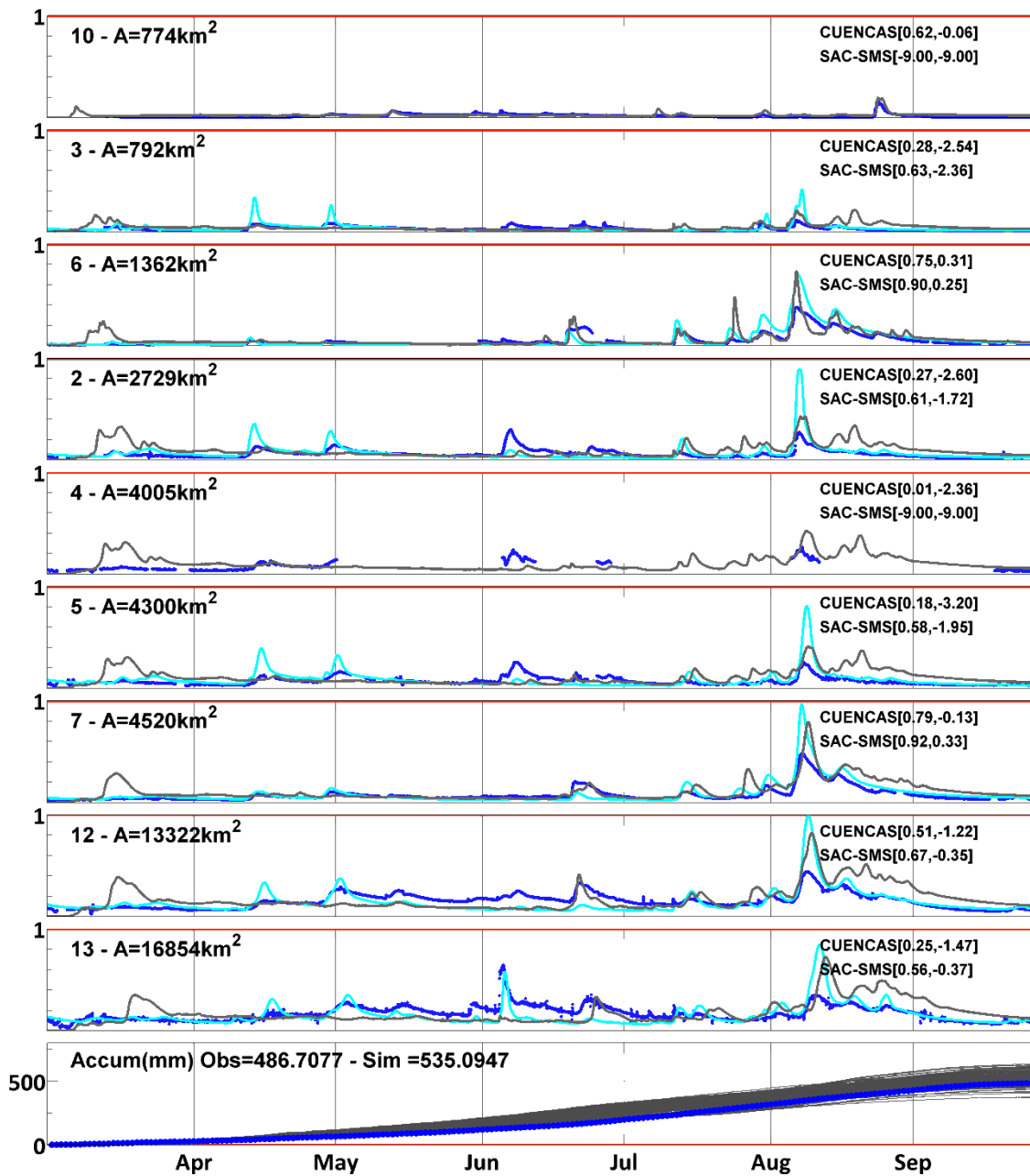


Figure III-7. Simulation of 2022 streamflow for Cedar River sites. Gray line is simulated by CUENCAS, light blue is simulated by SAC-SMS, and dark blue line is observed.

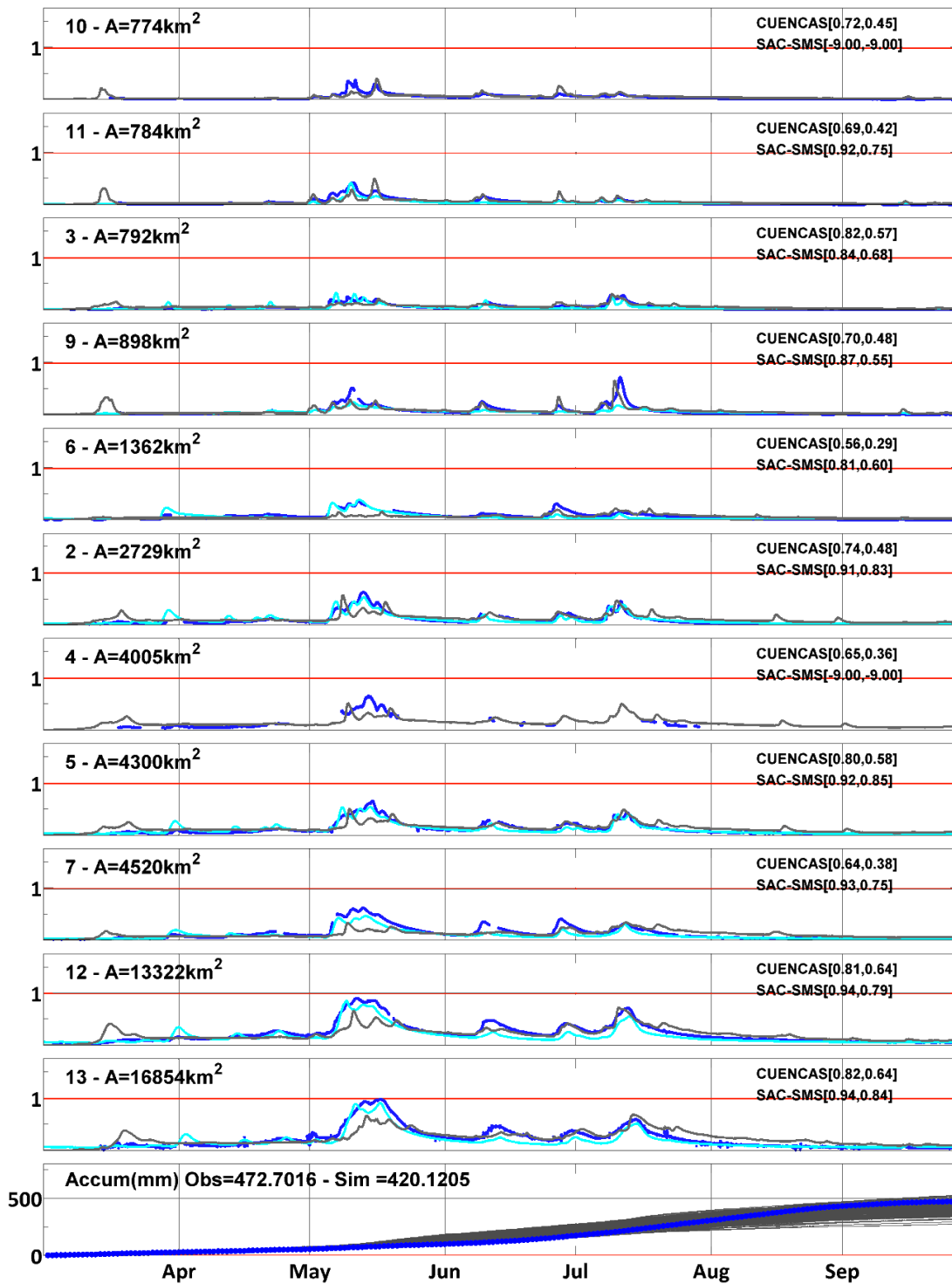


Figure III-8. Simulation of 2003 streamflow for Cedar River sites. Gray line is simulated by CUENCAS, light blue is simulated by SAC-SMS, and dark blue line is observed.

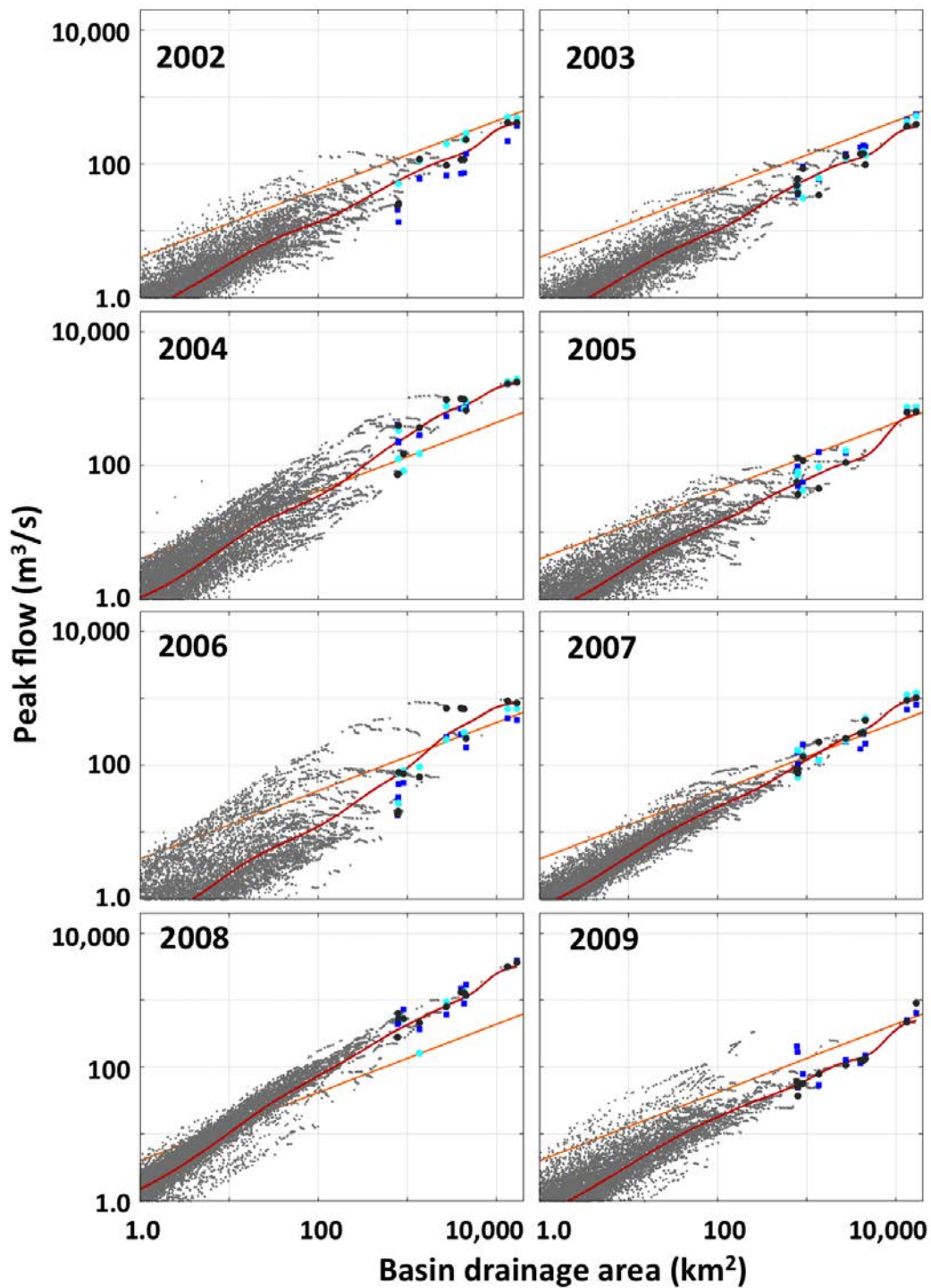


Figure III-9. Observed (dark blue dots) peak flow and peak flow predicted by CUENCAS (gray) and SAC-SMS (light blue, when available) for the Cedar River basin for 2002 to 2009. The red line is a non-parametric regression line that estimates the expected value of peak flow as a function of area. The orange line is the mean annual flow.

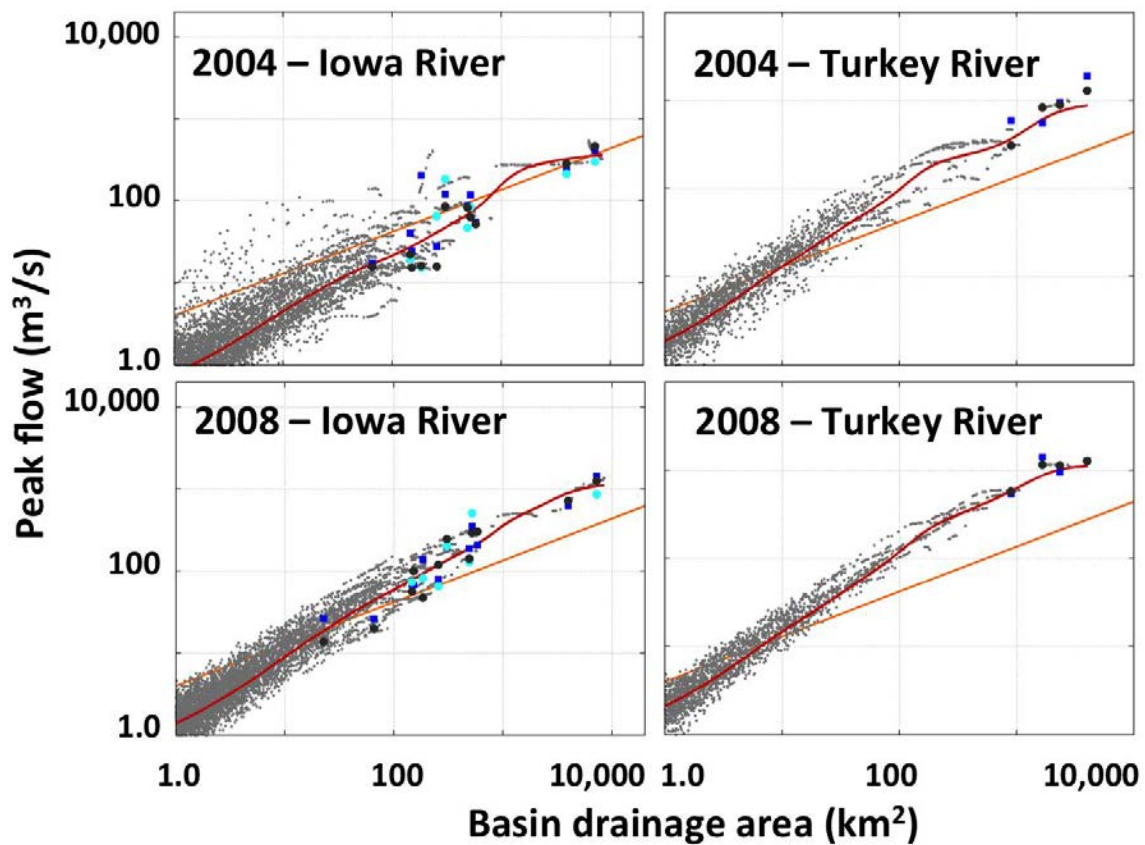


Figure III-10. Same as Figure 1-12, but for years 2004 and 2008 for the Iowa and Turkey Rivers.

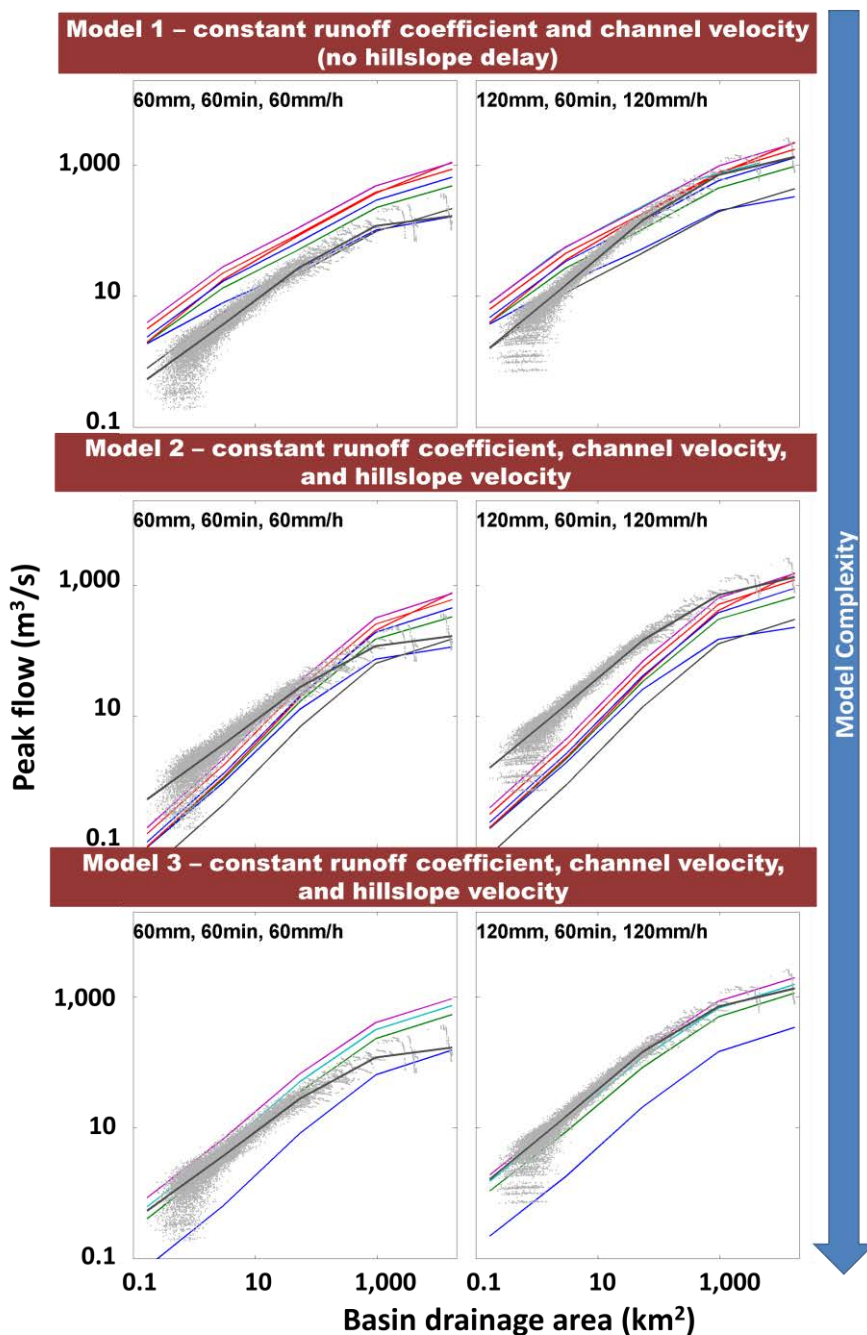


Figure III-11. Simulation results based on different rainfall total accumulations (60 and 120mm) with fixed duration (60 minutes). The different lines represent simulations with different channel velocities. The black line represents the most complete version of the hydrological model that was demonstrated to capture peak flow scaling for real events. Model specifications are specified in the top of each plot. Model complexity increases from the top to bottom.

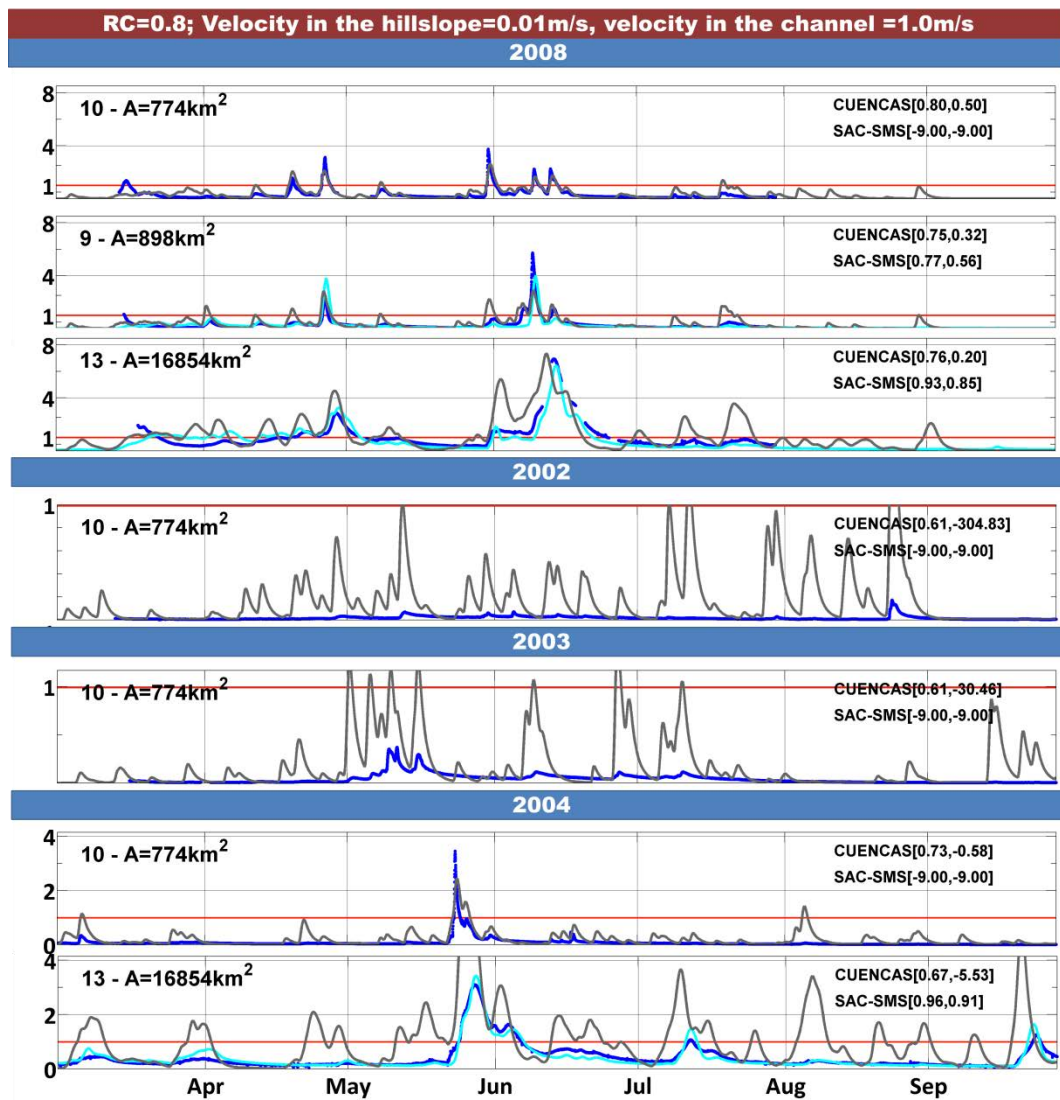


Figure III-12. Simulated streamflow (dark blue) based on the following parameters: 0.8 runoff coefficient, 1.0 m/s channel velocity, and 0.01 m/s hillslope velocity. Observed values are presented in gray, and simulated values based on SAC-SMS, used as a reference, are presented in light blue. I present results for 3 sites (Wolf Creek, Beaver Creek, and Cedar River) for 2008, 1 site (Wolf Creek) for 2002, 1 site (Wolf Creek) for 2003, and 2 sites (Wolf Creek and Cedar River) for 2004.

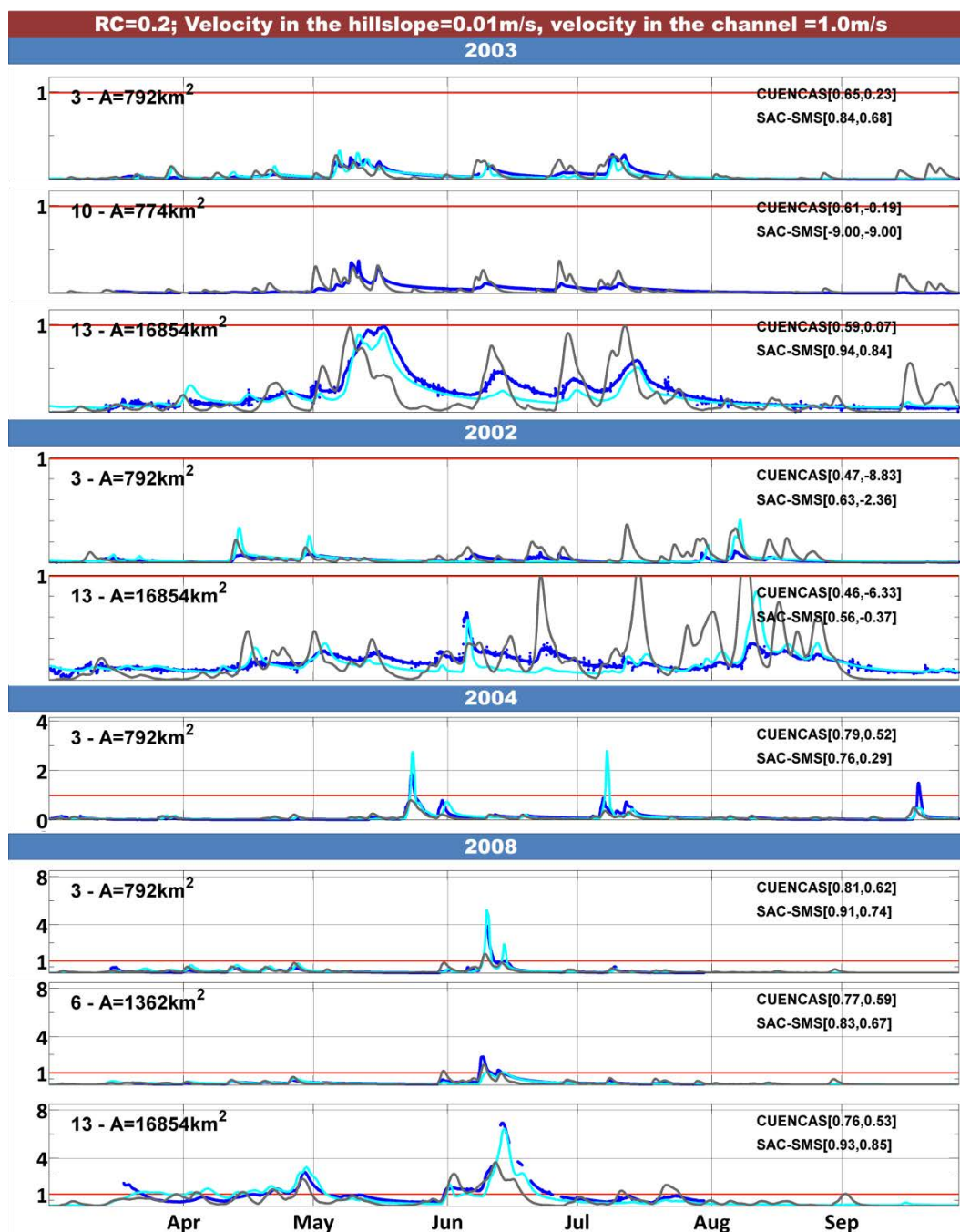


Figure III-13. Simulated streamflow (dark blue) based on the following parameters: 0.2 runoff coefficient, 1.0 m/s channel velocity, and 0.01 m/s hillslope velocity. Observed values are presented in gray, and simulated values based on SAC-SMS, used as a reference, are presented in light blue. I present results for 3 sites (Little Cedar River, Wolf Creek, and Cedar River) for 2003, 2 sites (Little Cedar River and Cedar Rapids) for 2002, one site (Little Cedar River) for 2004, and 3 sites (Little Cedar River, Winnebago River, and Cedar River) for 2008.

CHAPTER IV

IMPACT OF DEM SOURCE, RESOLUTION, AND NETWORK PRUNING ON THE CHARACTERIZATION OF THE RIVER NETWORK AND ON ESTIMATION OF PEAK FLOW MAGNITUDE AND TIMING ACROSS SCALES

Introduction

One of the major challenges for the hydrological community is the development of near-global flood forecasting systems based on remote sensing data (Lettenmaier and De Roo, 2006; Wood *et al.*, 2011). DEMs are the critical information for the implementation of these systems, since it provides a numerical representation of the land surface topography. DEMs are used to extract the river network, outline model control volumes (e.g grid, sub-watersheds, hillslopes), and to calculate land surface slopes, which controls runoff transport. While for some regions of the world different DEM datasets are available, with varying spatial resolution, and accuracy (e.g. USA), other regions rely entirely on satellite-based data (e.g. some regions in Africa, South America, and Asia). Satellite-based DEMs present coarse spatial resolution and low vertical and horizontal accuracy (Hirt et al 2010; Slater et al 2011, Smith and Berry 2011). Consequently, it is important to understand the effects of these uncertainties on peak flow simulation. The main goal of this study is to diagnose the manner in which DEM uncertainties affects river network extraction and peak flow simulation across scales.

Two remote sensing missions provide DEM with near-global coverage (including the most populated regions of the world): the Shuttle Radar Topography Mission (SRTM: Farr *et al.* 2007) and the Advanced Spaceborne Thermal Emission and Reflection Radiometer (ASTER: ASTER validation team, 2011). Both datasets are available online at no cost, at the spatial resolution of 3 arc seconds (~90 m) for SRTM and 1 arc second (~30 m) for ASTER. For USA, other sources of DEM, with higher spatial resolution and higher vertical and horizontal accuracy, are also available. The US Geological Service

(USGS) provides the National Elevation Dataset (NED), with 1/9 (for some regions), 1/3, and 1 arc seconds, ~3, 10, and ~30 respectively. NED is built from stereoscopic models and is frequently updated through the merging of higher resolution data. For specific regions, LIDAR data is also available. Table 1 presents a list with some of the available DEMs datasets and their main characteristics. Maune (2007) presents a comprehensive review about each dataset.

In this introduction I discuss previous studies that investigate the role of DEM on hydrological modeling. Various studies have demonstrated that DEM features, especially resolution and accuracy, affect landscape characterization and hydrological modeling (Zhang and Montgomery, 1994; Thompson *et al.*, 2001; Hancock and Evans, 2006; Martinez *et al.*, 2010). Zhang *et al.* (1999) compared landscape slopes calculated based on 20 to 2,000 m resolution DEMs and concluded that slope varies inversely with the DEM grid size. In the same line, Zhang and Montgomery (1994) concluded that the effects of DEM on hydrological simulations are mainly caused by differences in slope, and related model-derived quantities obtained using different resolution DEMs (2 to 90 m). Quinn *et al.* (1991) and Parsons *et al.* (1997) demonstrated the relevance of high-resolution features for channel and overland-flow routing. Li and Wong (2010) evaluated different DEMs sources and resolution and concluded that coarser data resolution does not necessarily lead to poorer characterization of landscape aspects. According to the author, slopes estimation changes for different resolution, however certain landscape features and characteristics may not be correctly identified or evaluated when higher resolution data is used. Mantilla and Gupta (2005) focus on the properties of the network and concluded that a 30 m DEM is sufficient to ensure that the extracted network closely corresponds to the network that exists in the actual terrain.

Although noteworthy literature is available in the subject, no consensus exists in terms of the optimal DEM resolution for hydrological simulations. One of the factors causing the lack of consensus is that errors are scale dependent (Endreny and Wood,

2000). All the previously mentioned studies are based on the results for a single watershed scale, usually on the order of 0.1-100 km². The exception was the study developed by Endreny and Wood (2000). The authors demonstrated the scale-dependency of errors through the evaluation of the effect of vertical errors on the estimation of geomorphological basin properties for micro, meso, and macro-scales, defining as having the size domain of approximately 0.5, 5 or more than 5 km respectively. Therefore, to comprehensively investigate how DEM errors affect landscape characterization and peak flow simulation a multi-scale approach that covers a large range of drainage area is required.

Another restraint of previous studies is the use of calibration to estimate hydrological model parameters. As demonstrated by Zhang and Montgomery (1994), Kenward (2000), Vazquez and Feyen (2007), among others, calibrated parameters are DEM dependent since parameter values are adjusted to compensate for uncertainties in the dataset used for calibration (Refsgaard, 2004; Ajami *et al.*, 2007). Those studies demonstrated the need for a simulation framework that isolates uncertainties due to model structure, parameter estimation and input, allowing an impartial assessment of different datasets.

In this study I adopt a multi-scale physically-based rainfall runoff model that simulates response to rainfall forcing at a wide range of scales. Parameters estimation is data-based and I do not adjust (calibrate) parameters to force better agreement with observed streamflow. Since calibration is not required, the framework isolates errors due to DEM uncertainties, allowing a fair comparison of different datasets. I use DEM data to decompose the terrain in hillslopes and links, so landscape characterization is affected by uncertainty and errors on the elevation data. The model simulates response to rainfall forcing for every link in the network, covering a wide range of scales, with the smallest being a hillslope scale (~0.01 km²). This feature allows the investigation of how DEM errors affect hydrological prediction across scales. A similar approach was used by

Cunha et al (in preparation) to investigate the impact of radar-rainfall error structure on estimated flood magnitude across scales.

I investigate different aspects that can introduce errors in the characterization of the landscape, including DEM accuracy and resolution. I also investigated the effect of pruning small order channels systematically transforming it into hillslopes. I examine the impact of vertical and horizontal accuracy by comparing DEMs from different sources. LIDAR and NED DEMs are expected to have considerably smaller errors than the satellite-based DEMs (ASTER, and SRTM). Second, I examine the effect of DEM resolution. As pointed out by Beven (2012), the use of high-resolution data might not be necessary, or even recommended, if processes that occurred at scales smaller than the model domain are realistically parameterized. The use of a very high-resolution DEM may result in the representation of features that are not relevant for the process being modeled (Kienzle, 2004; Lassueur *et al.*, 2006; Liu, 2008). The use of high-resolution DEM also leads to higher computational requirements. In some cases, the use of higher DEM resolution yields only small improvements in terms of accuracy (Sanders, 2007), but considerable increase of computational time. Moreover, losses in horizontal resolution can sometimes introduce considerable gains in vertical accuracy that might be essential for hydrological simulations (Endreny and Wood, 2000).

I also investigate the effects of simplifying the river network. These simplifications are very common in hydrological modeling, since they result in a lower number of model units (hillslope or sub-watersheds) for the same area, reducing the amount of parameters to be estimated, and the computational time to run the model. However, these simplifications impact runoff transport through the watershed.

Following this introduction, Section 2 offers the description of the different DEM databases used in this study. The description of the study area and hydrological model used in this study were previously presented in Chapter 1 and 2, respectively, and will not be repeated here. However, it is important to point out that in this Chapter I analyze only

the Cedar and Clear Creek basins. The analysis using high resolution LIDAR data was limited to the Clear Creek basin, since LIDAR data for the whole area was not available during the development of this study. In Section 3, I present methodological aspects of this work, focusing on the landscape decomposition method, the hydrological model, and the criteria used to compare different DEMs. Section 4 includes the main results of this study. First I compare hydro-geomorphological properties obtained with different DEMs. Second, I present results of hydrological simulations performed with real (Iowa 2008 event) and synthetic rainfall. I evaluate different simulations focusing on the scaling structure of peak flows. Section 5 summarizes and concludes the study.

Rainfall

For precipitation I use a Hydro-NEXRAD (HN) rainfall product produced based on a novel methodology to reduce the effects of relative calibration bias between multiple radars covering the same area. This bias produces an artificial artifact in the radar-rainfall Stage IV data provided by the National Weather Service (Seo, in preparation). The HN product was produced based on the radar Level II data provided by the National Climatic Data Center (NCDC) for four WSR-88D radars (The KARX, KDMX, KDVN, and KMPX; see Figure 2). The final radar rainfall product presents 1-hour resolution in time, and approximately 4-km resolution in space. Seo et al (2012, in preparation) presents more details about the Stage IV and HN rainfall dataset, the methods used to generate the HN product, and the improvements HN led to hydrological simulations.

Digital elevation models

For Cedar River basin I compared three sources of information: NED (30 m), SRTM (90 m), and ASTER (30 m). For detailed characteristics of these datasets see Maune (2007). For Clear Creek I also included high resolution LiDAR (Airborne light detection and ranging) data in the analysis. These datasets are aggregated in space to explore the effects of DEMs spatial resolutions. For Cedar Rapids the NED DEM was

aggregated from 30 meters to 90, 120, 150, and 180 meters, while for Clear Creek I aggregated the LiDAR data from 1 meter to 5, 10, 20, 30, 60 and 90 meters.

The LiDAR data used in this work was collected by the Iowa Department of Natural Resources (DNR) and is available for free on www.iowadnr.gov. Even though LiDAR data provides highly accurate information for the generation of digital elevation model (DEM), effective raw data processing, quality control, and large computational requirements add limitations to the use of this data. For example, the classification of LiDAR points into ground and non-ground is a critical and difficult process. Liu (2008) and Meng *et al.* (2010) presented a review about the main issues related to DEMs generation based on LiDAR measurements. In this study, the highest resolution dataset included in this study was the 5 meters DEM. I opted to aggregate the 1-meter LIDAR DEM to 5 meters, since computational requirements to process the 1-meter DEM for the study area was too high. I assume that the 5-meters DEM provides accurate information about the geometry of the hillslope, since the smallest hillslopes are in the order of 0.01km^2 , what correspond to 400 pixels of the 5-meters resolution DEM.

Methodology

Uncertainties on the representation of the landscape propagate through hydrological models affecting peak flow simulation. In this study I investigate how degrading DEM information affects the extraction of the main properties of the river network, and how these uncertainties propagate through hydrological models affecting hydrological predictions. I focus on three main aspects: DEM source, DEM resolution, and river network extraction thresholds.

In the following sections, I will focus on the description of the three main components of this work: (1) the landscape decomposition method; and (2) the criteria used to evaluate different DEMs.

Landscape decomposition method

Previous studies have demonstrated the role of the river network for flood prediction (Menabde *et al.*, 2001; Gupta, 2004; Mantilla *et al.*, 2006; Mantilla *et al.* 2011). To obtain a truthful representation of the river network I decompose the landscape in hillslope and links based on the DEM. To determine the location of the actual river network, a slope-dependent critical support area was used (Mantilla and Gupta, 2005). This decomposition method allows the simulation of hydrological processes close to the scales at which they occurred in nature. At the hillslopes scale I parameterize processes that account for partition of rainfall input into surface runoff, infiltration, and evapotranspiration. The river network transports the runoff produced at the hillslope scale, aggregating discharge as the water flows to higher order streams.

It is important to point out the difference between the decomposition method applied in this work and the one that decompose the terrain in square grids, commonly adopted in hydrological models (see a list of model in Kampf, 2007). Organized squared pixels are not truthful representation of the domains in which hydrological processes occurred in nature (Dehotin and Braud, 2008). A correct representation of the river network using square-grid requires the use of high-resolution DEM (in the order of the width of first order streams), what is not feasible due to the high computational requirements to run such models (Yang *et al.*, 2002). This is especially true if the goal is to apply the model in a global scale. To compensate for the artificial domain representation, and the use of coarser data resolution than required, the specification of all needed parameters has to be done by calibration. Furthermore, due to computational limitations, when applied to medium or large basin areas these models usually even coarser grids than available DEMs. Therefore, model that adopts square-grid landscape decomposition are not appropriate to investigate the benefits of different DEMs for hydrological predictions.

I extract the river network using different sources of DEM on their original resolution (5 m for LIDAR, 30 m for the NED, 30 m for the ASTER, and 90 m for the SRTM). I then aggregate the cells to coarser resolution areal grids (NED from 30 to 180 meters, and LIDAR from 5 to 90 meters) to investigating the effects of resolution.

To investigate the effects of simplifying the river network I also manipulated the final network obtained with the 90 meters NED DEM. I systematically pruned the lower Horton order links (one to four), increasing the size of the hillslope, but maintaining the general structure of the river network. Computational requirements increase linearly with the number of links simulated in a river watershed. Therefore, if the effects of pruning the network are known, it might be of interest to use a simplified river network for hydrological simulations since it would considerably decrease simulation time. These results would also provide insights for the development of global scale flood prediction system, based on simplified network structures (Wood *et al.*, 2011).

It is worthwhile mentioning that the pruning method used in this work preserves the fractal structure of the network. This method is different than the one adopted by many semi-distributed approaches for hydrological modelling, for which basin decomposition is chosen based on an ad-hoc criteria, such as stream-gauge site location (or data availability) or/and study goals. In some models the user is responsible for defining the spatial unit for rainfall–runoff calculations, that can vary from the entire watershed, or any smaller sub-watershed. I expect that this type of basin discretization would result in larger errors, since physical processes are modeled by the same equations for a large range of scales.

Criteria for DEM evaluation:

geomorphological properties and hydrological simulation

Many studies have evaluated different DEMs in terms of their vertical and horizontal accuracy (e.g. Reutebuch *et al.*, 2003; Fujisada *et al.*, 2005; Bhang *et al.*, 2007;

Hirt et al, 2010). However, the relevant aspect for flood prediction is the ability of the DEM to provide a good representation of the overall shape of the landscape and the river network. Moreover, it is important to understand how discrepancies in the river network affect hydrological prediction. Therefore, in this study I use two criteria to evaluate the potential of different DEMs for flood prediction. First, I evaluate their ability to estimate river network physical properties that controls flood generation. Secondly I investigate how uncertainties on landscape characterization propagate through hydrological models.

For the first criteria I evaluate two geomorphological descriptors that are relevant for flood generation: the width function and the scaling of the maximum of the width function. These functions correspond to to the hydrograph (width function) and peak flow scaling (width function maxima) obtained under the following idealized conditions: (1) spatially uniform instantaneous rainfall, (2) constant flow velocity, (3) negligible evaporation; (4) purely surface runoff (i.e., no infiltration and no subsurface runoff); and (5) instantaneous flow of runoff into the channel (Gupta et al, 1996; Troutman and Over, 2001). The width function, first introduced by (Shreve, 1969), is defined as the probability measure obtained by dividing the number of links at given distance x from the outlet by the total number of links in the network (Rinaldo *et al.*, 1993). I evaluate the shape and the maximum of the width function obtained for the outlet of the basin (Clear Creek and Cedar River) using river networks extracted from different DEMs. I then determine the maximum of the width function for each link in the network and use it to construct scaling plots (Gupta et al, 2010). I use least-squares regression between drainage area and the maximum of the width function to estimate the scaling parameters of the power law relationship, and I compare the parameters obtained based on different DEMs.

I then apply the hydrological model described in the previous section to investigate how landscape characterization uncertainties propagate through hydrological model. I first demonstrate the model skill by simulating an extreme rainfall event that

occurred in Iowa in the summer of 2008. The evaluation of the model performance was presented by Seo *et al.* (in preparation), and was based on (1) observed streamflow at the outlet of nested basins ranging in scale from about 20 to 16,000 km² and (2) streamflow simulated by a well-established and extensively calibrated hydrological model SAC-SMA used by the US National Weather Service (Burnash, 1995). These results were obtained based on the network extracted from the 90-m NED DEM. Since models results are accurate, I use this dataset as a reference, and evaluate differences on simulations obtained with different networks, based on varies DEM sources, resolution and network pruning criteria. Since the model was not best-fit to a particular DEM, difference between simulated values will be uniquely due to the effects of the DEM.

I then perform synthetic simulations, forcing the hydrological model with spatially uniform rainfall with different duration and intensity. In this case I isolated the effects of rainfall, and rainfall-runoff transformation spatial variability. I evaluated the difference in simulated peak flow scaling obtained with different network structures and rainfall intensities (mild to intense rainfall events).

Results

River network extraction

I used DEMs with different resolutions and from various sources to extract the river network for Cedar River (CR) and Clear Creek (CC) basin. I also systematically pruned the network generated using the NED 90 meters DEM removing rivers with Horton order 1 to 5, transforming the Cedar River network from an original 9th Horton-order into an 8th (HO8), 7th (HO7), 6th (HO6) and 5th (HO5) Horton order network. Clear Creek was originally a 6th Horton-order network and it was transformed to a 5th, 4th, 3th and 2nd Horton order network. A list of all DEMs used and the basic characteristic of the final networks for each one of them is presented in Table IV-1.

For Clear Creek basin, the inferred drainage area is very similar for all DEM, resolutions and network pruning. I used the LIDAR 5 meters DEM as reference to calculate the relative difference in drainage area. The maximum relative difference was equal to approximately 1% for the ASTER and the SRTM 90 meters DEM. In the case of Cedar River basin, the basin boundary was not correctly delineated using the 30 and 60 meters resolution ASTER. The Cedar River basin delineation obtained with the 30 meters NED DEM is presented in Figure IV-2 (a), while the delineation obtained with the 30 meters ASTER DEM is presented in Figure IV-2 (b). The first one matches closely the delineation provided by the United States Geological Survey (USGS) hydrologic unit system (HUC 07080200), while the second one includes a tributary that in actuality drains to the Mississippi River. The incorrect delineation arises from high vertical inaccuracies that can reach values up to 15 m according to the ASTER validation team (2011). In this case the relative difference in basin drainage area to the reference DEM (30 meters NED) was 17%.

Interestingly, the error disappears when I aggregate the ASTER data to 90 meters. In this case, the basin drainage area was correctly delineated with a relative error compared to the NED 30 meters DEM equal to around 0.5%. This demonstrates that care should be taken when using remotely sensed DEM due to low vertical accuracy. Some of the local vertical errors can be filtered if the DEM is aggregated to a coarser resolution in space. In this case, a gain in vertical accuracy overcome losses due to spatial resolution, since the smoother DEM produced by the aggregation in space provided a better estimation of the basin boundaries.

Table IV-2 also provides average hillslope information. DEM resolution has a significant impact on the final hillslope size. Coarser DEM resolution results in larger average hillslope area. This happens since I am using a slope-dependent threshold to define channel initiation and hillslope size, and average slope changes as the resolution of the DEM changes, as also indicated in Table IV-2.

River network properties:

width function and maximum of the width function

In this section I use the width function and the scaling of the maximum of the width function to evaluate differences in the river networks extracted from different DEMs. The importance of these two network properties for hydrological simulation has been previously discussed.

In Figure IV-3 and Figure IV-4 I present the width function extracted for Clear Creek and Cedar River, respectively. I normalized both axes by the width function maxima to be able to compare the shape of the width functions. The red line in the plot indicates the location of the maximum of the width function. The values in squared brackets show how many million DEM pixels are contained in the basin analyzed, which varies with DEM source and resolution.

For Clear Creek I included high-resolution LiDAR data, and I systematically aggregated this database to resolutions that varies from 5 to 90 meters. I also included the width function estimated based on the 90 meters resolution NED, ASTER, and SRTM datasets. Even though all the datasets captured the general shape of the width function, with three main local peaks, the maxima of the width function was not equally estimated for all datasets. For the 5, 10, and 30 meters resolution LIDAR DEM the maxima of the width function are in the second local peak, while for the other datasets they are in the third local peak. For the datasets with the same resolution (90 meters LIDAR, NED, ASTER, SRTM) the maximum of the width function was located almost at the same distance to the outlet. Based on these results, I conclude that for Clear Creek DEM resolution strongly affects the delineation of the width function, while the effects related to the DEM source, and consequently to the vertical accuracy, have a smaller impact.

For the Cedar River basin the shape of the width function is significantly different for different DEM sources. Contrary to the Clear Creek basin, the vertical accuracy in this case does play a role on the estimation of the width function. This might be caused

by vertical errors that are correlated in space, increasing the number of links in specific parts of the basin. On the other hand, the resolution of the DEM did not strongly affect the width function shape or the location of the peak. The effect of resolution is proportional to the number of DEM pixels contained in the basin, and the relative change in this number when the DEM resolution is modified. The change in the number of pixel caused by the decrease in DEM resolution was much more significant for the Clear Creek case. The last line of Figure IV-4 presents the width function for different pruning methods. The number in the Figure indicates the Horton order of the basin. We can see in the plots that the shape of the width function did not changed significantly with changes in “hillslope” size.

In Figure IV-5 I present the width function maxima for Cedar Rapids. I used ordinary least square regression to obtain the parameters of the power law relationship between drainage area and corresponding width function maxima. Even though the width function of a specific site is affected by the source and resolution of the DEM, all the DEM sources provide a good estimation of the statistical structure of the width function maxima. This shows that local vertical errors are filtered out when treated in a statistical way.

Effects on hydrological simulation:

2008 Iowa flood event

In this section I present the simulations results for an extreme flood event that occurred in Iowa in the summer of 2008. During this event, peak flows with 500 years return period were observed in some parts of the basin. For the simulations presented here all the models parameters were estimated based on the data presented in Table 2. Cunha et al (in preparation) presented the validation of the simulation results for Cedar River, and Iowa River, using constant initial conditions for the soil across the study. In the paper presented by Seo et al (in preparation), the same model was used, but NLDAS

data was used to setup space variable initial conditions for the soil. In this study I use the same model version adopted in Seo et al (in preparation) study. Validation of model results was also presented by the author and will not be repeated here.

Figure IV-6 presents the observed and simulated hydrographs for selected sites in the basin. I normalized the y-axis by the site mean annual flood, calculated as a power law function of the basin drainage area. Assuming that the mean annual flood is a good approximation for bankfull flood (Leopold et al 1964), any value above one means the site was flooded. Values in the left corner indicate the site number and drainage area (see Figure IV-1). Seo (in preparation) presented results for all the sites. I focus on showing the results for some selected sites, covering the whole spectrum of drainage area. In the right corner of each hydrograph I present the goodness-of-fit (correlation, and Nash coefficient) for the results obtained with the network extracted from the NED 90m DEM (blue line). Observed values are presented in gray. Note that for some of the sites, the streamflow series present a large amount of missing values (e.g site11). To be able to calculate the statistics I filled out the missing points using a simple linear interpolation method. Large number of missing points affects the goodness-of-fit statistics, and in this case the visual comparison provides a better way to evaluate model results. The figure demonstrates the skill of the model on simulating streamflow across scales.

To investigate the effect of the river network on flow simulation I also present the simulated values based on ASTER (green), 180 m resolution NED (magenta), and NED HO6 (cyan). Differences were especially significant for Clear Creek Site (site number 6), the same site for which I present the width function analyses (Figure IV-3). For this site there is a considerable difference on the shape of the basin response. Since parameters and inputs, other than the ones based on the DEM, are the same for all simulations, these differences reflect the effect of the width function on hydrological simulation. Looking at the figure we can see that the differences are not significant for all the sites. The

differences seem to decrease as the basin area increases what might be the result of small-scale uncertainties being filtered by the river network.

Figure IV-7 presents the scaling of peak flow for the 2008 Iowa flood event. The reader is directed to (Gupta *et al.*, 2010) for a review about the relevance of event-based peak flow power laws in flood prediction. Each one of the light gray dots represents simulated peak flow value for one link in the river network. In this plot I just included the simulated values obtained with the 90 m NED DEM. To estimate the relationship between peak flow and basin drainage area I used a non-parametric kernel regression. The object of nonparametric regression is to estimate the regression function between the independent variable (in this case drainage area), and the dependent variable (peak flow) directly, rather than to estimate parameters. This type of regression relaxes the linearity assumption required for parametric methods (Black and Smith, 2004). Another important reason to use non-parametric regression is the difference in the number of points for different DEMs, since the total number of hillslopes depends on the network (see Table 3). Different number of points might bias the estimation of parameters if the least square method is used. Observed values are presented in dark gray. Note that three sites present observed values below the fitted lines. These sites presented missing values exactly at the time of the peak, and the values of peak flow were obtained by linear interpolation and are likely to be underestimated. Figure IV-7 (a) presents the regression lines obtained with different DEM sources (NED, ASTER, SRTM) with 90 meters resolution, (b) presents the regression lines obtained with NED DEM aggregated to different resolutions (30,90, 120,180), and (c) present the regression lines obtained for different network pruning (original HO9, HO8, HO7, and HO6). These figure shows that space-based remotely sensed DEMs (specially the SRTM DEM) can be used to simulate the statistical structure of peak flows, even tough some uncertainty exists in the estimation of the hydrographs for small scale basin. The effects of DEM resolution and network pruning were more accentuate than the effect of DEM source.

Effects on hydrological simulation:
synthetic rainfall

In the previous section I demonstrated the skills of the hydrological model on simulating flood events. In this section I use CUENCAS to simulate synthetic flood events with different rainfall intensity. I assumed uniformly distributed rainfall throughout the basin with varying total volume (30, 60 and 120 mm) and fixed duration equal to 120 minutes, what corresponds to different rainfall intensities (15, 30, 60 mm/h). I performed simulations for Cedar River basin using the network extracted from the NED (30, 90, 120, and 150 m resolution), ASTER, SRTM 90 meters DEM, and the 90 meters DEM pruned to Horton order equal to eight (HO8) and seven (HO7), initially a Horton order 9 network (HO9). The initial conditions of the surface, soil and channel were set to zero (dry conditions). I use the same soil, channel, and surface parameters used to simulate the 2008 event.

I present the simulation results in Figure IV-8. The plots display the statistical peak flow scaling relationships for different rainfall scenarios (different panels, from top to bottom) obtained with networks extracted from different DEMs (different lines in the plots). Rainfall total volume (intensity) increases from the top to the bottom of the plot (30, 60, and 120 mm, that correspond to intensity of 15, 30, and 60 mm/h). Rainfall duration is always 120 min. From now on these events will be referred as mild, intense, and extreme, respectively. To estimate the relationship between peak flow and basin drainage area I used a non-parametric kernel regression, as described in the previous section.

The results for different DEM sources, resolution and network pruning are shown in column one, two, and three of Figure IV-8, respectively. The blue line in all the plots represents the simulation with the reference DEM (NED 90 meters). In the first columns I present the results based on ASTER (green line) and SRTM (red line). The results for NED and SRTM overlay, while the results for ASTER are slightly different for the mild

event. The difference decreases as the intensity of the event increases. This figure demonstrates that network extracted from remote sensed DEM can be used for hydrological simulation, especially if the focus is on intense to extreme flood events.

The second column presents results for NED DEM aggregated to different spatial resolution (30, 90, 120, 150 m). Brown, blue, gray, and magenta lines correspond to 30, 90, 120, and 150 meters DEM, respectively. In this case the results are significantly different for mild and intense events. As it happened in the case of different DEM sources, the differences decrease as the intensity of the events increases. However, the differences are still significant for intense events. The last column presents results for different network pruning. The pruning processes correspond to increasing the average hillslope area (A_H), since I remove small order streams transforming them into hillslopes. I show the results for the original Cedar River basin network that correspond to an Horton-order equal to 9 (HO9, $E[A_H] = 0.215 \text{ km}^2$), and pruning one (HO8, $E[A_H] = 0.293 \text{ km}^2$), two (HO7, $E[A_H] = 1.338 \text{ km}^2$), three (HO6, $E[A_H] = 6.118 \text{ km}^2$) orders. In this case the differences between the simulations with the different networks are substantial. These results demonstrate the importance of correctly representing the properties of the river network to simulate floods. If the river network were not fully represented in the model, other parameters would have to compensate for the differences observed in Figure IV-8. As for the other scenarios, the differences also decrease with event intensity, but in this case they are still very large for the extreme event case.

Conclusions

In this study I investigated how uncertainties on the extraction of the river network from DEM introduce errors on the characterization of hydrological relevant landscape properties and how these uncertainties propagate through hydrological models. Errors in the characterization of the landscape can arise from vertical and horizontal inaccuracy of the DEMs, coarse spatial resolution, and the method used to extract the

river network. The analysis was performed on the Clear Creek (254 km²) and Cedar River (16,853 km²) basins located in Iowa, in the Midwest of the US.

I included in the analyses DEMs from different sources (LIDAR, NED, ASTER, and SRTM), and different resolutions generated by the aggregation of the original DEMs (from 30 to 90, 120, 150 and 180 meters). In addition, I created supplementary river networks by systematically pruning the small Horton-order streams. For this process I used as reference the network obtained from the 90 meters DEM (originally Horton order 9 for Cedar Rapids) and transformed it in networks of Horton order 8 (pruned river channels of order 1) to 5 (pruned river channels of order lower than 4).

I compared the different networks to evaluate the corresponding characterization of river network properties that are relevant to hydrological simulations. I then use the hydrological model to account for more realistic situations, including rainfall events with different intensities and spatial variability of relevant hydrological processes like rainfall-runoff transformation, soil dynamics and evaporation.

The width function and the width function maxima provide information about the flow hydrograph under idealized conditions of precipitation and water transport. The width function is related to the hydrograph at a specific point in the watershed. The networks extracted with different DEMs did not provide a good estimation of the shape of the width function. Even when I used the same dataset, but changed the resolution by aggregation, the shape of the width function changed considerably. The impact of resolution depends on the ratio between basin area and DEM pixel size. Different sources of DEM might or might not have an impact on the final shape of the function. For Clear Creek, the shapes obtained with LIDAR, NED, ASTER and SRTM DEM were very similar. In contrast width function obtained for Cedar River revealed significant differences. I conjecture that this is due to spatially correlated errors that can strongly affect the estimation of the width function. Network pruning did not cause a big impact on the general shape of the width function or in the location of the maxima of the width

function. Width functions obtained for the pruned networks became smoother than the ones obtained for the entire network (order 9).

On the other hand, river networks extracted from the different data sources provided a good estimation of the scaling properties of the maximum of the width function. This function represents a statistical measure of the network. I conclude that, even though local properties of the network (width function) are sensitive to the DEM source and resolution, the statistical properties of the network are reasonably well estimated by all the DEMs analyzed in this work. However, pruning the network significantly changed the scaling properties of the width function maxima.

I then simulate a real flood event that occurred in Iowa during the summer of 2008. This event was classified as extreme. I demonstrate the model ability on reproducing observed hydrographs and peak flow. The hydrographs demonstrate that errors in estimating the width function propagate through the hydrological model. The results of the simulations demonstrated that differences on simulated flows are more significant when I pruned the network than when I use coarse resolution DEMs, or satellite-based DEM. This demonstrates the importance of correctly represent the river network and its property on hydrological models that focus on flood.

I then performed a simulation study, applying uniformly distributed rainfall throughout the basin with varying total volume (30, 60 and 120 mm) and duration equal to 120 minutes. The goal of this synthetic study was to investigate the role of event intensity, without including spatial variability of rainfall. Peak flow statistical scaling relationships obtained using the networks extracted from remotely sensed DEMs (specially SRTM) are very similar to the one obtained by the NED DEM (reference). The pruned DEM presented peak flow scaling with similar slope, but with a different intercept. In this case peak flow was underestimated across scales. An important conclusion is that uncertainty decrease as the amount of precipitation increases. In addition, these results demonstrate the importance of correctly representing the properties

of the river network to simulate floods. If the river network were not fully represented in the model, other parameters would have to compensate for the differences.

This work accomplishes the primary goal of demonstrating an approach to evaluate the potential of satellite-based DEM for flood prediction across multiple scales using a calibration-free model. However, our results are limited to regions that present errors similar to the study area. As demonstrate by Smith and Berry (2011), expected DEM errors are dependent on the region of interest. Much work remains to be done before we can comprehensively understand the effects of DEM errors for different regions of the world.

Table IV-1. Different sources of DEM data with main characteristics and links for data repository

Data source	Spatial Resolution	Coverage	Vertical Accuracy	Source
LIDAR	1 meter	Local/regional	0.1-1.0	www.iowadnr.gov
NED	1 Arc (~30m)	US	<=2.44m	seamless.usgs.gov
SRTM	3 Arc (~90m)	Globally	<=16m	seamless.usgs.gov
ASTER	1 Arc (~30)	Globally	6-15m	http://reverb.echo.nasa.gov/reverb/

Table IV-2. List of DEM used to extract the river network of Clear Creek and Cedar River basin and main properties of the extracted network

Basin	Res. (m)	Source/ Prunning	nlinks	Hor. Ord.	Area	Rel dif area	River length	Aver. hills. area	Aver. Hills. Slope	Aver. Hills. relief
CC	5	LIDAR	14739	7	253.97	Ref.	2078	0.017	0.022	11.90
CC	10	LIDAR	11912	7	254.10	0.05	1885	0.021	0.022	12.39
CC	20	LIDAR	8963	7	254.21	0.10	1692	0.028	0.023	12.78
CC	30	LIDAR	6774	6	254.34	0.15	1522	0.038	0.022	13.19
CC	60	LIDAR	2442	6	254.28	0.12	923	0.104	0.017	15.89
CC	90	NED	1580	5	254.86	0.35	686	0.161	0.016	17.12
CC	120	NED	886	5	254.73	0.30	527	0.288	0.012	19.60
CC	180	NED	400	5	254.16	0.07	348	0.635	0.009	21.35
CC	60	ASTER	4841	6	254.65	0.27	1204	0.053	0.013	15.78
CC	90	ASTER	1117	5	256.45	0.98	608	0.230	0.010	17.20
CC	90	SRTM	1360	5	256.27	0.91	687	0.188	0.013	18.21
CC	90	NED/HO8	1015	5	254.86	0.35	471	0.251	0.012	19.68
CC	90	NED/HO7	230	4	254.86	0.35	226	1.108	0.006	27.56
CC	90	NED/HO6	41	3	254.86	0.35	117	6.216	0.003	38.77
CC	90	NED/HO5	7	2	254.86	0.35	46	36.4	0.002	50.33
CR	30	NED	305352	9	16875	Ref.	81696	0.055	0.011	7.69
CR	90	NED	78503	8	16878	0.02	40701	0.215	0.008	10.18
CR	120	NED	43648	8	16799	-0.45	31502	0.385	0.007	11.83

Table IV-2 Continued

CR	150	NED	78503	8	16878	0.02	40701	0.215	0.008	10.18
CR	180	NED	20976	7	16780	-0.56	21895	0.800	0.006	13.84
CR	30	ASTER	349999	10	19917	18.03	106395	0.057	0.007	8.80
CR	60	ASTER	199307	9	19710	16.80	77134	0.099	0.007	9.65
CR	90	ASTER	77603	8	16787	-0.52	43481	0.216	0.005	10.54
CR	90	SRTM	88386	8	16785	-0.53	47356	0.190	0.006	12.90
CR	90	NED/HO8	57535	8	16878	0.02	29956	0.293	0.006	10.92
CR	90	NED/HO7	12615	7	16878	0.02	14590	1.338	0.004	17.84
CR	90	NED/HO6	2759	6	16878	0.02	7531	6.118	0.002	26.95
CR	90	NED/HO5	597	5	16878	0.02	3972	28.27	0.001	39.25
CR	90	NED/HO4	133	4	16878	0.02	1958	126.9	0.001	57.20

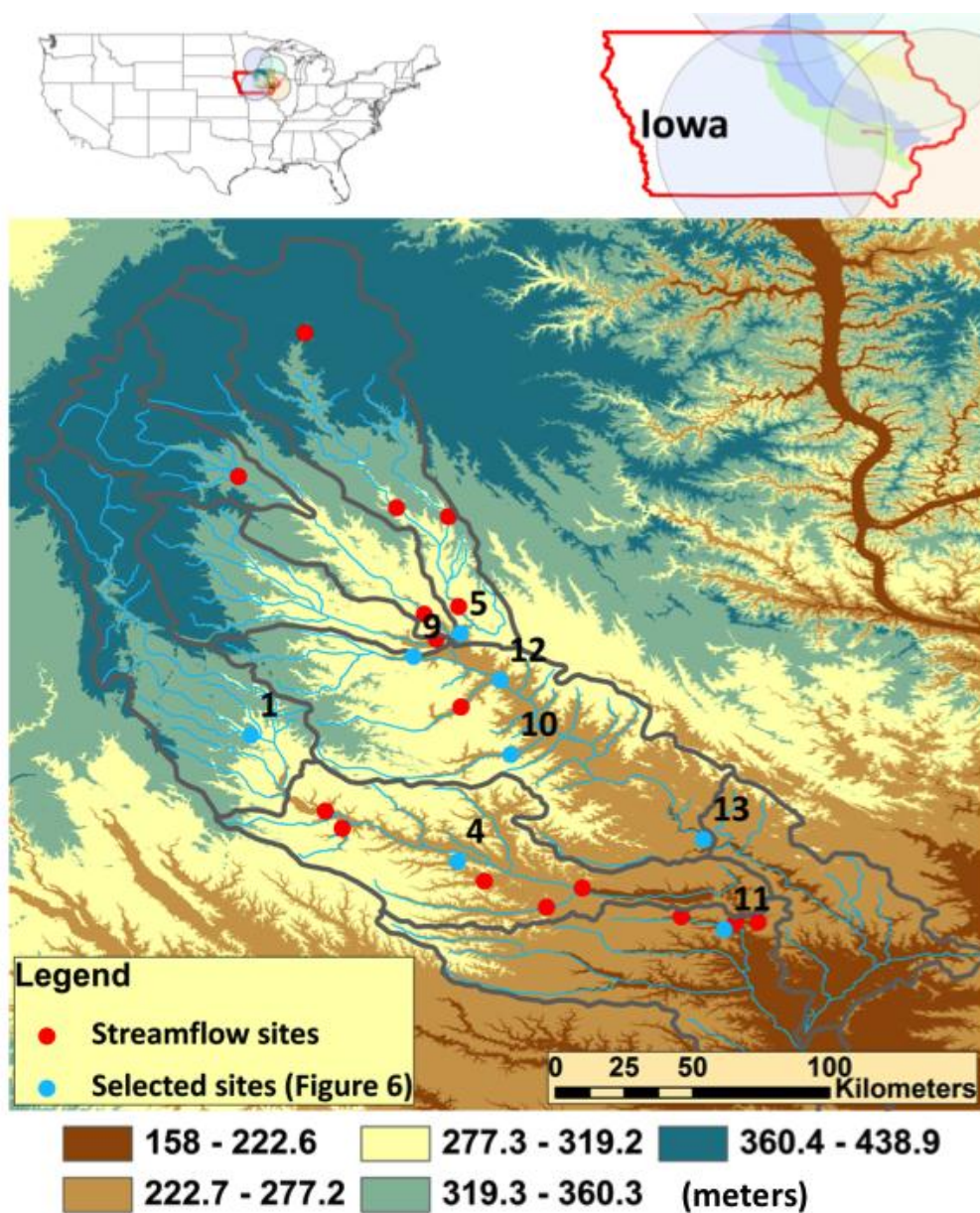


Figure IV-1. Study area. The background shows the 90 meters NED DEM. Blue (selected sites which hydrographs are shown in Figure 6) and red dots represented streamflow sites. In the state wide map I also present the location of the 4 weather radar that cover the area

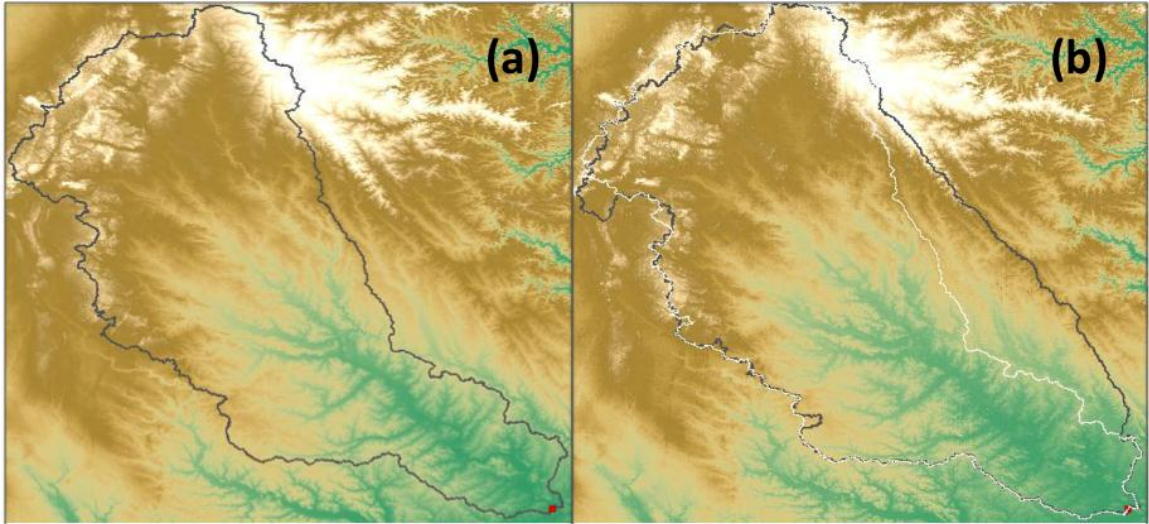


Figure IV-2. Cedar River basin boundaries delineated based on (a) NED 30 meters DEM and (b) ASTER 30 meters DEM. In Figure (b) I also include the NED 30 meters DEM delineation in white for a reference.

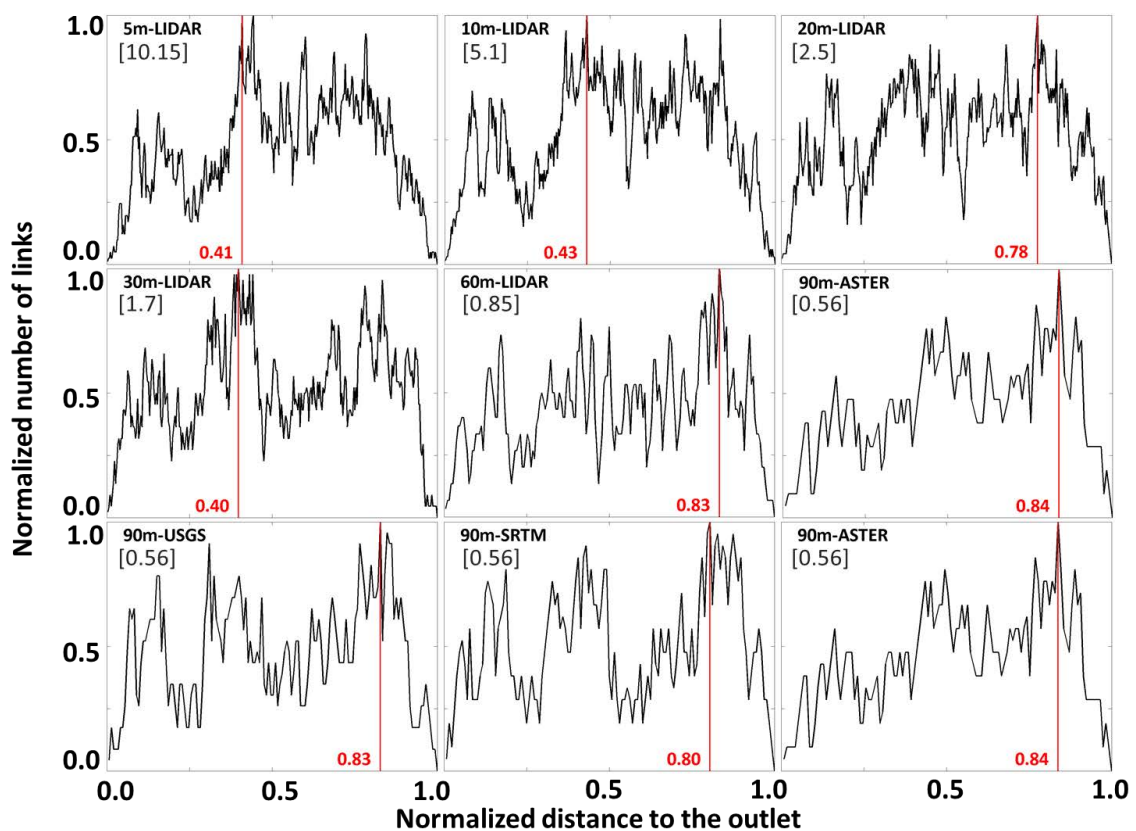


Figure IV-3. Width function for Clear Creek at Coralville extracted from different DEMs. The red line indicates the position of the maximum of the width function. The number in square brackets indicate the number of pixels in the DEM contained in the basin

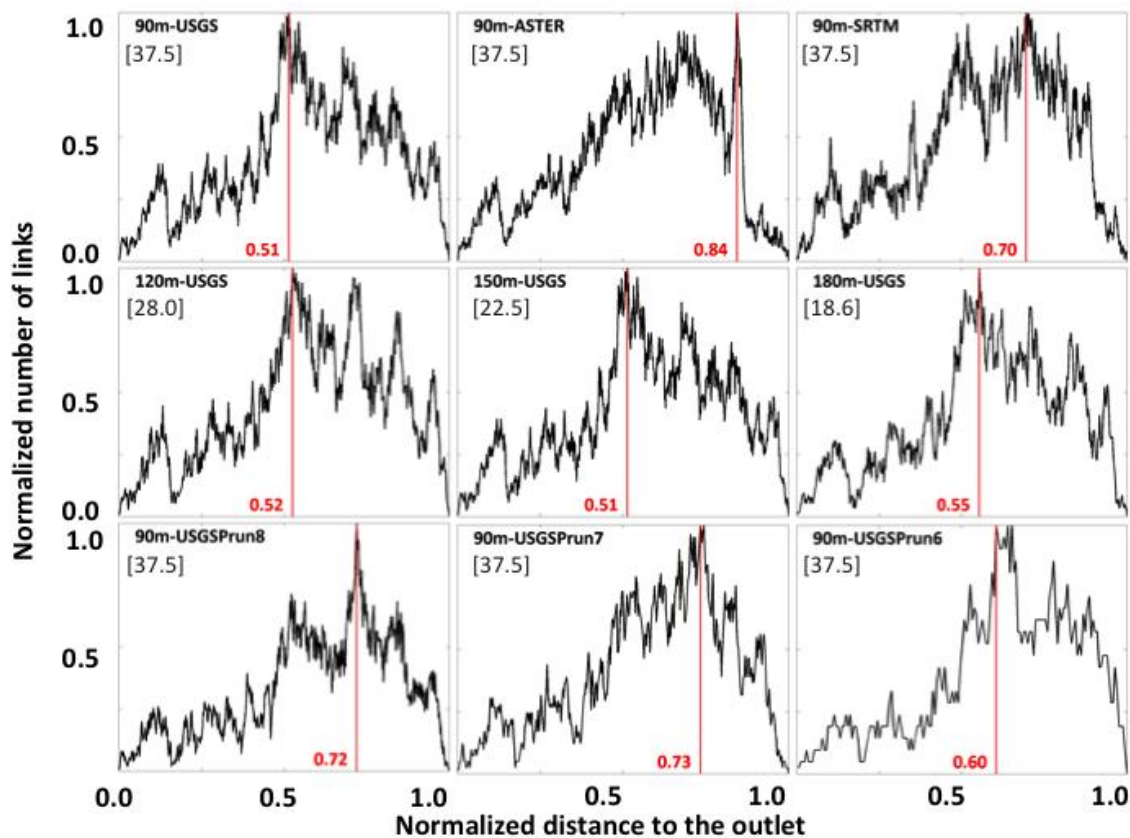


Figure IV-4. Width function for Cedar River basin at Cedar Rapids extracted from different DEMs. The red line indicates the position of the maximum of the width function. The number in square brackets indicate the number of pixels in the DEM contained in the basin

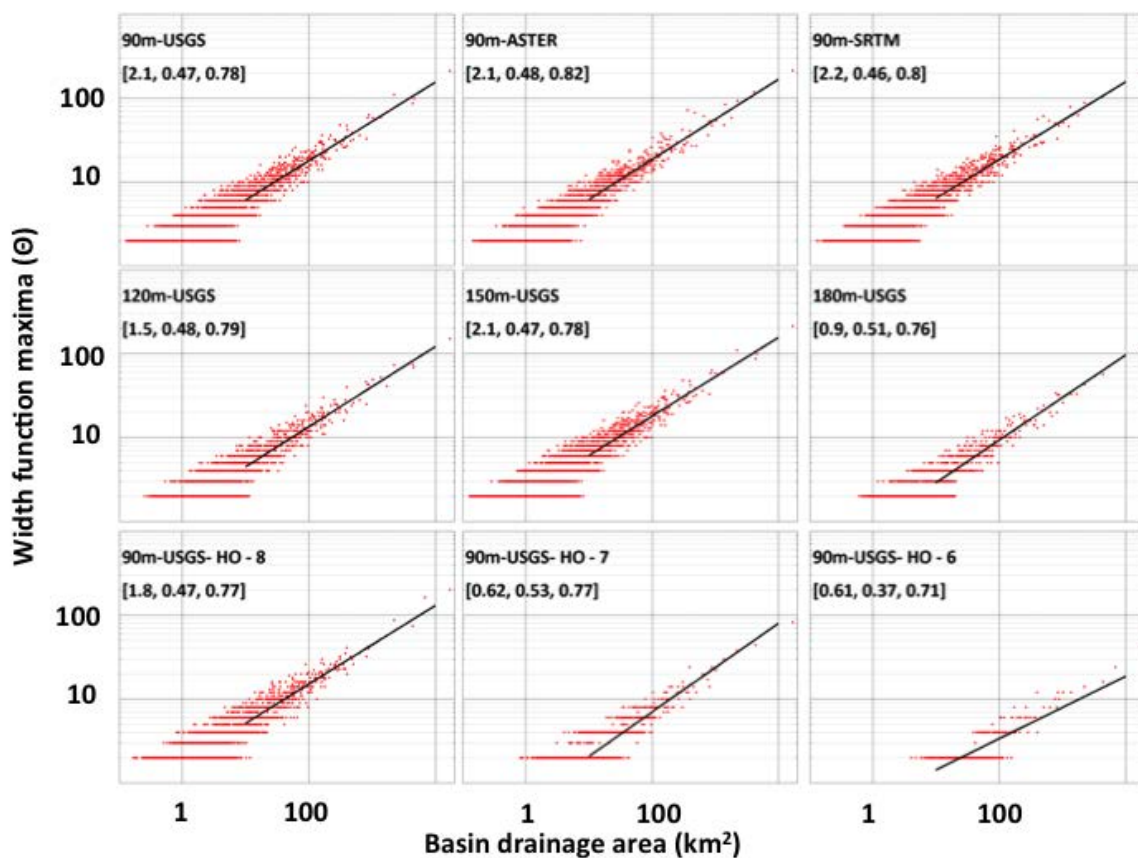


Figure IV-5. Width function maxima for Cedar River extracted from different DEMs. Statistical self-similarity of width function maxima in terms of drainage area obtained based on different DEMs for Cedar River basin. The ordinary least square regression is used to obtain the relationship between drainage area and width function maxima. The parameters of the scaling relationship are presented in the square brackets: [coefficient, exponent, correlation].

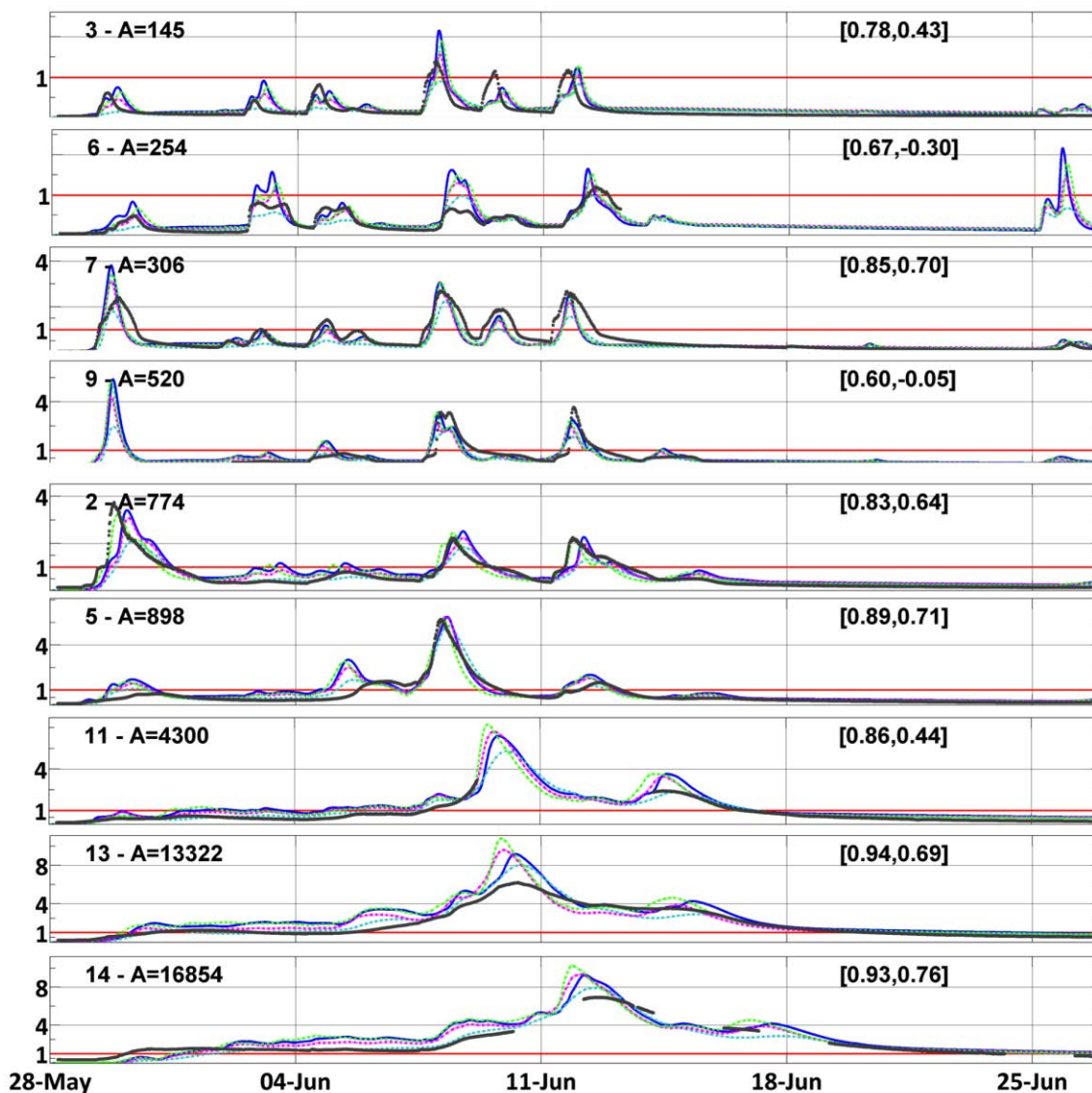


Figure IV-6. Normalized simulated and observed streamflow for sites located in the Clear Creek and Cedar River basin. Discharge was normalized by the mean annual flood. Observed values are plotted in gray, simulated using NED 90 m DEM in green, simulated with NED 180 m in magenta, and simulated with NED HO6 in cyan. Values in the left corner indicate the site number (figure 1) and drainage area, and the values in the right indicate goodness-of-fit statistics [correlation, Nash] for the simulation with 90m NED.

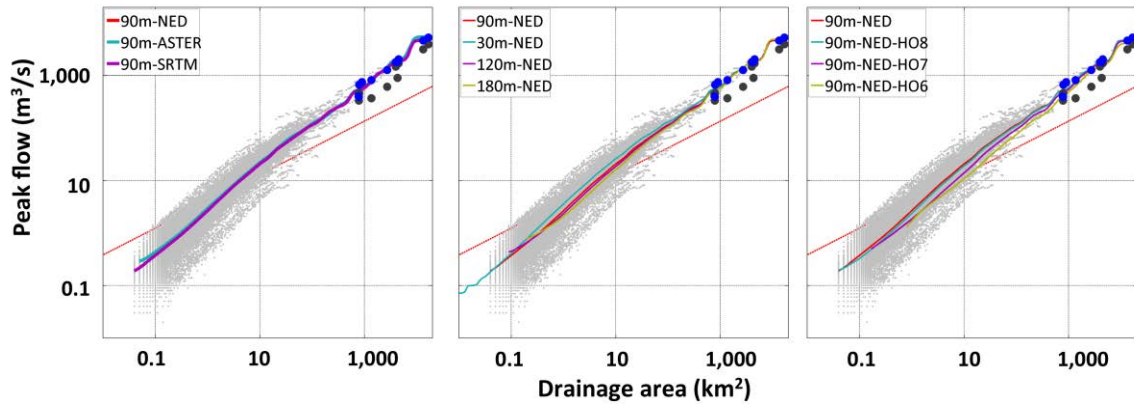


Figure IV-7. Scaling of peak flow for the 2008 Iowa flood event. Dark gray values are observed, dark blue are predicted with NED 90 m DEM. The lines were estimated based on non-parametric regression between basin drainage area and peak flows for all the links in the river network. Light gray dots represent the simulated peak flow obtained with the NED 90 m DEM. The red line correspond to the mean annual flood.

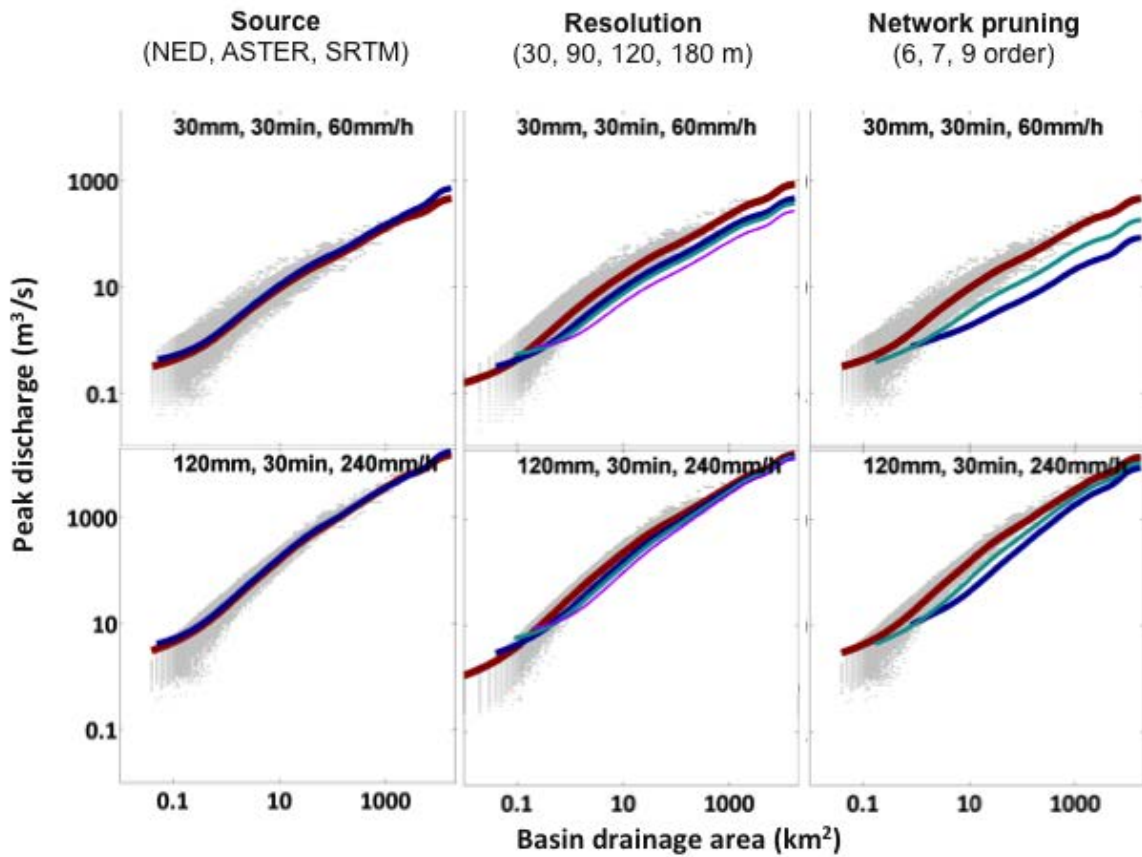


Figure IV-8. Results from the simulation based on synthetic rainfall. First and second lines present results based on accumulated rainfall equal to 30 and 120 mm, respectively. Simulation with the reference network (90 meters) is plotted in dark blue, and for this simulation the peak flow values for each link are represented by gray dots. Peak flow scaling obtained based on datasets with different source (column 1), resolution (column 2) and pruning (column 3) are presented in red, green and magenta.

CHAPTER V IMPACT OF RADAR-RAINFALL ERROR STRUCTURE ON ESTIMATED FLOOD MAGNITUDE ACROSS SCALES

Introduction

In this chapter, I explore the effects of uncertainties in radar-estimated rainfall on streamflow prediction at a range of spatial scales. Rainfall is the main input to hydrological models, and its uncertainties may strongly affect streamflow simulation (e.g. Arnaud et al., 2011). While a number of direct and indirect methods are available to estimate rainfall rate and accumulation, weather radars are the only operational instruments capable of providing rainfall estimates over large domains with a high space-time resolution. Even though the focus of this thesis is on satellite remote sensing data, radar rainfall is often used as a reference to evaluate satellite datasets. Since radar-rainfall estimates are subject to significant uncertainty (see Villarini and Krajewski, 2010 for a review), understand their uncertainty and how they propagate through hydrological models, is an essential step towards being able to use this datasets as a reference.

The main goal of this study is to evaluate the impact that radar rainfall uncertainties associated with NEXRAD-based (e.g. Fulton et al., 1998) products have on flood simulation. Our methodology can be viewed as a data-based simulation. It consists of generating ensembles of “equally probable” rainfall fields that are then propagated through a rainfall-runoff hydrological model that simulates streamflow at the outlet of a basin. This requires two main components: (1) a rainfall ensemble generator that provides maps of rainfall that mimic the actual radar-rainfall uncertainty and (2) a parsimonious hydrological model whose parameters can be prescribed a priori using physical properties of the watershed, thereby avoiding the need for parameter calibration. Our Introduction discusses the main features of two such components selected for our study.

Uncertainties in radar rainfall estimates have been studied for more than 30 years (Wilson and Brandes, 1979; Anderl et al., 1976; Cluckie and Collier, 1991), and several models have been proposed for the statistical description of radar-rainfall errors (see reviews by Villarini and Krajewski 2009; Mandapaka and Germann (2010)). Early methods of simulating synthetic radar-rainfall fields, i.e. rainfall fields that are corrupted by radar-like systematic and random errors, were based on a conceptual understanding of the uncertainties involved (Krajewski and Georgakakos, 1985). While these methods attempted to capture the main aspects of the factors that caused uncertainty, they lacked an empirically-based quantification of the deviations between the true and radar-estimated rainfall. Therefore, there was no guarantee that actual radar-rainfall uncertainty was realistically represented in studies that used these methods (Sharif et al., 2002; Sharif et al. 2004). To overcome this weakness, recent developments focus on the empirically-based modeling of radar-rainfall uncertainty (e.g. Germann et al. 2009). In this study, I adopted the radar-rainfall generator proposed by Villarini et al. (2009) which is based on the empirical radar rainfall error model by Ciach et al. (2007). This model characterizes the statistical structure of radar-rainfall errors with three components: (1) an overall multiplicative bias factor estimated using long-term accumulated radar-rainfall and gauge-rainfall values; (2) a systematic distortion function, conditioned on the radar-estimated rainfall value; and (3) a stochastic factor quantifying residual random errors. The model accounts for range dependency and for spatial and temporal correlation in errors. The generator uses a conditional simulation framework: given the estimates provided by a specific radar-rainfall estimation algorithm, the method returns rainfall fields that have the same error structure as that observed empirically for that algorithm. In our case, the algorithm is the Precipitation Processing System (Fulton et al. 1998) that converts the reflectivity data from the WSR-88D weather radars to the hourly accumulation with approximately 4 km by 4 km spatial resolution (see Ciach et al. 2007 and Villarini et al. 2009 for details). The fact that the generator is conditional on actual

radar-rainfall fields ensures relevance to practical applications and allows analysis of real events.

Once realistic radar-rainfall ensembles are generated, they are used as input to a hydrological model that simulates streamflow. Each member of the ensemble will result in a somewhat different hydrograph. Does the spread of different characteristics of the resultant hydrographs (such as the peak value or the time-to-peak) depend on the scale of the basin? How does the spread compare to the difference between the model output obtained using the “observed” field (i.e. the one on which the conditional simulation was based) and the streamflow observations? I address these questions herein.

Previous studies have demonstrated, albeit indirectly, that a fair investigation of how rainfall errors affect flood simulation requires a calibration-free hydrological model, since calibration camouflages uncertainties related to both the hydrologic model-structure and the rainfall input data uncertainty. Carpenter and Georgakakos (2004) investigated the impacts of rainfall input and rainfall-runoff model parametric uncertainty on flow simulation using a calibrated distributed hydrological model. Their results showed that errors due to model parameter estimation are of the same order of magnitude or even larger than the errors due to rainfall uncertainties. Schröter et al. (2011) used a probabilistic model to generate an ensemble of precipitation fields that were then used as input to a hydrological model. The authors calibrated the model based on the different rainfall ensembles and demonstrated that rainfall uncertainties might have a significant impact on the estimated parameter estimates. He et al. (2011) evaluated the impact of radar rainfall uncertainties on water resources modeling using a model that was calibrated based on rain gauge data. According to these authors, if radar precipitation were used to calibrate the model, sensitivity of simulated stream discharge to rainfall input would have changed. Fu et al. (2011) investigated the impact of precipitation spatial resolution on the hydrological response of an integrated distributed water resources model and concluded that, “the effects of precipitation input are so dominant that it could potentially impact the

estimates of model parameters when the hydrological model is calibrated.” The study further concluded that model parameters estimated by calibration would be biased in order to compensate for errors introduced by low-resolution precipitation. These studies demonstrate the need for a simulation framework that isolates uncertainties due to parameter estimation and input.

Such a framework requires that the hydrologic model have a certain level of skill merely due to its structure and ability to mimic the dominant processes of hydrologic response to rainfall. The numerical values of the required coefficients (parameters) should be “observable” from the characteristics of the basin, including topography, land cover, land use, soils, etc. The level of skill should be such that given a more accurate input, the model should provide better output. This is not always the case with calibrated models that adjust their parameter values to compensate for uncertainties in the input.

In this study, I used the fully distributed, physically-based, and calibration-free hydrological model developed in this thesis that allows the isolation of errors due to model structure and rainfall input. As discussed in the introduction of this thesis, the model provides an impartial evaluation of how rainfall errors propagate through hydrological models and affect flood prediction across a large range of scales. Calibration is avoided with the use of parameters that are directly linked to the physical properties of the watershed (e.g. soil water storage, hillslope shape, and channel flow velocity). The fine decomposition of the terrain into hillslopes and links results in a realistic representation of the stream and river drainage network, which allows us to apply model equations that represent processes close to the scales as they occur in nature (Mantilla and Gupta, 2005). Runoff is generated at hillslopes and water is transported via the drainage network of connected links. Model equations at the hillslope-link scale are based on mass and momentum conservation principles.

Previous studies have also demonstrated that flow simulation uncertainty is strongly dependent on catchment scale, with uncertainty decreasing as basin scale

increases (Carpenter, 2006). This is expected since the river network filters out small-scale variability and uncertainties (Mandapaka et al., 2009). In previous studies (Carpenter and Georgakakos, 2004; He et al. 2011) this conclusion was reached based on the analysis of mid-size basins, including a limited number of points in the watershed, for which streamflow observations were available and used to calibrate the model. In order to be able to characterize the scales for which radar data provide good information for flood prediction, a more comprehensive study involving a large number of sites covering a large range of scales (from few to thousands of square kilometers) is required. The basin decomposition method used in this study provides flow simulation for every link in the basin, which allows us to investigate error scale dependency using a large number of sites (more than 70,000) covering a wide range of spatial scales, from hillslope (~ 0.1 km²) to large watersheds ($\sim 16,000$ km²).

The model version used in this chapter is described in section 6.2. In section 6.3, I present methodological aspects of this work, focusing on the rainfall generator. Section 6.4 includes the main results of this study, including: (1) the validation of the hydrological model across multiple scales (model version 5 with constant soil initial condition), (2) the rainfall error scenarios and statistics for the generated rainfall ensembles, and (3) flow sensitivity to different rainfall error scenarios. The last section presents the main conclusions of this work.

Study area and model version

The study is carried out for the Iowa and the Cedar River basins, located almost entirely in the state of Iowa. The total drainage area is 7,234 km² for the Iowa River (in Marengo) and 16,853 km² for the Cedar River (in Cedar Rapids).

In this chapter, I used the most complete version of the hydrological model (model 5 in Table 2.1), with constant soil initial condition across the entire basin area. At this point of development, I have not included the NLDAS dataset to estimate soil initial

conditions that are variable in space. As the number of simulations performed in this study is large and this component is not expected to change the general conclusions of this study, I opt to not re-run the simulations. The remaining components of the model are the same ones adopted and described in Chapter 3. Model input includes rainfall and potential evapotranspiration (PET). For rainfall, I used the Stage IV rainfall product, which represents hourly accumulation given on an approximately 4 km by 4 km grid. Stage IV products are provided by the National Weather Service. Fulton et al. (1998) describe the methods and data used to produce the different multi-sensor precipitation products provided by the NWS. Stage IV is a post-processed product based on the merging of radar and rain gauge data in particular to remove the mean-field bias in the radar-only estimates. Hereafter, I refer to these overall bias corrected fields as reference rainfall. I used NEXRAD's Stage IV products as a reference in this study to compare how different rainfall error sources and scenarios affect hydrological prediction across scales.

For PET, I use the product produced by the North American Regional Reanalysis - NLDAS-2 with 1 hour resolution in time and 0.125° (~13 km) resolution in space. PET is used to estimate the actual evaporation from the surface and from the unsaturated and saturated layers of the soil. Dingman (2002) defines PET as "the rate at which evapotranspiration would occur from a large area completely and uniformly covered with growing vegetation which has access to an unlimited supply of soil water and without advection or heat-storage effect." Using PET to calculate actual evaporation presumes that the only factor limiting evaporation is water availability. No limitations are imposed on the evaporation of water from the surface storage.

I used the National Elevation Dataset (NED) with 90 m resolution to extract the stream and river network. Our procedure (Mantilla and Gupta, 2005) resulted in 78,503 hillslopes for the Cedar River basin with an average hillslope area of 0.20 km^2 and 44,527 hillslopes for the Iowa River basin with an average hillslope area of 0.16 km^2 . I

used the USGS hydraulic measurements to estimate the parameters of hydraulic geometry equations based on the formulation proposed by Dodov (2004), Paik (2004), and Mantilla (2007). To estimate soil hydraulic properties and water storage availability, I used the soil dataset SURGO. To estimate the roughness coefficient (Manning's) for the overland water transport equations, I used the high-resolution national land cover dataset (Homer et al., 2007).

Finally, I used two datasets to evaluate the model's performance. First, I used the USGS streamflow data for a total of 24 sites to compare observed and simulated discharge. It is important to point out that I did not use this information to calibrate the model's parameters; therefore, the comparison constitutes an independent evaluation of the model's performance. I also compared the streamflow simulations from CUENCAS with those from the Sacramento Soil Moisture Accounting (SAC-SMA) model (Burnash, 1995), which is used by the National Weather Service as the main component of their flood forecasting system (Welles et al., 2007).

Methodology

I performed a data-driven simulation study to investigate the effects of uncertainty in the radar-rainfall input on our hydrologic distributed model. I selected a month-long period with rainfall and streamflow data immediately preceding the 2008 flood in Iowa. Our flood prediction model is a physically-based rainfall-runoff model that simulates response to rainfall forcing at a wide range of scales, with the smallest being a hillslope scale. The geometry of the hillslope elements of the model is irregular, but each hillslope is connected to a channel link whose location is determined by analysis of the high-resolution topography data, as described above. The model uses the information on land cover and land use, soil types, and topography based on readily available data that are mapped to the scale of the hillslopes. The function of the hillslopes is to partition the rainfall input into surface runoff, infiltration, and evapotranspiration. This is

accomplished by using empirically based parameterizations of the relevant processes documented in the literature. I do not perform local adjustments (calibration) of the coefficients to force better agreement with the observed streamflow. Surface runoff and subsurface quick flow feed the channels, and the water is transported down the drainage network. The discharge is aggregated as the water flows to higher order streams. The aggregated discharge is attenuated by the selected water velocity model. The model has a power law functional form with the velocity dependent on the magnitude of the discharge and the upstream drainage area. The coefficients of the velocity model are calibrated by using the USGS collected and published discharge and water velocity data. The fact that the model parameters are not calibrated to fit the discharge data implies that the uncertainties in the input are independent of the errors in the predicted (simulated) discharge. This also means that I have avoided favoring the scales for which discharge observations are available. The model is, in principle, suitable for prediction at any scale provided that the velocity model (channel transport) is valid.

I evaluated the model performance prior to performing our simulation experiment. Clearly, if the model were not accurate, there would be little point in using it to study uncertainty in the input data. On the other hand, if the model were best-fit to a particular input (rainfall) product, it would, by construction, mask the effect of errors in a competing input product. For a calibrated model, it would be possible to perform better when forced by an inferior input product.

Once the model was ready, I forced it with the radar-rainfall input generated by a recently developed error model of the NEXRAD-based hourly rainfall maps (Ciach et al., 2007; Villarini and Krajewski, 2009b). The model is based on a large sample of empirical data and has a flexible structure that allows one to study the effects of different error components, particularly the effects of systematic and random components. Using the error model, I generated multiple realizations (equally probable) of radar-rainfall

fields that were conditional on the observed (reference) field. Each of the generated realizations has the same statistical error structure as the reference field.

I applied the generated ensemble of the radar-rainfall input to the hydrologic rainfall-runoff model and thus simulated multiple realizations of the discharge. I then calculated several performance measures to evaluate the spread of the obtained discharge values and compared it with the discrepancy (errors) between the discharge obtained using the reference input and the observed discharge. I calculated these measures at a range of spatial scales from very small to fairly large (~20,000 km²). I then repeated the above ensemble simulation for a different scenario of the radar-rainfall model.

This work is composed of two main components: (1) the distributed physically based hydrological model and (2) the radar-rainfall error model and the ensemble generator used to produce equally probable rainfall fields based on the reference rainfall (Stage IV) and the radar-rainfall error structure scenario. The hydrological model was described in the Chapter 2 of this thesis. In the next section I will focus on describing the second component of this work.

Radar rainfall error model and ensemble generator

I employed the radar rainfall error generator proposed by Villarini et al. (2009b) to produce ensembles of equally probable rainfall fields. The method uses an empirically derived error model to generate synthetic probable rainfall fields conditioned on a given rainfall map. The uncertainty model adopted in the generator was proposed by Ciach et al. (2007). In this model, the true pixel-scale average rainfall $R_A(x,y)$ at a location (x,y) within the basin is expressed as the product of a deterministic component and a random component, both conditioned on reference rainfall, $R_R(x,y)$,

$$R_A = h(R_R) \cdot \varepsilon(R_R) \quad \text{Equation V-1}$$

The deterministic distortion function, $h(R_R)$, accounts for the conditional (i.e. on rainfall magnitude) biases, whereas the stochastic factor, $\varepsilon(R_R)$, describes the random deviations from the true but unknown rainfall. Note that both components are a function of the reference rainfall rate R_R . This feature has important implications that will be revealed later. The deterministic distortion function is approximated by the two-parameter power law

$$h(R_R) = a \cdot [B_0 \cdot R_R]^b \quad \text{Equation V-2}$$

and the random component is approximated by a Gaussian distribution with the mean of 1 and its standard deviation modeled as a rapidly decreasing hyperbolic function of the reference rainfall.

$$\sigma [R_R(x, y)] = c + d \cdot [B_0 \cdot R_R(x, y)]^e \quad \text{Equation V-3}$$

In equations (2) and (3), B_0 is the overall (time integrated) bias, a and b are the parameters of the deterministic distortion function; and c , d , and e are the parameters of the random component. The parameters were estimated by Ciach et al. (2007) using six-years of level-II hourly rainfall data from the Oklahoma City WSR-88D radar site (KTLX) and rain gauge records from the Oklahoma Mesonet (Brock et al., 1995) and the Agricultural Research Service (ARS) Micronet. The parameters vary with season and distance from the radar site. In addition, the authors used the radar- and gauge-rainfall data to estimate the spatial and temporal correlation of random errors. Villarini and Krajewski (2009a) extended this work by proposing parametric functions to describe the correlations in the random component as

$$\rho(\Delta s) = c_1 \exp \left[-\frac{x}{c_2} \right]^{c_3} \quad \text{Equation V-4}$$

where c_1 is the nugget effect that characterizes the small-scale variability of the process and/or measurement errors, c_2 represents the correlation length, c_3 is the shape parameter that controls the shape of the fitted correlation function at the origin, and x is the

separation distance. Although parametric forms exist for the temporal correlation structure of random errors, they were not incorporated into the ensemble rainfall generator for the reasons described by Villarini and Krajewski (2009a).

The generation of ensemble radar-rainfall fields can be summarized as follows: (1) the reference rainfall field was corrected for conditional bias using equation (2); (2) an ensemble of spatially correlated Gaussian fields with a unit mean and standard deviation conditional on the reference rainfall field was then generated using the Cholesky decomposition method; and (3) the correlated Gaussian fields were then multiplied with the bias corrected reference field from step (1) to obtain an ensemble of equally probable rainfall fields. It should be noted that in the random error fields (step 2), any pixels with negative values are set to zero to avoid unrealistic rainfall values in step 3. More details about the radar error model and the rainfall generator were presented by Ciach et al. (2007) and Villarini and Krajewski (2009a).

In this work, I use as “reference” the Stage IV rainfall map products provided by the National Weather Service. Since, by construction, the radar-rainfall error model is specific to a radar-rainfall product, this raises the issue of whether the parameter values are appropriate for this product. Since the Stage IV dataset is corrected to match rain gauge accumulations, I considered it to be free of overall bias; therefore, I set B_0 to 1.0. I can also argue that the overall character of the microphysical rainfall processes in Iowa, especially in the summer convective storm, is similar to that in Oklahoma. In support of this argument, I cite a study by Seo and Krajewski (2010) which shows a similar behavior of the random error dependence on rainfall magnitude. Another potential issue with the transferability of the Ciach et al., (2007) results is the fact that their model is valid for a single radar whereas Stage IV is a multi-radar product. While, in principle, combining data from multiple radars reduces the random radar error, in our case, all radars that cover the Cedar and Iowa River basins do this at a far range, where errors are significant. To partially mitigate the problem of strict applicability of the radar-rainfall model to our

study area, I define and consider seven different scenarios of radar rainfall error and generate 50 ensembles for each one.

Results and Discussion

Radar error structure scenarios

Table 2 presents the rainfall error scenarios that resulted from different conditions of radar-rainfall error structure, which were conceptualized to allow the independent evaluation of the impacts of different aspects of the deterministic and random components of the rainfall error structure. All the parameters were empirically estimated by Villarini and Krajewski (2009a) and Ciach et al. (2007) for Oklahoma using a highly-dense rain gauge network. For this study, I systematically altered the original Oklahoma parameter values to obtain different error structure scenarios. I considered a total of seven rainfall error scenarios in this study (Table 2). As mentioned in section 3.1, the rainfall ensemble is obtained by imposing Gaussian random error fields on the bias corrected reference rainfall fields. For each scenario, I used the generator to produce an ensemble of 50 equally probable rainfall fields.

In scenarios 1 through 4, I focus only on the structure of the random errors. That is, I set the parameters a and b that control the deterministic distortion (conditional bias correction) to 1 and varied the parameters that control the standard deviation and spatial correlation structure of the random errors (Table 2). In scenario 1, the standard deviation of the random errors is equal to 0.2 (which is small), and the fields are characterized by an exponential spatial correlation structure. The parameters of the correlation function are the same as those reported by Villarini and Krajewski (2009a). Scenario 2 consists of random errors whose standard deviation is a function of the reference rain value, but the errors are not correlated in space. Scenario 3 is characterized by random errors that are a function of reference rain and are correlated in space. Scenario 4 contains the same error standard deviation as scenario 3 but with a longer correlation distance in space.

Scenarios 5 and 6 present the same random error structure as scenario 3 but also contain deterministic error that increases as reference rain rate increases. For scenario 5, radar overestimates the real rain, and for scenario 6, radar underestimates the rain. Scenario 7 uses the parameters empirically estimated for the Oklahoma radar (Ciach et al., 2007).

Figure V-1 shows the time series of the accumulated mean areal precipitation (AMAP) for all ensemble members and scenarios for the 2008 event, along with the reference AMAP (black line) and the median of the ensemble (dotted line). Different uncertainty scenarios translate into a different spread of the ensemble AMAP. Plots 2(a) to 2(g) are for the Cedar River basin and scenarios 1 to 7. Plots (h) and (i) are for the Iowa River basin, scenarios 2 and 5.

For the scenarios with no deterministic error, I would expect the median of the AMAP of the ensemble to be equal to that of reference rainfall. However, this is not always the case due to: (1) the effect of the non-negative rainfall condition imposed on the random error fields; (2) the interplay between the spatial correlation scale of the random error and the basin scale and shape; and (3) the skewness of the rainfall distribution combined with the non-linear character of the error model since, for some of the scenarios, random error is a non-linear function of the rain rate. These effects can be visualized in Figure 3-2 (a) that presents a schematic representation of the transformations that are made to the measured rainfall field to generate rainfall ensembles. Figure 3-2 (b) presents the deterministic distortion function for all scenarios as a function of rain rate. We can see that the distortion for the empirical scenario is smaller than the one defined for scenarios 6, that underestimate rainfall, and scenario 5, that overestimate rainfall. Scenarios 1, 2, 3 and 4 are free of deterministic distortion. Figure 3-2 (c) presents the standard deviation of the random error as a function of the observed rain rate. In this case random error decreases with rain rate. The spatial correlation of the random component is presented in Figure 3-2 (d). Scenario 4 presents the highest correlation in space.

For scenario 1, the spread in AMAP is very low since random errors are unconditional and are characterized by a small standard deviation of 0.2. Scenario 2 has larger, and more realistic, random errors that are conditional on the rain rates. However, the spread in the ensemble is still comparable to that of scenario 1 because of the lack of spatial correlation in the errors. The shift between the AMAP of the ensemble and that of reference rainfall is due to the reasons described in the previous paragraph (non-negative error fields and non-linear interaction of the error model with the rain rates). For scenarios 3 and 4, the introduction of correlation in space increases the scatter in AMAP due to the persistence in the error signal over a certain domain. The difference in the range of AMAP for scenarios 3 and 4 is very small. Scenarios 5 and 6 contain a deterministic component in addition to the random errors. For scenario 5, radar overestimates rainfall values, but for scenario 6, radar underestimates rainfall values. The same random error structure is applied for both scenarios; however, the spread for scenario 6 is larger than the spread for scenario 5. I also present two scenarios, 2 and 5, for the Iowa River basin, for which similar patterns are observed.

While it is probable that none of the scenarios I have considered represents the reality, collectively they allow us to develop a better understanding of the radar-rainfall uncertainty on basin-scale rainfall. The results demonstrate that the rainfall generator employed in this work is a useful tool to develop rainfall uncertainty scenarios for the hydrologic error propagation studies. The generated rainfall fields will allow us to map rainfall uncertainty to the response of the hydrological system.

Validation of hydrological simulations

Before I used our hydrologic model to study the effects of uncertainty propagation of the rainfall input, I needed to establish that the model accurately represents the hydrologic response to heavy rainfall. I did this by evaluating the model's performance using observed streamflow data for 24 sites in the Iowa area and by comparing the

simulated streamflow with that generated by a semi-distributed version of the SAC-SMA. Since 1960, the Sacramento soil moisture accounting model (Burnash, 1973) has been used by most of the NWS River Forecast Centers as the main flood prediction model (Welles et al., 2007). The model is classified as deterministic, continuous, and non-linear. SAC-SMA contains parameters that describe the rainfall-runoff and evaporation dynamics as well as parameters that describe channel flow transport between two sub-basins (Ajami et al., 2004). In the semi-distributed version, one set of parameters is calibrated for each sub-basin using 6-hour mean areal precipitation (MAP) products produced by the National Weather Service (Johnson et al., 1999). The model uses fourteen parameters to describe the rainfall-runoff processes and two parameters to describe channel routing, if the kinematic wave method is used.

In Table 3, I present goodness-of-fit statistics for both models. I begin with the mean streamflow values based on observations, CUENCAS simulations, and SAC-SMA simulations. I then present the correlation coefficient and the Nash-Sutcliffe coefficient for both models (Nash and Sutcliffe, 1970). I present these statistics since they are commonly used to evaluate the results of hydrological models (Krause et al., 2005). However, they do not provide a comprehensive overview of how well simulated values fit observed data. Based on these evaluation statistics, I conclude that both models represent a very similar level of performance.

Figure V-3 and Figure V-4 present the observed and simulated hydrographs produced by CUENCAS and SAC-SMA for all streamflow sites in the Cedar River and Iowa River basins, respectively. I normalized the hydrographs by the mean annual flood that is used as an approximation for the bankfull discharge (red line) (Leopold et al. 1964). The mean annual flood was calculated as a function of drainage area using USGS historical data for the Cedar and Iowa Rivers. Values above this line approximate flow levels above the riverbank. The area of each site is shown in the left corner, while the statistics and the site number (refer to Figure I-1) are shown in the right corner. In the

plots, dark blue lines represent the observed hydrographs, black lines show discharge simulated by CUENCAS using the reference rainfall, light blue lines show the hydrographs simulated by SAC-SMA, and red lines indicate mean annual flood. Differences between observed and predicted streamflow are due to uncertainties in the input, output, and model formulation and parameterization.

If rainfall input and observed streamflow are used to calibrate model parameters, uncertainties due to the different factors cannot be isolated. Since I did not calibrate our model parameters, I will demonstrate in this study that, depending on the basin area and on the error structure of the radar rainfall data, uncertainties due to input uncertainty can be as large as the discrepancies between simulated and observed streamflow.

As mentioned before, I use the Stage IV rainfall dataset provided by the NWS as input to the hydrological model. In another study, we demonstrate the existence of an undesirable feature in this dataset that arises from the merging of radars with different calibration offsets. The feature (due to radar miscalibration) is located at the equidistance zone between the KDMX and KDVN radars. We corrected this dataset using the results presented by Seo et al. (2012) and demonstrate the improvements in the hydrological prediction for the sites located in the affected area of the Cedar River basin (CR-10, 9, and 11).

It is important to point out that CUENCAS was not calibrated to fit the hydrographs at specific locations. In this sense, sometimes the model is able to reproduce the peak of the event rather well but is not able to correctly reproduce the time to peak (e.g. CR-7). In such cases, the performance statistics are reduced dramatically. When the model is calibrated to fit a specific hydrograph, the timing of the response is probably the most important criterion since it has a significant impact on the commonly used mean-square error objective functions. Another important aspect is the presence of uncertainties in the streamflow observations. Many of the streamflow time series presented long periods of missing data (e.g. CR-8, CR-2, CR-5). To be able to estimate

the statistics using observed time series containing missing values, I adopted a simple linear interpolation procedure to fill the gaps in the time series.

Values of the performance statistics are higher for the Cedar Rapids basin for both models. The lower values for the Iowa River basin are probably due to a large number of sites for small drainage areas and a large number of sites that experienced the backwater effect, which is not accounted for in the formulation of channel dynamics of both hydrological models. Another reason could be due to the spatially correlated errors on the input data that have a large effect over small basins. Better performance is expected for large basins since small-scale error and variability are averaged out by the effect of the river network. In general, I deem the results of the non-calibrated model acceptable in the context of this work.

Figure V-5 presents the observed and simulated peak flows versus drainage area for the Cedar River 3(a) and the Iowa River 3(b). Throughout this work, the simulated peak flow values obtained with Stage IV data will be referred to as reference value (Q_p^{ref}). The line in orange represents the mean annual flood, and the observed values are above this line for all sites. The line in red corresponds to a nonparametric regression between peak flow and drainage area. The simulated and observed peak flow values follow the same scaling patterns. Streamflow observations present many missing data, especially during the time of highest flow (e.g. Figure V-4, sites CR3 and CR8). Therefore, the direct comparison of the observed and simulated results based just on the peak flow values can be misleading. Unfortunately, there are no observed data for small scale sites to confirm the validity of the scaling relationships for small areas. The site with the smallest area is located in the Iowa River (IR-1 with approximately 22 km² of drainage area).

Analysis of error propagation

The hydrological model is executed using each rainfall error scenario listed in Table 2 as input to obtain an ensemble of streamflow hydrographs. I evaluate the rainfall error effects on hydrological prediction by comparing the ensemble of simulated hydrographs and the corresponding peak flows with the streamflows obtained using the reference rainfall. I also evaluate peak flow variability for each rainfall scenario ensemble and how it changes with basin drainage area.

Comparisons with the USGS streamflow observations

I propagate the resulting ensemble rainfall maps through the hydrological model to produce ensembles of flood hydrographs. Results obtained for the Iowa River and Cedar River basins are presented in Figure V-6 and Figure V-7, respectively. Both figures present results for error rainfall scenarios 2 (a) and 5 (b). Scenario 2 consists of random errors not correlated in space, and scenario 5 presents random errors correlated in space and deterministic bias. For the sake of simplicity and brevity, I opted to include 4 hydrographs for Iowa River and 6 hydrographs for Cedar River out of the total of 24 simulated hydrographs. The selected hydrographs cover a wide spectrum of basin areas and are spread around the study area.

Figure V-6 and Figure V-7 use the same symbol convention as Figure V-3 and 4, with the addition of gray shadows that represent the range of values simulated by CUENCAS using the 50 ensembles of rainfall. The range of values represented by the gray shadowed region represents uncertainty in streamflow simulation as a result of uncertainty in rainfall.

For the Cedar River basin in Cedar Rapids, the hydrograph ensemble reflects the findings of the evaluation in terms of AMAP for scenario 2: small spread and a bias between the median of the ensemble and the reference dataset. For scenario 5, which considers the radar overestimate rainfall, peaks were reduced across scales and some

spread is still observed at the scale of the Cedar River basin. Comparing both scenarios, we can see that the spread for the Cedar River is much smaller for scenario 2 than for scenario 5. However, when we look at the small-scale sites, the spread for scenario 2 is larger. This demonstrates that streamflow uncertainty scale dependency changes for different characteristics of rainfall error structure.

In Figure V-8, I present the relative difference between the ensemble and the reference areal mean accumulated rainfall (plots a and b) and maximum rainfall intensity (plots c and d), for scenarios 2 and 5, for all the USGS sites in the Iowa and Cedar River basins. The spread for areal mean accumulated rainfall is small since in this case the data was aggregation in space and time, and random errors canceled out. On the other hand, we observe significant variability for the maximum rainfall intensity for each watershed. Due to the purely random character of scenario 2, variability in areal mean accumulated rainfall and maximum rainfall intensity decreases with drainage area. Rainfall variability also decreases with drainage area for scenario 5, but some spread is still observed for the largest basin due to the spatial correlation of the random error. These errors are propagated through the hydrological model. In Figure V-9's plots (e) and (f), I present the relative difference between simulated peak flow using the reference rainfall (black dots) and the ensemble rainfall (gray dots) and observed peak flow for the same scenarios. The variability observed in simulated peak flow reflects the one observed for maximum rainfall intensity.

Figure V-9 presents the difference between the simulated peak flow and observed peak flow. For some of the basins, the difference is around 50%. It is important to point out that a considerable part of these differences might be the result of inconsistencies in the series of observed streamflow. Due to the extreme magnitude of the event, many of these stream gauges malfunctioned or even stopped working during the periods of large flow. Another source of error in streamflow is due to the extrapolation of the rating

curves. Some of the sites experienced water levels much higher than the maximum water levels used to determine the rating curve.

The results presented in this section demonstrate the dependence of the error on basin area. However, due to the limited number of points, it is difficult to understand how errors change with scale for different scenarios. In the next section, I present a more comprehensive analysis involving results for all links in the river network and a relative measure of the dispersion of the flow ensemble.

Peak flow structure in the river network

In this section, I evaluate the range of simulated peak flow for all the links in the river network using a normalized measure of peak flow spread. For each link in the watershed, I calculate the difference between the 95th (Q_{p95}) and 5th (Q_{p5}) percentiles of the ensemble flow values normalized by the median (Q_{p50}) ensemble flow value:

$$\Delta Q_p = \frac{Q_{p95} - Q_{p5}}{Q_{p50}} \quad \text{Equation V-5}$$

I also calculated the normalized difference between the median ensemble value and the reference peak discharge (Q_p^{ref}):

$$Q_p^* = \frac{Q_{p50} - Q_p^{ref}}{Q_p^{ref}} \quad \text{Equation V-6}$$

These results are presented in Figure V-9 for all the rainfall error scenarios and basin scales ranging from hillslopes ($<0.1 \text{ km}^2$) to the total basin area ($\sim 16,000 \text{ km}^2$). ΔQ_p represents the extension of the streamflow uncertainty band at the time of peak for each site. Bias in the average AMAP does not affect this variable, since it is independent of the reference. Values equal to one mean that the error band extension is as large as the median of the peak flow simulation. Values equal to zero mean that rainfall data is “error-free” or that errors do not affect streamflow prediction for that specific site. I

added a non-parametric regression line to the plots in order to demonstrate the tendency of these values to decrease with basin area.

For scenarios 1 and 2, values of ΔQ_p tend to zero as the basin area increases. This means that as the basin area increases, small-scale uncertainties are filtered out by the aggregation effect of the river network. This happens when the random errors are small or not correlated in space. For random errors that are spatially correlated (SC-3), the network was able to filter part of the uncertainty. In this case, the error bar for the outlet of the basin has an extension of approximately 0.4 times the median of the simulated peak flows.

Higher spatial correlation (SC-4) caused a slight increase in the error bar for the outlet (~ 0.45). These demonstrate that the spatial correlation of precipitation errors reduced the rate at which errors decreased with drainage area, as has been demonstrated by Nijssen (2004). For the scenarios with deterministic error, the extension of the error bar does not change significantly compared to SC-3 that presents the same random error. In this case, the error bar just shifts up or down, depending on whether radar overestimates (SC-5) or underestimates (SC-6) rainfall.

For small scales, ΔQ_p presents a high range of values. For basin areas close to the hillslope area, it can go from 0.4 to more than 3 for SC-2. This means that small-scale basins can go from a situation of receiving almost no water to receiving a large amount of water. The uncertainty for small scale basins will depend on the rainfall characteristics for the specific area, the rainfall error structure, and the properties of the basin.

The Q_p^* (green dots in Figure 6) represents the bias in the ensemble rainfall field compared to the reference. Scenarios without deterministic error should not present any bias for large basin areas, but, due to the reasons previously described, the rainfall ensemble generator introduces bias into mean rainfall for some of the cases. For SC-5, radar overestimates rain rates, and this is reflected in a negative value of Q_p^* ($Q_{p50} < Q_p^{ref}$). For this scenario, the random component of the error might overcome the

deterministic component, and Q_p^* is positive or close to zero in these cases. For SC-6, radar underestimates rainfall, and the effect of random error is not so important since Q_{p50} is always larger than Q_p^{ref} . The last two plots of Figure 6 show results for scenarios 2 and 5 for the Iowa River basin. The same conclusions hold for this basin.

For scenario 7, which is closest to the error model reported by Villarini and Krajewski (2009a), parameters were empirically estimated based on Oklahoma data (SC-7) and radar overestimates rainfall with the bias increasing non-linearly with rain rate. Based on the rainfall error model parameters, we can see that the deterministic error just affects rain rates larger than 10 mm/h. Since the number of pixels with a rain rate larger than 10 mm/h is low, the effect of deterministic error in this case is smaller than it was for SC-5, for which the deterministic correction also affected small rain rates.

Conclusions

In this study, I propagated radar derived rainfall uncertainties through a fully distributed hydrological model. I used a calibration-free hydrological model. I evaluated different sources of error that are likely to occur when precipitation is estimated using radar observations of rainfall.

I found that flood peak uncertainty is sensitive to both the deterministic and random components of rainfall error. The effect of the random component is filtered out by the aggregation effect of the river network, and uncertainty decreases as catchment area increases. When the random error is not correlated in space, error variability for small scales is very large, with uncertainty bands that vary from 0.4 to more than 4 times the reference peak flow discharge. However, uncertainty decreases considerably with basin areas, and peak flow error for the outlet of the Cedar River basin is practically negligible (this result is consistent for all the 50 ensemble members).

When rainfall errors are correlated in space, the process of aggregation and attenuation by the river network is not as effective at filtering out uncertainties, and error

bands at the scale of approximately 17,000 km² are still significant. For a very small random error independent of rain rate, 10% error is still present for the Cedar River in Cedar Rapids. For larger random errors dependent upon rain rate values, uncertainties are on the order of 45% of the reference value.

The deterministic component of the error tends to produce a shift in the value of simulated peak flow up or down, but the width of the error band is still determined by the magnitude of the random error component and its spatial correlation. It is important to point out that these results mark the first step towards understanding how rainfall errors propagate through a hydrological model and affect flood prediction across a large range of scales. Some conclusions are general and can be applied qualitatively for any radar with an error structure similar to the one applied here. However, quantitative error assessment depends on the specific radar-rainfall estimation algorithm and, thus, error model parameters for the radar and area of interest.

Our results are limited to the effect of hourly rainfall accumulation given on a 4 km by 4 km grid. Higher resolution of radar rainfall is unlikely to change our conclusions for the larger scales, but it may influence the scale where the errors begin to rapidly decrease. Much work remains to be done before we can comprehensively understand the propagation of uncertainty in the hydrologic prediction of rainfall.

This work accomplishes the primary goal of demonstrating the importance of using a calibration-free model to investigate the effect of input uncertainty on hydrological prediction by showing that a consistent modeling implementation provides an unbiased interpretation of the effect of errors in input data. The study also demonstrates that radar-rainfall uncertainty should be estimated independently of hydrologic models. Specialized networks of rain gauges and other in situ instruments are needed to provide an independent reference against which radar-rainfall estimates can be evaluated. In addition, by performing an evaluation of the results using a large number of nested sites

within the main basin, I have shown that streamflow sensitivity to input errors varies as a function of basin scale.

Table V-1. Rainfall error scenarios considered in this study.

	Basins	CR	CR, IC	CR	CR	CR, IC	CR	CR
Equation	Par.	SC1	SC2	SC3	SC4	SC5	SC6	SC7
Deterministic bias	a	1	1	1	1	1	1	1.34
	b	1	1	1	1	0.84	1.15	0.84
Random error – standard deviation	c	0.2	0.45	0.45	0.45	0.45	0.45	0.45
	d	0	0.59	0.59	0.59	0.59	0.59	0.59
	e	0	-0.62	-0.62	-0.62	-0.62	-0.62	-0.62
Random error - spatial correlation	C ₁	1	0	1	1	1	1	1
	C ₂	37	0	37	60	37	37	37
	C ₃	0.39	0	0.39	1	0.39	0.39	0.39

Table V-2. Statistics for CUENCAS and the Sacramento model

Sites Information					Model evaluation						
Basin	Id map	USGS ID	Site Name	Area	Mean			Correlation		Nash-Sutcliffe	
					Obs.	C*	SAC	C*	Sac	C*	SAC
CR	1	5457000	Cedar River near Austin, MN	1033	45.8	46.1	41.0	0.9	0.9	0.8	0.8
CR	2	5457700	Cedar River at Charles City, IA	2728.7	169.3	196.7	147	0.8	1.0	0.6	0.9
CR	3	5458000	Little Cedar River near Ionia, IA	792.2	65.4	68.1	54.8	0.9	0.9	0.8	0.7
CR	4	5458300	Cedar River at Waverly, IA	4005	284.0	298.3		0.9		0.8	
CR	5	5458500	Cedar River at Janesville, IA	4300.1	319.3	319.4	245.7	0.9	0.9	0.9	0.8
CR	6	5459500	Winnebago River at Mason City, IA	1361.8	79.6	91.5	56.2	0.8	0.8	0.0	0.5
CR	7	5462000	Shell Rock River at Shell Rock, IA	4520.2	274.1	320.0	224.5	0.8	1.0	0.4	0.9
CR	8	5458900	West Fork Cedar River at Finchford, IA	2190.2	164.5	153.4	151.8	0.6	0.7	-0.1	-0.3
CR	9	5463000	Beaver Creek at New Hartford, IA	898.3	75.0	69.3	53.1	0.8	0.4	0.6	0.5
CR	10	5464220	Wolf Creek near Dysart, IA	774.1	67.2	52.5		0.8		0.6	
CR	11	5463500	Black Hawk Creek at Hudson, IA	784.4	64.0	47.9	45.0	0.8	0.9	0.6	0.8

Table V-2 Continued

CR	12	5464000	Cedar River at Waterloo, IA	13322.4	883.2	933.6	754.2	0.9	1.0	0.8	0.9
CR	13	5464500	Cedar River at Cedar Rapids, IA	16853.6	1331	1178.3	980.4	0.9	1.0	0.8	0.8
IC	1	5451210	S. Fork Iowa River NE of N. Prov, IA	579.9	51.6	40.8		0.8		0.2	
IC	2	5451500	Iowa River at Marshalltown, IA	3966.2	286.3	268.3	275	0.9	1.0	0.2	0.8
IC	3	5451700	Timber Creek near Marshalltown, IA	305.5	41.0	23.5	23.7	0.9	0.9	0.7	0.6
IC	4	5451900	Richland Creek near Haven, IA	145.2	8.1	7.5	11.0	0.6	0.6	0.2	0.2
IC	5	5452200	Walnut Creek near Hartwick, IA	183.6	9.3	9.2	12.9	0.6	0.7	0.3	0.5
IC	6	5453000	Big Bear Creek at Ladora, IA	489.3	31.6	22.5	30.3	0.7	0.7	0.4	0.5
IC	7	5453100	Iowa River at Marengo, IA	7233.3	613.0	470.1	513	0.8	0.7	0.2	0.4
IC	8	5454090	Muddy Creek at Coralville, IA	22.5	1.6	1.5		0.6		0.3	
IC	9	5454000	Rapid Creek near Iowa City, IA	65.5	3.4	3.9		0.4		-0.2	
IC	10	5454220	Clear Creek near Oxford, IA	151.2	10.5	10.5		0.9		0.5	
IC	11	5454300	Clear Creek near Coralville, IA	254	21.8	14.7	6.7	0.7	0.7	0.5	0.3

C* - CUENCAS

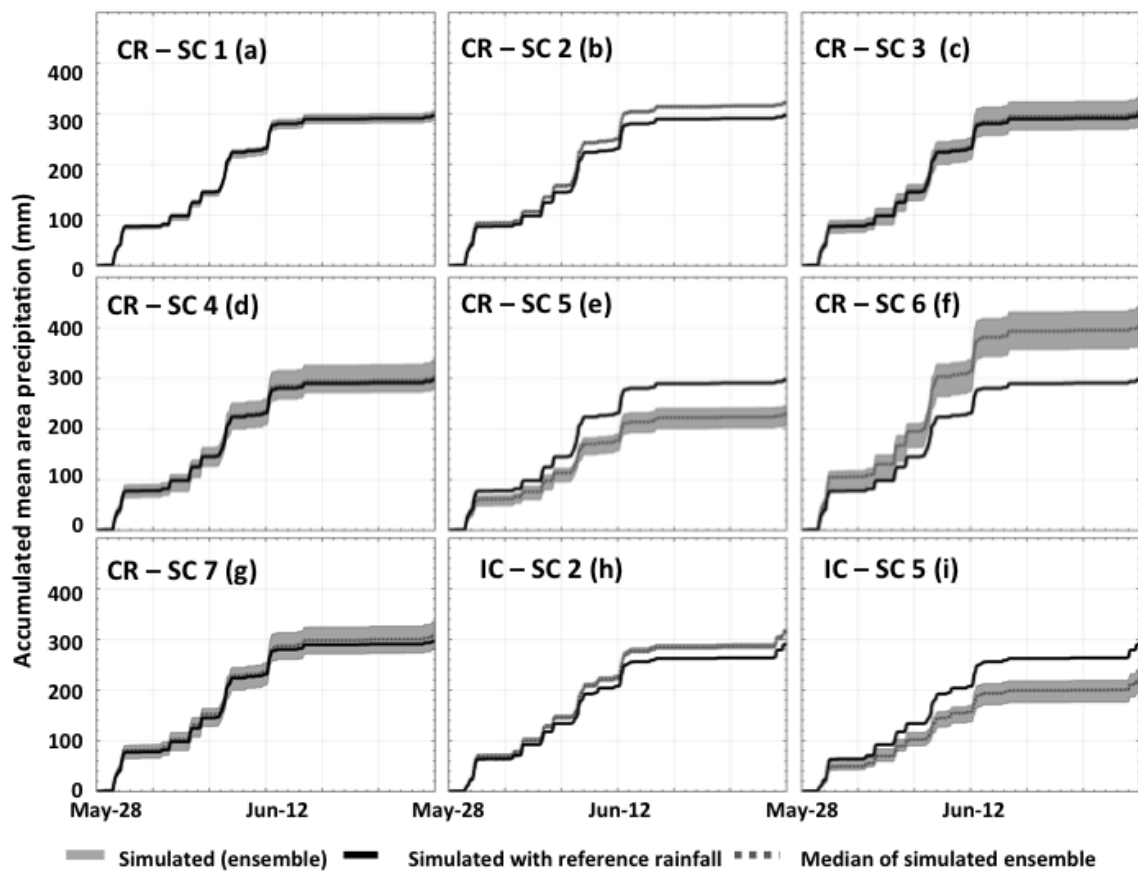


Figure V-1. Accumulated mean areal precipitation for the 7 rainfall error scenarios for the Cedar and Iowa Rivers

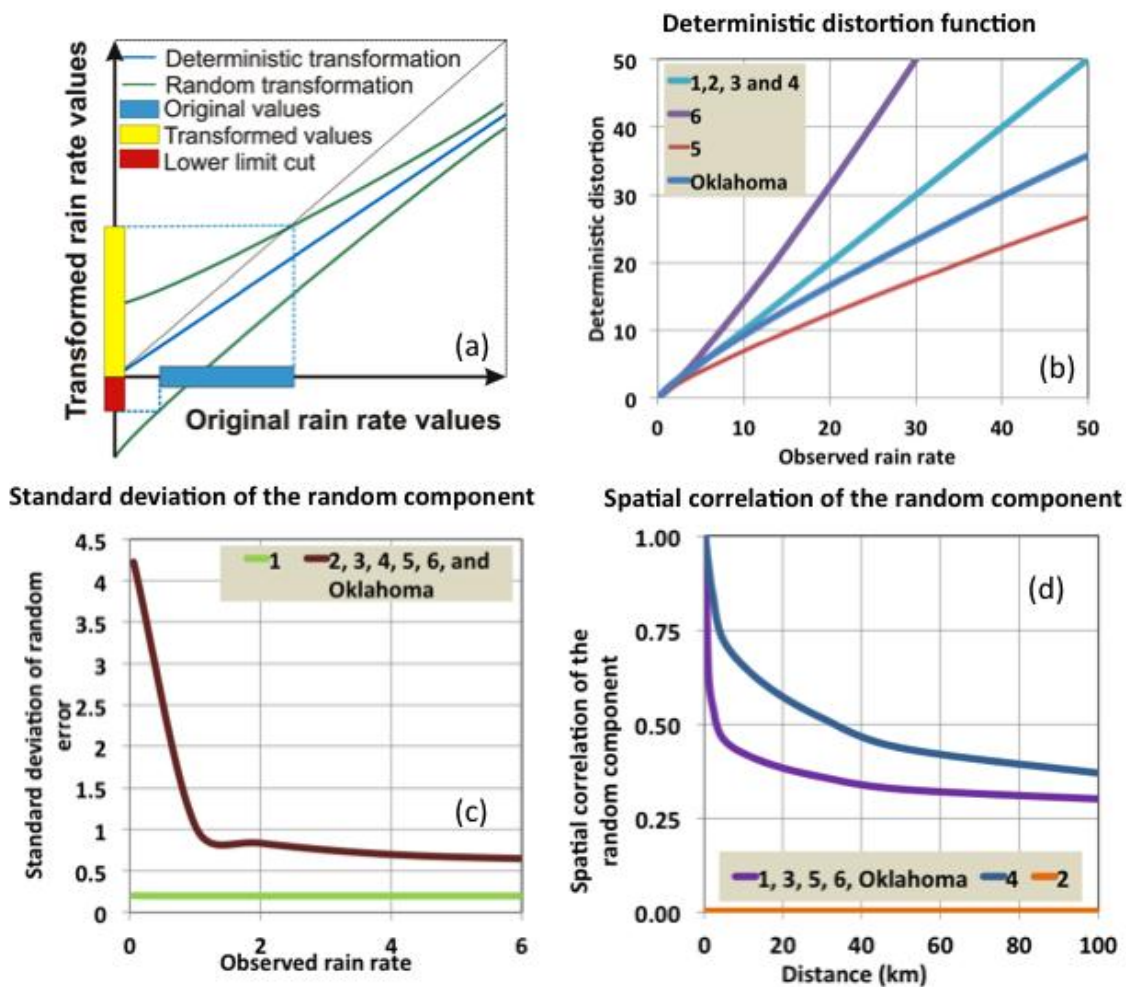


Figure V-2. (a) Schematic representation of the deterministic and random transformations; (b) Deterministic scenarios; (c) random scenarios; (d) spatial correlation scenarios

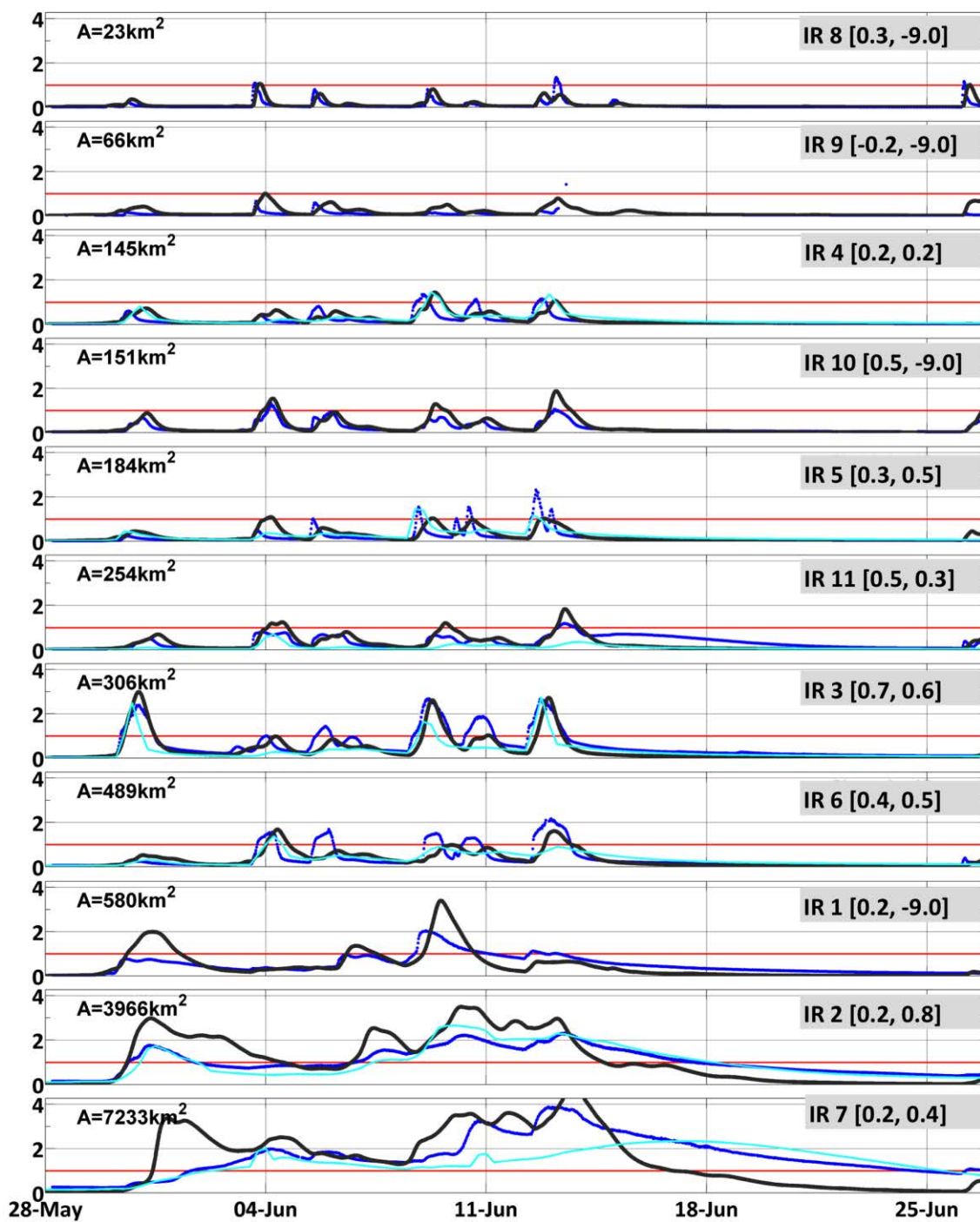


Figure V-3. Observed (dark blue line) and simulated hydrographs produced by CUENCAS (gray line) and SAC-SMA (light blue line) models for the Iowa River basin. The basin drainage area is presented on the left side, and the site number (refer to Figure 1) and Nash coefficients are presented on the right side (CUENCAS, SAC-SMA).

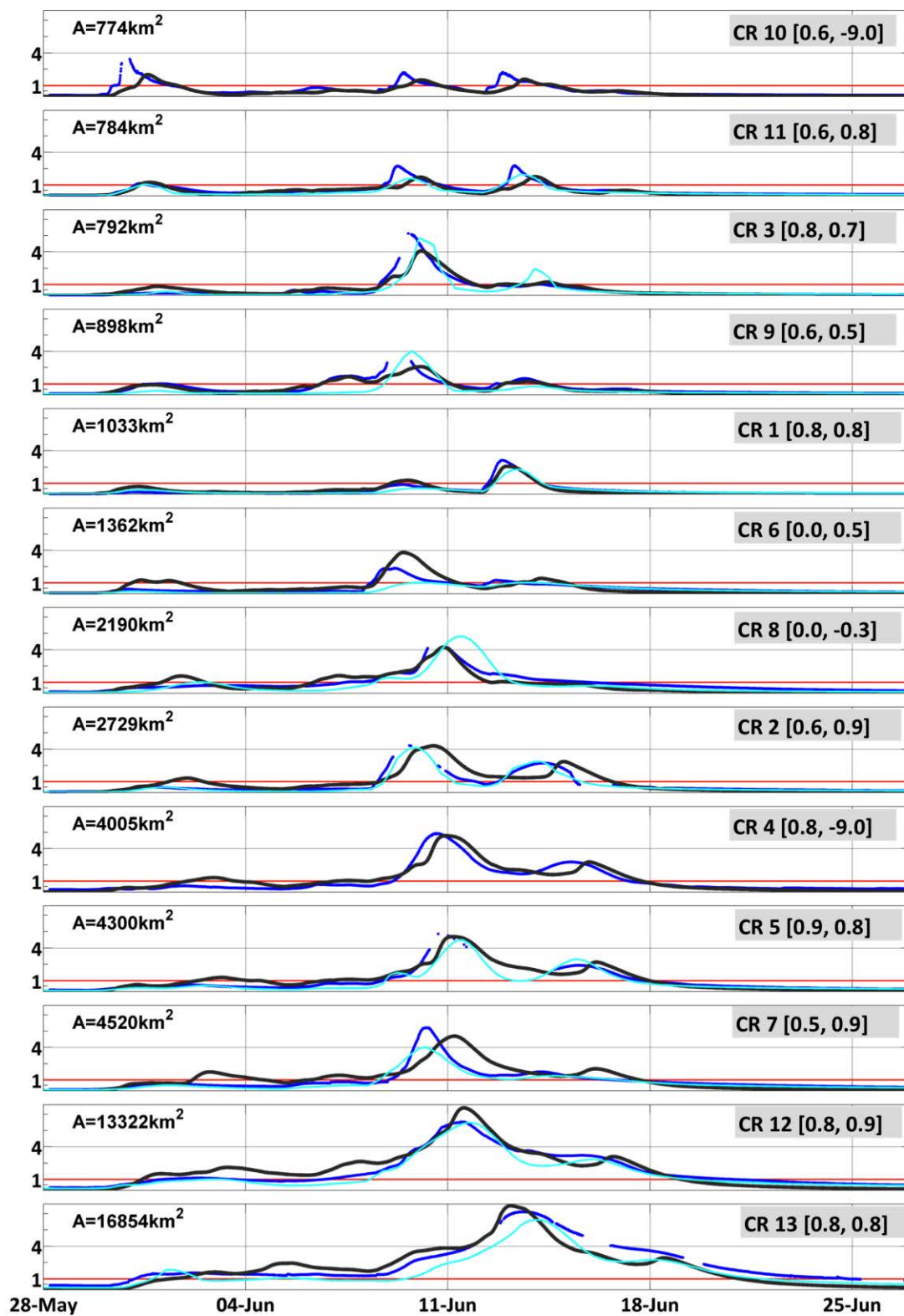


Figure V-4. Same as Figure 3 for the Cedar River basin

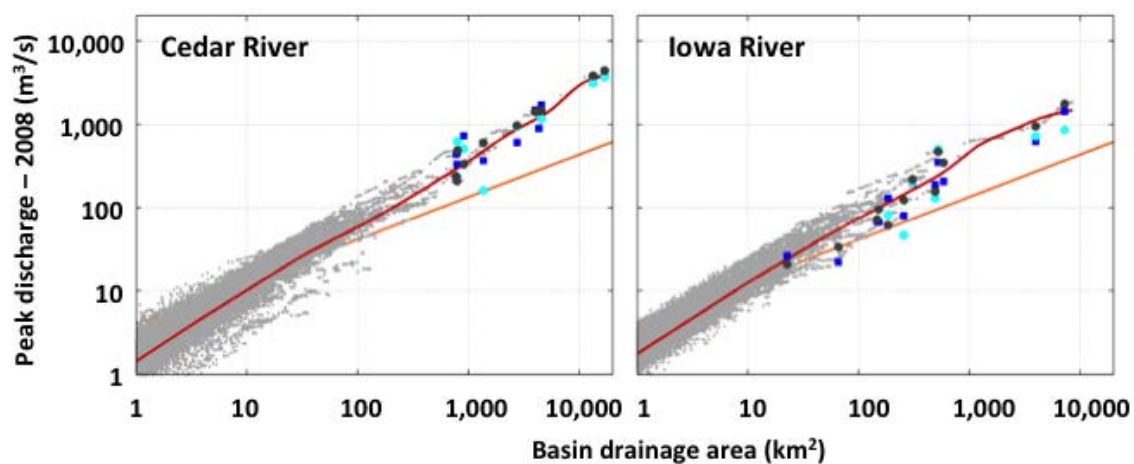


Figure V-5. Peak flow scaling for the Cedar and Iowa Rivers. Gray dots are simulated by CUENCAS, dark blue observed, and light blue simulated by SAC-SMS. The red line was obtained by non-parametric regression between drainage area and peak flow simulated by CUENCAS. The orange line represent mean annual flood

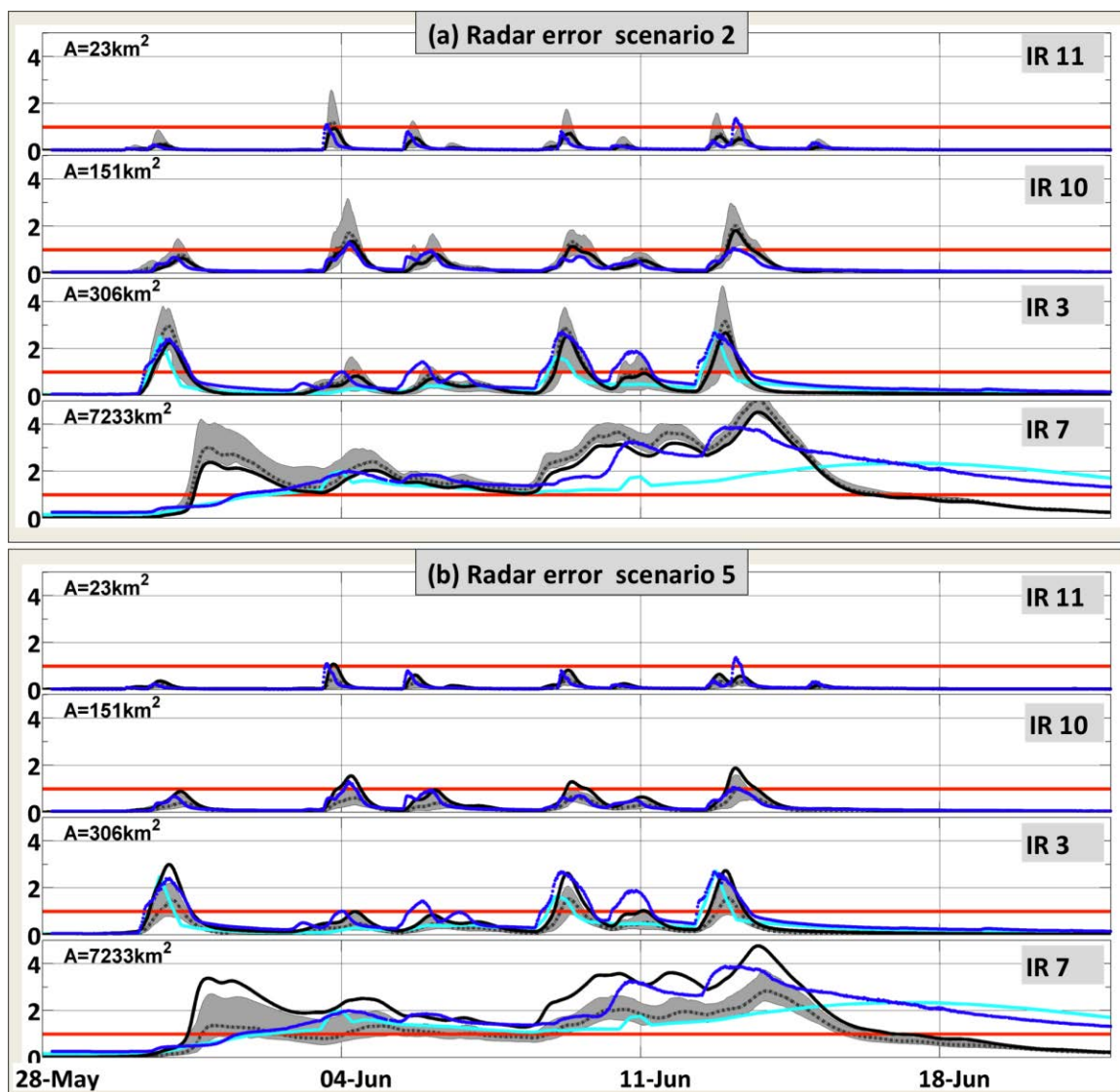


Figure V-6. Hydrographs for 4 sites on the Iowa River showing results of the simulation for rainfall error scenarios 2 (a) and 5 (b). The discharge is normalized by mean annual flood. The dark blue line represents observed hydrographs; the black line is simulated by CUENCAS using the reference rainfall; the gray shadow represents the lowest and highest values for the ensemble hydrographs simulated by CUENCAS using the 50 ensembles of rainfall; the dash gray line is the median of the ensemble; the light blue line represents the hydrographs simulated by SAC; and the red line reflects mean annual flood.

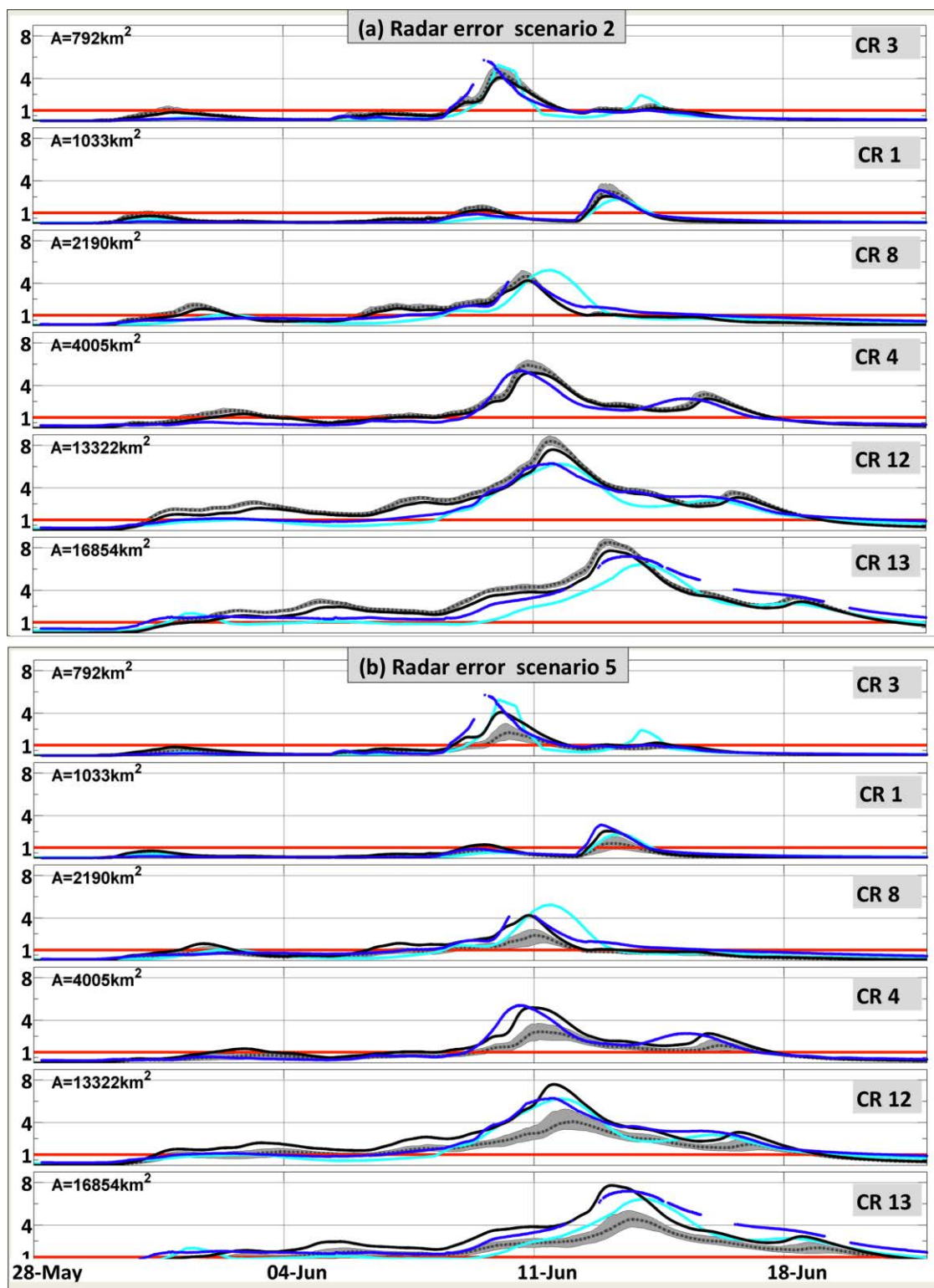


Figure V-7. Same as Figure 6 for 6 sites in the Cedar River basin.

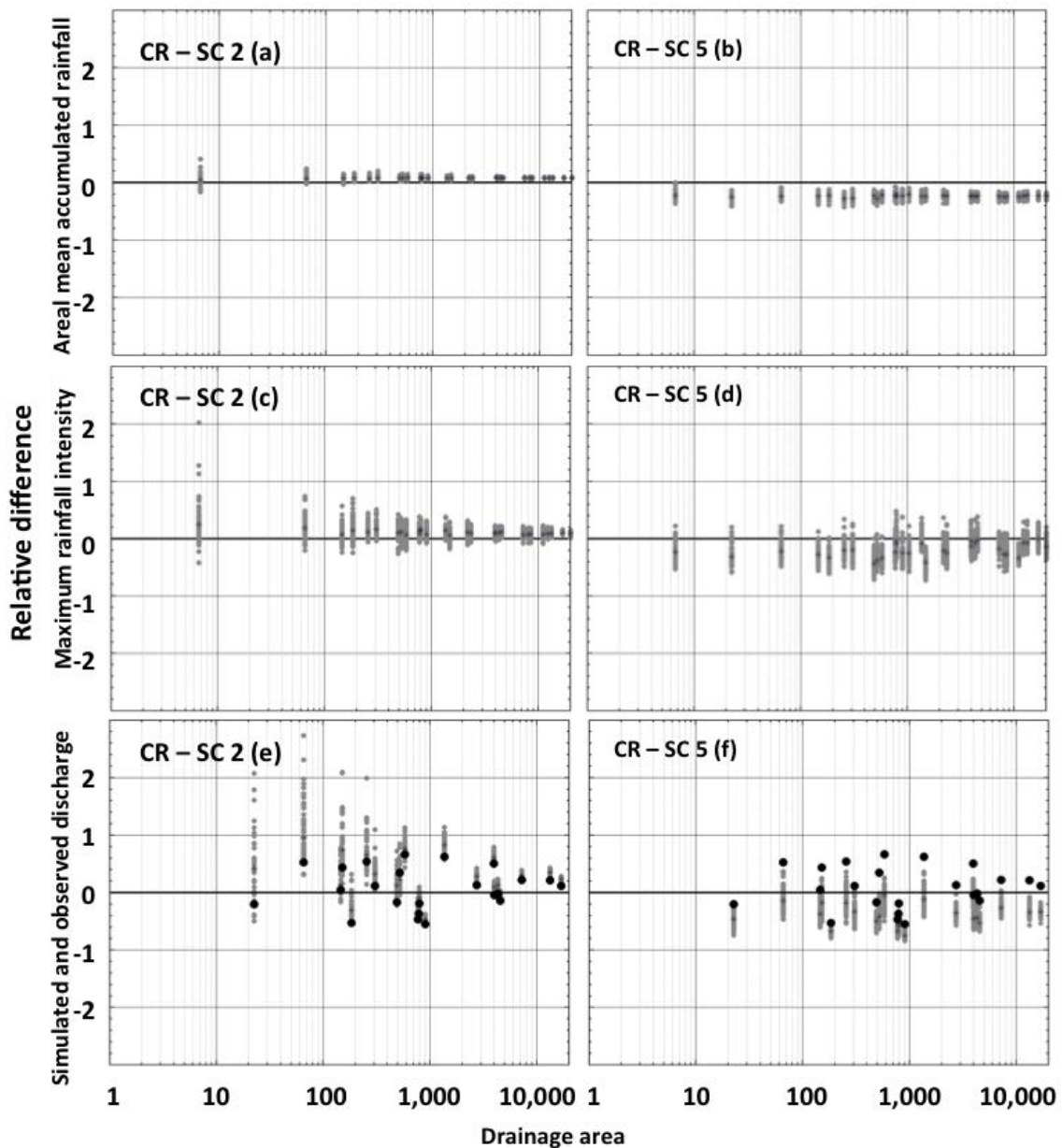


Figure V-8. Relative differences between the ensemble and the reference areal mean accumulated rainfall (a and b) and maximum rainfall intensity (c and d). Plots e and f presents the relative difference between simulated peak flow using the reference rainfall as input (black dots) and the ensemble rainfall (gray dots) and observed peak flow. Plots a, c, and e are for scenario 2, while plots b, d, and f are for scenario 5, Cedar River basin.

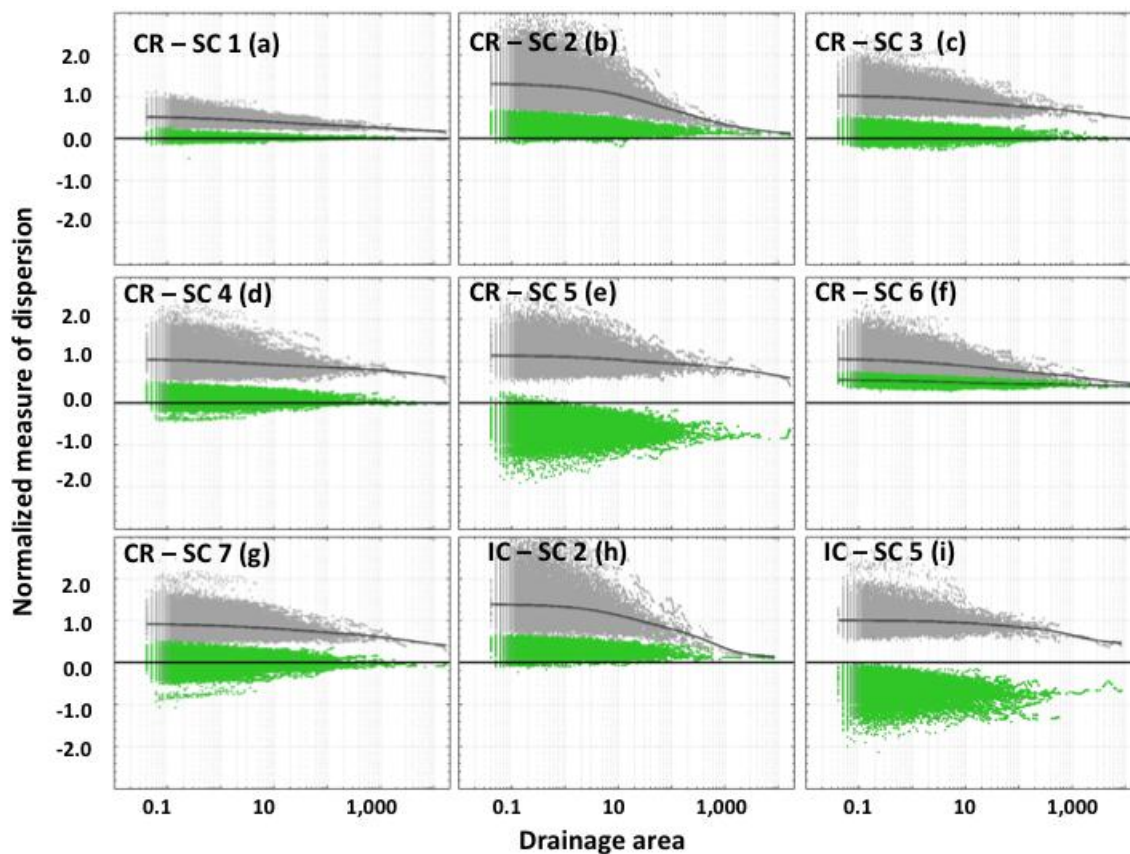


Figure V-9. Gray dots: difference between the 95th (Q_{p95}) and 5th (Q_{p5}) percentile ensemble flow values normalized by the median (Q_{p50}) ensemble flow value; Green dots: normalized difference between the median ensemble value and the reference peak discharge (Q_p^{ref})

CHAPTER VI IMPLICATIONS OF PRECIPITATION RESOLUTION AND SAMPLING INTERVAL FOR PEAK FLOW SIMULATION

Introduction

In the previous chapter, I investigated how radar rainfall errors that are propagated through the hydrological model affect peak flow simulations. Errors in radar rainfall are mainly caused by a weakness in the relationship between the measured variable (reflectivity) and rainfall. This type of error is denoted *retrieval error* and is common to all technologies that indirectly measure rainfall. In the case of weather radar, the standard procedure is to use a power law relationship between reflectivity and rainfall rate (Z-R). In the case of satellite rainfall, no unique approach exists and multiple remote-sensed products (e.g. infrared, microwave) and retrieval algorithms are used. Ebert et al. (2007) present a list of 7 different satellite-based rainfall products that are freely available through the Internet. Five of these products combine infrared and passive microwave data and two are infrared only. All seven products are based on different retrieval algorithms.

Due to the large number of different satellite-based rainfall products available, each one based on a different approach, I will not focus on estimating the expected retrieval errors of each one of these products. Moreover, current capabilities are about to change significantly with the launch of the new instruments proposed by the Global Precipitation Mission. With GPM in mind, many research groups are also concentrating their efforts on the development of new algorithms specially designed to use the new information generated by GPM (Le et al., 2010; Newell et al., 2010; Seto and Iguchi, 2011). These algorithms, together with different measurement technologies and a higher sampling frequency, have the potential to significantly improve current capabilities

Therefore, in this study, I focus on understanding the effects of known satellite-based rainfall limitations that will still be part of the new system and that might be critical

for flood simulation. Besides retrieval errors, the main sources of error in satellite based rainfall datasets are low temporal sampling frequency and coarse spatial and temporal resolution (McCollum et al., 2002; Hossain and Lettenmaier, 2006; Nikolopoulos and Anagnostou, 2010; Li et al., 2011). I independently investigate the effects of these two error components on flood simulation across scales.

Chapter 5 provided insight in terms of how rainfall retrieval errors propagate through hydrological models. Even though the study presented in that chapter focused on weather radar rainfall error structure, the multiple scenarios of rainfall error structure investigated were based on error properties that are common to any remotely –sensed rainfall dataset: deterministic and random errors that are correlated in space. I opted not to apply the ensemble satellite-based rainfall generator available in the literature (Bellerby and Sun, 2005; Hossain and Anagnostou, 2006) since they require the use of reference rainfall datasets, usually radar, for parameter calibration. Rain gauge datasets can be used, but very few regions in the world present a dense enough rain gauge network that can provide quality information about the spatial characteristics of rainfall. As was demonstrated in Chapter 5 and will also be discussed in Chapter 7, radar data is not error free and care should be taken when using these datasets as a reference to evaluate remote sensing products.

In this chapter, I evaluate the effects of coarse spatial and temporal resolution and infrequent temporal sampling on peak flow simulation across scales. The fundamental questions I address are:

1. How does rainfall's spatial and temporal resolution affect flood prediction across scales? Is there a scale for which remote sensing with currently available space-time resolution can provide useful information for flood prediction?
2. Can rainfall products obtained from infrequent observations be used for flood prediction? Does the error caused by infrequent sampling change with basin scale?

The temporal and spatial resolutions of input datasets are known to affect hydrological predictions (Shah et al., 1996; Liang and Guo, 2004; Fu et al., 2011). This impact has been shown to be scale dependent (Lopes, 1996). Faures et al. (1995) demonstrated the importance of correctly representing spatial rainfall variability to simulate flood events in the Walnut Gulch watershed. The authors also showed that uncertainties are scale dependent and increase as basin scale decreases, due to dampening effects. Satellite information is usually provided in resolutions that are recognized as too coarse for small to medium scale hydrological applications. For example, the resolution of the TMPA-RT and PERSIANN products is five times the NWS Stage IV radar resolution ($0.25^{\circ} \times 0.25^{\circ}$) and fifteen times the super-resolution radar product available for the period after Jun 2008 (Seo and Krajewski, 2010). CMORPH presents better spatial and temporal resolution ($0.07^{\circ} \times 0.07^{\circ}$) since it uses morphing techniques, combined with IR data, to propagate in space and time the precipitation derived from the PMW estimation of rainfall. The product with the best resolution is the HYDRO-estimator with 4×4 km resolution, but in this case only IR measurements are used and products are only available to the US. In this study, I systematically investigate how errors due to rainfall resolution affect flow prediction across a large range of basin scales. Our goal is to estimate for which scales remote sensing can provide useful information for flood prediction.

With the current constellation of microwave satellites, passive and active instruments typically pass over the same location less than twice a day. GPM promises to increase this to a frequency of 3 hours for 90% of the time. Infrared (IR) measurements obtained by a geostationary satellite are used to fill the gaps between consecutive visits. However, the relationships between IR measured variables, expressed by different cloud indices, and rainfall are not so strong, and retrieval errors tend to be very large. Passive and active microwave data obtained by low earth orbit satellites display significantly more physical direct relationships to rainfall than geostationary cloud indices (Iguchi et

al., 2002). The effect of sampling errors will depend on the temporal and spatial characteristics of the storm. It is most likely that with current capabilities, satellite remote sensing cannot be used to predict small-scale rainfall events. However, these technologies are probably valuable to predict floods with medium to large magnitudes, as in the case of the Iowa flood event that occurred in 2008, and I will evaluate the effects that sampling has on predicting this extreme flood event.

In this chapter, I do not include a description of the study area or of the hydrological model, since these topics were already discussed in Chapter 1 and Chapter 2, respectively. In the next section, I describe the rainfall dataset used in this study. I then describe the simulation framework used to independently evaluate the effects of coarse rainfall resolution and low frequency sampling interval on flood simulation across scales. I conclude with a summary of the limitations of the proposed approach and a discussion of future work.

Dataset - rainfall

In this study, I used the rainfall dataset produced by Seo et al (in preparation) and an offline version of the Hydro-NEXRAD system. The motivation for the production of this dataset was the identification of inconsistencies in the Stage IV data due to different calibration offsets (i.e. relative calibration bias) among radars that cover the same region. These offsets cause systematic artifacts that are observable in radar-rainfall maps because most merging methods currently implemented (e.g. Lin and Mitchell, 2005; Zhang et al., 2011; Seo et al., 2011) are likely to disregard the systematic differences among radars.

Seo et al (in preparation) propose a method to minimize the effects of these undesirable systematic features. The method is based on the results presented in Seo et al. (2012) with the generation of customized radar-rainfall estimates using the Hydro-NEXRAD system (Krajewski et al., 2011; Kruger et al., 2011; Seo et al., 2011).

In this analysis, I used Hydro-NEXRAD data with the same spatial and temporal resolution (60 minutes in time and 4 km in space) as the Stage IV dataset. Chapter 7 provides more details about the method used to generate the Hydro-NEXRAD dataset.

Methodology

As indicated in the introduction, the error structures of near-future satellite-based rainfall products are yet to be defined and will depend on many factors, including improvement of retrieval algorithms and sampling frequency. The error structure of future products will not correspond to the current products since algorithms will not be the same and the sampling frequency of microwave sensors will increase considerably. For the aforementioned reasons, I will not perform an extensive statistical evaluation of currently available products, but I will provide insight into the expected errors, taking into consideration such basic characteristics of these datasets as spatial and temporal resolution or sampling frequency.

I performed the following steps in this work:

- To estimate the effects of coarse spatial resolution on flood prediction, I aggregated the original rainfall fields to spatial resolutions similar to the ones provided by remote-sensed rainfall products or to the resolution adopted by land surface models (NLDAS-2). I forced the hydrological model with the aggregate (in space) and integrated (in time) rainfall maps. I compared peak flow simulated based on the high-resolution dataset (NH3-5min in time, 1km in space) to those obtained based on the degraded datasets.
- The effects of sampling errors are more difficult to evaluate since instantaneous rainfall fields are not available. Because instantaneous rainfall fields are unknown, I used the available radar rainfall dataset that consists of accumulated rainfall for the period of 60-min intervals to generate 3-hour resolution rainfall maps that mimic the properties of satellite products based on PMW. For each

interval of 3 hours, I randomly sampled n-values of the 60 minute rainfall maps to simulate n-samplings of the satellite in each interval.

Results and Analysis

Impact of coarse spatial and temporal resolution

In this section, I evaluate the effects of spatial and temporal rainfall resolution on flood simulation. I first aggregated the radar data to spatial scales that correspond to common satellite rainfall products: from $\Delta S=0.05'$ (radar Stage IV) to $\Delta S=0.1'$, $\Delta S=0.15'$, and $\Delta S=0.25'$. Next, I integrated the information in time from 1 to 3-hour resolution that also corresponds to remote sensing products. I forced the hydrological model using different resolution products and compared the results to the reference simulation.

Figure VI-1 presents the relative difference in peak flow due exclusively to the spatial effect (first line) and the spatial and temporal effects (second line). A value above one means that peak flows were overestimated when simulated with the modified source of rainfall as compared to the reference simulation. The aggregation of rainfall in space presents two opposite effects that might affect the peak flow simulation. First, it smoothes the high intensity rainfall clusters, decreasing the peak flow in some of the sites. Second, the aggregation causes transferability of some water from one hillslope to the other, and in this case it can add more water to specific areas, which increases peak flow. Both effects are represented in Figure VI-1, where we can see that for some sites the spatial aggregated rainfall fields caused underestimation and for others overestimation of peak flow. The second effect becomes very clear for the spatial resolution of $\Delta S=0.25'$. Hillslopes that were out of the storm path and did not present high peak flows for the reference simulation started to receive part of the storm. In this case, due to the initially low value of peak flow, the relative difference in peak flow reached values close to 500%.

As we saw with the retrieval error, the effects of precipitation resolution on flood prediction decreases with increasing catchment size. This is expected when the transformation of the data does not introduce any bias into the total volume of water reaching the basin. Ten percent of relative error is achieved for an area equal to approximately 50km^2 for spatial aggregations on the order of $\Delta S=0.1'$ and $\Delta S=0.15'$. However, for an aggregation on the order of $\Delta S=0.25'$, the same uncertainty level is reached for a basin with an area close to 1000 km^2 . This result is in accordance with Fu et al. (2011), who investigated the impact of the spatial resolution on stream flow prediction. The authors compared simulations that were obtained with rainfall fields with $500\times 500\text{m}$ spatial resolution to those obtained with a $10 \times 10\text{km}$ rainfall grid and concluded that the effect of spatial resolution was negligible for catchment sizes above 1000 km^2 .

In Figure VI-1, to evaluate the effects of temporal resolution, we can compare the plots in line 1 (1-hour) to the plots in line 2 (3-hours). We can see that the cloud of points moved slightly down, which indicates that for some of the basins, temporal aggregation decreased the simulated peak flow. However, this effect is not very significant for catchments larger than 100km^2 , as indicated by the similarity between the plots in lines 1 and 2. The 3-hour integrated rainfall fields are not the correct representation of actual satellite rainfall data. Even though stationary satellites continuously monitor the same location on the Earth, IR does not present a strong relationship with precipitation, and rainfall estimated based solely on this information is very uncertain (Kidd, 2011). PMW provides a much better estimation of precipitation, but in this case the sampling frequency is very low. In the next section, I will investigate the effect of low temporal sampling on flood prediction.

Impact of low temporal sampling

Rainfall estimation based on PMW data suffers from gaps in temporal sampling. With the current constellation of PMW sensors (4 total with a sampling frequency of about once per day), the average sampling frequency is approximately 6 hours. Infrared (IR) measurements are used to fill the gaps between observations. However, IR is sensitive only to the uppermost layer of clouds and presents a low relationship with rainfall. The Global Precipitation Mission is set to be launched in 2012 and will assure PMW 3-hour sampling at any given Earth coordinate 90% of the time.

In this work, I use a simulation approach to quantify the effect of sampling frequency on flood prediction. I use 5-minute Hydro-NEXRAD rainfall data to generate ensembles that mimic the sampling frequency of the future GPM mission. The ensembles were generated by randomly selecting one hour (out of the three available hours) to represent 3 hour rainfall intervals. Fifty ensembles were generated and used as input into the hydrological model. This method provides an approximation of the expected error since instantaneous rainfall fields should have been used instead of 1-hour accumulated. However, information about the instantaneous fields is not available. In this sense, I expect that real errors due to sampling frequency are even larger than the ones presented in this work. Nevertheless, the results of this study help us understand the magnitude of the sampling error compared to other sources of errors previously discussed.

Figure VI-2 (a) presents the areal average rainfall accumulation over the basin for the reference rainfall field (red line) and the lower and upper limit of the 50 sampling frequency ensembles. We can directly compare this figure to Figure 6-1, which presents the same plot for different scenarios of retrieval error. Even though the present scenario represents the lower limit of errors due to sampling interval, Figure VI-2 (a) demonstrates the strong impact of this type of error. Total accumulated precipitation in the basin

varied from around 220mm to almost 400mm. This large range of rainfall uncertainty had a substantial impact on flood prediction.

Figure VI-2 (b) use the same metrics applied to generate Figure V-9. The distance between the blue dots and the zero line represents the width of the error band at the time of the peak. Values equal to 1 indicate that the magnitude of the difference between the lower and the highest value of predict peak flow is equal to the median of the values. In this case, even for the outlet of the basin, the error band is very large (equal to 0.9 times the medium of peak flow). In Figure VI-3 I included the Cedar River hydrographs with the error band due to sampling frequency error. The error due to sampling frequency does not decrease with basin area, as was the case with retrieval error and errors due to coarse resolution data.

Even though the error due to sampling is very large, different methodologies are available that combine the information of infrared and microwave observations to compensate for the poor sampling of PMW (Ebert et al., 2007). These products generally merge geostationary infrared data and polar-orbiting passive microwave data to take advantage of the frequent sampling of the infrared and the better rainfall estimation of the microwave. One example is the Climate Prediction Center morphing (CMORPH) technique that combines PMW observations with the cloud motion derived from the IR data (Kidd and Huffman, 2011). At times and locations at which PMW data are unavailable, PMW estimates are propagated/interpolated using motion vectors derived from the IR data (Joyce et al., 2004). Consequently, this method does not rely directly on rainfall estimated by IR but, instead, takes advantage of the information IR provides with high accuracy.

Conclusions

In this study, I use a calibration-free hydrological model to investigate the impact of rainfall resolution and sampling frequency on flood prediction. At present, a new

Global Precipitation Mission is being planned. This mission is going to significantly improve the potential to predict rainfall from space since it increases PMW sampling frequency and adds information to the current systems, including information from sensors that were not available until this point (active microwave measurements). At this moment, it is hard to predict how much improvement will be achieved with the addition of this new information and methods. Therefore, this study did not focus on currently available products, but I independently evaluated different sources of uncertainty with the goal of identifying which components potentially compromise the satellite remote sensing rainfall data for flood prediction.

Spatial and temporal resolution of rainfall fields has a significant impact on simulated peak flow. This impact is scale dependent, and it decreases as basin area increases. When information is aggregated in space, two main factors contribute to uncertainties in peak flow prediction. First, rainfall fields are smoothed out, which cause the underestimation of peak flow for some hillslopes and catchments. Second, when aggregated to coarser spatial resolution, storm water is transferred from one hillslope/basin to the other, which causes peak flow overestimation for some areas and underestimation for others. This effect is visible when the simulation is performed with rainfall data that present the same spatial resolution of currently available satellite rainfall products. Nevertheless, this uncertainty is also filtered out by the river network and decreases as basin area increases.

At some scales, the impact of rainfall spatial resolution disappears. For the event and basin analyzed, this happened at a scale of 50 km^2 for a spatial resolution equal to $\Delta S=0.10'$ (twice the radar resolution) and 1000 km^2 for spatial resolution equal to $\Delta S=0.25'$ (five times the radar resolution). The effect of temporal resolution can only be seen for basin areas below 100 km^2 . I conclude that peak flow uncertainties will be low if the average precipitation over the catchment is accurately estimated. Errors introduced

at small scales will disappear at some scales, depending on the storm properties and data resolution.

Our results demonstrate that sampling frequency errors are critical for flood prediction since the errors are not filtered out by the river network. I simulated the expected error by considering the expected sampling frequency of the Global Precipitation Mission (once every 3 hours at 90% of the time). I used a simulation approach that simulates the best-case scenario, since 1-hour accumulations are used instead of instantaneous fields. Even for this scenario, uncertainties due to sampling are very large, with an order of magnitude of 90% for the outlet of the basin. At the hillslope scale, errors reached 500%. For basins on the order of 10km^2 , errors were on the order of 100% to 250%, which demonstrates the importance of using retrieval error algorithms that merge different sources of satellite information.

The effects of rainfall sampling and resolution will depend on the spatial and temporal variability of the precipitation and the runoff response. It was not the intent of this study to provide a comprehensive answer to the challenging question of how satellite rainfall errors impact hydrological modeling predictions for any hydrological condition. Instead, I attempted to provide insight into the potential to use these technologies for flood simulation, the magnitude of the errors involved, and how they change across scales. Therefore, I chose an event of large magnitude that was likely to be captured by remote instruments.

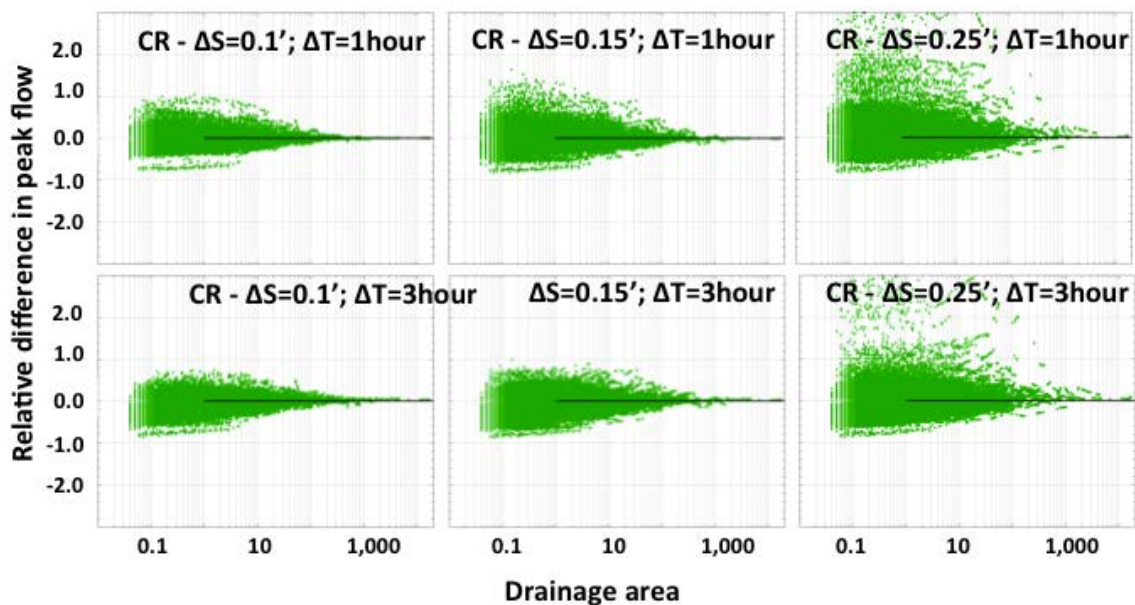


Figure VI-1. The relative difference in simulated peak flow due to spatial and temporal precipitation resolution.

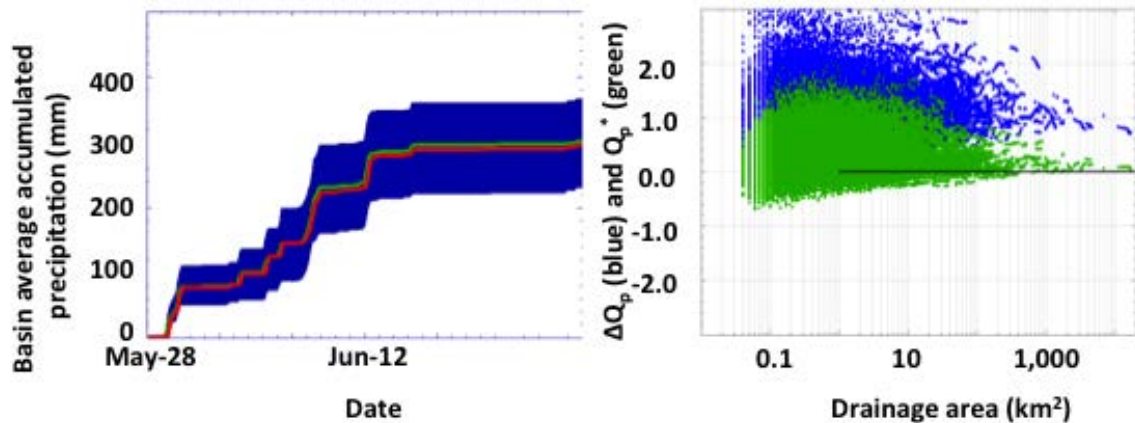


Figure VI-2. The effect of sampling frequency on flood prediction uncertainty (a) and error band of 50 samples generated based on the simulation of temporal sampling (b). Blue dots: the difference between the 95th (Q_{p95}) and 5th (Q_{p5}) percentile ensemble flow values normalized by the median (Q_{p50}) ensemble flow value; Green dots: the normalized difference between the median ensemble value and the reference peak discharge (Q_p^*).

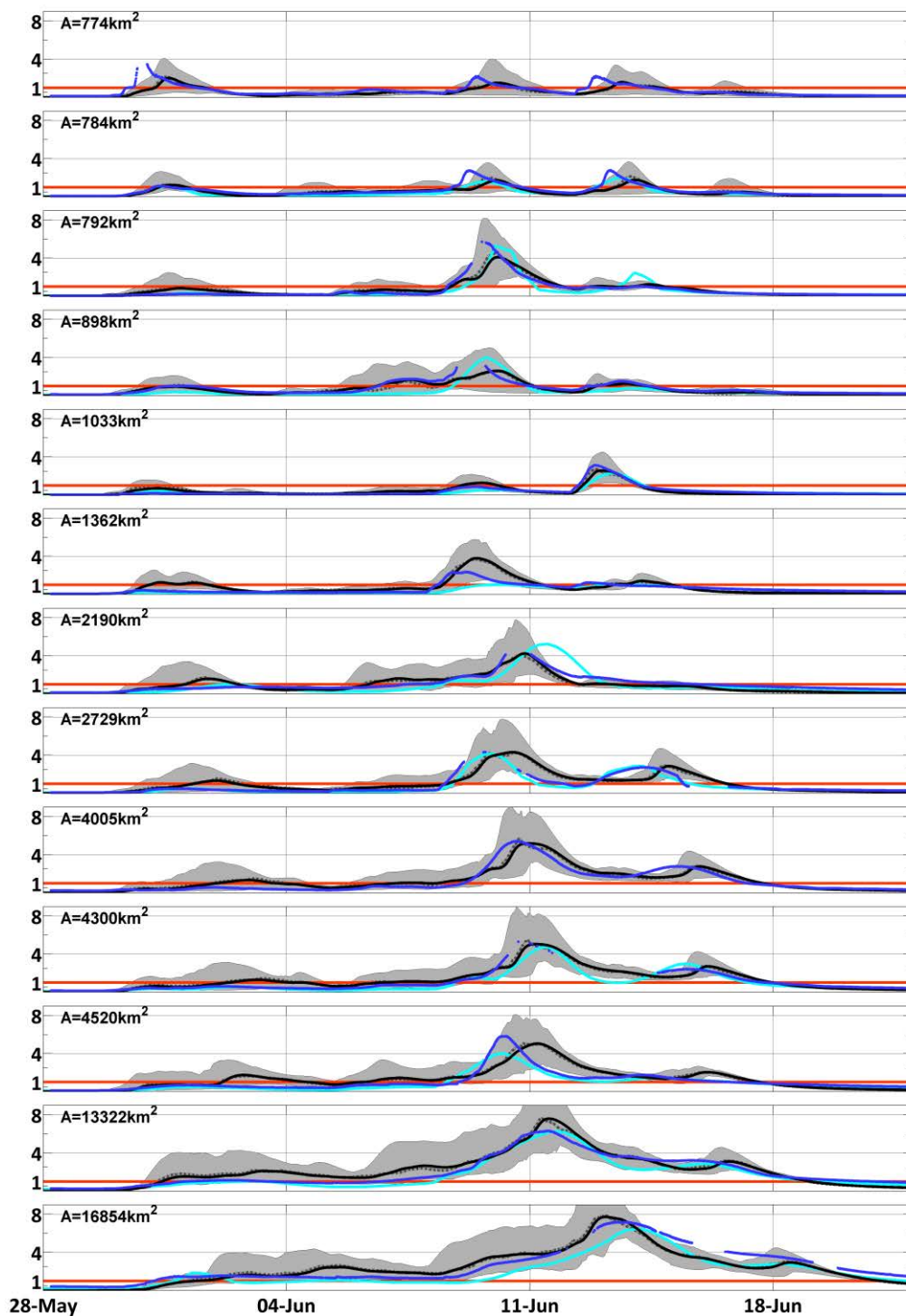


Figure VI-3. Hydrographs with error bands for Cedar Rapids sites using 50 different ensembles that mimic uncertainty due to sampling frequency. These results simulate the case for which one sample is obtained each three hours. Observed values are presented in dark blue and simulated based on SAC-SMS in light blue

CHAPTER VII

EVALUATION OF DIFFERENT PRECIPITATION DATASETS AND THEIR IMPACT ON FLOOD PREDICTION

Introduction

In Chapters 5 and 6, I investigated how different sources of rainfall uncertainty (e.g., coarse resolution and retrieval error) affect peak flow simulation. In Chapter 5, I focused on uncertainties caused by instrument limitations or observational system capabilities, by weak relationships between the measured variable and rainfall (e.g. reflectivity), or by lack of knowledge about physical processes. These uncertainties result in random and deterministic errors that are usually a function of rain rate. I evaluated the effect of different error structure scenarios on simulated peak flow and hydrographs across multiple scales for the 2008 Iowa flood event. In Chapter 6, I independently evaluated how errors caused by coarse spatial and temporal resolution and low temporal sampling affect simulations. The final rainfall products obtained by radar or satellite-based techniques contain a combination of these different sources of errors. In this chapter, I perform simulations using the real products to evaluate how different they are from each other and to assess how these differences propagate through the hydrological model.

I evaluate different datasets in terms of how well they perform in terms of simulating peak flow across a large range of scales. As a reference, I use a peak flow simulation obtained using a Stage IV rainfall dataset, although higher resolution datasets are available. I chose this dataset as a reference because it is the highest resolution dataset available for years other than 2008. The analyses in this chapter were performed for the Cedar River basin.

In the next section, I describe the datasets included in this study. I then present the methodology and model results for the 2008 flood event, for which higher resolution

rainfall data based on the Hydro-NEXRAD system is available, and for the years 2002, 2003, and 2004. I close this chapter with conclusions.

Datasets

In this section, I describe the rainfall datasets analyzed in this study, which are also listed in Table VII-1. I begin by describing weather radar based products, including the Stage IV product provided by The National Weather Service Next Generation Weather Radar (NEXRAD) and the higher resolution/accuracy datasets generated based on the Hydro-NEXRAD system. I demonstrate some undesirable features in the Stage IV data that are caused by the calibration offset between different radars covering the same region. Seo et al (in preparation) provided a methodology to correct this miscalibration and generated higher resolution rainfall products using an offline version of the Hydro-NEXRAD system. I then describe the rainfall datasets based on satellite remote sensing measurements, including simulations performed using TRMM-3B42, PRSIANN, and CMORPH. For details on the algorithms, refer to Sapiano and Arkin (2009). The final section describes the dataset used to force the SAC-SMS model. The Mean Areal Precipitation (MAP) dataset is produced based on rain gauge data using Thiessen polygon weighting as the interpolation method.

Weather radar datasets

Stage IV

The US is covered by a dense network of weather radars operated by the NOAA National Weather Service (NWS). The Stage IV rainfall dataset is one of the products of this network and is freely available on the web in an operational base. Stage IV presents hourly rainfall accumulations given on an approximately 4 km by 4 km grid. Stage IV is a post-processed product based on the merging of radar and rain gauge data. This is done to remove the mean-field bias in the radar-only estimates. Fulton et al. (1998) present

more details about the procedure applied to generate this dataset. Hereafter, I refer to this dataset and the results obtained using it as the input to the hydrological model in reference to rainfall and simulated peak flow.

Figure I-1 shows the four radars from the NEXRAD system that partially covers the study area. The Stage IV dataset is produced by mosaicking these multiple datasets into a unique product (e.g., Lin and Mitchell, 2005; Zhang et al., 2011; Krajewski et al., 2011a). However, different radars are likely to contain different sources of errors, and merging all information in a unique product is not a straightforward task. Figure VII-1, for example, illustrates rainfall totals of the Stage IV data over the period of May 30 to June 15, when extreme flooding took place in the Iowa River and Cedar River basins. I speculate that radar data from four WSR-88Ds, the Des Moines (KDMX in Iowa), Davenport (KDVN in Iowa), Minneapolis (KMPX in Minnesota), and La Crosse (KARX in Wisconsin) radars, were combined for this product (three radar locations are clearly visible in Figure VII-1). Exact information on how many radars were used for the product generation in Figure VII-1 is unknown. However, I recognize a vertically stretched border at the middle of the horizontal domain that is positioned at the equidistance zone between the KDMX and KDVN radars. The line reveals that individual rainfall estimates (before they were combined) from the two radars are not on the same level due to different calibration offsets (see Marks et al., 2009; Wang and Wolff, 2009; Seo et al., 2012). This fact verifies that the merging procedure for the Stage IV product does not effectively deal with this relative bias problem. A similar systematic feature could also be perceptible in other merged products (e.g., Zhang et al., 2011; Krajewski et al., 2011a) when the relative bias among radars is not quantified and adjusted properly.

The systematic rainfall differences along the border line may be translated into over- or under-estimation of total water volume or discharge rate for some basins located in or downstream from the affected area. To investigate the effects of these uncertainties

on rainfall products, and consequently on hydrologic simulations, we corrected these fields based on the results presented in Seo et al. (2012). We adjusted one (the KDMX) of the radars to the same level as the other radar (KDVN), assuming that the KDVN and other radars are well-calibrated. Although the reference radar (here, the KDVN) might be mis-calibrated, the merged rainfall field could be uniformly corrected using rain gauge data. Seo et al. (in preparation) describe the procedures used to correct the Stage IV dataset in more detail.

Hydro-NEXRAD

To generate Hydro-NEXRAD estimates, Seo et al. (in preparation) collected radar Level II data from the National Climatic Data Center (NCDC) for four WSR-88D radars (The KARX, KDMX, KDVN, and KMPX; see Figure 1-1). As shown in Figure 1-1, four radars illuminate the Iowa River and Cedar River basins, but none of them fully covers the entire area. Since there was a resolution upgrade of radar Level II volume data during the period of this study (the timings of this switch are different for each radar), the collected data for all four radars exist in two phases of data format: legacy- (before the change) and super-resolution (after the change) (see e.g., Seo and Krajewski, 2010). The sampling geometry of radar measurement for legacy-resolution is represented by 1° in azimuth by 1-km in radar range. In the super-resolution radar volume data, the lowest three elevation angle data of legacy resolution were replaced with the new resolution of 0.5° by 250-m.

We define procedures to yield merged radar-rainfall estimates using the Level II volume data collected from the four radars around the Iowa River and Cedar River basins. In this section, the description for the estimation procedures is limited to generation of customized Hydro-NEXRAD estimates. For detailed information on the estimation of the NCEP products, refer to Fulton et al. (1998) and Lin and Mitchell (2005).

To process a massive radar volume data set for four months (March through June 2008) from four WSR-88Ds (the KARX, KDMX, KDVN, and KMPX radars), Seo et al. (in preparation) used the offline Hydro-NEXRAD system that can deliver radar-rainfall estimates with user-specified algorithms and resolutions (time and space). The main procedures to create radar-rainfall estimates over the Iowa River and Cedar River basins are delineated as two steps: (1) individual (single) radar data processing and (2) multiple radar data merging.

Since the polar-based resolution and data format between the legacy- and super-resolution Level II data are different, the legacy- and super-resolution data were processed separately. Data processing algorithms for super-resolution is discussed in Krajewski et al. (2012), but the basic concepts and algorithm components are the same as in Seo et al. (2011). Non-precipitation radar echoes caused by ground clutter and anomalous propagation (AP) effects (e.g., Moszkowicz et al., 1994; Grecu and Krajewski, 2000; Berenguer et al., 2006; Cho et al., 2006) were removed by the implementation of Steiner and Smith (2002) that classifies non-precipitation echoes using the horizontal and vertical structure of measured radar reflectivity. Seo et al (in preparation) applied two threshold values (10 and 53 dBZ) to identify effective minimum rainfall and hail contamination and constructed reflectivity maps using a non-parametric kernel function (see Seo et al., 2011). The NEXRAD default Z-R relationship, $Z = 300R^{1.4}$, (Fulton et al., 1998) was then applied to transform radar reflectivity fields into rainfall intensities.

To merge multiple radar data, we translated all single radar fields (either radar reflectivity or rainfall accumulation) based on a spherical coordinate system denoted by azimuth, radar range, and elevation angle plane onto the common grid of $1' \times 1'$ geographic coordinates. The merging of different polar-based resolution data (for periods when both legacy- and super-resolution data coexist) arising from the different timings of the resolution switches for four radars can be resolved by the common grid translation.

Seo et al (in preparation) then used two types of merging options, namely “data-based” and “product-based” merging (refer to Seo et al., 2011), that combine radar reflectivity and rainfall accumulation fields, respectively. Using a distance weighting function (e.g., Zhang et al., 2005; Langston et al., 2007) may reduce significant range effects (see e.g., Andrieu and Creutin, 1995; Vignal and Krajewski 2001; Krajewski et al., 2011b) at the very far range from the radar. In this study, I show only the results for the second type of merging procedure: product-based merging.

The Hydro-NEXRAD products also present the sharp border at the equidistance zone between radars. The primary reason that the border line appears in merged radar-rainfall products is because the merging procedure assumes that all involved radars are well-calibrated and does not consider different calibration offsets among radars (see e.g., Anagnostou et al., 2001; Marks et al., 2009; Wang and Wolff, 2009). Direct information on this relative calibration bias is not yet available through operational agencies. In an attempt to quantify the relative differences in reflectivity (relative calibration bias) between two ground-based radars, Seo et al. (2012) proposed a methodology to compare radar reflectivity measurements observed for the same meteorological targets. Their study also reported the magnitude of the bias information between the KDMX and KDVN radars from 2003 to 2010. Fortunately, the most significant relative bias in Figure VII-1 seems to occur between the KDMX and KDVN radars, and the KDVN and KARX radars do not show systematic differences in rainfall amounts. This implies that the KDMX radar is the key to correcting the sharp border. Therefore, the author used the relative bias information quantified in Seo et al. (2012) and adjusted the KDMX radar reflectivity data to account for the problem mentioned in section 2. We applied monthly mean values of the relative bias (i.e., 1-2 dBZ) and obtained enhanced radar-rainfall estimates for both merging options.

Satellite-based datasets

In this section, I describe the satellite-based datasets investigated in this study. For a fair comparison, I included products with the same spatial (~25km) and temporal (3h) resolution.

PERSIANN

Precipitation Estimation from Remotely Sensed Information using Artificial Neural Networks (PERSIANN) product is generated based on artificial neural networks methods that routinely adjust the model parameters of the precipitation estimation from remotely sensed information using coincident rainfall derived from the microwave imager (TMI). The algorithm classifies the clouds and extracts local and regional information from infrared and geostationary satellites. The cloud images are then transformed into rain rate based on the main cloud characteristics that can be related to rainfall. Hong et al. (2004) present more details about the method used to generate PERSIANN.

CMORPH

One of the main sources of uncertainty in remotely sensed rainfall products arises from the difficulties in estimating rainfall based on a cloud–precipitation relationship using geostationary information (Arkin and Xie, 1994). CMORPH attempts to overcome this problem by combining passive microwave measurements with images of geostationary satellites using an alternative method. The method consists of using precipitation estimates derived from low-orbiter-satellite (PMW) observations, which have a more direct relationship with rainfall, and geostationary satellite IR to track the clouds and transport it via spatial propagation during the periods when instantaneous PMW data are not available. Precipitation features such as shape and intensity are estimated for 30 minute intervals by “performing a time- weighted interpolation between PMW-derived estimates that have been propagated forward in time from the last

available PMW observation and those that have been propagated backward in time from the next available PMW scan,” This procedure is referred to as “morphing” (Joyce et al., 2004).

TMPA-3B42

TMPA is a calibration-based sequential scheme that combines precipitation estimates from multiple satellites, as well as gauge data where available, at fine scales (Huffman et al., 2007). TMPA-3B42 is based on the calibration of TRMM Combined Instrument (TCI) and TRMM Microwave Imager (TMI) precipitation products. In this study, I evaluate the research product version 6 (3B42 V.6).

The research product (3B42 V.6) uses the TRMM Combined Instrument (TCI) estimate for calibration, which is considered to be better than the TMI but is not available in real time (Huffman et al., 2007). The research product is also corrected for bias by comparing the monthly sums of the 3-hourly fields to a monthly gauge analysis (Su and Hong, 2008).

Other datasets

National weather service – mean areal precipitation

The National Weather Service calibrates rainfall runoff models using 6-hour mean areal precipitation (MAP) inputs derived from rain gauge networks. Each river forecast center (RFC) within the NWS produces MAP for the basins for which streamflow forecasts are performed. The gauge-derived MAPs are computed using Thiessen polygon weighting. These datasets were used to calibrate the parameters for the SAC-SMS model’s results presented in this thesis.

The SAC-SMS model performs well using this rainfall dataset since it was specially calibrated using this data. However, as demonstrated by Finnerty et al. (1997), runoff timing and volume are biased when hydrological simulations are performed based

on datasets that have space-time scales that differ from the ones for which the model parameters were calibrated. The authors demonstrated that hydrologic model parameters are essentially tied to the space-time scales at which they were calibrated. The authors also showed that surface runoff, interflow, supplemental baseflow runoff components, water balance components of evapotranspiration, and total channel inflow are sensitive to the space-time scales of the rainfall. As I did not have the tools to run the SAC-SMS model using different datasets, I ran CUENCAS using the MAP dataset used to generate the SAC-SMS predictions presented in this work.

Johnson et al. (1999) compared mean areal precipitation values (MAPX) derived from next generation weather radar (NEXRAD) Stage III data with those generated by the NWS based on gauge values (MAP). The authors concluded that mean areal estimates derived from NEXRAD are generally 5–10% below gauge-derived estimates. However, this pattern is not consistent in all regions as MAPX is greater than MAP for the smallest basins. The authors also demonstrated a tendency for NEXRAD to measure fewer yet more intense intervals of precipitation during extreme storm events. They also performed simulations using the two different datasets and demonstrated that hydrologic simulations based on MAPX and MAP differ considerably. These results show that the parameters of the hydrological models will need to be recalibrated if the NWS intends to use radar data for hydrological simulations.

NLDAS-2 forcing

This precipitation dataset is used as forcing for the land surface data assimilation system (NLDAS-2) and constitutes a product of a temporal disaggregation of a gauge-only CPC analysis of daily precipitation, which was performed directly on the NLDAS grid and included an orographic adjustment based on the widely-applied PRISM climatology (Xia et al., 2012).

Comparison of rainfall totals for different products

For the 2008 flood event

The three Hydro-NEXRAD estimates in Table 1 are basically categorized into products with (HN-1) and without (HN-2 and HN-3) relative bias adjustment. We corrected the overall bias of the HN-1 and HN-2 product by multiplying each rainfall map by 0.7. This coefficient was estimated by the ratio between accumulated HN-1 and Stage IV data over the period of the 2008 flood (May 28th to June 1st). Regarding the HN-3, we used the radar-gauge comparison results to perform daily bias correction.

Figure VII-2 shows examples of rain totals from May 28th to July 1st of 2008 for all products listed in Table VII-1. As we have discussed, Stage IV and HN-1 products present an artificial feature due to the mis-calibration of multiple radars. This feature disappears from the HN-2 and HN-3 products. Accordingly, the increased rainfall quantity in the left area of the line (for the HN-2 and HN-3) leads to more water volume at this location, which also affects the sub-basins located downstream from this region. While overall bias was applied for the HN-1 and HN-2, bias values estimated from a shorter time span were applied for the Stage IV (1-hour) and HN-3 (1-day) values. The HN-3 values in the wet season (May and June) also indicate that more water exists in both basins when compared to the Stage IV values.

We then compared the radar-based products with the gauged-based and satellite based rainfall products included in this study. The NLDAS-2 products were generated using gauge-only data. While Stage IV data has a spatial resolution of 4 km, the NLDAS-2 has an approximately spatial resolution of 13 km. The spatial distribution of the NLDAS-2 rainfall field seems to be similar to Stage IV, but very large values are smoothed out by the resolution of the dataset. For the MAP-NWS, rainfall is estimated for each sub-basin for which streamflow predictions are generated by the NWS. In this case, we can see the pattern of higher precipitation in the upstream region of the basin

and lower total precipitation in the southeastern area. However, some watersheds seem to not follow the correct pattern. For example, right in the middle of the Cedar River basin there is a sub-watershed with a low total rainfall value that is surrounded by sub-basins with larger total values.

In terms of the remotely-sensed datasets, both products overestimated rainfall for the southern part of the area and underestimated rainfall in the northwestern part of the area. The spatial pattern of remotely-sensed rainfall is completely different from the pattern observed in the radar- or gauged-based products.

For years 2002, 2003, and 2004

Figure VII-3 shows rainfall totals from March 1st to October 1st of 2002 (column 1), 2003 (column 2), and 2004 (column 3). For 2003 and 2004, the gauge-based products (NLDAS-2 and MAP-NWS) present spatial patterns and values that are similar to the radar-based products (Stage IV). This is expected since the Stage IV data is corrected by bias based on the gauge data. This is not true for 2002, for which NLDAS-2 seems to present slightly higher rainfall total values that are more homogeneous in space than the other two products. In all the cases, precipitation is overestimated by the satellite products.

Comparison of simulated peak flow
based on different products

For the 2008 flood event

Figure VII-4 presents observed (gray lines) and simulated hydrographs (light blue line for SAC, continuous dark blue line for C-Stage IV, and dashed dark blue line for C-HN-3) for selected sites in the study area. I first discuss the results for sites 2, 3, and 5. These sites are located in the region affected by the inaccurate matching of different

individual radar-rainfall maps. Site 5 is entirely included in the affected area and, especially for this site, results obtained with HN-3 products are significantly better than the ones obtained using Stage IV. Sites 2 and 3 are partially located in the affected area, and HN-3 results are also slightly better for these sites. Site 7 is located in the northern part of the Cedar River Basin and is one of the sites for which Stage IV presented better results than HN-3. Both Stage IV and HN-3 overestimated discharge for this site, while SAC-SMS underestimated discharge for this site. The reason for these discrepancies is clear when we look at the accumulated values in Figure VII-2. For product HN-3, there is a cluster with very high rainfall located at the northern part of the basin. Further studies are required to explain the origin of these inconsistencies; however, they might be a consequence of uncertainties in observed streamflow or result from the merging of the KMPX and KARX radars that was not adjusted in this study. The last hydrograph presents an example of streamflow time series with missing data. In this case, no data is available for the likely period when peak flow happened.

In Figure VII-5, I present the relative difference between simulated peak flow based on Stage IV data and simulated peak flow based on the rainfall datasets evaluated in this study for the 2008 event. Positive values mean that the simulated peak flow was underestimated compared to results obtained using the Stage IV data. In each plot, I present the rainfall product used as forcing for the simulation on the right and the relative peak flow difference for the outlet on the left. Even though higher resolution datasets are available, I opted to use Stage IV as a reference, since it is the dataset available for all the events analyzed in this chapter. Moreover, this study attempts to demonstrate the magnitude of the difference in simulated peak flow that one can obtain when forcing the

hydrological model by different rainfall products. This evaluation cannot be performed when parameters are calibrated since parameter values compensate for errors in the input.

I present results for all different radar-based products. These products are all based on the same raw data (radar reflectivity) but use different methodologies to process this data and transform it into final rainfall products. Even in this case, large relative differences (on the order of 20%) are observed for the peak flow at the outlet of the basin. For smaller scales, differences are even larger. For example, for scales around 1 km², differences vary from +40 (underestimated compared to Stage IV) to -100% (overestimated compared to Stage IV). For the NLDAS-2 products, differences for small scales are significant, but as the basin scale increases differences decrease. The value for the outlet of the basin is practically the same as the one obtained using Stage IV data, which indicates that the volume of rainfall estimated by both products might be very similar. However, both products present differences in terms of where and when the rainfall occurred.

The CMORPH product presents a small difference in terms of peak flow for the outlet of the basin (20%). When we look at the total rainfall maps, we see that over the study area, the product compares relatively well with Stage IV data in terms of accumulated rainfall. However, the same did not occur in the southern part of the area, where rainfall was overestimated. The PERSIANN products basically did not capture the rainfall events that occurred over the Cedar River basin, and peak flow was underestimated in this case (0.71% for the outlet).

Results in this section were based on short term simulations (May 28th to July 1st) since high-resolution radar rainfall data was only available for that period. However, in Figure VII-6, I present results for long term simulation (March 1st to October 1st) to demonstrate some features of the satellite products. In this figure, we can see that CMORPH captured well the main event that occurred during June of 2008 but

overestimated an event that occurred in July, for which simulated peak flows were even higher than the ones observed during June.

Peak flow simulation for years 2002, 2003, and 2004

For the years 2002, 2003, and 2004, I evaluated two gauged-based products (NLDAS-2 and MAP-NWS), one radar based product (Stage IV), and two satellite-based products (PERSIANN and CMORPH). Figure VII-7 presents the relative difference between peak flow predicted using the reference dataset (Stage IV) and other datasets (NLDAS-2, MAP-NWS, PERSIANN, and CMORPH). As expected, differences in simulated peak flow for small scales are very large for all products. For gauged-based products, differences for the outlet of the basin vary from around 10% for NLDAS-2 product year 2003 to 66% for MAP-NWS product year 2004. For the satellite-based products, differences are enormous for all scales and all years. This is due to the high differences observed in the rainfall accumulated values.

Figure VII-8 Figure VII-9 show simulated hydrographs based on different rainfall products for 2003 and 2004, respectively. For 2003, I present results from the gauged-based and satellite-based products. Comparing the results of gauged-based products and the result obtained with Stage IV, I conclude that the first peak was underestimated in all cases. It is difficult to define the cause of this underestimation. All the products successfully capture the base and the second peak that occurred in July. This figure also demonstrates the cause of large differences in peak flow observed for the satellite-based products. The first peak is captured well by the PERISANN dataset. However, the CMORPH dataset did not capture this event at all. For the second peak, both products overestimate rainfall values.

For 2004, I present one example for a gauged-based product (MAP-NWS) and one example for a satellite-based product (PERSIANN). In the first case, the peak is underestimated. For 2004, the rainfall totals and spatial pattern provided by the gauged

and radar based products are very similar. Therefore, the underestimation in peak flow might be the result of coarse resolution of the data and underestimation of peaks during the main events. For this event, satellite products also overestimate rainfall values.

Conclusions

Rainfall is the main forcing for floods. For the US, different sources of rainfall datasets are available based on gauge (MAP-NWS, and NLDAS-2), radar (Stage IV and Hydro-Nexrad datasets), and satellite (PERSIANN, CMORPH, and TRMM) information. In this chapter, I compare these different products in terms of total rainfall amounts and how differences in rainfall estimation propagate through the hydrological model and affect simulated peak flow.

I began by analyzing rainfall products for the 2008 flood event. I demonstrated inconsistencies in the Stage IV weather radar rainfall product provided by the National Weather Service that arise from the calibration mismatch between different radars covering the same area. This mismatch causes artificial features in the merged dataset. Seo et al. (in preparation) used an online version of the Hydro-NEXRAD and a methodology proposed by Seo et al (2012) to remove this undesirable feature and produce higher quality rainfall datasets. I first confirmed that using higher quality rainfall datasets improves hydrological prediction for the affected areas. This is not always true when a model is calibrated based on a “lower quality” dataset, since parameters will compensate through the specific error structure of this dataset.

I then compare the different datasets in terms of total accumulated rainfall during the 2008 event. While weather radar and gauged-based products present similar values and spatial distribution, satellite products present significantly different features. I forced the hydrological model with the different products to investigate the effects on peak flow simulation. This exercise demonstrated that even products based on the same raw data (weather radar) can provide significantly different results for simulated peak flow for

small scale basins. However, this difference tends to decrease as basin area increases. Simulations based on satellite products presented large differences across scales. The hydrographs showed that CMORPH was able to correctly capture the main rainfall event that occurred in 2008 but overestimated an event in July that resulted in even higher simulated peak flows.

I repeated the same experiment for the years of 2002, 2003, and 2004, comparing total accumulated rainfall for different rainfall products and using these different products to force the hydrological model. I confirmed high uncertainties in remote sensing information. I used the hydrographs to reveal that satellite-based rainfall product uncertainties are not deterministic: rainfall can be detected but overestimated (normally the case), detected and underestimated, not detected, or falsely detected. A better understanding of the causes of these uncertainties is required to use this data to predict floods.

The results presented in this chapter point to a big challenge for flood prediction: the correct estimation of rainfall intensity and space and time variability using satellite-based remote sensing information. Even in cases for which ground instruments (gauge and weather radar) are available, as for the study area, large discrepancies are observed among the different products, especially when considering large watersheds covered by different instruments. The development of global datasets will require methodologies to aggregate all available rainfall information (e.g., weather radar, gauge data, and satellite base rainfall) in a consistent and optimized way to reduce uncertainties in rainfall estimation. Moreover, more analyses are required to understand event-by-event uncertainties in satellite-based rainfall estimation instead of focusing on the analyses of monthly or yearly accumulated total rainfall.

Table VII-1. Precipitation satellite products.

Short Name	Provider	ΔS	ΔT	Type	Period	Reference
Radar Products						
Stage IV	NWS	0.05°	1h	Non-polarimetric radar	1998-2011	(Fulton et al., 1998)
Hydro-Nexrad product 1	IIHR	0.05°	60 min	Non-polarimetric radar	By request	(Seo et al., 2011)
Hydro-Nexrad product 2	IIHR	0.05°	60 min	Non-polarimetric radar	By request	(Seo et al., 2011)
Hydro-Nexrad product 3	IIHR	0.05°	60 min	Non-polarimetric radar	By request	(Seo et al., 2011)
Hydro-Nexrad product 3	IIHR	0.016°	5 min	Non-polarimetric radar	By request	(Seo et al., 2011)
Satellite Products						
TMPA-RT	NASA-GSFC	0.25°	3h	IR-PMW	1998-2011	(Huffman et al., 2007)
PERSIAN N	University of California, Irvine	0.25°	3h	IR-PMW	2000-2011	(Sooroshian et al., 2000)
CMORPH	NOAA/CP C	0.07°	30 min	IR-PMW	2002-2011	(Joyce et al., 2004)
Other datasets						
NWS – MAP**	NWS	Sub-basin	6h	Combined radar and GM*	1998-2011	(Huffman et al., 2007)
NLDAS2 forcing	NASA-GSFC	1/8°	1h	Combined and GM*	2000-2011	(Sooroshian et al., 2000)

Source: Ebert, E.E., Janowiak, J.E., Kidd, C., 2007. Comparison of near-real-time precipitation estimates from satellite observations and numerical models. *Bolletin of American Meteorological Society* 88, 47–64

* GM – Ground measurement - ** MAP – Mean areal precipitation.

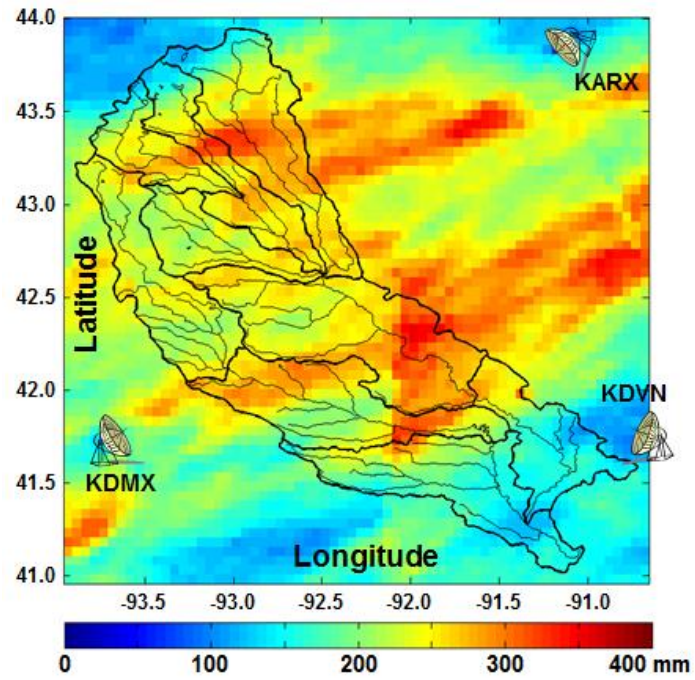


Figure VII-1. Rain total map of the Stage IV for May 30 to June 15 in 2008 over the Iowa River and Cedar River Basins.

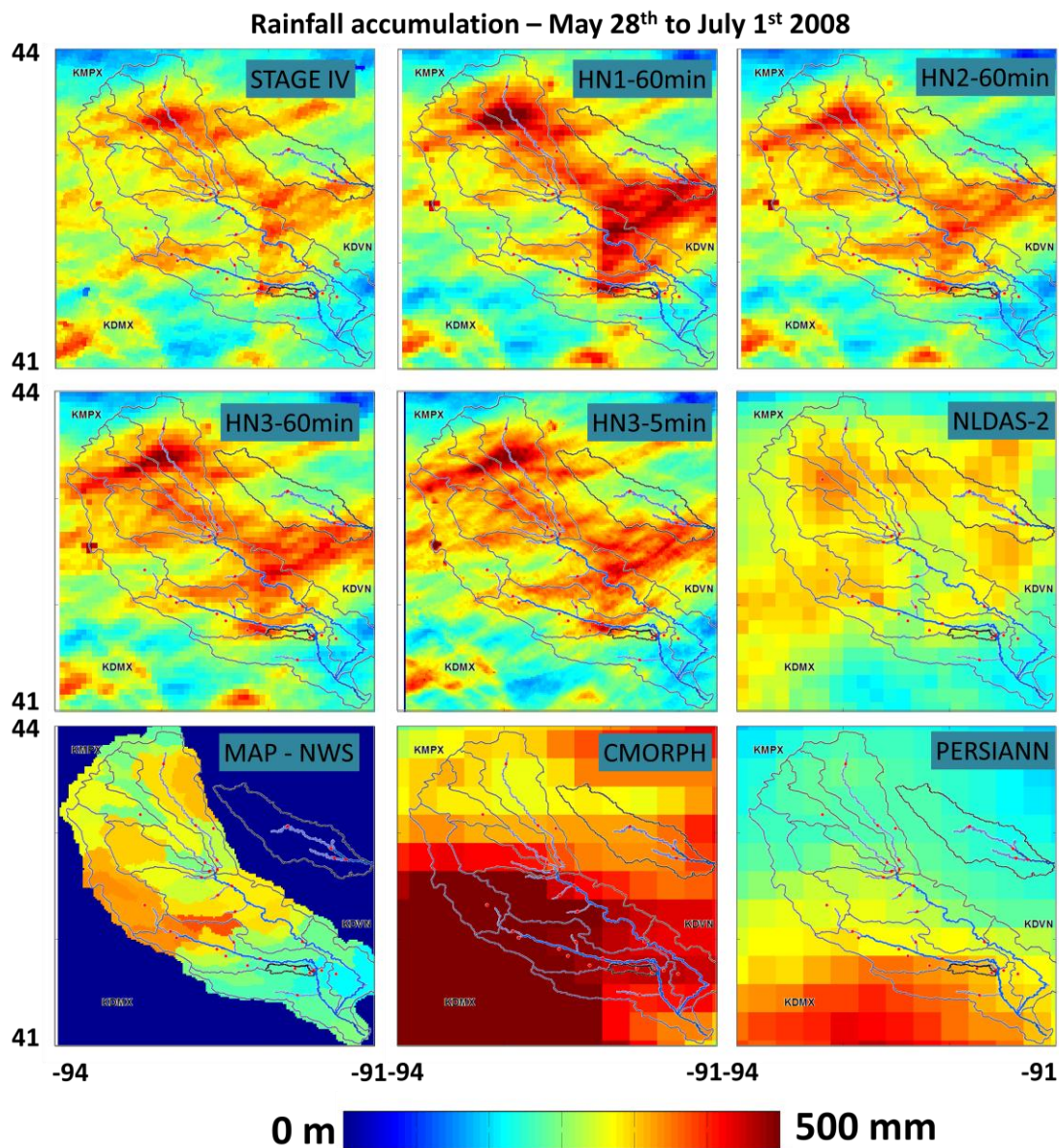


Figure VII-2. Rain total maps for different products (indicated in the figure) for the period of May 28th to July 1st 2008.

Note: HN- Hydro-Nexrad, NLDAS-2 – North Land Data Assimilation System 2, MAP – NWS – mean areal precipitation from the National Weather Service, CMORPH - Climate Prediction Center morphing technique, and PERSIANN - Precipitation Estimation from Remotely Sensed Information using Artificial Neural Network

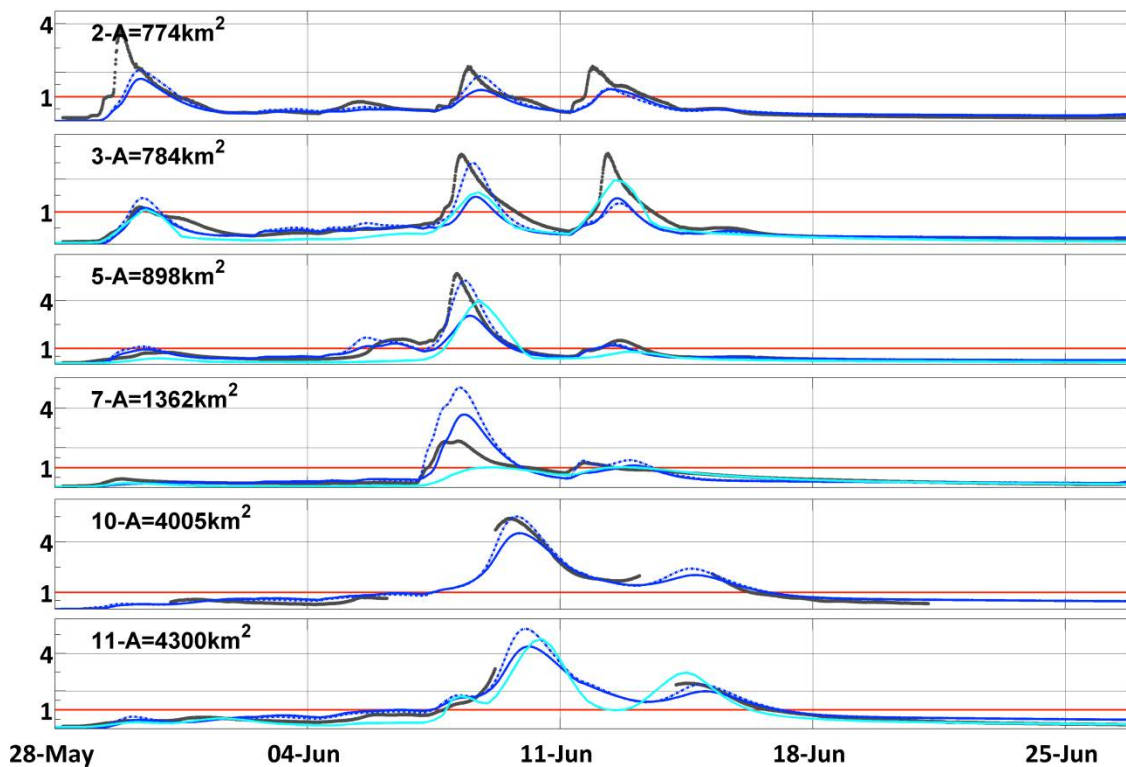


Figure VII-4. Selected hydrographs showing observed and simulated hydrographs: gray lines represent observed, light blue light simulated using SAC, dark blue continuous line simulated by CUENCAS forced by Stage IV, and dark blue dashed line simulated by CUENCAS forced by HN-3 – 60 min.

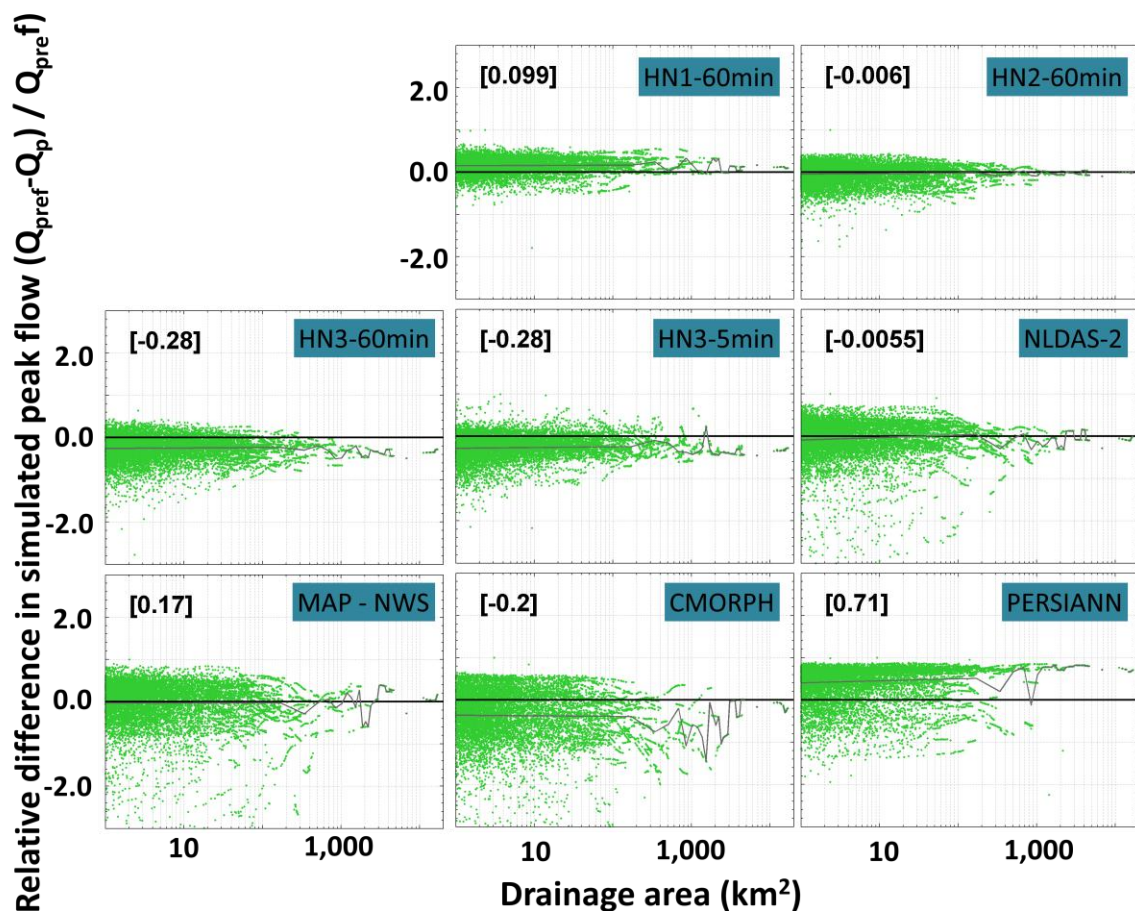


Figure VII-5. Relative difference in simulated peak flow based on Stage IV (reference) and other rainfall datasets for the 2008 events. The rainfall dataset is indicated in each plot.

Note: HN- Hydro-Nexrad, NLDAS-2 – North Land Data Assimilation System 2, MAP – NWS – mean areal precipitation from the National Weather Service, CMORPH - Climate Prediction Center morphing technique, and PERSIANN - Precipitation Estimation from Remotely Sensed Information using Artificial Neural Network

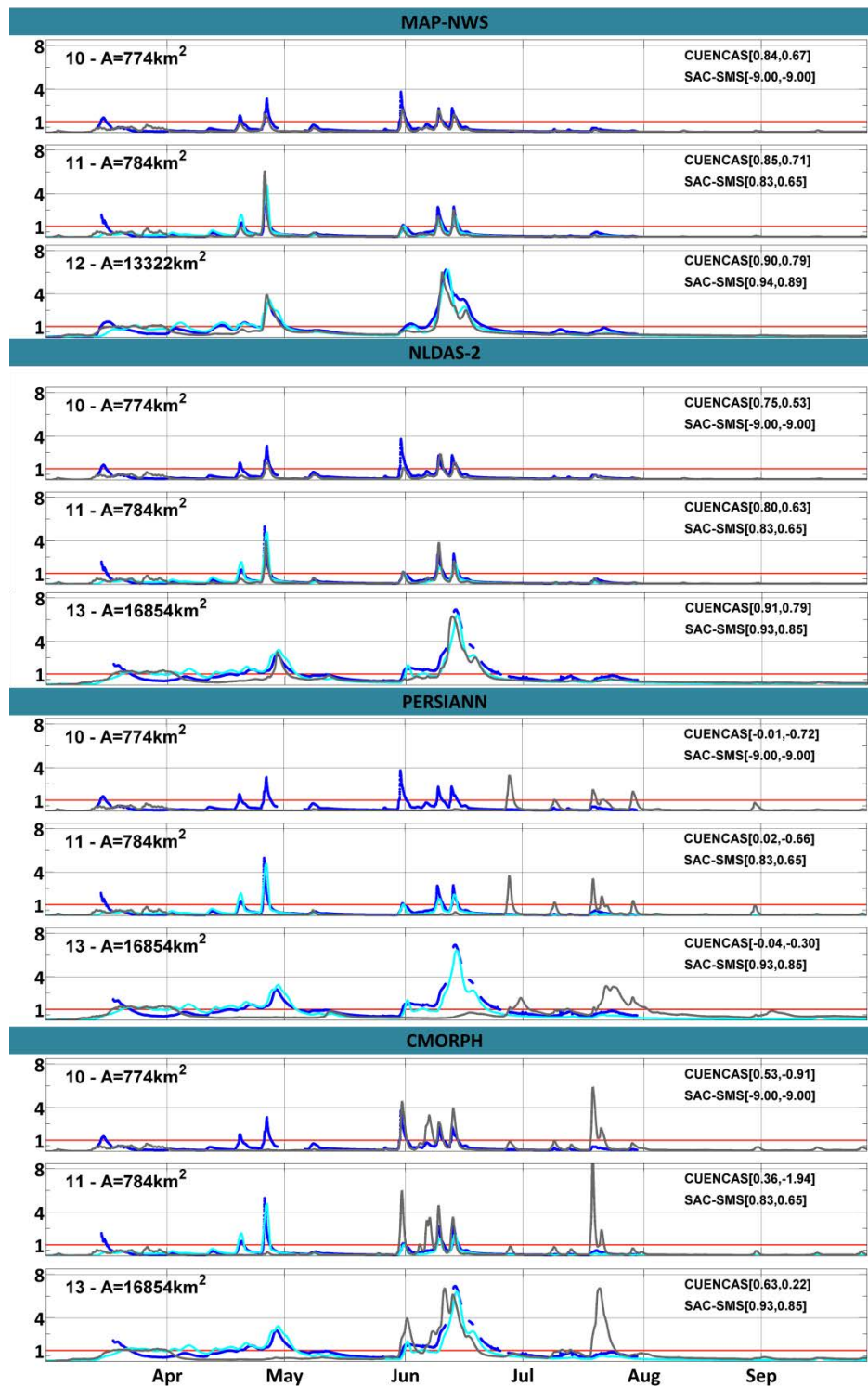


Figure VII-6. 2008 hydrographs simulated based on (1) NLDAS-2, (2) NWS-MAP, (3) CMORPH, and (4) PERSIANN.

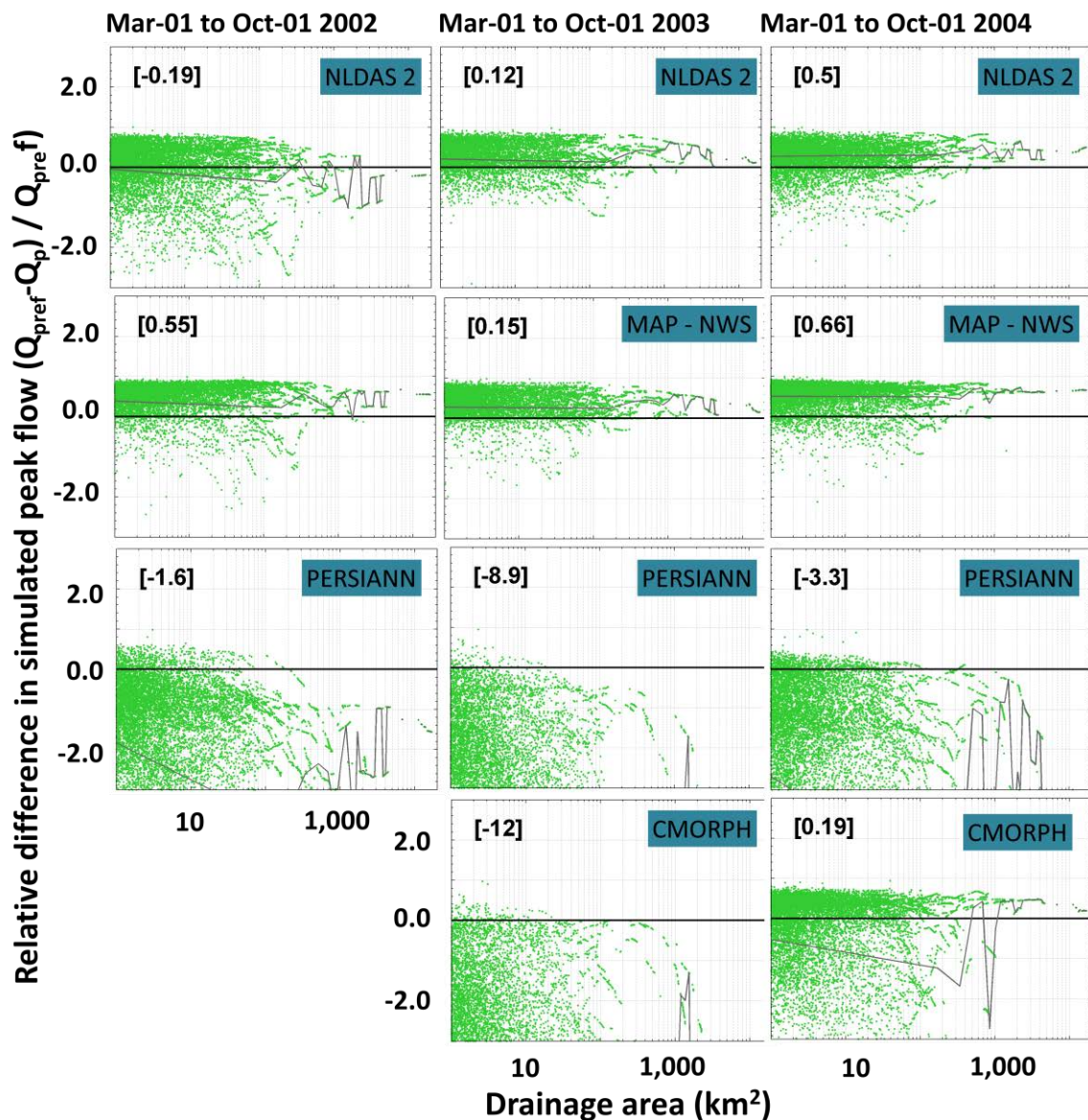


Figure VII-7. Relative difference in simulated peak flow based on Stage IV (reference) rainfall and other rainfall datasets for 2002 (column 1), 2003 (column 2), and 2004 (column 3). The rainfall dataset is indicated in each plot.

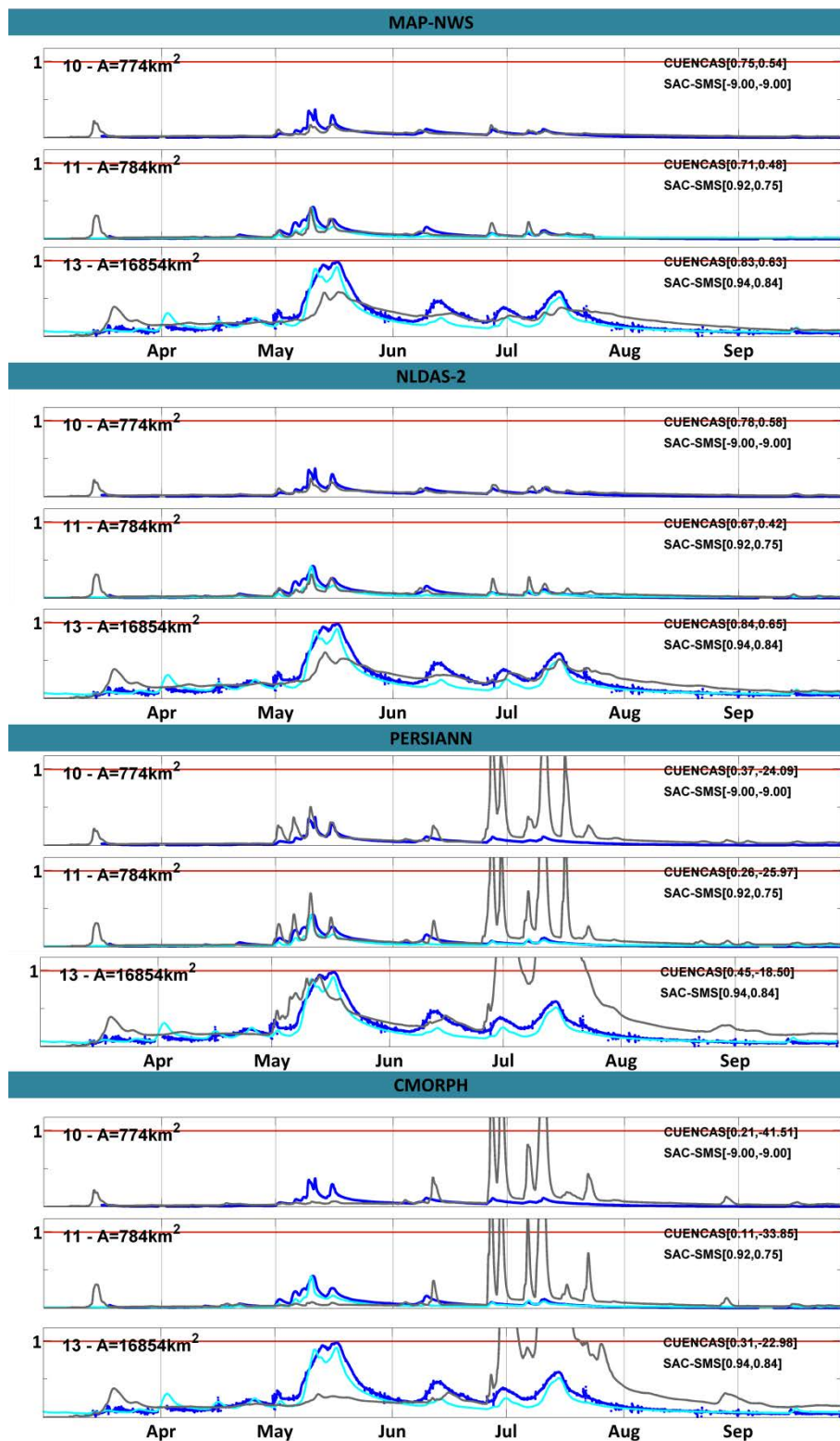


Figure VII-8. 2003 hydrographs simulated based on (1) NLDAS-2, (2) NWS-MAP, (3) CMORPH, and (4) PERSIANN.

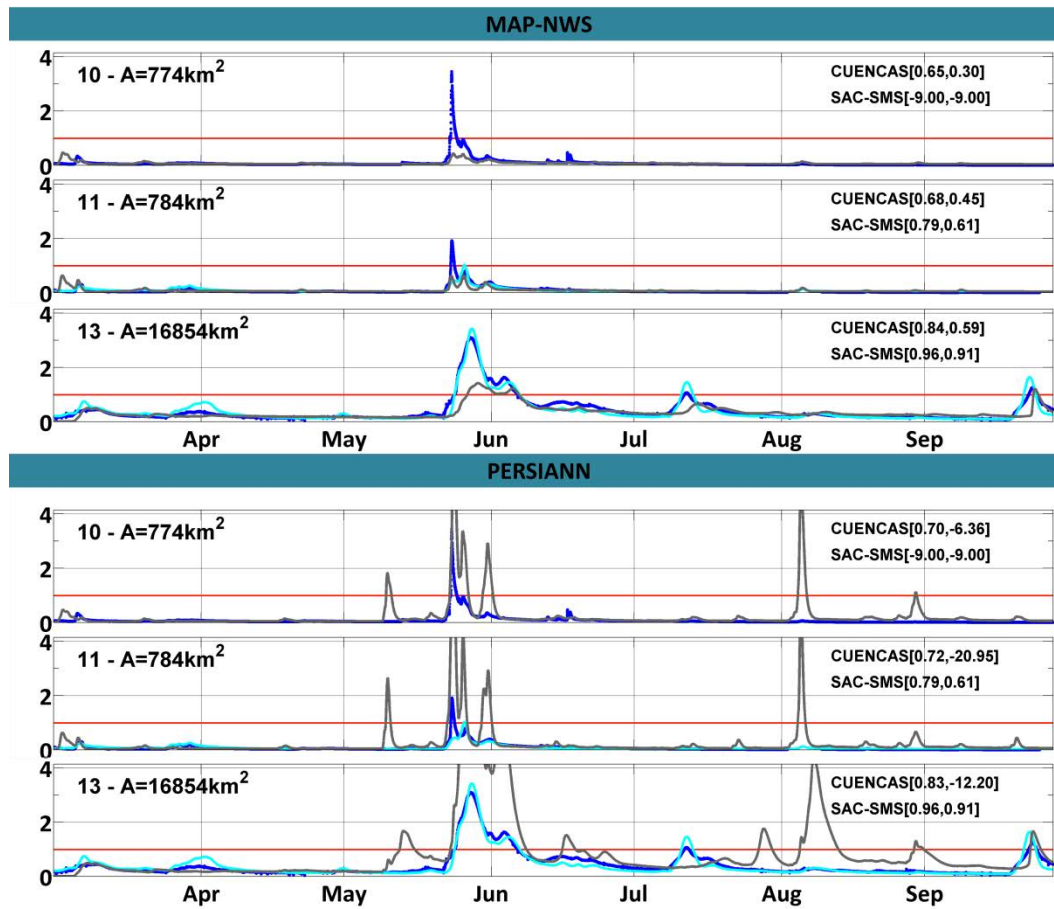


Figure VII-9. 2004 hydrographs predicted based on (1) NWS-MAP and (2) PERSIANN.

CHAPTER VIII THE IMPACT OF EVAPOTRANSPIRATION AND SOIL MOISTURE INITIAL CONDITION ON FLOOD PEAK SCALING

Introduction

Potential evapotranspiration (PE) is one of the forcings of the model. Even though contributions from evapotranspiration are not expected to be significant during the period of a single rainfall event (hours, days, or even weeks), in the long term (months and seasons), evapotranspiration dynamics strongly affect the soil moisture initial condition and can be the determining factor shaping the magnitude of a flood. As demonstrated in Figure 1-1, evapotranspiration accounts for an average of around 60% of the water balance, while runoff accounts for an average of around 40%.

Evapotranspiration strongly affects soil moisture content, especially between rainfall events in the summer and spring seasons, and consequently plays an important role in floods that occur during these seasons.

In this study, I performed continuous streamflow simulation from March to September. I did not perform simulations for the winter season since the model does not have a component that accounts for infiltration and percolation in frozen soils. I first needed to estimate the surface, channel, and soil moisture initial conditions for the beginning of the simulation, and I assumed that the channel and surface were empty at the beginning of the simulation since these reservoirs have a relatively low concentration time. This assumption affected results for the initial period of the simulation. However, soil presents a higher time of concentration, and an incorrect assignment of initial conditions in March might affect simulations of floods during the spring and summer seasons.

In this chapter, I present the preliminary results from a sensitivity analysis to assess the impact that bias in the estimation of PE or soil moisture initial conditions has on simulated peak flow across scales. I investigate the impact of these variables on

simulated peak flow for the following years: 2002 (dry condition), 2003 (medium condition), 2004 (intense flood), and 2008 (extreme flood). In Chapter 3, I presented simulation results for these years. This chapter complements the analysis presented in Chapter 4, which evaluated the impacts of DEM uncertainties, and Chapters 5, 6 and 7, which evaluated the impact of precipitation uncertainties.

This chapter is organized as follows: I first describe the datasets used to estimate PE and soil moisture initial conditions. I then describe the methodology adopted for the sensitivity analysis and the main results. I close the chapter with conclusions.

Datasets

Potential evapotranspiration

PE is an input into the hydrological model which is used to estimate the actual evaporation from the surface and from the unsaturated and saturated layers of the soil. Dingman (2002) defines PE as “the rate at which evapotranspiration would occur from a large area completely and uniformly covered with growing vegetation which has access to an unlimited supply of soil water and without advection or heat-storage effect”. Using PE to calculate actual evaporation corresponds to assuming that the only limitation for evaporation is water availability. In the model formulation, no limitations are imposed on the evaporation of water from the surface storage. Limitations are imposed to evaporation from the unsaturated and saturated layers of the soil. In the current version of the model, the percentage of available water that evaporates from the soil is a function of the soil’s volumetric moisture and the water table.

I adopted two different data sources: (1) PE estimated based on remote sensing (MODIS 16, see a review in Mu et al., 2011) and (2) PE used as forcing by NLDAS-2 that was computed in the NCEP North American Regional Reanalysis using the modified Penman scheme of Mahrt and Ek (1984). MODIS products are provided with 1 km in

space and 8 days resolution in time, while the NLDAS-2 products are provided with 1-hour resolution in time and $1/8^\circ$ ($\sim 13\text{km}$) resolution in space.

Soil moisture initial conditions

The initial conditions of the soil are estimated based on the NLDAS output that provides spatially distributed total soil column wetness (0-200 cm) with hourly and 0.125° resolution (Fan et al., 2006).

Methodology

First, I compared the simulations obtained using the two different datasets for PE described in the previous section, using peak flow simulated based on the NLDAS dataset as a reference. Next, I modified the NLDAS dataset, increasing or decreasing PE by a constant ratio equal to -20% (decrease in PE), 20%, 40%, and 70% to evaluate the effects that bias in PE estimation has on simulated peak flow.

For the evaluation of the sensitivity of peak flow to initial soil moisture, I used as reference the simulation generated based on soil initial conditions estimated using the NLDAS-2 output for the soil moisture condition. NLDAS-2 provides spatially distributed total soil column wetness (0-200 cm) with hourly and 0.125° resolution. I compared this result with results obtained by setting the spatially constant initial moisture conditions equal to 0.3, 0.5, and 0.7 volumetric soil moisture in the unsaturated layer of the soil. In all of the cases, the water table is set initially to zero.

In this chapter, I use the same metrics used in chapters 6 and 7 and 8 to evaluate the effects of precipitation on simulated peak across scales. I evaluate the relative difference in peak flow simulated based on the different potential evapotranspiration and soil moisture scenarios.

Results and Analysis

In Figure VIII-1, I present the results from the sensitivity to potential evapotranspiration. I plot the relative difference between peak flow values that were simulated based on NLDAS and MODIS potential evapotranspiration (line 1) and on the modified NLDAS potential evapotranspiration datasets produced by decreasing (0.8-line 2) or increasing (1.2 -line 3, 1.4 -line 4, and 1.7-line 5) potential evapotranspiration by a constant rate for the years 2002 (column 1), 2003 (column 2), 2004 (column 3), and 2008 (column 4). For all the simulations, I adopted the same DEM (90 meters NED) and rainfall products (Stage IV). The sensitivity to potential evapotranspiration varies from year to year. It is interesting to note that for the years 2002, 2003, and 2004, reduction in peak flow due to an increase in potential evapotranspiration for the outlet of the basin was almost linearly related to the rate of change in the potential evapotranspiration. However, the same is not true for the 2008 flood, for which an increase in potential evapotranspiration of 40%, for example, caused a decrease in peak of just 13% for the outlet of the basin. This result confirms that the major flood that occurred in the Cedar River in 2008, previously denominated the perfect storm, was caused mainly by the spatial distribution and the timing of the storm events as well as their relation to the movement of the water in the river network.

Figure VIII-2 presents results for the soil moisture analyses. In this case, I fixed the soil moisture initial conditions in March 1st to a constant spatial value of 0.3, 0.5, 0.7, and 1.0 and compared them with the results for which the initial condition was estimated based on the NLDAS-2 dataset. Results demonstrated that simulated peak flow is affected by the initial condition; however, the effect decreases as basin scale increases. The sensibility to soil moisture initial conditions changes from year to year, and the magnitude of the effect probably depends on when the flood event occurred. If the flood event occurred during the spring or at the beginning of the summer season, as was the case in 2003 and 2004, the effect of initial moisture conditions is larger. When the event

happens at end of the summer or in the fall, it is not strongly affected by the initial condition set on March 1st since a couple of months, including the wet season, seems to be enough for the spin-up process.

The results demonstrate that evapotranspiration strongly affects peak flow simulation, while the effects of initial soil moisture are not so significant. The small sensibility to soil moisture initial conditions might be the effect of model spin up. Therefore, if the event occurs at the beginning of the simulation, the effects of errors on the definition of the initial soil moisture conditions will be larger than if the event occurs at the end of the season.

Conclusions

The goal of the analyses presented in this chapter was to understand the impact of errors on the estimation of potential evapotranspiration and soil moisture on peak flow simulation. I demonstrated that simulated peak flow is affected by errors in the estimation of potential evapotranspiration. As errors in the estimation of evapotranspiration introduce positive or negative bias on runoff generation and, consequently, peak flow, errors tend to increase as basin scale increases. However, for the 2008 event, potential evapotranspiration had a smaller effect since peak flows were determined by rainfall space time variability and transport through the river network. In these cases, when a large volume of water reaches the basin in an optimized manner to generate floods, evapotranspiration is not efficient in removing enough water from the landscape to significantly reduce peaks.

The small sensibility to soil moisture initial conditions might be the effect of model spin-up. If the main flood event during a specific year occurs at the beginning of the simulation period (March 1st), the effects of errors on the definition of the initial soil moisture conditions will be larger than if the event occurs at the end of the season.

Even though I have used very simple methods to simulate evapotranspiration and to estimate soil moisture initial conditions, these processes do not have a strong effect on peak flow simulation as compared to the effects of rainfall uncertainties. However, I believe that model results could be significantly improved, especially for dry periods, if the dynamics of the soil and evapotranspiration processes were better represented.

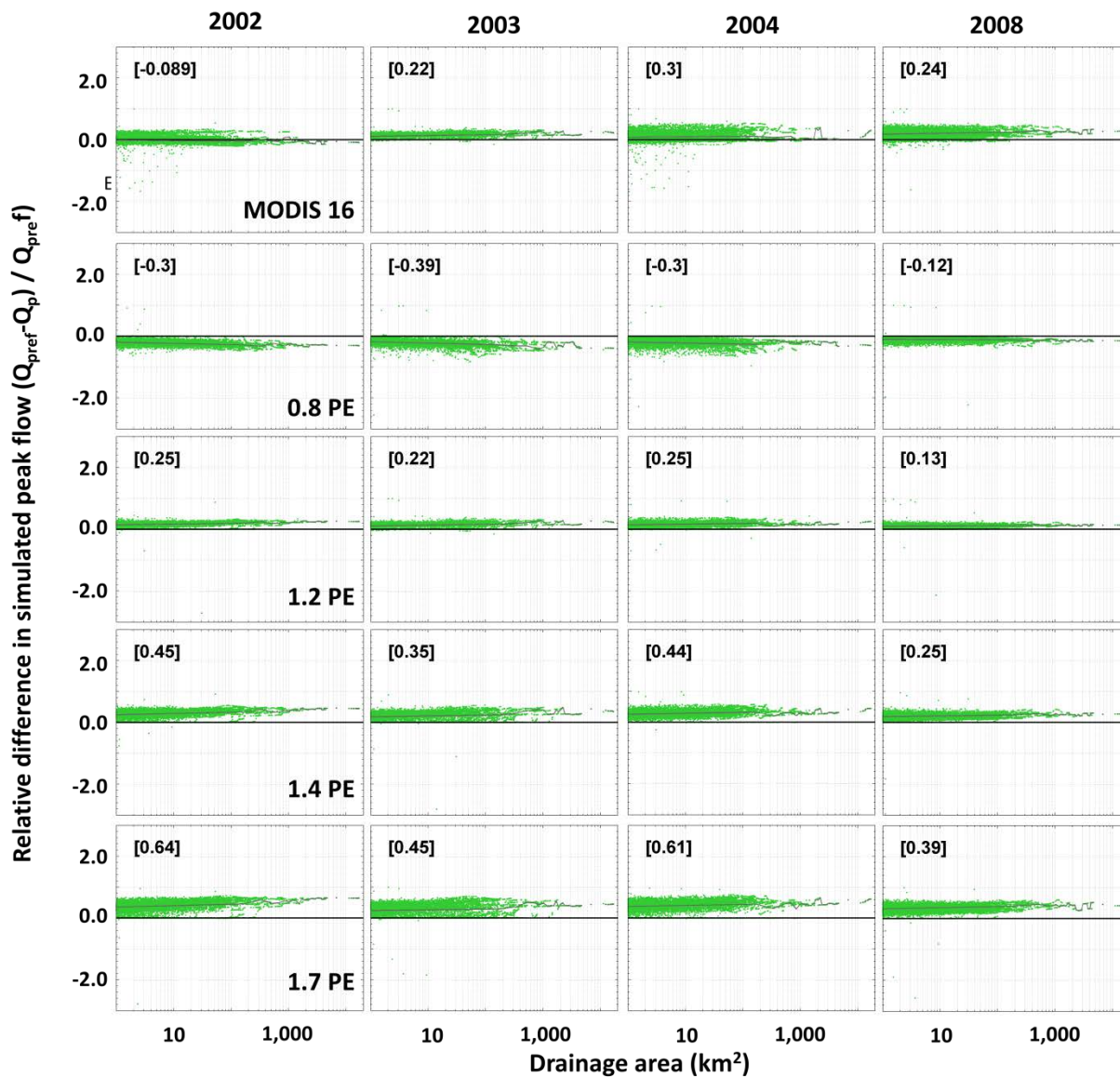


Figure VIII-1. Relative difference between peak flow simulated based on NLDAS and MODIS potential evapotranspiration (line 1) and for the modified NLDAS potential evapotranspiration datasets by a constant rate of 0.8 (line 2), 1.2 (line 3), 1.4 (line 4), and 1.7 (line 5) for the years 2002 (column 1), 2003 (column 2), 2004 (column 3), and 2008 (column 4), respectively.

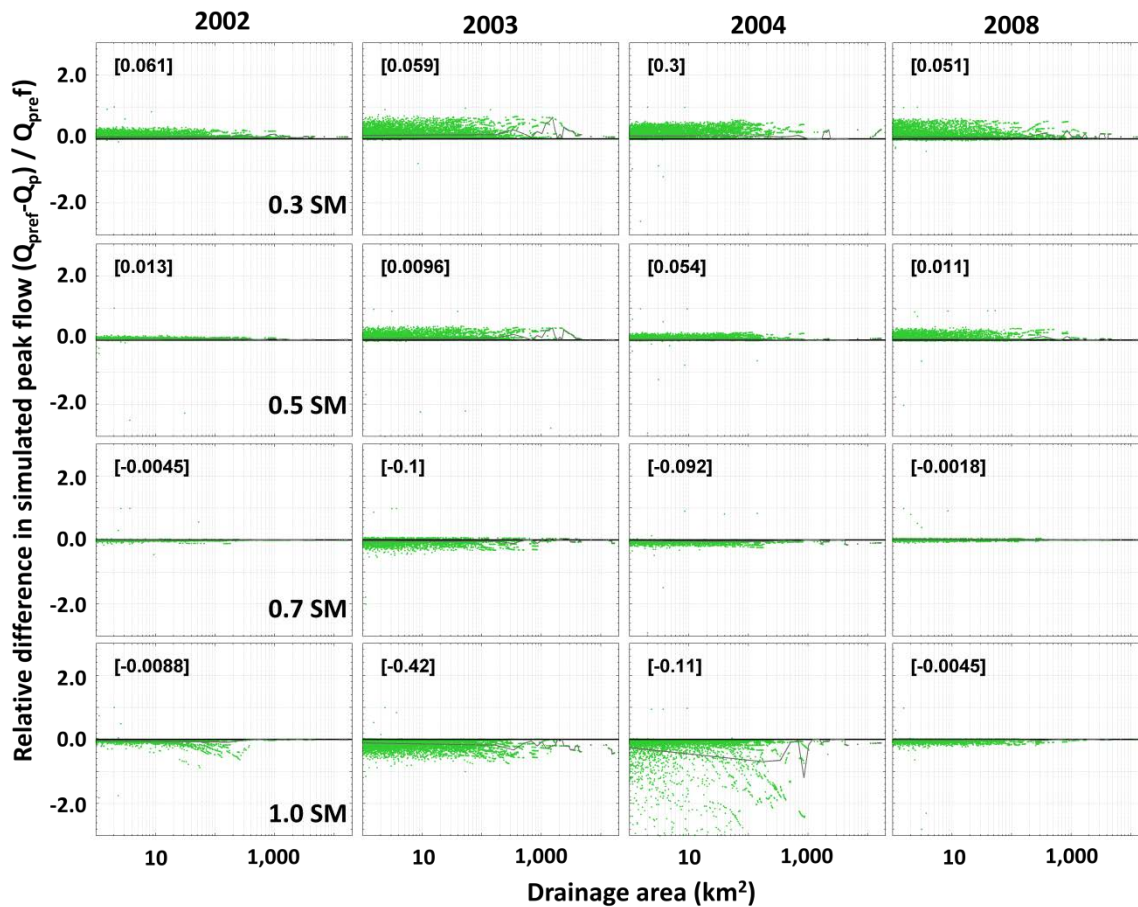


Figure VIII-2. Relative difference between peak flow simulated based on spatially variable soil volumetric moisture; initial condition provided by NLDAS output and constant soil volumetric moisture initial condition equal to 0.3 (line 1), 0.5 (line 2), and 0.7 (line 3).

CHAPTER IX

CONCLUSIONS AND RECOMMENDATIONS FOR FURTHER STUDIES

This thesis investigates the benefits and limitations of using satellite-based data for flood prediction. An un-biased evaluation of different datasets requires a hydrological model whose parameters are not calibrated with historical hydro-meteorological data since parameter calibration that is based on the optimal match between observed and simulated streamflow masks uncertainties in the data and model structure. Therefore, the first part of this thesis consists of the development and validation of a multi-scale, explicitly distributed hydrological model whose parameters are directly linked to physical properties of the watershed, thereby eliminating the need for calibration. The major conclusions of the first part of this study (Chapters 2 and 3) are summarized as follows:

- I demonstrated that, if an iterative approach for model building is adopted, it is possible to construct skillful models for flood prediction that do not rely on intensive parameter calibration. Rather than appealing for model calibration, this approach consists of systematically adding complexity to the model and evaluating the model's results to identify possible causes of mismatches with observed data.
- I revealed that when developing a calibration-free hydrological model, the complexity adopted in the conceptualization of physical processes is limited by data availability.
- I demonstrated the model's predictability skills by simulating the 2008 flood event for the Cedar River, Iowa River and Turkey River basins using the high-quality datasets that are available for the study area. I also performed simulations for drier years and, in this case, the model did not perform as well due to the high-nonlinearity of soil and evapotranspiration dynamics.

- I presented a study based on synthetic rainfall to illustrate the importance of using a multi-scale framework when validating the results of hydrological models.
- I demonstrated the model's predictability skills by simulating the 2008 flood event for the Cedar River, Iowa River and Turkey River basins using the high-quality datasets that are available for the study area. I also performed simulations for drier years and, in this case, the model did not perform as well due to the high-nonlinearity of soil and evapotranspiration dynamics.

The second part of this thesis uses the developed model to evaluate different datasets for flood prediction. The major conclusions of the second part of this study (Chapters 4 and 8) are summarized as follows:

- In Chapter 4, I evaluated how uncertainties in the extraction of the river network from DEM introduce errors into the characterization of hydrologically-relevant landscape properties and how these uncertainties propagate through hydrological models. I analyzed DEMs from different sources (LIDAR, NED, ASTER, and SRTM) and with different resolutions (from 30 to 90, 120, 150, and 180 meters). In addition, I created supplementary river networks by systematically pruning the small Horton-order streams. Results demonstrated that differences in simulated flows are more significant when I pruned the network than when I used coarse resolution DEMs or satellite-based DEM. This study highlights the importance of correctly representing the river network and its properties in hydrological models that focus on floods.
- In Chapter 5, I propagated radar-derived rainfall uncertainties through the hydrological model and demonstrated that peak flow uncertainty that arises from random errors, correlated or not in space, are scale dependent and decrease as the basin scale increases. When rainfall random errors are correlated in space, the process of aggregation and attenuation by the river network is not as effective at filtering out uncertainties. The deterministic component of the error tends to

produce a shift in the value of simulated peak flow up or down, but the width of the error band is still determined by the magnitude of the random error component and its spatial correlation.

- In Chapter 5, I investigated the impacts that rainfall resolution and low sampling frequency, features inherent in satellite-based rainfall data, have on flood prediction. The spatial and temporal resolution of the rainfall fields has a significant impact on simulated peak flow for small scales. However, this impact is also scale dependent and decreases as basin area increases. At some scales, the impact of rainfall spatial resolution disappears. Our results demonstrate that sampling frequency errors are critical for flood prediction since errors are not always filtered out by the river network.
- In Chapter 6, I performed simulations using the real products to evaluate how they differ from each other and to assess how these differences propagate through the hydrological model. This exercise demonstrated that even products based on the same raw data (weather radar) can provide significantly different results for simulated peak flow for small scale basins but that uncertainties tend to decrease as basin area increases. Rainfall satellite products presented large differences when compared to weather radar and gauged-based products, and both products failed to predict floods for the event evaluated in this study. The results presented in this chapter point to the great need in the hydrological community for the correct estimation of rainfall intensity and space-time variability.
- In Chapter 7, I performed hydrological simulations using various rainfall products to evaluate how different they are from each other and to assess how these differences propagate through the hydrological model. I demonstrated that significant differences are observed even for products based on the same raw data (weather radar or gauge data). However, in this case, uncertainties are also scale dependent and decrease as the basin area increases. Rainfall satellite products

presented large differences when compared to weather radar and gauged-based products, and both products (PERSIANN and CMORPH) analyzed in this study failed to correctly capture rainfall events over the study area for the analyzed events. I revealed that satellite-based rainfall product uncertainties are not systematic: rainfall can be detected but overestimated (normally the case), detected and underestimated, not detected, or falsely detected. A better understanding of the causes of these uncertainties is required before I can use this data to predict floods accurately. The results presented in this chapter illustrate the challenge of correctly estimating rainfall intensity and space-time variability over large areas.

- In Chapter 8, I presented the preliminary results from a sensitivity analysis to assess the impact that biases in the estimation of PE or soil moisture initial conditions have on simulated peak flow across scales. I demonstrated that the effect of PE bias on simulated peak flow depends on basin scale and slightly increases as basin area increases since this type of error introduces positive or negative bias into the estimation of runoff. The effect also depends on the intensity of the rainfall event and decreases as the rainfall intensity increases. I also demonstrated that the sensibility to soil moisture initial conditions is probably caused by the effect of the model's spin-up. If the main flood event of the year occurs at the beginning of the simulation period (March 1st), the effects of errors on the definition of the initial soil moisture conditions will be greater than if the event occurs at the end of the season.

APPENDIX

NETWORK HYDRAULIC GEOMETRY

Introduction

Understanding variation in river hydraulic geometry throughout stream networks is essential to solving water- and ecosystem-related problems due to the influence of this variation on flow and sediment routing, physical habitats, and channel–floodplain interactions (Stewardson, 2005). Hydraulic geometry (HG) equations were first presented by Leopold and Maddock (1953) to describe mean channel properties (water surface width W , average depth D , and average velocity V) as a power function of discharge (Q). Since then, these relationships have been widely applied to represent/model geomorphological, hydrological, ecological, and water management systems (e. g. Hogan and Church, 1989; Rhoads et al., 2003).

HG relationships can also be used to monitor relevant hydraulic and geometric river properties from space, and it has already been demonstrated that average surface water width can be accurately estimated from space (Smith, 1997; Stewardson, 2005; Ashmore and Sauks, 2006; Smith and Pavelsky, 2008). Combined with HG relationships, these measurements indirectly estimate channel discharge, velocity, and geometry, which constitute essential information for hydrological, geomorphologic, and ecological models. Remote sensing information will not replace the need for streamflow gauges, since high-resolution remote sensors usually present low temporal sampling rates (weeks to months for resolution of 10-30 meters). However, satellites observe river conditions with dense spatial sampling over large areas, providing a type of information that cannot be obtained by localized gauge instruments. Moreover, remote sensing systems provide continuous, low cost information with nearly global coverage, even for areas that are inaccessible, impoverished, or politically unstable.

Currently, different HG formulations are being used and investigated. At-a-station HG (AAS-HG) describes hydraulic and flow variations with discharge in a single river cross-section. River reach HG (R-HG) was proposed by Stewardson (2005) and attempts to describe mean and variance of hydraulic properties in a river reach, defined as being approximately 10-20 channel widths in length. In this version of HG, short-scale variability of natural river morphology, including pool and riffle sequences, are integrated into the calculation. Using the same functional form proposed by Leopold (1953) to describe river properties as a function of discharge into a river reach, the author concluded that five reach hydraulic variables are sufficient to characterize the gross hydraulic conditions along a river reach. The author also demonstrated that there is strong potential to develop empirical models to predict reach hydraulic geometry parameters. However, this version of HG neglects scale effects.

In this work, I investigate a third formulation called *Network HG (N-HG)*, which is shaped by the hypothesis that channel and flow properties are scale dependent and that the parameters that describe HG relationships are controlled by physical and climatic regional properties as well as by the characteristics of the river network. N-HG describes the relationship between flows and channel properties for rivers located in regions with similar characteristics. N-HG attempts to represent the average processes and properties that define river flow and geometry patterns, without focusing on local channel variations or specific locations (e.g. bridges and pools).

In the first part of this study, I demonstrate the scale dependence of the AAS-HG, which has already been demonstrated in the literature (Dodov, 2003; Mantilla, 2007) but has never been tested using a large dataset including multiple climatic regions. I estimated the AAS-HG parameters for a dataset with more than 18,000 sites covering a large range of drainage areas and climatic/physical regions. I concluded that coefficients of the HG relationships are scale dependent, while exponents present a weaker

dependency on drainage area. Motivated by these results, I adopted the *N-HG* functional form proposed by Paik (2004) and Mantilla (2007).

In the second part of this study, I used the same dataset to estimate N-HG parameters for the whole US territory. I demonstrate how parameters change in space and provide evidence for the link between N-HG parameters and physical and climatological aspects of the watershed. Further studies are required to define the functional relationship between these watershed properties and N-HG parameters.

Subsequently, I discuss the application of N-HG for flood simulation. I first present some limitations imposed by the assumptions adopted for the derivation of N-HG. I demonstrate the difference between “*flood wave velocity*” and “*water velocity*” in kinematic models, as it pertains to the model applied in this work. These differences limit the direct use of N-HG parameters estimated from the USGS hydraulic measurements for flood routing. I demonstrate that in order to correctly capture time to peak, the empirical parameter has to be corrected by a constant coefficient. I then estimate the N-HG parameters for the study area.

In the last part of this chapter, I demonstrate peak flow sensibility to N-HG parameters. NH-G relationships represent the variability of river channel and flow properties in space (area) and time (discharge). These properties impose an important control on the shape and propagation of flood waves throughout the river network, which controls flood generation. Paik (2004) and Mantilla et al. (2006) demonstrated that nonlinearities in flood generation could be explained by river network variability. Gupta (1998) and Mantilla et al. (2006) investigated the effects of different flow dynamics on peak flow scaling and found that different flow conditions strongly affect scaling parameters. I demonstrate how NH-G parameters affect peak flow generation across different scales and reveal that NH-G plays an important role in flood generation, especially for larger scale basins.

Data

This study is based on USGS measurement data, including channel average properties (velocity, discharge, water depth, section area, and surface water width) surveyed across the US and covering multiple climatic and physiographic regions and hydrological conditions. The survey serves the primary purpose of collecting data for the estimation of rating curves. Data has been collected since 1900, and the adopted measurement methods and expected measurement's uncertainty have changed during this period. To guarantee the use of high quality data, I used only the data that were flagged as good or excellent and that were not obtained under clear river conditions. A total of 709,400 measurements, for 18,857 different locations ranging in area from 0.016 to 2,925,460 km², were used.

Hirsch and Costa (2004) present a brief description of the measurement methods used by the USGS. Discharge is estimated based on the velocity-area method that consists of dividing the river into multiple sections. Vertical velocity distribution, section width, and depth are measured for each section. Unit discharge is estimated by the mean velocity times the cross-section area, and total discharge is the sum of the discharge of each section. Low to medium flows are typically measured by a technician who enters the river and wades along a stream's cross section. High flows with depths exceeding 3 feet are usually measured from a bridge near the gauge installation, from a cable car if available, or from a boat. Uncertainties in the estimation of these three parameters affect the estimation of channel discharge. Hirsch and Costa (2004), Stewardson (2005), and Harman et al. (2008) used typical uncertainty values specified in the ISO 748 (1997) to estimate an average value of expected relative error in the estimation of discharge equal to ± 5.7 percent. Stewardson (2005) and Harman et al. (2008) explored the contribution of error to apparent variation in hydraulic geometry parameters estimated from field measurements and models. Castro and Jackson (2001), Sweet (2003), Stewardson (2005), Faustini et al. (2009), and Mejia and Reed (2011) concluded that, despite the

uncertainties involved, HG parameters estimated from surveys, especially the ones including a large discharge range, are more reliable than parameters estimated by hydraulic models since models are likely to bias any exponent values.

USGS flow measurement sites are usually located at well-defined stream cross sections and sites with specific characteristics because shallower locations or locations on bridges are usually chosen. I acknowledge that this factor can introduce some bias into the estimation of the N-HG parameters (e.g. bridges are usually located in narrower sections of the river). However, the use of this dataset is justified since I focus on estimating average properties in a region and consider the main factors that shape these properties. The large amount of high quality data guarantees the estimation of significant N-HG parameters. Other authors have already applied part of this dataset to estimate the HG relationship for specific regions (Leopold, 1953; Castro and Jackson, 2001; Sweet, 2003; Faustini et al., 2009; Mejia and Reed, 2011).

At-a-station HG and scaling dependence

AAS-HG hydraulic geometry refers to the power laws relating the channel mean velocity V , width W , mean depth D , and section area (S) to discharge Q : $V = kQ^m$, $W = aQ^b$, $D = cQ^f$, and $S = dQ^g$. The dataset previously described was used to estimate AAS-HG exponents and coefficients in order to investigate whether there is evidence of scale dependency.

I used ordinary log-log least squares regression to estimate the relationships between velocity (V), water depth (D), surface water width (W), section area (S), and discharge (Does discharge have a letter variable?) using the original formulation proposed by Leopold (1953) and Western et al. (1997). I used sites with more than 50 samples to guarantee a reasonable sample size. This resulted in a total of 5,812 sites and 687,966 measurements. I estimated the coefficient of determination (R^2) for all sites and hydraulic variables. On average, discharge can explain approximately 58, 62, 76, and

87% of the river channel velocity, surface water width, water depth, and area cross section variability, respectively.

The dependence of AAS-HG parameters on the upstream contributing area has already been discussed in the literature. Western et al. (1997) and Dodov and Fofoula-Georgiou (2004) observed changes in stream shape for single channels and demonstrated trends in channel cross-sectional area and depth with distance downstream. Dodov (2004) and Dodov and Fofoula-Georgiou (2004) demonstrated the scaling effects on HG parameters and proposed a multi-scaling model to estimate the cross section area and velocity for which the coefficients of the AAS- HG are explicit functions of scale. Dodov (2004) and Mantilla (2007) provided a physical explanation for the scale dependency of HG parameters. Dodov (2004) hypothesized that the scale dependence of HG is a direct consequence of the systematic increase in channel cross sectional asymmetry over reaches of increasing scale and tested the hypothesis using observed data and a physical model of meandering rivers. Wooding (1965), Robinson et al. (1995), D'Odorico and Rigon (2003), and Mantilla (2007) hypothesized that the inclusion of drainage area in HG relationships accounts for scaling effects imposed by self-similar river networks and, consequently, physically derived the N-HG relationship for stream velocity.

Figure A.1 presents the relationship between AAS-HG parameters (coefficient and exponent) and basin area for the four hydraulic variables considered in this work (velocity, water surface width, depth, and cross-section area). The AAS-HG parameters present different levels of scale dependence. The coefficients for velocity, depth, and section area decrease with basin area, while the coefficient for surface water width presents the opposite effect. Exponents present a weak scale dependency, as demonstrated by the slope of the fitting lines presented in Figure A.1. The large spread observed in Figure A.1 demonstrates that AAS- HG parameters present a large variability that is not explained by the scale dependency. This variability is the result of

physical and climatic features that control channel morphology or of uncertainties in the measurements of hydraulic properties.

Network hydraulic geometry (N-HG)

Network HG (NHG) describes the relationship between flows and channel properties for regions with similar properties. Combining information for many sites in the same river network minimizes the local effects controlling channel local variability and provides information about the large-scale processes controlling river and flow properties. N-HG hydraulic geometry refers to the power laws governing the channel's mean velocity V , width W , and mean depth D to discharge Q and basin drainage area A : $V = v_0 Q^{\lambda_1} A^{\lambda_2}$, $W = w_0 Q^{\lambda_3} A^{\lambda_4}$, and $D = d_0 Q^{\lambda_5} A^{\lambda_6}$. The dataset previously described was used to estimate N-HG parameters: exponents for area and discharge as well as the coefficient. Assuming that N-HG is a property of the river network, the sites were grouped according to hydrological units (HU6), and the parameters for the sub-group were calculated if at least 3 sites (and, consequently, three different drainage areas) and 20 measurements were available.

Figure A.2 presents the geographic distribution of N-HG parameters. In the top of the figure, three relevant physical and climatologic maps are presented: (1) average terrain slope, (2) soil hydrological group, and (3) average annual precipitation. These maps were chosen to demonstrate some of the expected factors controlling hydraulic properties. It is expected that a combination of these factors, and likely others not included in this analyses, shapes the values of N-HG parameters in a certain region. However, the comparison of the thematic maps with N-HG parameters maps provides insight into the dominant aspects for each hydraulic variable. Velocity parameters are mainly controlled by terrain slope. I observe that regions with high slope (e.g. the Appalachian Highlands and Pacific Mountain System) present high coefficients and discharge exponents but low (negative) area exponents. The opposite pattern is observed

for flatter regions (e.g. the Atlantic Plain). Soil properties seem to exert an important control on water surface width. In this case, high coefficients and discharge exponents, and low area coefficients, occur in regions that present soils with high runoff potential (red - Group D, e.g. the Atlantic Plain and Intermontane Plateaus). The opposite effects are observed in regions that present soil with high infiltration potential (green - Group A, e.g. the Appalachian Highlands). Climatology, grossly represented in this study by the average annual precipitation, seems to impose a control on water depth parameters. Humid regions present higher coefficients and discharge exponents, while area exponents tend to be negative or close to zero. Very dry regions present low coefficients and discharge exponents, while the area exponent tends to be close to zero or positive.

Application for flood simulation

Flood wave velocity versus water velocity

Flood routing is an essential component of hydrological models. In an attempt to develop a calibration-free hydrological model, I have selected a flood routing method whose parameters could be directly obtained through data. I tried to avoid formulations that are computationally expensive, since I adopt a very fine discretization of the landscape and the number of links in the network is large.

While I apply the complete form of the Saint Venant Equations for flood routing, the solution to these equations requires the implementation of numerical methods to solve partial differential equations, which is computationally expensive. Hydrological models usually adopt simplified versions of the Saint Venant equations, which are simpler and require less time-consuming numerical solutions. The convection-diffusion equation neglects the effects of acceleration, while the kinematic-wave equations neglect the effects of acceleration and pressure-force. In the last case, it is assumed that the depth of the flow does not change in the channel. Therefore, the kinematic term refers to the flow

caused by mass and force only, without accelerations due to changes in depth and velocity.

Chezy and Manning's equations, which are widely applied in hydrology and hydraulics, are special cases of the kinematic wave formulation. One difficulty in applying these equations is the need to define roughness coefficients and slopes for each link. The slope of a link (with an approximate length of 200 m) cannot be accurately estimated based on digital elevation models because they do not provide elevation of the channel bottom. The estimation of the roughness coefficients can theoretically be determined based on field investigation. However, these coefficients change considerably from site to site, and for the same site they also change with flow depth. Due to this difficulty, the roughness coefficient is usually calibrated based on observed streamflow data. Therefore, this formulation is not appropriate for our calibration-free approach.

The N-HG formulation is also a special case of the kinematic wave equation since one of the assumptions used by Mantilla (2007) to derive this equation is that channel depth does not change across the link. The advantage of this formulation is that parameters can be obtained through low cost field campaigns that measure flow velocity and discharge throughout the river network. These measurements can be obtained at any time, so there is no need for historical records.

The kinematic assumption imposes some limitations on the direct use of the empirically estimated parameters for flood simulation. By definition, the speed that the water moves downstream (flood wave velocity or celerity) is different from the velocity of the water at a point. Water velocity is equal to $v=Q/A$, while the celerity or kinematic velocity is defined by $c=\partial Q/\partial A$. This means that the flood wave travels at a speed determined by the incremental change in discharge with respect to changes in the channel area. Field campaigns measure the velocity of the water, while the model propagates the flood wave based on celerity. Therefore, I need to correct the velocity obtained by the

USGS measurements by a coefficient that is the inverse of the kinematic ratio $k=c/v$.

This ratio is defined by:

$$k = \frac{c}{v} = \frac{1}{v} \frac{\partial Q}{\partial A} = \frac{1}{v} \frac{\partial(vA)}{\partial A} = 1 + \frac{A}{v} \frac{\partial(v)}{\partial A} \quad \text{Equation 1}$$

If I assume that the width of a link is constant, the cross-section area is equal to the average depth times the width:

$$k = 1 + \frac{d}{v} \frac{\partial v}{\partial d} \quad \text{Equation 2}$$

Based on hydraulic similarity, Mantilla (2007) defined velocity in a link as:

$$v = f_r d^m \gamma^n \quad \text{Equation 3}$$

Where f_r is a friction factor, d is the water depth, and γ is the link slope. If I substitute this equation in Equation 4-2, I can calculate the kinematic ratio k :

$$k = 1 + \frac{d}{v} \frac{\partial f_r d^m \gamma^n}{\partial d} = 1 + m \frac{d}{v} f_r d^{m-1} \gamma^n = 1 + m \quad \text{Equation 4}$$

Where m defines the rate at which velocity changes with water depth. This value can also be obtained by field campaign measurements. In many hydraulic models (e.g. Manning), m is equal to $2/3$, which results in a final $k=5/3$. Therefore, to correctly estimate celerity in the flood routing model, I need to multiply the velocity estimated based on USGS measurements (v) by $3/5$ (0.6).

Parameter estimation for real events simulation

I estimated the parameters of the N-HG relationships for the Cedar River, Iowa River, and Turkey River basins. Figure A.6 presents the observed versus predicted velocity based on the N-HG equation for velocity and the parameters estimated based on the least equation regression. To estimate these parameters, I use an extensive search method and minimize the total residue. I opted not to use least square regression in this case since there are few measurements for high velocity and a large number of measurements for low velocity. The measurements for high velocities would dominate the regression and bias the coefficients. I opted to minimize the relative difference

between observed and simulated velocity. For future research, a comprehensive evaluation of different regression methods is recommended to determine which methods would better apply to the type of available dataset.

The estimated parameters, shown in Figure A.6, are corrected by the coefficient described in the previous section and used for the simulation of real events. Figure A.6 also shows the residue (observed-predicted) as a function of discharge and basin drainage area. Residues are larger for high values of discharge. The effects of this bias for large discharge warrant future research. However, the parameters estimated based on the method presented here successfully predict time to peak for the 2008 and 2004 flood events.

Effects of N-HG on the scaling properties of flood

The dominant processes that control the hydrological basin response are scale dependent. Transport through the river network mainly governs the hydrological response of medium to large-scale basins (Wooding, 1965; Robinson et al., 1995; D'Odorico and Rigon, 2003), while rainfall-runoff processes dominate the response of small-scale basins. Hydrological models that attempt to accurately simulate hydrological systems should include a realistic representation of both processes at the scales at which they occur in nature. N-HG relationships provide an important tool to properly represent transport of flow through the river network and are able to describe non-linearities in the transport processes and their variability, in space as a function of drainage area and in time as a function of channel discharge.

In this section, I present a case study developed for the Cedar River basin (~17,000km²) to evaluate the effects of N-HG parameters and parameter uncertainties on the prediction of peak flow (Q_p) scaling. Many studies have demonstrated that peak flows are related to basin drainage area through a power-law ($Q_p = aA^b$), characterizing a scale-invariance process. The parameters that describe this relationship are the fitted

line intercept (a), the exponent (b), and the scale break if present (Stewardson, 2005; Mandapaka et al., 2009). The development of the geophysical theory of floods depends upon an understanding of how peak flow scaling parameters are affected by river flow dynamics.

In this study, I implement a simulation to investigate how HG affects peak flow scaling slopes and intercepts using a simple version of the hydrological model described in Chapter 2. Spatially uniform rainfall was applied to the basin, and infiltration (runoff coefficient equal to 1) was considered equal to zero in all cases. The total volume of precipitation added to the basin was equal to 60mm, and this volume was applied to the basin, considering the following rain event intensities and durations: 30mm/h during 120 minutes (low intensity – column 1 of Figure A.3) 60mm/h during 60 minutes (medium intensity – column 2 of Figure A.3), and 240mm/h during 15minutes (high intensity – column 3 of Figure A.3). I used empirically-estimated N-HG parameters to simulate channel routing velocities and then varied these parameters and analyzed their effects on peak flow.

Figure A.3 presents the scaling of peak flow and the relative difference between simulated peak flow obtained with the true N-HG parameters (empirically estimated) and the modified ones. The plots allow us to evaluate the results for multiple basin scales. As stated by Mantilla, the coefficient v_0 is a random variable. In the first panel, I add variability to the velocity coefficient through the definition of an average value (equal to 0.9) and a standard deviation ($\sigma=0.15$, also data-based, and 0.30). These values are used to generate random values of the coefficient for each link in the river network based on a normal distribution. Peak flow values obtained using these scenarios are compared to peak flow values obtained with the coefficient equal to 0.9 and $\sigma=0.0$. Larger errors are expected for more intense events (high intensity and short duration) with errors on the order of $\pm 10\%$ for $\sigma=0.15$ and $\pm 25\%$ for $\sigma=0.30$. However, velocity coefficient variability does not affect the statistical scaling of peak flow. These results demonstrate

that the accurate prediction of peak flow can be obtained if the average patterns of flow propagation are known.

Figure A.4 and Figure A.5 present the results for different values of discharge and area exponents, respectively. Simulated peak flow values obtained based on the empirically estimated parameter value ($\gamma_1=0.25$ and $\gamma_2=-0.15$) were compared to the ones obtained with discharge exponents equal to 0.20 and 0.30 and area exponents equal to -0.1 and -0.2. Results demonstrate that the effects of N-HG exponents on peak flow scaling are scale dependent and increase as basin drainage area increases. In both cases, peak flow changed for basin areas larger than 10 km^2 . This result is expected since the hydrological response of large scale basins are dominated by flow transport processes, while the response of small scales basins is controlled by hillslope processes. The position of the scale break is also affected and moves toward smaller scales for higher areator discharge exponents. The effects of N-HG parameters are more intense for precipitation events of higher intensity and lower duration.

Conclusions

In this chapter, I described the different formulations for the Hydraulic Geometry relationship and used a large dataset of hydraulic measurements covering a wide range of drainage areas and climatic/physical regions to demonstrate the scale dependency of hydraulic geometry parameters. I then used the same dataset to estimate N-HG parameters for the whole US territory and to provide insight into the relationship between N-HG parameters and the physical/climatological/topological characteristics of the area. More detailed studies are required to fully comprehend the functional form of these relationships and to derive empirical models to estimate N-HG parameters based on physical properties of the basin area.

I then discuss the application of N-HG equations for flood simulations. The derivation of N-HG was based on simplified assumptions that limit the direct application

of the parameters obtained using USGS measurement data for flood simulation. The main problem is that I used USGS measurements to estimate water velocity as Q/A , whereas the model requires the specification of the flood wave velocity that is defined as $c = \partial Q / \partial A$. I demonstrate that a constant coefficient can be used to correct the empirically based parameters, and I estimate this coefficient based on the relationship between velocity and water depth. I obtain the results presented in Chapter 3 using the empirically-estimated parameters that are corrected using the constant coefficient defined in this chapter. Further studies are necessary to ascertain the validity of the constant correction coefficient applied in this study, including theoretical studies that demonstrate the effects of the simplifications on flow propagation or simulation studies that apply the coefficients derived here to other study areas.

In the last part of this study, I demonstrated how channel morphology affects peak flows across scales. Results show that N-HG parameters play an important role in flood generation, especially for larger scales basins. First, I investigated the effects of coefficient variability on peak flow scaling. Some error can be introduced into peak flow simulation due to the lack of consideration of local variability. However, it does not affect the parameters of the scaling of peak flow power law relationship. Then, I investigated peak flow sensitivity to the area and discharge N-HG exponents and demonstrated that the effects of the N-HG exponents on peak flow scaling are scale dependent and increase as basin drainage area increases. This is expected since channel transport dominates the response of large-scale basins. Given the same precipitation volume, sensitivity also increases as the intensity of the rainfall event increases (duration decreases).

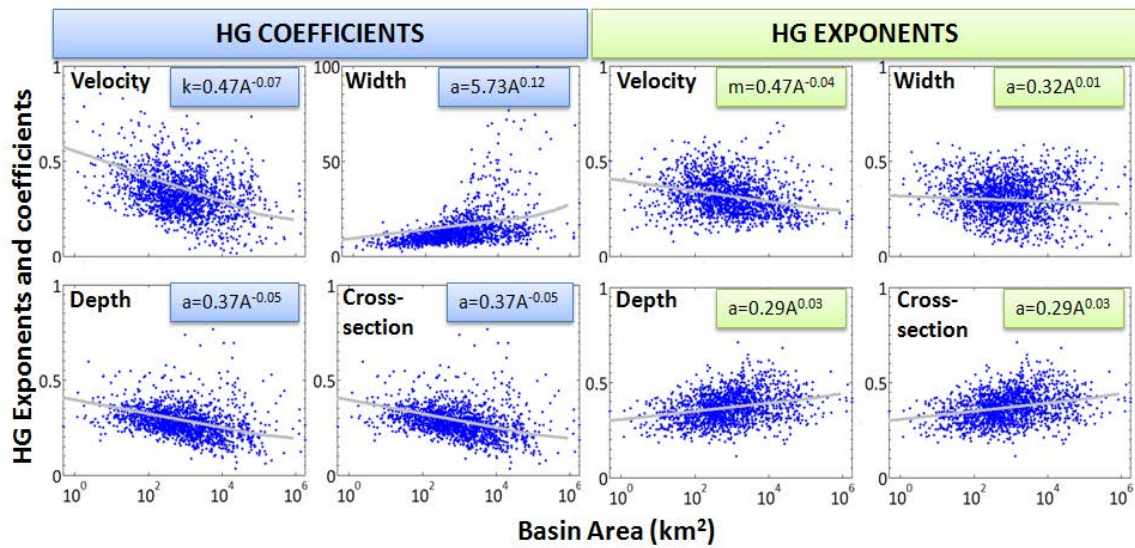


Figure A.1. Relationship between at-a-station HG parameters (coefficient and exponent) and basin area for the four hydraulic variables considered in this work.

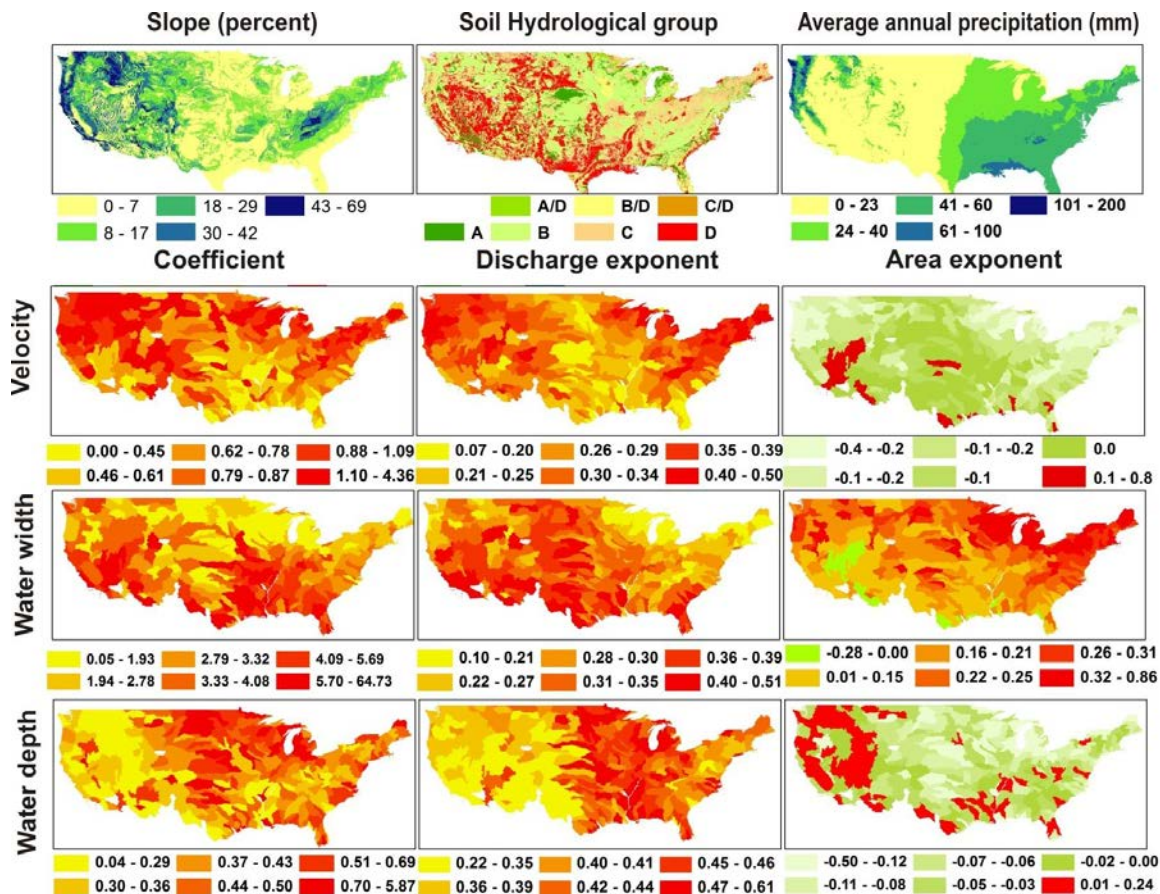


Figure A.2. N-HG parameters estimated for the US. The top plots are reference maps that provide insight into the dominant processes that control parameter variability. The second, third, and fourth lines present the parameters for velocity, water surface width, and water depth, respectively. The coefficient, discharge exponent, and area exponent of the N-HG relationships are presented in the first, second, and third columns, respectively.

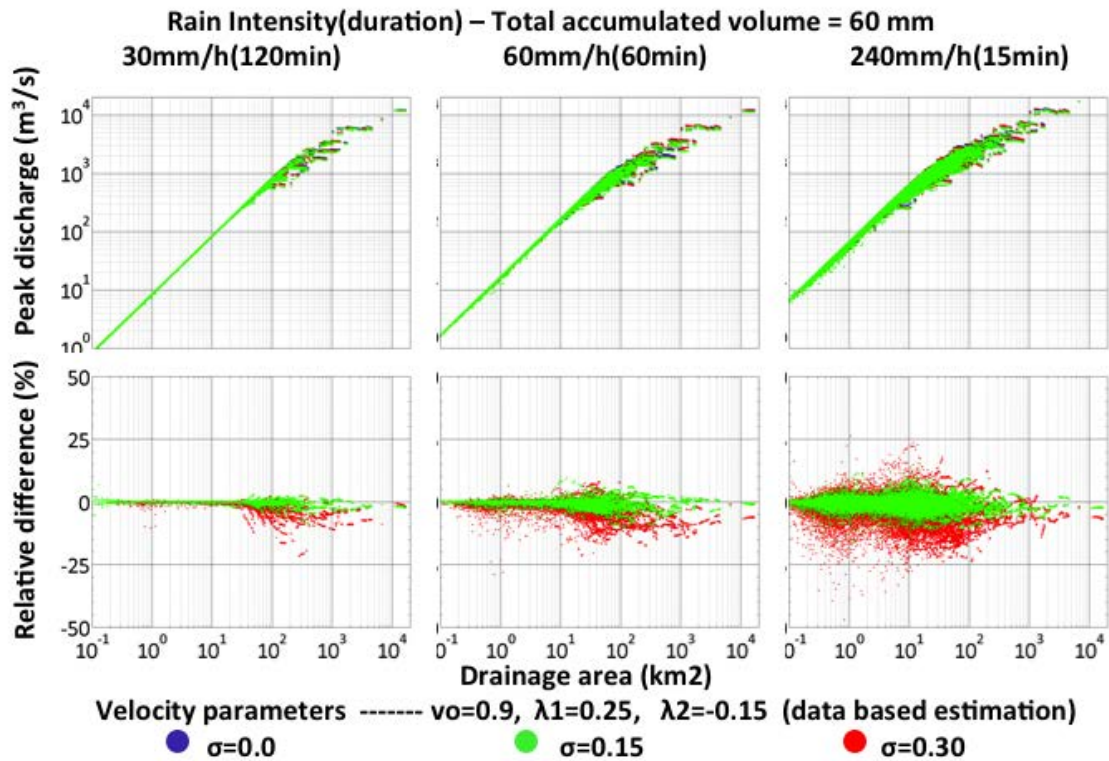


Figure A.3. Scaling of peak flow for different sets of N-HG parameters and rainfall events' intensity and duration (rainfall volume=60mm): variability was added to the velocity coefficient through the definition of an average value (equal to 0.9) and a standard deviation.

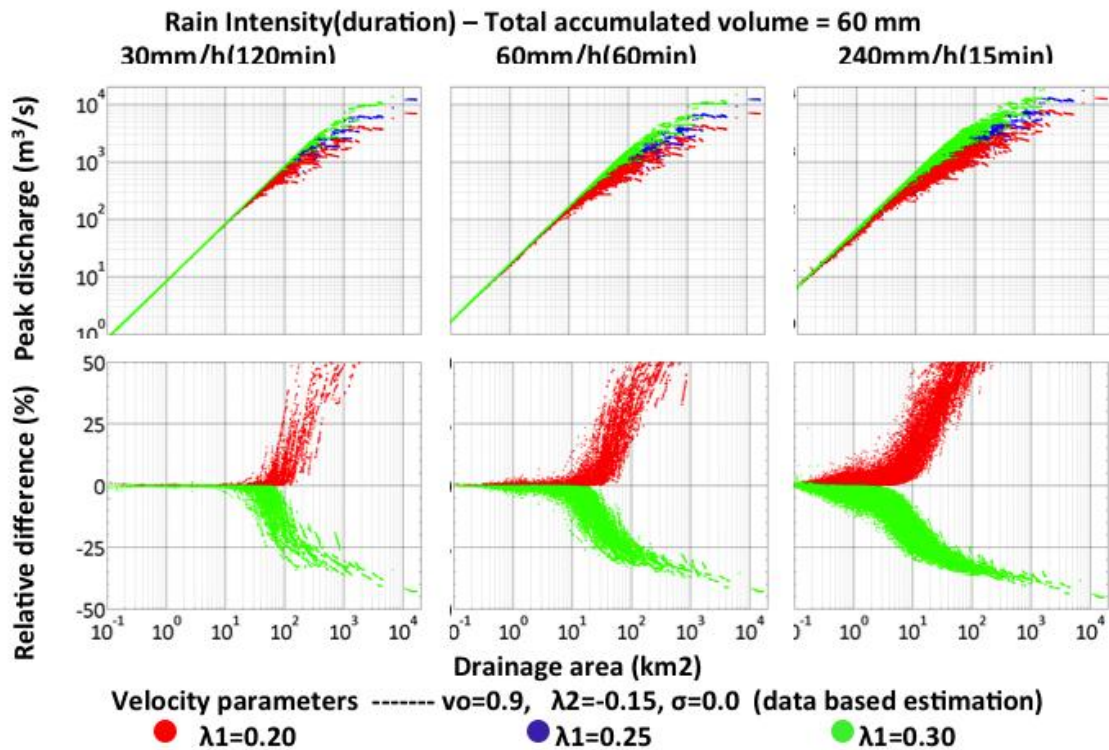


Figure A.4. Scaling of peak flow for different sets of N-HG parameters and rainfall events' intensity and duration (rainfall volume=60mm): results for different values of the discharge exponent.

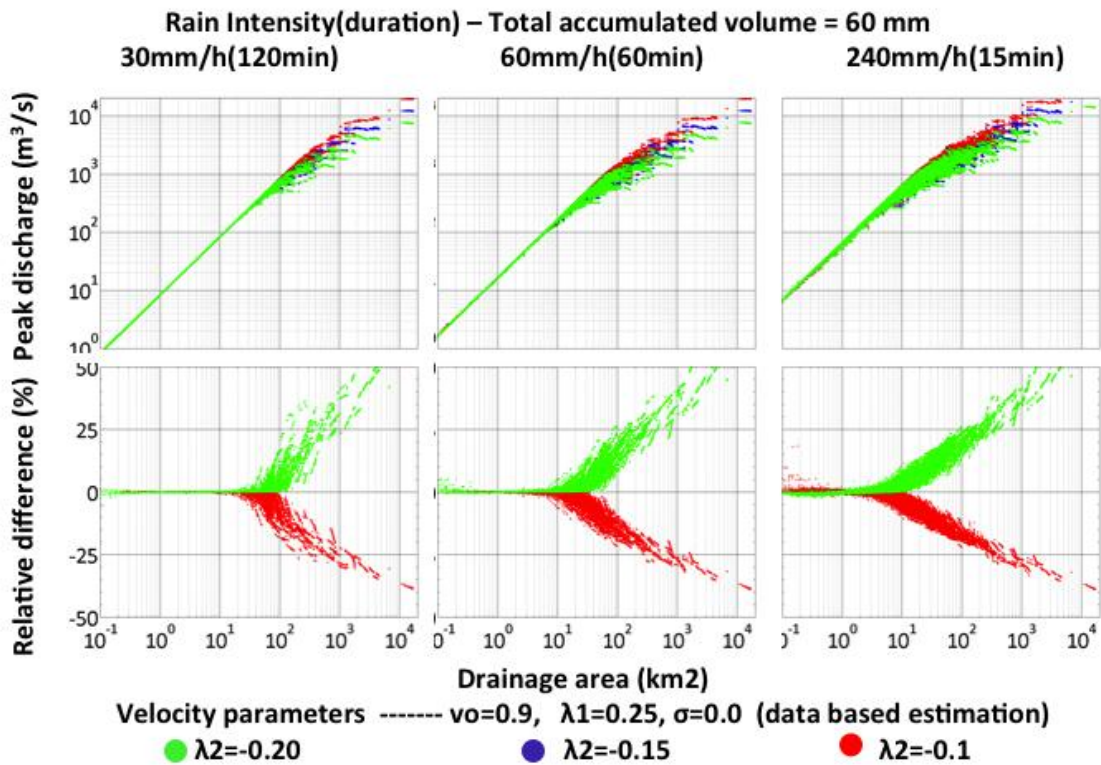


Figure A.5. Scaling of peak flow for different sets of N-HG parameters and rainfall events' intensity and duration (rainfall volume=60mm): results for different values of the area exponent

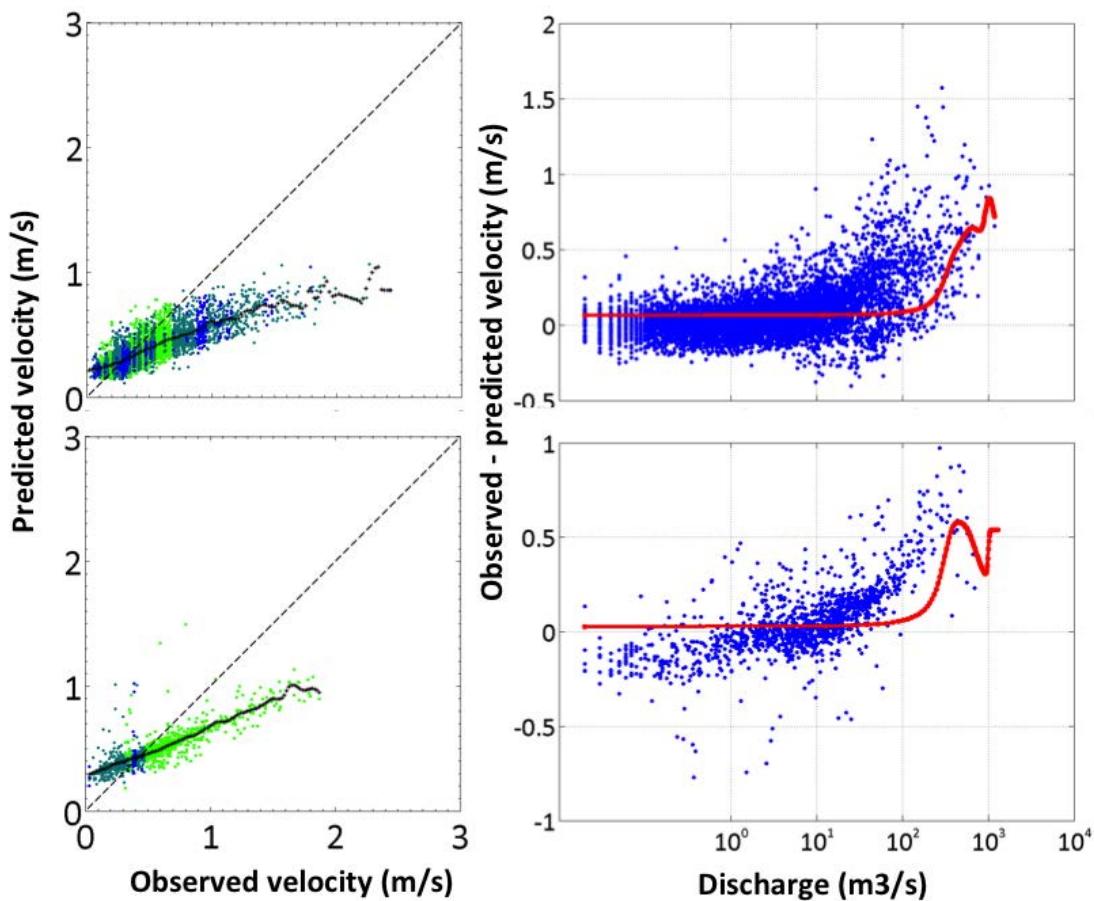


Figure A.6. N-HG velocity parameters for the Iowa River, Cedar River, and Turkey River basins.

REFERENCES

- Ajami, N.H., Gupta, H., Wagener, T., Sorooshian, S., 2004. Calibration of a semi-distributed hydrologic model for streamflow estimation along a river system. *Journal of Hydrology* 298, 112–135.
- Ajami, N.K., Duan, Q., Sorooshian, S., 2007. An integrated hydrologic Bayesian multimodel combination framework: Confronting input, parameter, and model structural uncertainty in hydrologic prediction. *Water Resources Research* 43.
- Anderl, B., Attmannspacher, W., Schultz, G. A., 1976. Accuracy of reservoir inflow forecasts based on radar rainfall measurements. *Water Resources Research*, 12(2), 217, doi:10.1029/WR012i002p00217.
- Anderson, M., Chen, Z., Kavvas, M., 2004. Modeling low flows on the Cosumnes River. *Journal of Hydrological Engineering* 9 (2), 126–134.
- Ashmore, P., Sauks, E., 2006. Prediction of discharge from water surface width in a braided river with implications for at-a-station hydraulic geometry. *Water Resources Research* 42 (3), 1–11.
- ASTER validation team, 2011. ASTER global digital elevation model version 2 - Summary of validation results. Available through: lpdaac.usgs.gov [accessed Aug 2011].
- Barnes, C.J., 1995. The Art of Catchment Modeling - What Is a Good Model? *Environmental International* 21(5), 747–751.
- Basha, H., Maalouf, S., 2005. Theoretical and conceptual models of subsurface hillslope flows. *Water Resources Research* 41, 1–13.
- Batjes, N., 2005. ISRIC-WISE global data set of derived soil properties on a 0.5 by 0.5 degree grid (Version 3.0). Available through: <http://www.isric.org/data/isric-wise-global-data-set-derived-soil-properties-05-05-degree-grid-ver-30> [accessed Jan 2011].
- Beven, K. J., Cloke, H. L., 2012. Comment on “Hyperresolution global land surface modeling: Meeting a grand challenge for monitoring Earth's terrestrial water” by Eric F. Wood et al., *Water Resources Research* 48, W01801.
- Beven, K., 1995. Linking parameters across scales: Subgrid parameterizations and scale dependent hydrological models. *Hydrological Process* 9, 507–525.
- Beven, K., 2007. Towards integrated environmental models of everywhere: uncertainty, data and modelling as a learning process. *Hydrological & Earth System Science* 11 (1), 460–467.
- Bhang, K.J., Schwartz, F.W., Braun, A., 2007. Verification of the vertical error in C-band SRTM DEM using ICESat and Landsat-7, Otter Tail County, MN. *IEEE Transactions on Geoscience and Remote Sensing* 45, 36–44.
- Bindlish, R., Crow, W.T., Jackson, T.J., 2009. Role of Passive Microwave Remote Sensing in Improving Flood Forecasts. *IEEE Geoscience and Remote Sensing Letters* 6, 112–116.

- Black, D., Smith, J., 2004. How robust is the evidence on the effects of college quality? Evidence from matching. *Journal of Econometrics* 121 (1-2), 99–124.
- Blöschl, G., 2001. Scaling in hydrology. *Hydrological Process* 15, 709–711.
- Blöschl, G., 2001. Spatial observations and interpolation, in: Grayson, R. (Ed.), *Spatial Patterns in Catchment Hydrology: Observations and Modelling*. Cambridge University Press, Cambridge, U. K.
- Breuer, L., Eckhardt, K., Frede, H., 2003. Plant parameter values for models in temperate climates. *Ecological Modelling* 169(2-3), 237–293.
- Brock, F. V., Crawford, K. C., Elliot, R. L., Cuperus, G. W., Stadler, S. J., Johnson, H. L., Eilts, and M. D., 1995. The Oklahoma Mesonet - a Technical Overview. *Journal of Atmospheric and Oceanic Technology* 12(1), 5–19.
- Burnash, R. J. C., 1995. The NWS river forecast system—catchment modeling. In: Singh, V. P. (Ed.), *Computer Models of Watershed Hydrology*. Water Resources Publications, Littleton, Colorado, 311–366.
- Burnash, Robert J. C.; Ferral, R. Larry; McGuire, Richard A., 1973. A generalized streamflow simulation system, conceptual modeling for digital computers, National Weather Service and California Department of Water Resources.
- Buttle, J., 2006. Mapping first-order controls on streamflow from drainage basins: the T3 template. *Hydrological Process* 20, 3415–3422.
- Carpenter, T. M., 2006. Discretization scale dependencies of the ensemble flow range versus catchment area relationship in distributed hydrologic modeling. *Journal of Hydrology* 328(1-2), 242–257.
- Carpenter, T. M., Georgakakos, K., 2004. Impacts of parametric and radar rainfall uncertainty on the ensemble streamflow simulations of a distributed hydrologic model. *Journal of Hydrology* 298(1-4), 202–221.
- Castro, J., Jackson, P., 2001. Bankfull discharge recurrence intervals and regional hydraulic geometry relationships: Patterns in the Pacific Northwest, USA. *Journal of American Water Resources Association* 37, 1249–1262.
- Ciach, G. J., Krajewski, W. F., Villarini, G., 2007. Product-Error-Driven Uncertainty Model for Probabilistic Quantitative Precipitation Estimation with NEXRAD Data. *Journal of Hydrometeorology* 8(6), 1325–1347.
- Ciach, G. J., Krajewski, W. F., 1999. On the estimation of radar rainfall error variance. *Advances in Water Resources* 98, 585–595.
- Clark, M.P., Kavetski, D., 2010. Ancient numerical demons of conceptual hydrological modeling: 1. Fidelity and efficiency of time stepping schemes. *Water Resources Research* 46, W10510.
- Cluckie, I. D., Collier, C. G., 1991. *Hydrological Applications of Weather Radar*. World Meteorological Organization Bulletin, Chichester.

- Conesa-Garcia, C., Caselles-Miralles, V., Sanchez Tomas, J.M., Garcia-Lorenzo, R., 2010. Hydraulic Geometry, GIS and Remote Sensing, Techniques against Rainfall-Runoff Models for Estimating Flood Magnitude in Ephemeral Fluvial Systems. *Remote Sensing* 2, 2607–2628.
- Cunha, L. K., Mandapaka, P. V., Krajewski, W. F., Mantilla, R., Bradley, A. A., submitted to *Water Resources Research*. Impact of Radar-Rainfall Error Structure on Estimated Flood Magnitude Across Scales: An Investigation Based on a Parsimonious Distributed Hydrological Model.
- Cunha, L. K., Krajewski, W. F., Mantilla, R., 2011. A framework for flood risk assessment under nonstationary conditions or in the absence of historical data. *Journal of Flood Risk Management* 4(1), 3–22.
- Davidson, J. M., Stone, L. R., Nielsen, D. R. Larue, M. E., 1969. Field Measurement and Use of Soil-Water Properties. *Water Resources Research* 5(6), 1312–1321.
- Dehotin, J., Braud, I., 2008. Which spatial discretization for distributed hydrological models? Proposition of a methodology and illustration for medium to large-scale catchments. *Hydrology and Earth System Sciences* 12(3), 769-796
- Dingman, S. L. 2002. *Physical Hydrology*, second edition. Prentice Hall, Englewood Cliffs, NJ.
- D'Odorico, P., Rigon, R., 2003. Hillslope and channel contributions to the hydrologic response. *Water Resources Research* 39, 1–9.
- Dodov, B., 2003. Generalized Hydraulic Geometry Based on a Multiscaling Formalism. *Water Resources Research* 40, W06302.
- Dodov, B., 2004. Generalized hydraulic geometry: Derivation based on a multiscaling formalism. *Water Resources Research* 40, 1–22.
- Dodov, B., Foufoula-Georgiou, E., 2004. Generalized hydraulic geometry: Insights based on fluvial instability analysis and a physical model. *Water Resources Research* 40, W12201.
- Dooge, J.C.I., 1986. Looking for Hydrologic Laws. *Water Resources Research* 22, 46–58.
- Duffy, C.J., 2007. A semidiscrete finite volume formulation for multiprocess watershed simulation. *Water Resources Research* 43, 1–18.
- Durand, M., Fu, L.-L., Lettenmaier, D.P., Alsdorf, D.E., Rodriguez, E., Esteban-Fernandez, D., 2010. The Surface Water and Ocean Topography Mission: Observing Terrestrial Surface Water and Oceanic Submesoscale Eddies. *Proceedings of the IEEE*, 766–779.
- Durbude, D.G., Jain, M.K., Mishra, S.K., 2011. Long-term hydrologic simulation using SCS-CN-based improved soil moisture accounting procedure. *Hydrological Process* 25, 561–579.
- Durner, W., 1994. Hydraulic conductivity estimation for soils with heterogeneous pore structure. *Water Resources Research* 30, 211–223.

- Ebel, B.A., Loague, K., 2006. Physics-based hydrologic-response simulation: Seeing through the fog of equifinality. *Hydrological Process* 20, 2887–2900.
- Ebert, E.E., Janowiak, J.E., Kidd, C., 2007. Comparison of near-real-time precipitation estimates from satellite observations and numerical models. *Bolletín of American Meteorological Society* 88, 47–64.
- Endreny, T., Wood, E.F., 2000. Satellite-derived digital elevation model accuracy: Hydrogeomorphological analysis requirements. *Hydrological Process* 14, 1–20.
- Entekhabi, D., Njoku, E., O'Neill, P., Kellogg, K., Crow, W., Edelstein, W., Entin, J., Goodman, S., Jackson, T., Johnson, J., Kimball, J., Piepmeier, J., Koster, R., Martin, N., McDonald, K., Moghaddam, M., Moran, S., Reichle, R., Shi, J., Spencer, M., Thurman, S., Tsang, L.T.L., Van Zyl, J., 2010. The Soil Moisture Active Passive (SMAP) Mission. *Proceeding of the IEEE* 98, 704–716.
- Fan, Y., Van den Dool, H.M., Lohmann, D., Mitchell, K., 2006. 1948–98 U.S. Hydrological Reanalysis by the Noah Land Data Assimilation System. *Journal of Climate* 19, 1214–1237.
- Faures, J., Goodrich, D.C., Woolhiser, D. A., Sorooshian, S., 1995. Impact of small-scale spatial rainfall variability on runoff modeling. *Journal of Hydrology* 173, 309–326.
- Faustini, J.M., Kaufmann, P.R., Herlihy, A.T., 2009. Downstream variation in bankfull width of wadeable streams across the conterminous United States. *Geomorphology* 108, 292–311.
- Feyen, L., Dankers, R., Barredo, J., 2006. Flood risk in Europe in a changing climate, European Commission Joint Research Centre, Institute of Environment and Sustainability, Italy, 22.
- Finnerty, B., Smith, M., Seo, D., Koren, V., Moglen, G., 1997. Space-time scale sensitivity of the Sacramento model to radar-gage precipitation inputs. *Journal of Hydrology* 203, 21–38.
- Fleckenstein, J.H., Niswonger, R.G., Fogg, G.E., 2006. River-aquifer interactions, geologic heterogeneity, and low-flow management. *Ground Water* 44, 837–852.
- Freeze, R., 1980. A Stochastic-Conceptual Analysis of Rainfall-Runoff Processes on a Hillslope. *Water Resources Research* 16(2), 391–408.
- Fu, S., T. O. Sonnenborg, K. H. Jensen, and X. He, 2011. Impact of Precipitation Spatial Resolution on the Hydrological Response of an Integrated Distributed Water Resources Model. *Vadose Zone Journal* 10(1), 25–36.
- Fujisada, H., Bailey, G.B., Kelly, G.G., Hara, S., Abrams, M.J., 2005. ASTER DEM performance. *IEEE Transactions on Geoscience and Remote Sensing* 43, 2707–2714.
- Fulton, R., Breidenbach, J., Seo, D., Miller, D., 1998. The WSR-88D rainfall algorithm. *Weather and Forecasting* 13, 377–395.
- Germann, U., Berenguer, M., Sempere-Torres, D., Zappa, M., (2009), REAL-ensemble radar precipitation estimation for hydrology in a mountainous region. *Quarterly Journal of the Royal Meteorological Society* 135, 445–456.

- Graham, C. B., McDonnell, J. J. (2010), Hillslope threshold response to rainfall: (2) Development and use of a macroscale model. *Journal of Hydrology* 393, 77–93.
- Gray, D.M., Toth, B., Zhao, L., Pomeroy, J.W., Granger, R.J., 2001. Estimating areal snowmelt infiltration into frozen soils. *Hydrological Process* 15, 3095–3111.
- Grayman, W. M., Eagleson, P. S., 1971. Evaluation of radar and rain-gage systems for flood forecasting, R. M. Parsons Lab. Rep. 138, Mass. Inst. of Technol., Cambridge, Mass.
- Gu, R.R., Zhao, X., Jha, M., 2010. Hydrologic impact of climate change on the Mississippi River, in: *Environmental Science and Information Application Technology (ESIAT) 1*, 36–39.
- Gupta, V. K., 2004. Emergence of statistical scaling in floods on channel networks from complex runoff dynamics, *Chaos, Soliton & Fractals* 19(2), 357–365.
- Gupta, V. K., Castro, S., Over, T., 1996. On scaling exponents of spatial peak flows from rainfall and river network geometry. *Journal of Hydrology* 187, 81–104.
- Gupta, V. K., Mantilla, R., Troutman, B. M., Dawdy, D., Krajewski, W. F., 2010. Generalizing a nonlinear geophysical flood theory to medium-sized river networks. *Geophysical Research Letters* 37(11).
- Gupta, V. K., Waymire, E. C., 1998. Spatial Variability and Scale Invariance in Hydrologic Regionalization, in *Scale Dependence and Scale Invariance in Hydrology*, G. Sposito (Ed), 62–88, Cambridge University Press, Cambridge.
- Gupta, V.K., Castro, S., Over, T., 1996. On scaling exponents of spatial peak flows from rainfall and river network geometry, *Journal of Hydrology* 187(1-2), 81–104.
- Habib, E., A. V. Aduvala, E. A. Meselhe, 2008. Analysis of radar-rainfall error characteristics and implications for stream flow simulation uncertainty. *Hydrological Sciences Journal* 53, 568–587.
- Hancock, G.R., Evans, K.G., 2006. Channel head location and characteristics using digital elevation models. *Earth Surface Processes Landforms* 31, 809–824.
- Harman, C., Stewardson, M., DeRose, R., 2008. Variability and uncertainty in reach bankfull hydraulic geometry. *Journal of Hydrology* 351, 13–25.
- Hayashi, M., van der Kamp, G., Schmidt, R., 2003. Focused infiltration of snowmelt water in partially frozen soil under small depressions. *Journal of Hydrology* 270, 214–229.
- He, X., Refsgaard, J. C., Sonnenborg, T. O., Vejen, F., Jensen, K. H., 2011. Statistical analysis of the impact of radar rainfall uncertainties on water resources modeling, *Water Resources Research* 47(9), 1–17.
- Herron, N., Croke, B., 2009. Including the influence of groundwater exchanges in a lumped rainfall-runoff model. *Mathematics and Computers in Simulation* 79, 2689–2700.

- Hirsch, R.M., Costa, J.E., 2004. US stream flow measurement and data dissemination improve. *EOS Transactions AGU* 85(20), 197-203
- Hirt, C., Filmer, M.S., Featherstone, W.E., 2010. Comparison and validation of the recent freely available ASTER-GDEM ver1, SRTM ver4.1 and GEODATA DEM-9S ver3 digital elevation models over Australia. *Australian Journal of Earth Sciences* 57(3), 337–347.
- Hogan, D.L., Church, M., 1989. Hydraulic Geometry in Small, Coastal Streams - Progress Toward Quantification of Salmonid Habitat. *Canadian Journal of Fisheries and Aquatic Sciences* 46(5), 844–852.
- Homer, C., Dewitz, J., Fry, J., Coan, M., 2007. Completion of the 2001 National Land Cover Database for the Conterminous United States. *Photogrammetric engineering and Remote Sensing* 73, 337–341.
- Hong, Y., Hsu, K., Sorooshian, S., Gao, X., 2004. Precipitation Estimation from Remotely Sensed Imagery using an Artificial Neural Network Cloud Classification System. *Journal of Applied Meteorology* 43, 1834–1852.
- Huffman, G.J., Bolvin, D., Nelkin, E., 2007. The TRMM multisatellite precipitation analysis (TMPA): Quasi-global, multiyear, combined-sensor precipitation estimates at fine scales. *Journal of Hydrometeorology* 8, 38–54.
- Hughes, D.A., 2004. Incorporating groundwater recharge and discharge functions into an existing monthly rainfall–runoff model. *Hydrological Science Journal* 49.
- Hunukumbura, P. B Tachikawa, Y., Shiiba, M., 2011. Distributed hydrological model transferability across basins with different hydro-climatic characteristics. *Hydrological Processes* 26 (6).
- Hunukumbura, P.B., Tachikawa, Y., Shiiba, M., 2011. Distributed hydrological model transferability across basins with different hydro-climatic characteristics. *Hydrological Process* 26, 793–808.
- Iwata, Y., Hayashi, M., Suzuki, S., Hirota, T., Hasegawa, S., 2010. Effects of snow cover on soil freezing, water movement, and snowmelt infiltration: A paired plot experiment. *Water Resources Research* 46.
- Jin, C.X., Romkens, M.J.M., 2000. Estimating manning's roughness coefficient for shallow overland flow in non-submerged vegetative filter strips. *Transactions of the ASABE* 43, 1459–1466.
- Johnson, D., Smith, M., Koren, V., Finnerty, B., 1999. Comparing Mean Areal Precipitation Estimates From Nexrad and Rain Gauge Networks. *Journal of Hydrologic Engineering* 4(2), 117–124.
- Jones, J.A., Swanson, F.J., 2001. Hydrologic inferences from comparisons among small basin experiments. *Hydrological Process* 15, 2363–2366.
- Joyce, R.J., Janowiak, J.E., Arkin, P.A., Xie, P., 2004. CMORPH: A Method that Produces Global Precipitation Estimates from Passive Microwave and Infrared Data at High Spatial and Temporal Resolution. *Journal of Hydrometeorology* 5, 487–503.

- Kampf, S., 2007. A framework for classifying and comparing distributed hillslope and catchment hydrologic models. *Water Resources Research* 43, W05423.
- Kavetski, D., 2011. Numerical troubles in conceptual hydrology: Approximations, absurdities and impact on hypothesis testing. *Hydrological Process* 25, 661–670.
- Kavetski, D., Fenicia, F., 2011. Impact of temporal data resolution on parameter inference and model identification in conceptual hydrological modeling: Insights from an experimental catchment. *Water Resources Research* 47.
- Kenward, T., 2000. Effects of Digital Elevation Model Accuracy on Hydrologic Predictions. *Remote Sensing of Environment* 74, 432–444.
- Kienzle, S., 2004. The Effect of DEM Raster Resolution on First Order, Second Order and Compound Terrain Derivatives. *Transactions in GIS* 8, 83–111.
- Kim, H.S. Croke, B.F.W., Jakeman, A.J., Chiew, F.H.S, 2011. An assessment of modelling capacity to identify the impacts of climate variability on catchment hydrology, *Mathematics and Computers in Simulation* 81(7), 1419-1429.
- Kirchner, J., 2006. Getting the right answers for the right reasons: Linking measurements, analyses, and models to advance the science of hydrology. *Water Resources Research* 42, 1–5.
- Klemes, V. 1983. Conceptualization and scale in hydrology. *Journal of Hydrology* 65, 1–23.
- Köhne, J.M., Köhne, S., Šimůnek, J., 2009. A Review of Model Applications for Structured Soils: a) Water Flow and Tracer Transport. *Journal of Contaminant Hydrology* 104 (1-4), 4–35.
- Krajewski, W. F., 2007. Ground networks: Are we doing the right thing? in: Levizzani, V., Bauer, P., Turk, F. J. (Eds). *Measuring Precipitation From Space*, 403–417, Springer, Dordrecht, The Netherlands.
- Krajewski, W. F., Georgakakos, K., 1985. Synthesis of radar rainfall data. *Water Resources Research* 21(5), 764–768.
- Krajewski, W.F., Mantilla, R., 2010. Why were the 2008 floods so large? in: Mustel, C. (ed.). *A Watershed Year: Anatomy of the Iowa Floods of 2008*, University of Iowa Press, Iowa City, IA.
- Krause, P., Boyle, D. P., Bäse, F., 2005. Comparison of different efficiency criteria for hydrological model assessment. *Advances in Geosciences* 5, 89–97.
- Lakshmi, V., 2004. The role of satellite remote sensing in the Prediction of Ungauged Basins. *Hydrol Process* 18, 1029–1034.
- Lang, C., Gille, E., Francois, D., Drogue, G., 2008. Improvement of a lumped rainfall-runoff structure and calibration procedure for predicting daily low flow discharges. *J Hydrol Hydromech* 56, 59–71.
- Lassueur, T., Joost, S., Randin, C.F., 2006. Very high resolution digital elevation models: Do they improve models of plant species distribution? *Ecol Model* 198, 139–153.

- Leopold, L., 1953. The hydraulic geometry of stream channels and some physiographic implications. No. 252, United States Geological Survey.
- Leopold, L.B., M.G. Wolman, J.P. Miller, 1964. *Fluvial processes in Geomorphology*. W.H. Freeman Press, New York.
- Lettenmaier, D.P., De Roo, A., 2006. Towards a capability for global flood forecasting. *Bulletin of the WMO* 55.
- Li, J., Wong, D.W.S., 2010. Effects of DEM sources on hydrologic applications. *Computers, Environment and Urban Systems* 34, 251–261.
- Liden, R., Harlin J., 2000. Analysis of conceptual rainfall-runoff modelling performance in different climates. *Journal of Hydrology* 238, 231–247
- Liu, X., 2008. Airborne LiDAR for DEM generation: some critical issues. *Progress in Physical Geography* 32, 31–49.
- Loague, K., Heppner, C.S., Ebel, B.A., 2010. The quixotic search for a comprehensive understanding of hydrologic response at the surface: Horton, Dunne, Dunton, and the role of concept-development simulation. *Hydrological Process* 24, 2499–2505.
- Lohmann, D., Mitchell, K., Houser, P., Wood, E.F., Schaake, J., Robock, A., Cosgrove, B., Sheffield, J., Duan, Q., Luo, L., Higgins, R., Pinker, R., Tarpley, J., 2004. Streamflow and water balance intercomparisons of four land surface models in the North American Land Data Assimilation System project. *Journal of Geophysical Research-Atmosphere* 109, D07S9.
- Lombardi, L., Toth, E., Castellarin, A., Montanari, A., Brath, A., 2011. Calibration of a rainfall–runoff model at regional scale by optimising river discharge statistics: Performance analysis for the average/low flow regime. *Physics and Chemistry of the Earth, Parts A/B/C*, in press.
- Lopes, V., 1996. On the effect of uncertainty in spatial distribution of rainfall on catchment modeling. *Catena* 28 (1), 107–119.
- Luo, J. Xie, J., Ma, Y., Zhang, G., 2011. An improved genetic algorithm for hydrological model calibration. *Seventh International Conference on Natural Computation (ICNC)* 4, 1964–1968.
- Luo, J., Xie, J., Ma, Y., Zhang, G., 2011. An improved genetic algorithm for hydrological model calibration, in: *Natural Computation (ICNC), 2011 Seventh International Conference on*. Presented at the *Natural Computation (ICNC), 2011 Seventh International Conference on* (Indicate what the conference is on), 1964–1968.
- Mahrt, L., Ek, M., 1984. The Influence of Atmospheric Stability on Potential Evaporation *Journal of Applied Meteorology* 23(2), 222–234.
- Mandapaka, P. V., Germann, U., 2010. Radar-rainfall error models and ensemble generators, *Rainfall: State of Science*, Gebremichael, M., and F. Testik (Eds.), *Geophysical Monograph Series* 191, 247–264, American Geophysical Union.
- Mandapaka, P., 2009. Role of rainfall variability in the statistical structure of peak flow. , Ph.D. thesis, The University of Iowa, Iowa City.

- Mandapaka, P., Krajewski, W.F., Mantilla, R., 2009. Dissecting the effect of rainfall variability on the statistical structure of peak flows. *Advances in Water Resources* 32, 1508–1525.
- Mantilla, R., 2007. Physical Basis of Statistical Scaling in Peak Flows and Stream Flow Hydrographs for Topologic and Spatially Embedded Random Self-similar Channel Networks, Ph.D. thesis, University of Colorado, Boulder, CO.
- Mantilla, R., Gupta, V. K., 2005. A GIS numerical framework to study the process basis of scaling statistics in river networks. *Geoscience and Remote Sensing Letters, IEEE* 2(4), 404–408.
- Mantilla, R., Gupta, V.K., Mesa, O., 2006. Role of coupled flow dynamics and real network structures on Hortonian scaling of peak flows. *Journal of Hydrology* 322(1-4), 155–167.
- Mantilla, R., Gupta, V.K., Troutman, B.M., 2011. Scaling of peak flows with constant flow velocity in random self-similar networks. *Nonlinear Processes in Geophysics* 18(4), 489-502.
- Martinez, C., Hancock, G.R., Kalma, J.D., Wells, T., Boland, L., 2010. An assessment of digital elevation models and their ability to capture geomorphic and hydrologic properties at the catchment scale. *International Journal of Remote Sensing* 31, 6239–6257.
- Maune, D., 2007. Digital Elevation Model Technologies and Applications: The DEM User's Manual. American Society for Photogrammetry and Remote Sensing, Bethesda, Maryland.
- McDonnell, J.J., Sivapalan, M., Vaché, K., 2007. Moving beyond heterogeneity and process complexity: A new vision for watershed hydrology. *Water Resources Research* 43, 1–6.
- McGlynn, B., McDonnell, J., Brammer, D., 2002. A review of the evolving perceptual model of hillslope flowpaths at the Maimai catchments, New Zealand. *Journal of Hydrology* 257, 1–26.
- Mejia, A.I., Reed, S.M., 2011. Role of channel and floodplain cross-section geometry in the basin response. *Water Resources Research* 47, W09518.
- Menabde, M., Veitzer, S., Gupta, V., 2001. Tests of peak flow scaling in simulated self-similar river networks, *Advances in Water Resources* 24, 991–999.
- Meng, X., Currit, N., Zhao, K., 2010. Ground Filtering Algorithms for Airborne LiDAR Data: A Review of Critical Issues. *Remote Sensing* 2, 833–860.
- Michel, C., 2005. Soil Conservation Service Curve Number method: How to mend a wrong soil moisture accounting procedure? *Water Resources Research* 41.
- Mishra, S.K., Singh, V.P., 1999. Another Look at Scs-Cn Method. *Journal of Hydrologic Engineering*, 4(3), 257–264.
- Mishra, S.K., Singh, V.P., 2004. Long-term hydrological simulation based on the Soil Conservation Service curve number. *Hydrological Process* 18, 1291–1313.

- Mohanty, B., 2007. Effective hydraulic parameters in horizontally and vertically heterogeneous soils for steady-state land-atmosphere interaction. *Journal of Hydrometeorology* 8 (4), 715
- Mohanty, B., Bowman, R., 1997. New piecewise-continuous hydraulic functions for modeling preferential flow in an intermittent-flood-irrigated field. *Water Resources Research* 33, 2049–2063.
- Montgomery, D.R., Dietrich, W.E., 1994. *Landscape Dissection and Drainage Area-Slope Thresholds. Process Models and Theoretical Geomorphology*, New York.
- Mu, Q., Heinsch, F., Zhao, M., 2007. Development of a global evapotranspiration algorithm based on MODIS and global meteorology data. *Remote Sensing of Environment*. 111 (4), 519–536
- Mu, Q., Zhao, M., Running, S. W., 2011. Improvements to a MODIS Global Terrestrial Evapotranspiration Algorithm. *Remote Sensing of Environment*, 115, 1781–1800.
- Nash, J. E., Sutcliffe, J., 1970, Flow forecasting through conceptual models part I - A discussion of principles. *Journal of Hydrology* 10, 282–290.
- National Agricultural Statistics Service. 2007 Census of Agriculture, Washington DC. Available through:
http://www.agcensus.usda.gov/Publications/2007/Full_Report/usv1.pdf30 [accessed Jan 2011].
- Nijssen, B., 2004. Effect of precipitation sampling error on simulated hydrological fluxes and states: Anticipating the Global Precipitation Measurement satellites. *Journal of Geophysical Research* 109.
- O'Loughlin, E., 1981. Saturation regions in catchments and their relations to soil and topographic properties. *Journal of Hydrology* 53, 229–246.
- Paik, K., 2004. Hydraulic geometry and the nonlinearity of the network instantaneous response. *Water Resources Research* 40, W03602.
- Pan, M., Sheffield, J., Wood, E.F., 2003. Snow process modeling in the North American Land Data Assimilation System (NLDAS): 2. Evaluation of model simulated snow water equivalent. *Journal of Geophysical Research* 108, 11.1–11.14.
- Peckham, S.D., 1995. New Results for Self-Similar Trees with Applications to River Networks. *Water Resources Research* 31, 1023–1029.
- Quinn, P., Beven, K., Chevallier, P., Planchon, O., 1991. The prediction of hillslope flow paths for distributed hydrological modelling using digital terrain models. *Hydrological Process* 5, 59–79.
- Reed, S.M., Koren, V., Smith, M., Zhang, Z., Moreda, F., Seo, D.-J, and DMIP participants, 2004. Overall Distributed Model Intercomparison Project Results. *Journal of Hydrology DMIP Special Issue* 198, (1-4), 27-60.
- Refsgaard, J., 2004. Modelling guidelines-terminology and guiding principles. *Advances in Water Resources* 27, 71–82.

- Refsgaard, J.C., 2001. Spatial patterns in catchment hydrology: observations and modelling, in: Grayson, R., Bloschl, G. (Eds.). *Towards a Formal Approach to Calibration and Validation of Model Using Spatial Data*, 329–254.
- Reggiani, P., Sivapalan, M., 1998. A unifying framework for watershed thermodynamics: balance equations for mass, momentum, energy and entropy, and the second law of thermodynamics. *Advances in Water Resources* 22, 367–398.
- Reutebuch, S., McGaughey, R., Andersen, H., Carson, W., 2003. Accuracy of a high-resolution lidar terrain model under a conifer forest canopy. *Canadian Journal of Remote Sensing* 29(5), 527–535.
- Rhoads, B.L., Schwartz, J.S., Porter, S., 2003. Stream geomorphology, bank vegetation, and three-dimensional habitat hydraulics for fish in midwestern agricultural streams. *Water Resources Research* 39.
- Rinaldo, A., Rodríguez-Iturbe, I., Rigon, R., Ijjasz-Vasquez, E., Bras, R., 1993. Self-organized fractal river networks. *Physical Review Letters* 70, 822–825.
- Robinson, J., Sivapalan, M., Snell, J., 1995. On the relative roles of hillslope processes, channel routing, and network geomorphology in the hydrologic response of natural catchments. *Water Resources Research* 31, 3089–3101.
- Rott, H., Yueh, S.H., Cline, D.W., Duguay, C., Essery, R., Haas, C., Hélière, F., Kern, M., Macelloni, G., Malnes, E., Nagler, T., Pulliainen, J., Rebhan, H., Thompson, A., 2010. Cold Regions Hydrology High-Resolution Observatory for Snow and Cold Land Processes. *Proceeding of the IEEE* 98, 752–765.
- Sabzevari, T., Talebi, A., Ardakanian, R., Shamsai, A., 2010. A steady-state saturation model to determine the subsurface travel time (STT) in complex hillslopes. *Hydrological Earth System Science* 14(6), 891–900.
- Sanders, B.F., 2007. Evaluation of on-line DEMs for flood inundation modeling. *Advances in Water Resources* 30, 1831–1843.
- Sapiano, M.R.P., Arkin, P.A., 2009. An Intercomparison and Validation of High-Resolution Satellite Precipitation Estimates with 3-Hourly Gauge Data. *Journal of Hydrometeorology* 10, 149–166.
- Sawicz, K., Wagener, T., Sivapalan, M., Troch, P., 2011. Catchment classification: empirical analysis of hydrologic similarity based on catchment function in the eastern USA. *Hydrology and Earth System Science Discussion* 8, 4495–4534.
- Schanze, J., 2006. *Flood Risk Management: A Basic Framework*, NATO Science Series. Springer Netherlands, Dordrecht.
- Schneider, L.E., McCuen, R.H., 2005. Statistical Guidelines for Curve Number Generation. *Journal of Irrigation and Drainage Engineering*, 131, 282.
- Schröter, K., Llort, X., Velasco-Forero, C., Ostrowski, M., Sempere-Torres, D. 2011. Implications of radar rainfall estimates uncertainty on distributed hydrological model predictions, *Atmospheric Research* 100(2-3), 237–245.

- Schultz, G., 1996. Remote sensing applications to hydrology: runoff. *Hydrological Sciences Journal/Journal des Sciences* 41 (4).
- Seo, B.-C., Cunha, L. K., Krajewski, W. F., Smith, J. A., in preparation to be submitted to *Water Resources Research*. Impact of radar-rainfall calibration offsets on the hydrological simulation of the 2008 Iowa flood.
- Seo, B.-C., Krajewski, W. F., Smith, J. A., submitted to *Hydrological Sciences Journal*. Four-dimensional reflectivity data comparison between two ground-based radars: Methodology and statistical analysis.
- Seo, B.-C., Krajewski, W.F., Kruger, A., Domaszczynski, P., Smith, J.A., Steiner, M., 2011. Radar-rainfall estimation algorithms of Hydro-NEXRAD. *Journal of Hydroinformatics* 13, 277–291.
- Sharif, H.O., Ogden, F.L., Krajewski, W.F., Xue, M., (2004), Statistical analysis of radar-rainfall error propagation. *Journal of Hydrometeorology* 5(1), 199-212.
- Sharif, H.O., Ogden, F.L., Krajewski, W.F., Xue, M., 2002. Numerical simulations of radar-rainfall error propagation. *Water Resources Research* 38(8), 1140.
- Shreve, R., 1969. Stream Lengths and Basin Areas in Topologically Random Channel Networks. *The Journal of Geology* 77, 397–414.
- Sidle, R., 2006. Field observations and process understanding in hydrology: essential components in scaling. *Hydrological Process* 20, 1439–1445.
- Sivapalan, M., 2009. The secret to “doing better hydrological science”: change the question! . *Hydrological Process* 23, 1391–1369.
- Sivapalan, M., Blöschl, G., Zhang, L., Vertessy, R., 2003. Downward approach to hydrological prediction. *Hydrological Processes* 17(11), 2101–2111.
- Sivapalan, M., Grayson, R., Woods, R., 2004. Scale and scaling in hydrology. *Hydrological Process* 18, 1369–1371.
- Sivapalan, M., Kalma, J.D., 1995. Scale problems in hydrology: Contributions of the Robertson workshop. *Hydrological Process* 9, 243–250.
- Slater, J.A., Heady, B., Kroenung, G., Curtis, W., Haase, J., Hoegemann, D., Shockley, C., Tracy, K., 2011. Global Assessment of the New ASTER Global Digital Elevation Model. *Photogrammetric Engineering & Remote Sensing* 77, 335–349.
- Small, S.J., Jay, L.O., Mantilla, R., Curtu, R., Cunha, L.K., Morgan, F., Krajewski, W.F., submitted to *Water Resources Research*. An asynchronous solver for systems of ODEs linked by a directed tree structure.
- Smith E, Asrar G, Furuhashi Y, Ginati A, Mugnai A, Nakamura K, Adler R, Chou M, Desbois M, Durning J, et al., 2007. International Global Precipitation Measurement (GPM) Program and Mission: An Overview. In: Levizzani, V., Bauer, P., Turk, F. (eds.). *Measuring Precipitation From Space*. Springer, 611-653.
- Smith, L.C., 1997. Satellite remote sensing of river inundation area, stage, and discharge: A review, *Hydrological Processes* 11(10) 1427–1439.

- Smith, L.C., Pavelsky, T.M., 2008. Estimation of river discharge, propagation speed, and hydraulic geometry from space: Lena River, Siberia. *Water Resources Research* 44.
- Smith, M.B., Seo, D.-J., Koren, V.I., Reed, S.M., Zhang, Z., Duan, Q., Moreda, F., Cong, S., 2004. The distributed model intercomparison project (DMIP): motivation and experiment design. *Journal of Hydrology* 298, 4–26.
- Smith, R.G., Berry, P.A.M., 2011. Evaluation of the differences between the SRTM and satellite radar altimetry height measurements and the approach taken for the ACE2 GDEM in areas of large disagreement. *Journal of Environmental Monitoring* 13, 1646–1652.
- Soil Survey Staff, Natural Resources Conservation Service, United States Department of Agriculture. Soil Survey Geographic (SSURGO) Database for Iowa and Minnesota. Available through: <http://soildatamart.nrcs.usda.gov>. [Accessed by Jun 2009].
- Sooroshian, S., Hsu, K.L., Gao, X., Gupta, H.V., Imam, B., Braithwaite, D., 2000. Evaluation of PERSIANN system satellite-based estimates of tropical rainfall. *Bulletin of the American Meteorological Society* 81, 2035–2046.
- Soulsby, C., Tetzlaff, D., Dunn, S.M., Waldron, S., 2006. Scaling up and out in runoff process understanding: insights from nested experimental catchment studies. *Hydrological Process* 20, 2461–2465.
- Stall, J.B., Fok, Y., 1968. Hydraulic geometry of Illinois Streams. No. B-005-ILL, Illinois State Water Survey, Urbana.
- Staudinger, M., Stahl, K., Seibert, J., Clark, M.P., Tallaksen, L.M., 2011. Comparison of hydrological model structures based on recession and low flow simulations. *Hydrologic Earth System Science Discussion* 8, 6833–6866.
- Stensrud, D., 2007. Parameterization Schemes. Keys to Understanding Numerical Weather Prediction Models. Cambridge Univ. Press, Cambridge (UK).
- Stewardson, M., 2005. Hydraulic geometry of stream reaches. *Journal of Hydrology* 306, 97–111.
- Su, F., Hong, Y., 2008. Evaluation of TRMM Multisatellite Precipitation Analysis (TMPA) and its utility in hydrologic prediction in the La Plata Basin. *Journal of Hydrometeorology* 9(4), 622–640.
- Sweet, W., 2003. Bankfull hydraulic geometry relationships and recurrence intervals for North Carolina's Coastal Plain. *Journal of American Water Resources Association* 39, 861–871.
- Talebi, A., Troch, P.A., Uijlenhoet, R., 2008. A steady-state analytical slope stability model for complex hillslopes. *Hydrological Process* 22, 546–553.
- Tedesco, M., Narvekar, P.S., 2010. Assessment of the NASA AMSR-E SWE Product. Selected Topics in Applied Earth Observations and Remote Sensing, IEEE 3, 141–159.

- Tetzlaff, D., McDonnell, J. J., Uhlenbrook, S., McGuire, K. J., Bogaart, P. W., Naef, F., Baird, A. J., Dunn, S. M. and Soulsby, C., 2008. Conceptualizing catchment processes: simply too complex?. *Hydrological Processes* 22(11), 1727–1730.
- Tetzlaff, D., McDonnell, J.J., Uhlenbrook, S., 2008. Conceptualizing catchment processes: simply too complex? *Hydrological Process* 22, 1727–1730.
- Thompson, J.A., Bell, J.C., Butler, C.A., 2001. Digital elevation model resolution: effects on terrain attribute calculation and quantitative soil-landscape modeling. *Geoderma*, 100, 67–89.
- Troutman, B., Over, T., 2001. River flow mass exponents with fractal channel networks and rainfall. *Advances in Water Resources* 24, 967–989.
- Tsihrintzis, V., 1997. Urban stormwater quantity/quality modeling using the SCS method and empirical equations. *Journal of the American Water Resources Association* 33, 163–176.
- Vazquez, R.F., Feyen, J., 2007. Assessment of the effects of DEM gridding on the predictions of basin runoff using MIKE SHE and a modelling resolution of 600 m. *Journal of Hydrology* 334, 73–87.
- Villarini, G., Krajewski, W. F., 2009a. Empirically based modelling of radar-rainfall uncertainties for a C-band radar at different time-scales. *Quarterly Journal of the Royal Meteorological Society* 135(643), 1424–1438.
- Villarini, G., Krajewski, W. F., 2010. Review of the Different Sources of Uncertainty in Single Polarization Radar-Based Estimates of Rainfall. *Surveys in Geophysics* 31(1), 107–129.
- Villarini, G., Krajewski, W. F., Ciach, G. J Zimmerman, D. L., 2009b. Product-error-driven generator of probable rainfall conditioned on WSR-88D precipitation estimates, *Water Resources Research*, 45(1).
- Wang, Y., Lei, X., Jiang, Y., Wang, H., 2010. Performance comparison of three multi-objective optimization algorithms on calibration of hydrological model. *Sixth International Conference on Natural Computation (ICNC)*, 2798–2803.
- Welles, E., S. Sorooshian, G. Carter, B. Olsen (2007), Hydrologic verification: A call for action and collaboration. *Bulletin of American Meteorological Society* 88, 503–511.
- Western, A., Finlayson, B., McMahon, T., 1997. A method for characterizing longitudinal irregularity in river channels. *Geomorphology* 21, 39–51.
- Wilson, J.W., Brandes, E.A., 1979. Radar Measurement of Rainfall-A Summary. *Bulletin of American Meteorological Society* 60, 1048–1060.
- Wolfe, R.E.; Ridgway, B.L.; Patt, F.S.; Masuoka, E.J., 2009. MODIS science algorithms and data systems lessons learned. *Geoscience and Remote Sensing Symposium, 2009 IEEE International, IGARSS 2009* 5, V-473-V-476.

- Wood, E.F., Roundy, J.K., Troy, T.J., van Beek, L.P.H., Bierkens, M.F.P., Blyth, E., de Roo, A.A., Doll, P., Ek, M., Famiglietti, J., Gochis, D., van de Giesen, N., Houser, P., Jaffe, P.R., Kollet, S., Lehner, B., Lettenmaier, D.P., Peters-Liedard, C., Sivapalan, M., Sheffield, J., Wade, A., Whitehead, P., 2011. Hyperresolution global land surface modeling: Meeting a grand challenge for monitoring Earth's terrestrial water. *Water Resources Research* 47.
- Wood, E.F., Sivapalan, M., Beven, K., Band, L., 1988. Effects of Spatial Variability and Scale with Implications to Hydrologic Modeling. *Journal of Hydrology* 102, 29–47.
- Wooding, R., 1965. A hydraulic model for the catchment-stream problem: I. Kinematic-wave theory. *Journal of Hydrology* 3, 254–267.
- Xia, Y., Mitchell, K., Ek, M., Sheffield, J., Cosgrove, B., Wood, E., Luo, L., Alonge, C., Wei, H., MENG, J., Livneh, B., Lettenmaier, D., Koren, V., Duan, Q., Mo, K., Fan, Y., Mocko, D., 2012. Continental-scale water and energy flux analysis and validation for the North American Land Data Assimilation System project phase 2 (NLDAS-2): 1. Intercomparison and application of model products. *Journal of Geophysical Research* 117, D03109.
- Yang, D., Herath, S., Musiak, K., 2002. A hillslope-based hydrological model using catchment area and width functions. *Hydrological Science Journal* 47(1), 49–65.
- Yilmaz, K., Gupta, H., 2008. A process-based diagnostic approach to model evaluation: Application to the NWS distributed hydrologic model. *Water Resources Research* 44, 1–18.
- Zaitchik, B.F., Rodell, M., Reichle, R.H., 2008. Assimilation of GRACE Terrestrial Water Storage Data into a Land Surface Model: Results for the Mississippi River Basin. *Journal of Hydrometeorology* 9, 535–548.
- Zhang, W., Montgomery, D.R., 1994. Digital elevation model grid size, landscape representation, and hydrologic simulations. *Water Resources Research* 30, 1019.
- Zhang, X., Drake, N., Wainwright, J., 1999. Comparison of slope estimates from low resolution DEMs: scaling issues and a fractal method for their solution. *Earth Surface Processes and Landforms* 24, 763–779.
- Zhang, Y., Adams, T., Bonta, J. V., 2007. Subpixel-scale rainfall variability and the effects on separation of radar and gauge rainfall errors. *Journal of Hydrometeorology* 8(6), 1348–1363.